The dissertation committee for Aliya Siegel Lapp certifies that this is the approved version of the following dissertation:

Experimental and theoretical investigation of electrochemically synthesized AuPt dendrimer-encapsulated nanoparticles (DENs)

Committee:

Richard M. Crooks, Supervisor

Graeme Henkelman

Charles B. Mullins

Sean T. Roberts

Simon M. Humphrey

Experimental and theoretical investigation of electrochemically synthesized AuPt dendrimer-encapsulated nanoparticles (DENs)

by

Aliya Siegel Lapp

Dissertation

Presented to the Faculty of the Graduate School of

The University of Texas at Austin

in Partial Fulfillment

of the Requirements

for the Degree of

Doctor of Philosophy

The University of Texas at Austin

May 2020

Dedication

This dissertation is dedicated to my mother and sister, who have had every faith in my success.

Acknowledgements

First and foremost, I thank my advisor, Dr. Richard M. Crooks, for his support, patience, and wise guidance over the years. Under your tutelage, I have grown as both a scientist and a human being. I am forever indebted to you. I would also like to thank Drs. Graeme Henkelman and Anatoly Frenkel for providing their expertise in collaborative projects. Additionally, I thank Drs. Graeme Henkelman, Buddie Mullins, Simon Humphrey, and Sean Roberts for serving on my PhD committee.

I would also like to acknowledge my talented collaborators over the years: Zhiyao Duan, Long Luo, Nicholas Marcella, and Janis Timoshenko. Zhiyao, you have both dazzled me with your ingenuity and proven to be a dependable collaborator. I have relished the opportunity to share scientific endeavors with someone that has such a zeal for science. Long, the same comments apply to you. I feel truly lucky to have had the opportunity to work with you. Nick and Janis, thank you for your assistance with EXAFS measurements and analysis. I have learned a great deal from our discussions.

Finally, I thank my grandmother for pushing me from an early age to achieve my potential (who knew she meant electrode potential?).

Abstract

Experimental and theoretical investigation of electrochemically synthesized AuPt dendrimer-encapsulated nanoparticles (DENs)

Aliya Siegel Lapp, PhD.

The University of Texas at Austin, 2020

Supervisor: Richard M. Crooks

Herein, experiment and theory are combined to study the efficacy of synthesizing core@shell Au@Pt dendrimer-encapsulated nanoparticles (DENs) through electrochemical means. DENs are small (~1-2 nm), catalytically active nanoparticles (NPs) with precise sizes and compositions. These features assist pairing experiment with theory and catalytic interpretation. The small sizes of DENs can impart interesting physical and chemical properties that differ from bulk phase materials.

Core@Pt shell NPs with monolayer (ML)-thick shells minimize the use of Pt, which is a key catalyst for various

reactions but is expensive and scarce. Owing to the fact that the available techniques for Pt ML deposition were originally developed for bulk Au, their applicability to ~1.6 nm Au DEN cores is not trivial.

In this dissertation, we explore several electrochemical strategies for synthesizing Au@Pt DENS: hydride-terminated (HT) Pt electrodeposition and underpotential deposition, followed by galvanic exchange with Pt (UPD/Pt GE) using two different UPD metals (Cu and Pb). Each of these techniques deposits a single Pt ML onto bulk Au surfaces. However, when they are applied to ~1.6 nm Au DENs, the AuPt NP structures that form are both dissimilar to one another and to the corresponding structures for bulk Au.

The HT synthesis is found to lead to an alloy structure, whereas AuPt NP structure formed upon UPD/Pt GE depends on the choice of the UPD metal (Cu or Pb). More specifically, Cu UPD/Pt GE produces a core@shell structure, whereas an alloy structure is afforded by Pb UPD/Pt GE. These conclusions are supported by extensive experimental characterization and density functional theory (DFT) calculations. For the HT method, a core@shell structure can ultimately be obtained, but requires 3-5 total HT pulses.

Due to the fact that catalysis tends to be highly structure sensitive, the results of these studies are important for rational design of catalysts. Indeed, we show that varying the number of HT pulses (from 1-10) can be used to tune electrocatalysis for formic acid oxidation (FAO).

Table of Contents

List of Tables

List of Figures

List of Illustrations

Chapter 1: Introduction

1.1. Synopsis

Dendrimers (Chapter 1.2) are polymers that can be used as molecular templates for nanoparticle (NP) synthesis. Importantly, dendrimers help control NP size, without imparting significant metal-ligand interactions.[1-4] The combination of size control and minimal metal-ligand interactions allows for the synthesis of catalytically active NPs with well-defined structures and compositions.[1-4] These features aid meaningful interpretation of catalytic results and facilitate the pairing of experiment with theory.[1] One application of dendrimer-encapsulated nanoparticles (DENs; Chapter 1.3) is the use of NP architecture (e.g., core@shell and alloy) to fine-tune electrocatalysis.[1,5]

Core@shell structuring, in particular, can be used to harness the catalytic power of expensive, low-abundance metals (e.g., Pt) while restricting loading to an atomically thin shell (e.g., a monolayer (ML)).[1,6-8] Direct electrodeposition of Pt typically results in three-dimensional growth.[9,10] Three-dimensional Pt shell growth complicates sample reproducibility and the correlation between structure and function for catalytic studies. Several techniques have been designed to bypass this limitation, the most

popular of which is underpotential deposition followed by galvanic exchange with Pt (UPD/Pt GE; Chapter 1.4).[6,7,11-21] However, UPD/Pt GE is indirect and suffers from complications associated with incomplete GE.[22-26] Chapter 1.5 discusses a recently developed, more direct method for electrodepositing Pt MLs onto Au substrates: hydride-terminated (HT) Pt electrodeposition.

1.2. Dendrimers

Dendrimers, (e.g., left frame of Illustration 1.1a) are spherical, tree-like polymers. Since their advent in 1978,[27] various types of dendrimers have been synthesized.[28-31] The dendrimers relevant to the work presented in this dissertation are poly(amido)amine (PAMAM) dendrimers.[28] PAMAM dendrimers are named according to two criteria: (1) the generation of the dendrimer (G*n*), which is the number of branch points (*n* = 0-10) beyond the ethylene diamine core and (2) the identity of the terminal functional groups (e.g., $-NH_2$).[2,28] G*n* is controlled by the number of iterations of the two steps in Illustration 1.2, whereas the identity of the terminal functional groups depends on the reagent used in Step 2 of the final iteration.[28] For example, a single iteration of Steps 1 and 2 in Illustration 1.2 generates G1-NH_2 dendrimers (Figure 1.1) which possess a single set of branch points (circled in red) and terminal amine groups (circled in blue). Using

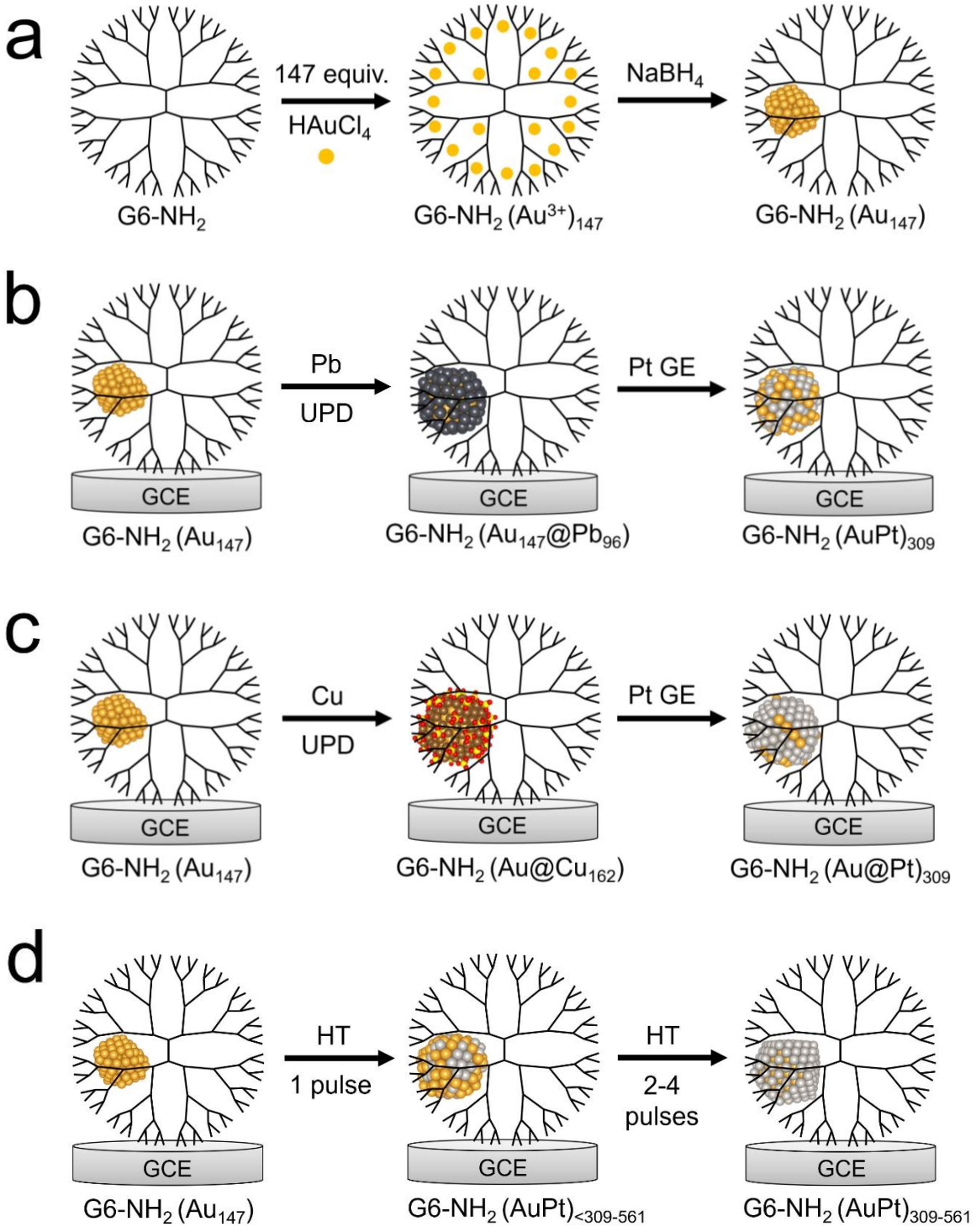

Illustration 1.1

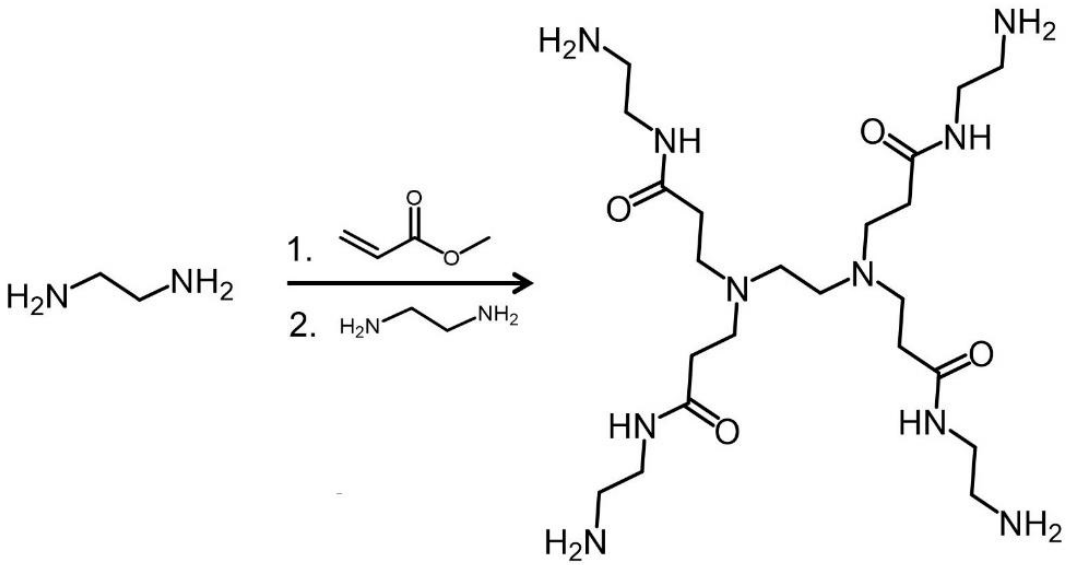

Illustration 1.2

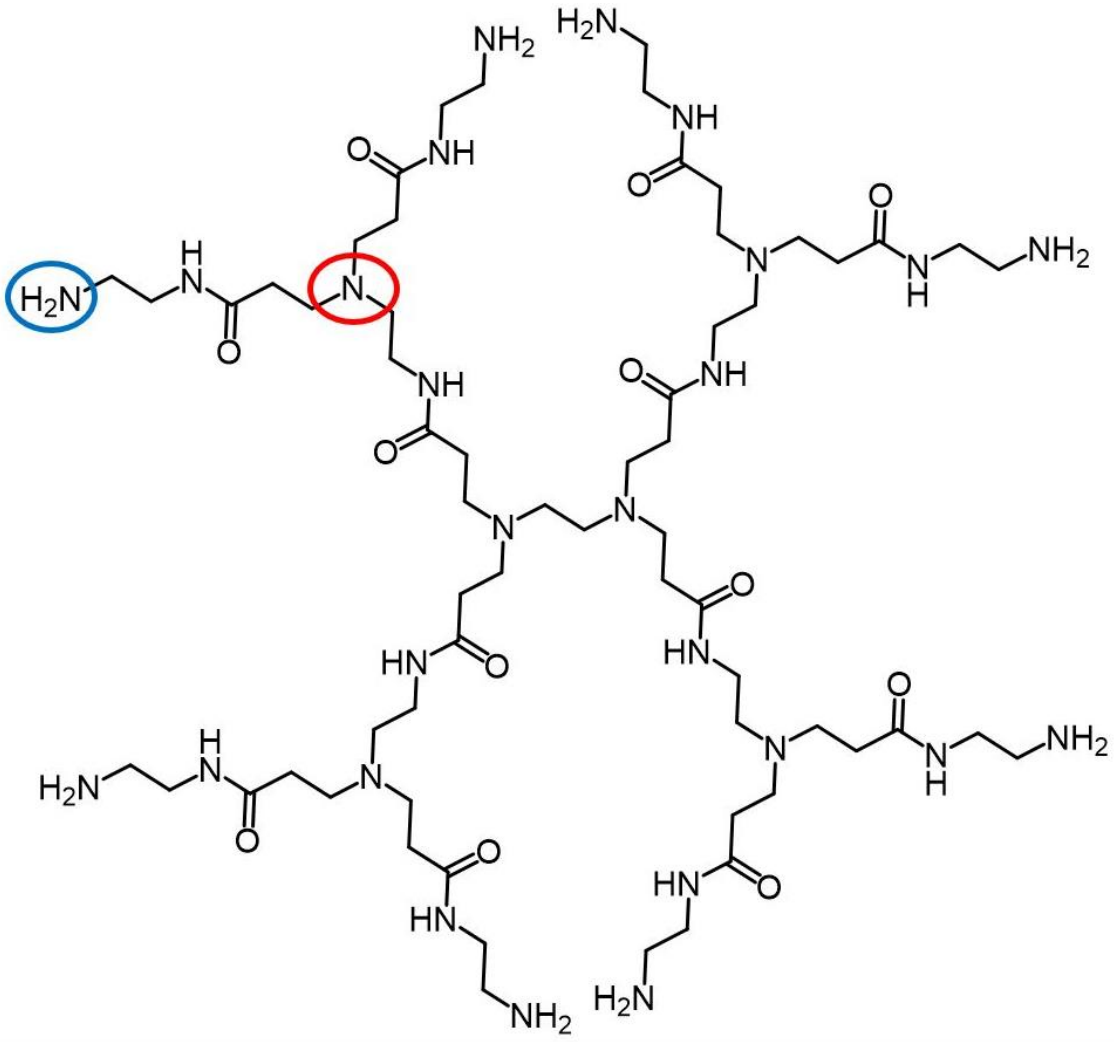

Figure 1.1

Depiction of a generation 1, poly(amido)amine (PAMAM) dendrimer (G1-NH_2). As shown, a G1-NH_2 dendrimer contains a single set of branch points (G1) and amine (-NH_2) terminal groups. These features are highlighted by the red and blue circles, respectively.

ethanolamine instead of ethylene diamine in Step 2 of the final synthetic iteration would have resulted in G1-OH dendrimers.[28]

The most relevant application of dendrimers for the work presented in this dissertation is the use of higher generation dendrimers (≥G4) as molecular templates for NP synthesis.[1,2,28–30] The ability of higher generation dendrimers to serve as molecular templates for NP synthesis arises from their crowded peripheries.[2,28] Dendrimer diameter grows nearly linearly with generation number, while the number (N) of terminal functional groups scales exponentially ($N = 2^{Gn+2}$ for $n = 0,1,2,\ldots$).[28] For example, G6-NH_2 dendrimers have a diameter of 6.7 nm and 256 terminal amine groups.[28] Mismatched rates of growth in dendrimer diameter and the number of terminal groups leads to steric crowding at the dendrimer periphery for ≥G4 dendrimers (e.g., left frame of Illustration 1.1a).[2,28]

Accordingly, higher generation dendrimers act like molecular cages for the NPs synthesized within.[2,28] This condition holds true as long as NP size is smaller than the diameter of the dendrimers.[2,28] NPs encapsulated by PAMAM dendrimers are referred to as dendrimer-encapsulated NPs (DENs) and are discussed in the next sub-section.[1,2,28,32]

1.3 Dendrimer-encapsulated nanoparticles (DENs)

General overview

DENs were first synthesized by Crooks and coworkers in 1998.[28,33] Entrapment of NPs inside of dendrimers prevents NP agglomeration, leading to narrow size distributions.[1,2,28,32] Size control for conventional small NPs is typically obtained by using strongly binding ligands, rendering the NPs inactive for catalysis.[1] DENs, however, have narrow size-distributions, small sizes (~1-2 nm), and minimal metal-ligand interactions.[1,2,28] These factors allow for the preparation of catalytically active NPs with precise sizes and structures.[1,2,28]

Well-defined NP characteristics facilitate the isolation of factors contributing to catalysis. They also aid the correlation of experimental results with theoretical calculations, which assume homogeneous sizes and structures.[1] The small size of DENs further enables the coupling of experiment and theory, as theoretical computations are expensive beyond a few hundred atoms.[1] Overall, DENs have been shown to be catalytically active for a variety of reactions, including allyl alcohol hydrogenation,[28,34] carbon-carbon coupling,[28] the oxygen reduction reaction (ORR),[1,2,35] formic acid oxidation (FAO),[16,36] CO oxidation,[12,37] and CO_2 reduction.[38]

Monometallic DENs

Synthesis of monometallic DENs consists of encapsulation of metal ions inside of dendrimer voids, followed by reduction to form zerovalent NPs (Illustration 1.1a).[1,2,28] NP size (~1-2 nm) is chosen to be significantly smaller than the diameter of the dendrimers to ensure NP encapsulation, but large enough for characterization via standard techniques (e.g., TEM).[1,2,28] To achieve such small sizes, magic number metal ion: dendrimer ratios are used.[1,2,28] Magic number ratios correspond to atom numbers with special stability and closed shell structures.[39] For example, the $AuCl_4^-$:G6-NH_2 ratio in Illustration 1.1a is 147:1. This ratio corresponds to the magic number (147) for a cuboctahedral ~1.6 nm Au NP (Au_{147}).[15,39,40] The method in Illustration 1.1a has been used to synthesize Cu, Au, Pt, Pd, Ag, Ni, Fe, and Rh monometallic DENs.[1,2,28,41] Within the size range of DENs (~1-2 nm), small changes in the number of atoms can create significant changes in electronic, structural, magnetic, and chemical properties.[1,2,28,42,43]

Multimetallic DENs

In addition to monometallic DENs, multimetallic DENs (alloy, core@shell, and alloy-core@shell) have been synthesized.[1,2,28,32] Multimetallic DENs are synthesized through several routes, depending on the desired structure. For example, random alloy DENs

are synthesized using a co-complexation strategy, wherein two metals are complexed to the dendrimers and then reduced simultaneously.[2,28] This strategy has been used to synthesize PdAu, PdPt, AuAg, NiSn, PdCu, PtCu, PtAu, and RhAu DENs.[2,3,34,41,44]

Core@shell DENs, have been synthesized both chemically[2,28] and electrochemically.[1,2,13,36,37] Chemical preparation of core@shell DENs entails a sequential reduction strategy, wherein a second metal is chemically reduced on top of pre-formed monometallic DEN cores.[2,28] Electrochemically, underpotential deposition (UPD) of Pb or Cu,[12-15,37,45,46] UPD followed by Pt GE (UPD/Pt GE) (Illustrations 1.1b and 1.1c),[12-14,16] and most recently, hydride-terminated (HT) Pt electrodeposition (Illustration 1.1d)[36] have been used to synthesize core@shell DENs. These methods will be discussed in detail in the next two sub-sections. Using these core@shell techniques, Au, Pt, and AuPd DEN cores have been adorned with Cu, Pb, Pd, and Pt shells.[1,2,13,36,37,40] However, as we will show in this dissertation, these techniques do not always afford the expected core@shell structures.

1.4. Underpotential Deposition and Pt Galvanic Exchange (UPD/Pt GE)

General overview

UPD is a process by which a single atomic ML of a metal

electrodeposits onto an underlying substrate.[47–49] UPD occurs at electrode potentials positive of bulk deposition due to favorable interactions between the UPD metal and the underlying substrate.[47–49] Specifically, the depositing metal must bind more strongly to the substrate than it does to itself.[48] Thus, only certain combinations of metals undergo UPD.

While multiple metals can perform UPD on Au (such as Cu, Pb, Hg, Cd, Bi, and Tl),[47,48] Pt is an example of a metal that cannot undergo UPD on Au.[10,50] A common way to bypass this challenge is to use a two-step process: UPD of an appropriate metal, like Pb or Cu, followed by Pt GE (UPD/Pt GE; Illustrations 1.1b and 1.1c).[6,7,11–21] UPD/Pt GE is frequently used to prepare core@shell Au@Pt NPs, which have been shown to be electrocatalytically active for reactions such as the ORR,[15,51–53] CO oxidation,[16,54] the methanol oxidation reaction (MOR),[54,55] and FAO.[16,56]

UPD on nanoparticles (NPs)

Two prevalent UPD metals used for synthesizing core@Pt shell NPs via UPD/Pt GE are Pb and Cu.[6,7,12,13,15,16,18,57] Pb and Cu UPD on macroscopic Au surfaces have been studied extensively.[20,47,58,59] Comparatively little is known about UPD onto NPs.[11–15,34,37,45,46,60–68] As we have recently shown, the structure (e.g., alloy vs. core@shell) of AuPt NPs obtained upon UPD/Pt GE on Au NPs depends

on the properties of the UPD layer.[13] Therefore, in-depth knowledge of UPD processes and the resulting structures on Au NPs is important for rational design of AuPt catalysts.

Among the studies that have been carried out for UPD on NPs, most have used >3 nm (bulk-like) NPs.[11,60-65,67,69] There are several factors that suggest that UPD on small NPs is apt to proceed differently than on macro-surfaces and larger NPs. First, NPs have a greater proportion of high energy sites (e.g., corner and edge sites), which are difficult to deposit onto.[15,37,45] Indeed, sub-ML coverages are commonly reported for UPD on NPs and the presence of high energy sites is an oft-invoked explanation.[13,14,36,45,46,68,70] The fraction of high energy sites increases as NP size decreases, exacerbating their influence on surface-dependent processes.[1] For example, corner and edge sites make up 65% of the surface of a 147-atom cuboctahedral NP[37] and 85% of the surface of a 55-atom cuboctahedral NP.[71]

Second, key UPD features, such as the potentials for UPD and the structures formed, tend to be facet dependent for bulk surfaces.[47] NPs have smaller facets than bulk systems and curved geometries, both of which disrupt long-range order.[46] This discrepancy grows as NP size decreases. For instance, the (111) and (100) facets of 147-atom cuboctahedral NPs contain just 10 and 16 atoms, respectively.[46] Third, there is considerable sharing of

atoms between facets for small NPs. For example, each (111) facet of a 147-atom cuboctahedral NP has just a single atom that is unshared with adjacent (100) facets.[13,46] Fourth, it has previously been shown that the boundary between UPD and overpotential deposition (OPD), which yields three-dimensional layer growth, is unclear for NPs.[69,70] In fact, several theoretical studies have predicted that UPD is not possible when NP size is sufficiently small (although the exact threshold has not yet been delineated).[69]

UPD on DENs

As noted in Chapter 1.3, DENs are uniquely positioned for combining experimental results with theoretical calculations, due to small numbers of atoms (typically ~55-309) and nearly uniform NP sizes and structures.[1,2,28] This combined experimental-theoretical approach has been applied to studying UPD on DENs.[13,15,16,46] In these studies, density functional theory (DFT) was employed to calculate the binding energies of UPD atoms on DENs surfaces[13,15,46] and molecular dynamics (MD) was used to equilibrate the resulting NP structures.[13,15,46] Using this method, DFT was shown to be a powerful technique for accurately predicting experimental peak positions for Cu[13,46] and Pb[13,15,16] UPD on Au[13,15,16] and Pt[46] DENs.

The combination of DFT and MD (DFT-MD) in our preliminary studies of UPD on DENs, however, was limited; MD was performed on

just the final NP structures (e.g., after the completion of UPD).[15,46] Recently, the DFT-MD approach for studying UPD on DENs was expanded.[13] In particular, MD was performed at each stage of the UPD process: before UPD and in 10 atom increments during UPD.[13] This analysis provided accurate predictions of UPD metal coverages, as well an in-depth UPD mechanism, on Au_{147} DENs. Additionally, this study[13] served to refine the mechanism that we had proposed in earlier studies (*vide infra*)[15,16,45,46] for UPD on DENs.

Early studies of UPD on DENs suggested a sequential, facet-by-facet deposition mechanism.[15,16,45,46] Specifically, UPD was believed to coat the (100) facets of the DENs substrates before the (111) facets.[15,16,45,46] This claim was supported theoretically by DFT predictions that UPD was more energetically favorable on (100) facets than on (111) facets,[15,16,46] and experimentally, by the presence of multiple UPD peaks.[15,45,46] Our most recent analysis of Pb and Cu UPD on Au_{147} DENs, however, suggested that this mechanism is unlikely for three reasons.[13] First, MD simulations before UPD showed that Au_{147} spontaneously deforms from cuboctahedral to a (111)-like structure, containing just a single type of facet. Second, in-depth DFT-MD mechanistic analysis performed at various stages of UPD indicated that Pb electrodeposits randomly on Au_{147}. Random Pb electrodeposition was supported experimentally by the

formation of a surface alloy structure after Pt GE (e.g., Illustration 1.1b). Third, experimental results suggested that in analogy to Cu UPD on bulk Au,[47,68] the presence of two Cu UPD CV peaks was related to the co-adsorption of UPD metal cations and sulfate anions.[13]

UPD/Pt GE on DENs

As described in Chapter 1.3, UPD/Pt GE has been used to synthesize core@shell Au@Pt DENs[13–16] and alloy-core@shell AuPd@Pt DENs.[12] These DENs have been shown to be active electrocatalysts for the ORR,[14,15] FAO,[16] and CO oxidation.[12] For the purposes of synthesizing Au@Pt DENs, in particular, both Cu[13,14] and Pb[13,15,16] UPD/Pt GE have been used. Cu UPD/Pt GE on Au DENs led to a nearly complete Pt shell (~0.74-0.85 ML).[14] This first study was primarily proof-of-concept and characterization of the Au@Pt DENs was limited to cyclic voltammetry (CV) and ORR electrocatalysis. UPD/Pt GE on Au_{147} DENs was analyzed more completely in a later study, with Pb as the UPD metal.[15] For the purposes of the work presented here, the most important result from the latter study is that Pb UPD/Pt GE led to significantly lower Pt coverage (~0.55-0.57 ML) than Cu UPD/Pt GE.[15]

Although initial investigations of UPD/Pt GE on Au_{147} DENs suggested that the choice of UPD metal might alter the ultimate Pt

coverage,[14–16] the lack of a side-by-side comparison precluded definite conclusions from being drawn. For the purposes of UPD/Pt GE onto Au, several factors suggest that the Pb and Cu UPD processes are not interchangeable. For example, Pb UPD on bulk Au(111) leads to an incommensurate ML,[47] whereas a commensurate ML forms for Cu.[47,72] Other factors also differentiate Cu and Pb as UPD precursors for forming Pt MLs on Au substrates: the role played by electrolyte anions,[13,20,47,68,73,74] different propensities for the UPD metals to alloy with the Pt shell,[21] and the smoothness of the Pt films that result upon Pt GE.[59]

Recently, Pb and Cu UPD/Pt GE on Au DENs were directly compared using a combined experimental-theoretical approach.[13] Electrochemical analysis (CV) confirmed the discrepancy in Pt coverage for Pb and Cu UPD/Pt GE on Au_{147} DENs. Specifically, Cu UPD/Pt GE afforded ~20% higher Pt coverage than Pb UPD/Pt GE. Importantly, these differences were predicted by DFT-MD simulations. The MD component of this study (equilibration before, during, and after UPD/Pt GE) also enhanced understanding of the NP structures that form during each step of the UPD/Pt GE process. In particular, an alloy structure was predicted to form for Pb UPD/Pt GE (Illustration 1.1b), whereas a core@shell structure was predicted for Cu UPD/Pt GE (Illustration 1.1c). These structural

differences were validated by dissimilar signatures for FAO electrocatalysis (Figure 1.2).

1.5. Hydride-terminated (HT) electrodeposition

As mentioned earlier, direct electrodeposition of Pt typically results in three dimensional growth.[9,10] Despite the prevalence of UPD/Pt GE as a technique for sidestepping this issue, UPD/Pt GE has several complications that make it less than ideal. For instance, it is indirect and the UPD metal does not always exchange completely with Pt.[22-26] Leftover UPD metal can serve as an obstacle to straightforward interpretation of the factors governing the electrocatalytic activity of UPD/Pt GE-prepared core@Pt shell NPs.[37]

Recently, Moffat and coworkers introduced an elegant method for direct electrodeposition of Pt MLs without incurring three-dimensional growth.[75] This technique, termed the HT method, relies on the propensity of Pt to adsorb a ML of hydrogen at sufficiently negative potentials.[75] The HT method obviates many of the challenges associated with UPD/Pt GE, as it eliminates the sacrificial metal.[75-77] This method is depicted in Illustration 1.3. The electrode potential (vs. RHE, at pH 4.0) is pulsed between 0.86 V, where the surface is cleaned of adsorbates (Steps 1 and 3) and -0.34 V, where Pt electrodeposits (Step 2). Importantly, the

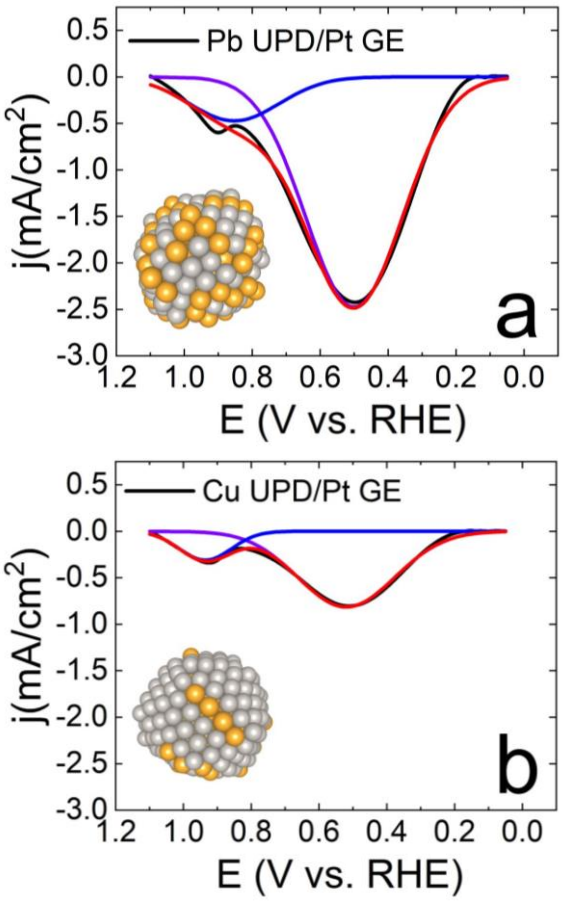

Figure 1.2

Positive going scans of the FAO CVs for AuPt DENs prepared by (a) Pb UPD/Pt GE and (b) Cu UPD/Pt GE onto Au_{147} DEN cores. The black, red, blue, and purple traces correspond to the experimental data, overall fit, and the two deconvoluted peaks, respectively. R^2 values for the fitted curves are 0.994 and 0.993 for Pb and Cu UPD/Pt GE, respectively. The insets of (a) and (b) show DFT-MD simulated atomic models for the corresponding 309 atom AuPt NPs. Gold and gray spheres represent Au and Pt atoms, respectively. The electrolyte was N_2-purged 0.10 M $HClO_4$ containing 0.10 M formic acid and the scan rate was 50 mV/s.

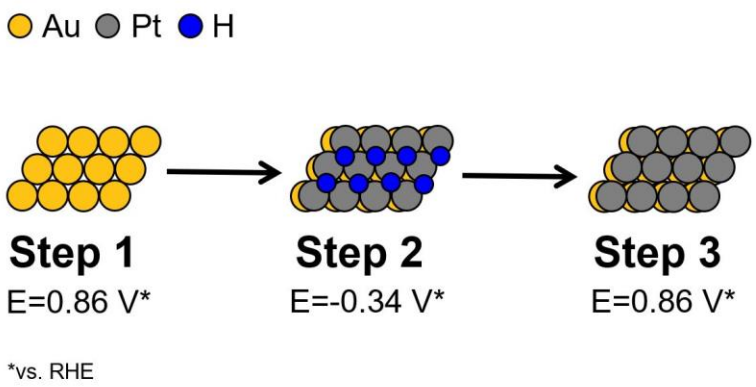

Illustration 1.3

electrode potential used for Step 2 is sufficiently negative that both Pt electrodeposition and hydrogen evolution on the Pt surface are diffusion limited. In other words, as soon as a Pt atom is deposited onto the Au surface, it is rapidly capped by adsorbed hydrogen (H_{ads}). This capping layer prevents the deposition of additional Pt atoms, restricting Pt growth to a single ML. In Step 3, the electrode potential is pulsed positive, to desorb H_{ads} from the electrode surface. Steps 2 and 3 can be repeated to deposit additional Pt MLs.[75,76,78–80] Moffat and coworkers showed a nearly one-to-one correspondence between the number of repetitions of Steps 2 and 3 and the number of Pt MLs.[75,76] In this way, the HT method serves as an electrochemical analog of atomic layer deposition.[75,76,78–80]

Since its inception,[75] the HT method and its general concept have been extended from bulk Au[75,76,78,81] to: (1) other substrates, such as Ni,[77,82] star-shaped dendritic Au rods (DARs),[79,80] nanoporous Au,[83,84] and carbon,[85–88] (2) other depositing metals, such as Ir,[89] Ni, Fe, and Co,[90,91] and (3) other terminating agents, such as OH[91] and CO.[10] However, until recently,[36,40] its application to NPs had not been explored. As we will show in Chapters 3 and 5, the AuPt structures formed upon HT Pt electrodeposition onto Au_{147} DENs are substantially different than those formed using a bulk Au

substrate.[36,40] Chapter 5 highlights the implications of these differences on FAO electrocatalysis.

1.6. Summary of dissertation research

There are several unifying themes in the work presented in this dissertation. First, in all cases, Pt was electrodeposited onto Au_{147} DENs with the goal of obtaining a core@shell Au@Pt structure. Accordingly, we used two techniques that have been shown to reliably yield Pt MLs on bulk Au substrates: the HT method[75,76] and UPD/Pt GE.[19,23,92] Chapters 3 and 5 discuss HT Pt electrodeposition onto Au_{147} DENs, while UPD/Pt GE (with Pb and Cu UPD metals) is the electrodeposition method of choice in Chapter 4.

Second, the AuPt structures derived upon the application of these two electrodeposition methods to Au_{147} DENs deviate from the corresponding structures for bulk Au. As mentioned earlier, a core@shell Au@Pt structure was anticipated based on the Pt MLs obtained on bulk Au using these techniques. Chapters 3-5 and Illustrations 1.1b-1.1d show that despite this expectation, a core@shell structure was only obtained in two cases: after Cu UPD/Pt GE and after multiple iterations of the HT method. A single iteration of the HT method and the use of Pb UPD/Pt GE were found to result in surface alloy AuPt NPs. These results underscore the

differences in geometrical and physicochemical properties for small Au NPs, relative to bulk Au. Clearly, care must be taken when choosing a method for electrodepositing Pt onto small Au NPs.

Third, Chapters 3-5 all involve the combination of experiment and theory, albeit to different extents. In Chapter 3, theoretical calculations were used to draft several plausible NP models based on experimentally obtained atomic and surface compositions. Theoretical EXAFS spectra were generated from these NP models and were compared to experimental EXAFS spectra. This comparison helped distinguish between the two most likely NP structures (alloy vs. core@partial shell). Finally, a tentative mechanism for AuPt alloying during the HT method was obtained via DFT-MD simulations. In Chapter 4, DFT-MD calculations were performed at each stage of UPD/Pt GE (before UPD, during UPD, and after Pt GE). The predicted UPD metal (Pb and Cu) coverages were in good agreement with those obtained experimentally.

Additionally, the in-depth DFT-MD simulations were able to provide a more realistic mechanism of UPD on DENs than the facet-by-facet mechanism we previously proposed. Chapter 5 focuses primarily on experimental characterization but uses simple theoretical calculations to aid validation of the number of Pt layers, as a function of the number of HT pulses. Overall, our results show that combining experimental results with theoretical

calculations is a powerful method for characterizing small NP structures.

Chapter 2: Experimental

2.1. Chemicals and materials

A 9.0 wt% solution containing sixth-generation, NH_2-terminated poly(amidoamine) (PAMAM) dendrimers dissolved in methanol was acquired from Dendritech, Inc. (Midland, MI). Before these dendrimers were used for DENs synthesis, a 100 µM stock solution in water was made. To this end, the original methanol solvent was evaporated under vacuum and the resulting solid was reconstituted in water. Deionized (DI) Milli-Q water (18.2 MΩ-cm; Millipore, Bedford, MA) was used to prepare all solutions.

A standardized 0.50 M NaOH solution, $NaBH_4$ (99.9%), $HAuCl_4$ (≥99.9%), $Pb(NO_3)_2$ (99.9%), HPLC-grade isopropanol (99.9%), formic acid (88-91%), and H_2SO_4 (95-98%) were obtained from Sigma-Aldrich. K_2PtCl_4 (99.9%), $CuSO_4$ (98%, anhydrous), 70% $HClO_4$ (in H_2O), and NaCl were purchased from Fisher (New Jersey, USA).

Cu TEM grids coated with lacey-carbon (catalog number LC400-Cu-UL) and C-film (catalog number CF400-Cu-UL) were purchased from EM Sciences (Gibbstown, NJ). Vulcan carbon (EC-72R) was obtained from ElectroChem, Inc. (Woburn, MA). PTFE membrane filters (0.5 µm pore size) were acquired from Advantec MFS, Inc. (Dublin, CA). CH Instruments (Austin, TX) was used to purchase the reference (Hg/Hg_2SO_4), working (glassy carbon, 3.0 mm), and counter (glassy

carbon rod) electrodes. All electrode potentials reported in this chapter were converted to the reversible hydrogen electrode (RHE) scale. EXAFS sample preparation used a working electrode made from Toray Teflon-treated carbon paper (TGP-H-120), acquired from The Fuel Cell Store (Boulder, CO).

2.2. Synthesis of Au_{147} DEN cores

Au_{147} DENs (2.0 μM) were synthesized using a method that we have previously reported.[2,28,40] While vigorously stirring an aqueous solution of 2.0 μM G6-NH_2 dendrimers, 147 equiv of $HAuCl_4$ were added dropwise in less than 2 min. Subsequently, 1.0 mL of 0.30 M NaOH containing an 11-fold excess of $NaBH_4$ was transferred to the reaction vial to reduce the dendrimer-$AuCl_4^-$ composites. Upon reduction, the color of the solution changed from light yellow to brown. The final solution volume was 10 mL. The BH_4^- in the Au_{147} DENs solution was allowed to deactivate for at least 12 hours before NP characterization was carried out.

Initial characterization of the Au_{147} DENs was performed via UV-vis spectroscopy with a Hewlett-Packard 8453 spectrometer, a 2.0 mm quartz cuvette, and MilliQ water as the reference.

2.3. Immobilization of Au_{147} DEN cores

For the electrochemical experiments described herein, Au_{147} DENs were immobilized onto Vulcan carbon (VC) and the resulting electrochemical ink was dropcast onto a glassy carbon electrode (GCE). The GCE used for this purpose was polished sequentially with three different alumina slurries (1.0 µm, 0.3 µm, and 0.05 µm), for 2 min per slurry. Residual alumina was removed by sonicating the polished GCE in water for ~10 min.

Electrochemical inks were prepared in three steps. First, a VC/isopropanol (VC/IPA) slurry was obtained by sonicating ~1.0 mg of VC together with 200 µL of IPA for ~10-15 min. Care was taken to ensure that this slurry was homogeneous (clump-free). Second, 1.0 mL of 2.0 µM Au_{147} DENs was added to the VC/IPA slurry. Third, the resulting mixture was sonicated for ~10-15 min. Finally, 6.0 µL of the electrochemical ink was dropcast onto the polished GCE. The Au_{147} DENs/VC-modified GCE was then used for electrochemical characterization and AuPt DENs synthesis.

2.4. Transmission electron microscopy (TEM)

Au_{147} and AuPt DENs were imaged using either transmission electron microscopy (TEM) or scanning TEM (STEM). In either case, a JEOL 2010F TEM with a 0.19 nm point-to-point resolution and an operating voltage of 200 kV was used. The Au_{147} DENs were prepared

for TEM by dropcasting an aliquot (2.0 μL) of the 2.0 μM DENs solution onto a carbon-coated Cu TEM grid and letting it air-dry. The electrochemical ink containing Au_{147} DENs supported on VC (described in Chapter 2.3) was prepared for TEM by making a 1:6 (ink: water) dilution, sonicating that mixture (~10 min), and then dropcasting 0.5 μL onto a lacey-carbon-coated Cu TEM grid. The AuPt DENs were loaded onto TEM grids by dragging a lacey-carbon-coated TEM grid gently across the surface of the GCE used for electrochemical synthesis and characterization.

The Au_{147} and AuPt DENs described in Chapter 5 were subjected to additional TEM characterization. Specifically, aberration-corrected STEM (acSTEM) imaging was carried out using a JEOL NEOARM TEM, operated at 80 kV and having a point-to-point resolution (at 80 kV) of 0.11 nm.

2.5. Cyclic voltammetry (CV)

CV was used to electrochemically clean and characterize the Au_{147} DENs surface. Electrochemical cleaning scans were performed by scanning the electrode potential from 0.7 V to 1.57 V and then back to 0 V in N_2-purged 0.10 M $HClO_4$, at a rate of 200 mV/s. A total of 20 cleaning cycles were used for this purpose. For Au_{147} DENs surface characterization, the scan rate was slowed to 100 mV/s and three CV cycles were recorded. The electrode potentials

used in this step were identical to those used for electrochemical cleaning. The AuPt DENs synthesized via the procedures outlined in Chapter 2.6 were electrochemically characterized in the same way as the Au_{147} DENs, except that a total of nine CV cycles were recorded.

2.6. Electrochemical synthesis of AuPt DENs

After electrochemical cleaning and characterization, Pt was electrodeposited onto the Au_{147} DENs. In Chapters 3 and 5, the HT method was used for this purpose, whereas Chapter 4 used UPD/Pt GE (with Pb and Cu UPD metals). HT Pt electrodeposition was carried out in N_2-purged 3.0 mM K_2PtCl_4 dissolved in 0.50 M NaCl at pH 4.0. The electrodeposition procedure followed the method shown in Illustration 1.3. Step 1 served to clear the electrode surface of any adsorbates that might have been introduced by immersion into the deposition solution. To this end, the electrode potential was held at 0.86 V for 30 s. After this brief cleaning step, the electrode potential was pulsed to -0.34 V for 1 s to electrodeposit Pt (Step 2). Subsequently, the electrode was pulsed back to 0.86 V to desorb H_{ads} (Step 3). In Chapter 3, synthesis was halted at this point. In Chapter 5, however, the synthetic scheme in Illustration 1.3 was repeated multiple times to obtain multiple Pt layers.

UPD/Pt GE with either Pb or Cu (Chapter 4) was performed using a two step procedure. First, the electrode potential was held at either -0.15 V (for Pb UPD) or 0.32 V (for Cu UPD) for 300 s. Second, Pt GE was carried out by adding 2.5 mM K_2PtCl_4 (pre-dissolved in ~1.0 mL of 0.10 M $HClO_4$) into the cell and monitoring the open circuit potential for 400 s (Figure 2.1).

In all cases (Chapters 3-5), Pt electrodeposition was followed by a sequential rinsing procedure. Specifically, the working electrode was rinsed in water for ~20 s, 20 mL of 0.10 M $HClO_4$ (5 min, with vigorous stirring), and again in water. As discussed in Chapter 3, this rinsing procedure serves to remove remaining Pt^{2+} ions. CV surface characterization of the AuPt DENs was subsequently performed in N_2-purged 0.10 M $HClO_4$, as described in Chapter 2.5.

2.7. Underpotential deposition (UPD) as a surface characterization technique

In addition to its use in AuPt DENs synthesis (via UPD/Pt GE), UPD was also employed for surface characterization of the HT-prepared AuPt DENs in Chapter 3 and as a way to study Pb and Cu UPD processes on Au_{147} DENs in Chapter 4.

Cu UPD onto AuPt (Chapter 3) and Au_{147} (Chapter 4) DENs was carried out in four steps. First, a control CV was recorded in N_2-purged 0.10 M $HClO_4$. This CV served to confirm the absence of

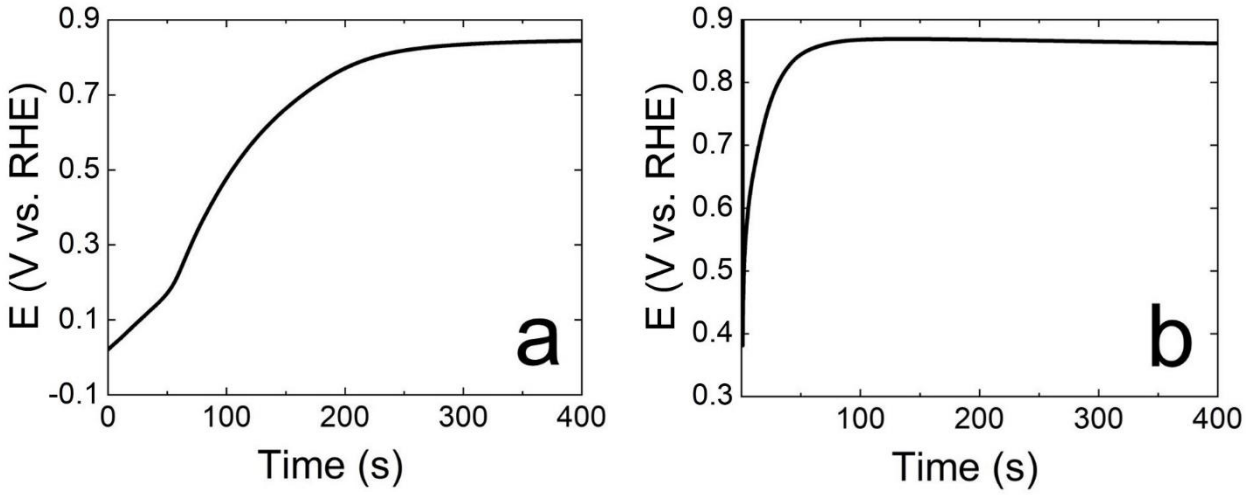

Figure 2.1

Open-circuit potential (OCP) vs. time plots for the Pt GE step of (a) Pb UPD/Pt GE and (b) Cu UPD/Pt GE on Au_{147} DEN cores. In each case, OCP measurement was initiated after adding 2.5 mM K_2PtCl_4 into the electrochemical cell.

contaminants and unwanted electrochemical process within the potential range pertinent to Cu UPD (0.30 V to 0.85 V). Second, 5.0 mM $CuSO_4$ was added into the cell and a Cu UPD CV was recorded. This step was accomplished by scanning the electrode potential from 0.70 V to 0.85 V and then back to 0.30 V, at a scan rate of 10 mV/s.

Third, Cu was deposited for 300 s at an electrode potential just positive of the onset of bulk Cu deposition. For the AuPt DENs in Chapter 3 this potential was determined to be 0.35 V and for the Au_{147} DENs in Chapter 4, it was 0.32 V. Fourth, the deposited Cu layer was stripped off by scanning the electrode potential from the value in the previous step to 0.85 V, at a rate of 10 mV/s. The resulting linear sweep voltammogram (LSV) was integrated to determine the surface area (SA) of the deposited Cu layer. In Chapter 3, the AuPt surface composition was determined by dividing the Pt SA determined from CV characterization in Cu-free 0.10 M $HClO_4$ by the Cu SA determined from the Cu LSV (as Cu coats both Pt and Au, but H only adsorbs to Pt). In Chapter 4, the Cu SA was used to calculate the coverage provided by Cu UPD. More details for each of these calculation methods are provided in Chapters 3 and 4.

Pb UPD onto Au_{147} DENs (Chapter 4) was executed using a similar procedure, except that the control CV was omitted due to a

competing hydrogen evolution process that occurs in the absence of Pb^{2+} ions.[47] We note that this process is avoided in the presence of Pb^{2+} ions.[47] The Pb UPD CV was obtained by scanning the electrode potential from 0.60 V to 0.70 V and back to -0.17 V in N_2-purged 1.0 mM $Pb(NO_3)_2$ dissolved in 0.10 M $HClO_4$, at a scan rate of 5.0 mV/s. Next, Pb was deposited at -0.15 V for 300 s. Pb was then oxidatively stripped by scanning the electrode potential from -0.15 V to 0.70 V at a rate of 5.0 mV/s. The corresponding LSV was integrated to determine the Pb SA. As discussed in detail in Chapter 4, the Pb SA was used to compute the Pb UPD coverage on Au_{147} DENs.

2.8. Energy dispersive spectroscopy (EDS)

EDS was carried out in Chapter 3 to confirm the specificity of HT Pt electrodeposition for the Au_{147} DEN surfaces. More specifically, it was used to show that Pt was deposited only on the NPs (and not on the VC support). EDS in Chapter 3 was accomplished using a Thermo Scientific Themis Z microscope with a Super-X EDS detector. A more detailed description of this microscope is provided in Chapter 3. The AuPt DENs prepared for EXAFS were also analyzed using EDS but used a JEOL 2010F TEM for this purpose.

The AuPt DENs in Chapter 5 were characterized using aberration corrected (ac) EDS with a JEOL NEOARM TEM equipped with properties described in Chapter 2.4. Unlike Chapter 3, EDS in Chapter 5 was used to assess NP structure (e.g., the extent of alloying) and to get a rough sense of the Pt shell thickness.

2.9. Extended x-ray absorption fine structure (EXAFS)

Sample preparation

Au_{147} DENs synthesis for EXAFS sample preparation was carried out in an analogous way to the method described in Chapter 2.3. However, we note the following exceptions. In order to get sufficient mass loading for EXAFS measurements, two 5.0 mL batches of 10 μM DENs were prepared. The exact recipe is provided in Chapter 3. Reduction was achieved by adding a 10-fold excess of $NaBH_4$, dissolved in 0.30 M NaOH, ~2.5 min after the first drop of $HAuCl_4$ was added to the reaction vial. The BH_4^- was allowed to deactivate for ~12 h. Subsequently, the DENs were purified by dialysis with 12 kDa MWCO cellulose tubing in 4.0 L of water for at least 12 hours.

Five electrochemical inks were prepared for AuPt synthesis. Each ink contained 2.0 mg of VC, 400 μL of IPA, and 2.0 mL of the dialyzed DENs. The inks were made into a spreadable paste by vacuum

filtration with 0.5 μm Advantec PTFE filters. The vacuum filtered paste was immediately spread onto a 0.9 x 0.5 cm^2 strip of Toray Teflon-treated carbon paper. Each DENs-modified electrode contained ~2.0 mg of the paste. The time associated with HT Pt electrodeposition was increased to 100 s due to the high loading of DENs and VC relative to the corresponding GCE procedure (Chapter 2.3). As discussed in greater detail in Chapter 3, this higher mass loading also necessitated the use of a low-sensitivity potentiostat and IR compensation. In all other respects, the HT Pt electrodeposition steps were the same as those detailed in Chapter 2.6. Five AuPt DENs-modified carbon paper strips were stacked together (with Kapton tape) for EXAFS analysis.

Measurements

EXAFS measurements of the Au-L_3 and Pt-L_3 edges were carried out at the Stanford Synchrotron Radiation Light Source (SSRL). Both transmission and fluorescence measurements were obtained. Fluorescence was analyzed in order to improve the signal-to-noise ratio for the Pt-L_3 edge, as it is a more sensitive technique. More details on the collection of EXAFS measurements can be found in Chapter 3.

2.10. X-RAY PHOTOELECTRON SPECTROSCOPY (XPS)

Compositional data for the AuPt DENs prepared in Chapter 5 was accomplished via XPS, using a Kratos Axis Ultra DLD spectrometer with a 0.1 eV step size and a 20 eV band pass energy. As we have previously described, the peak position for C 1s (284.5 eV) was used to calibrate the Au and Pt 4f peak positions.[14,93,94] Peak fitting parameters are discussed in Chapter 5. The purpose of XPS in Chapter 5 was to help validate the number of Pt layers deposited after multiple iterations of the HT method. XPS has a penetration depth of 10 nm,[95] and is thus able to provide atomic compositions for the AuPt DENs in Chapter 5, which ranged in size from ~2.1-3.9 nm.

2.11. FORMIC ACID OXIDATION (FAO)

In Chapter 5, FAO electrocatalysis was carried out using AuPt DENs synthesized with 1,3,5, and 10 HT pulses. In each case, the AuPt DENs-modified GCE was placed into an electrochemical cell containing 0.50 M H_2SO_4 and 0.50 M formic acid, while holding the electrode potential at 0.01 V. After the electrode was immersed, the electrode potential was cycled 20 times from 0.01 V to 1.26 V and back to 0.01 V at a rate of 10 mV/s.

Chapter 3: Experimental and Theoretical Structural Investigation of AuPt Nanoparticles Synthesized using a Direct Electrochemical Method[1]

3.1. Synopsis

In this report we examine the structure of bimetallic nanomaterials prepared by an electrochemical approach known as hydride-terminated (HT) electrodeposition. It has been shown previously that this method can lead to deposition of a single Pt monolayer on bulk-phase Au surfaces. Specifically, under appropriate electrochemical conditions and using a solution containing $PtCl_4^{2-}$, a monolayer of Pt atoms electrodeposits onto bulk-phase Au immediately followed by a monolayer of H atoms. The H-atom capping layer prevents deposition of Pt multilayers. We applied this method to ~1.6 nm Au nanoparticles (AuNPs) immobilized on an inert electrode surface. In contrast to the well-defined, segregated Au/Pt structure of the bulk-phase surface, we observe that HT electrodeposition leads to the formation of AuPt quasi-random alloy NPs rather than the core@shell structure anticipated

[1]The research in this chapter was previously published (see below). The dissertator was the primary contributor: Lapp, A.S.; Duan, Z.; Marcella, N.; Luo,L.; Genc, A.; Ringnalda, J.; Frenkel, A.I.; Henkelman, G.; Crooks, R.M. Experimental and Theoretical Structural Investigation of AuPt Nanoparticles Synthesized Using a Direct Electrochemical Method. *J. Am. Chem. Soc.* **2018**, *140*, 6249-6259.

from earlier reports relating to deposition onto bulk phases. The results provide a good example of how the phase behavior of macro materials does not always translate to the nano world. A key component of this study was the structure determination of the AuPt NPs, which required a combination of electrochemical methods, electron microscopy, X-ray absorption spectroscopy, and theory (DFT and MD).

3.2. Introduction

Pt is an important catalyst for many reactions, but it is expensive and hence there is a strong motivation for reducing its usage.[6] One strategy for minimizing the need for Pt, yet retaining its desirable catalytic properties, is to form atomically thin Pt layers on more abundant, less expensive materials.[1,6-8] One might imagine this could be accomplished by direct deposition of Pt, but that approach can lead to three dimensional growth (rather than stopping at a single monolayer (ML)).[9,10] In recent years, however, new methods have been discovered that are much more effective for depositing Pt ML and controlled multilayer films onto underlying metals.

One of the most intriguing methods for controlled deposition of Pt was recently reported by Moffat and coworkers.[75-77] Specifically, they showed that close to a single Pt ML can be

deposited onto a macroscopic Au surface using a hydride-termination (HT) process (Illustration 3.1).[75,76] In this approach, an Au electrode potential is pulsed to a value that sequentially deposits Pt and then adsorbed H atoms (H_{ads}) atop the newly deposited Pt atoms. The presence of H_{ads} prevents three-dimensional growth of Pt multilayers.[75] Finally, the potential is pulsed positive to remove H_{ads}. Repetition of steps 2 and 3 (Illustration 3.1) can be repeated to deposit up to 10 Pt layers,[75,76] though iterations 2-10 do not necessarily result in complete additional MLs.[76,78]

Following the original study of the HT method,[75] related self-terminating electrodeposition[10,23,77,89-91,96-98] and chemical deposition[6,99] methods were reported. For example, Behm and coworkers[10] demonstrated that CO_{ads} could replace H_{ads} as the capping agent for Pt, and Vanpaemel and coworkers[96] reported that ultrathin Ni films could be deposited onto TiN. The HT method has also been adapted for Pt deposition onto: Ni,[77] star-shaped dendritic Au nanorods,[79] and carbon fiber substrates;[85,86] Ir deposition on Au, Pt, and Ni;[89] and for PtCoNi alloy formation.[90] To the best of our knowledge, however, the efficacy of this method has not been tested for ML shell deposition onto nanoparticles (NPs). In the present article, therefore, we report in-depth characterization of NPs prepared by the HT method, and specifically Pt deposition onto

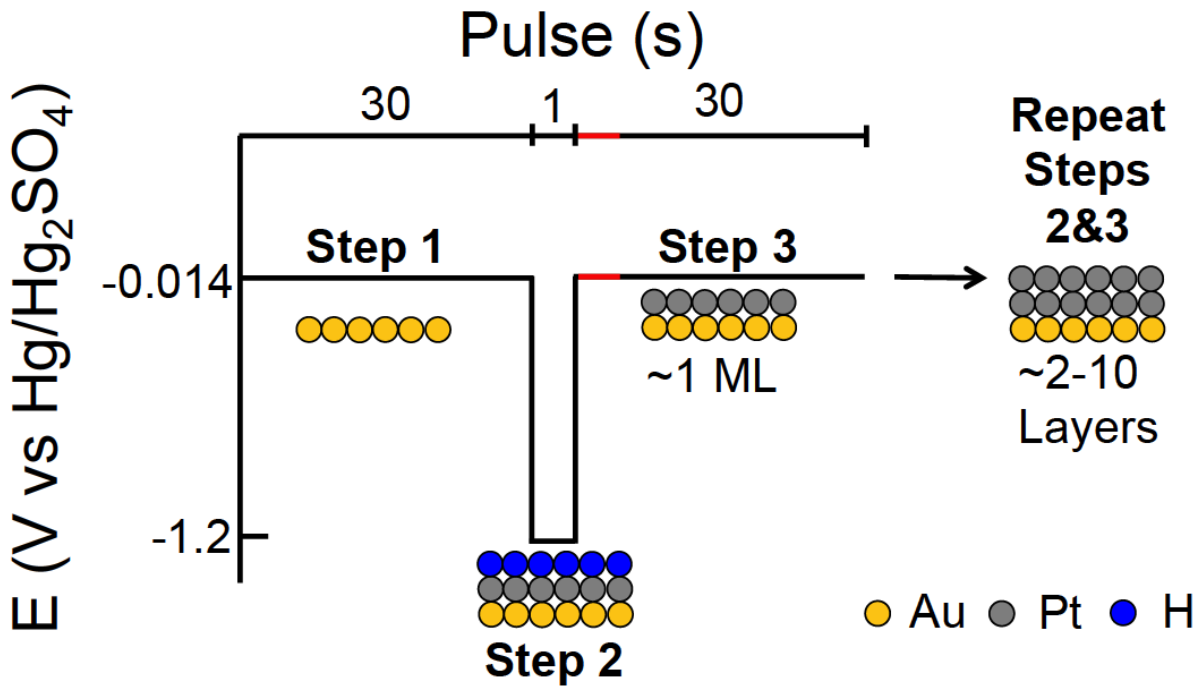

Illustration 3.1

~1-2 nm AuNP cores.

The Au cores were prepared by a dendrimer templating method we[1,2,28,33,100] and others[29,31,101] have described previously. On the basis of the original reports of HT Pt deposition onto bulk materials,[75–77] we anticipated that Pt deposition onto AuNPs would yield Au@Pt core@shell structures. However, the results of extensive structural characterization suggest the resulting materials more closely resemble quasi-random alloys.

The results described here are interesting for two primary reasons. First, the HT method could be very useful for preparing, for example, catalytic NPs, but its extension from bulk to NP surfaces is not a foregone conclusion. This is because the geometric and electronic properties of the surfaces of 1-2 nm NPs, such as those used here, are very different from bulk surfaces.[1,42,43] Successful application of the HT method to NPs has the potential to greatly expand the scope of the HT-deposition approach.[75–77,89,90]

Second, the HT method for NPs could be more versatile than the most common method used for depositing ML shells of metals onto small cores: underpotential deposition (UPD) followed by galvanic exchange (GE).[7,12,14–16,19,22,45,47,52,93,99,102–104] UPD is an electrochemical method that provides a means for depositing a

single ML of a shell metal (e.g., Cu) onto a core at a potential more positive than that of the onset for bulk metal deposition.[47] Once deposited, the UPD metal can be galvanically exchanged for a second, more noble metal (e.g., Pt). There are some significant limitations of the UPD/GE approach, however. For example, the preparation of multiple, discrete ML shells using combined UPD/GE is challenging and can result in alloying between the UPD and final shell metals if exchange is incomplete.[21,22,25,26,98] For catalysis this is important, because as we have shown, even a few heteroatoms can dramatically change the catalytic properties of NPs.[25] Additionally, the UPD/GE method is limited to shell metals more noble than the UPD metal.[19] The HT method directly addresses these types of problems and limitations.

For this first article, we chose to study Au@Pt NPs in part because this was the same combination of metals used in the original report of the HT method on bulk surfaces.[75] Also, we have previously synthesized Au@Pt NPs using either Cu[14] or Pb[15,16] UPD followed by GE with Pt^{2+}, and therefore have direct experience with this alternative synthetic method. The results show that the HT method does lead to deposition of Pt on ~1.6 nm AuNPs, but that the resulting structure is more consistent with that of a quasi-random alloy than a simple core@shell model. We reached this conclusion by combining data from electrochemical measurements,

electron microscopy, X-ray absorption spectroscopy, and theory. The main conclusion of this work, that alloying occurs in NPs using the HT method, is in contrast to the segregation of the two metals observed in bulk phase, and it provides a good example of how the phase behavior of macro materials does not always translate to the nano world.

3.3. Experimental Section

Chemicals and materials

Sixth-generation poly(amidoamine) (PAMAM) dendrimers, terminated with amine (G6-NH_2) groups were purchased from Dendritech, Inc. (Midland, MI) as a 9.0 wt% solution in methanol. Prior to use, the methanol was removed under vacuum, and then the dendrimers were reconstituted in water to yield a 100 μM stock solution. A 0.50 M NaOH solution, $NaBH_4$ (99.9%), $HAuCl_4$ (≥99.9%), and HPLC grade 2-propanol (99.9%) were purchased from Sigma-Aldrich. K_2PtCl_4 (99.9%), $CuSO_4$ (98%, anhydrous), 70% $HClO_4$ (in H_2O), and NaCl were obtained from Fisher (New Jersey, USA).

Deionized (DI) Milli-Q water (18.2 MΩ-cm; Millipore, Bedford, MA) was used for all solutions. Carbon- and lacey-carbon-coated Cu TEM grids were purchased from EM Sciences (Gibbstown, NJ, catalog numbers CF400-Cu-UL and LC400-Cu). Vulcan carbon (EC-72R) was

obtained from ElectroChem, Inc. (Woburn, MA). PTFE membrane filters (0.5 µm pore size) were from Advantec MFS, Inc. (Dublin, CA). All electrodes were purchased from CH Instruments (Austin, TX) with the exception of the working electrode used to prepare the EXAFS sample, which was Toray Teflon-treated carbon paper (TGP-H-120) from The Fuel Cell Store (Boulder, CO).

Synthesis of Au dendrimer-encapsulated nanoparticles (DENs)

DENs are NPs synthesized using dendrimer templates, and they are characterized by a high-degree of monodispersity in size, composition, and structure.[1,2,28] For this study, Au DENs were synthesized according to a literature procedure[105] with slight adjustments. Briefly, 147 equiv of $HAuCl_4$ (20 mM; 147 µL) were added dropwise to an aqueous G6-NH_2 solution with vigorous stirring. This results in encapsulation of $AuCl_4^-$ within the dendrimer. Reduction of this composite was achieved by adding an 11-12-fold excess of NaBH4, contained in 0.3 M NaOH (1.0 mL), within <2 min. For this step, the NaOH was added to a weigh boat containing the NaBH4 just before the mixture was transferred to the reaction solution. A color change from light yellow to brown signaled successful formation of Au147 DENs. Note that the Au_{147} DENs notation is not intended to imply that all DENs contain exactly 147 atoms, but rather the initial $AuCl_4^-$:G6-NH_2

stoichiometry. Following reduction, excess BH_4^- was deactivated by exposing the solution to air >12 h. No further purification was necessary. The final solution volume was 10 mL and the concentration, with respect to the dendrimer, was 2.0 μM.

The DENs synthesis was slightly modified for EXAFS sample preparation. A total of 10 mL of 10 μM DENs were synthesized in two separate 5 mL batches, which each contained 500 μL of 100 μM G6-NH_2, 367.5 μL of 20 mM $HAuCl_4$, and ~2.8 mg of $NaBH_4$ (a 10-fold excess) in 500 μL of 0.3 M NaOH. After ~2.5 min of stirring, $NaBH_4$ and NaOH were added together to the solution as previously described. After deactivation of excess BH_4^- in air for >12 h, these DENs were dialyzed against 4.0 L of Milli-Q water for >12 h using 12 kDa MWCO dialysis tubing (Sigma-Aldrich).

NP characterization

UV-vis spectroscopy was performed using a Hewlett-Packard 8453 spectrometer. Transmission electron microscopy (TEM) and scanning TEM (STEM) were performed using a JEOL 2010F TEM, having a point-to-point resolution of 0.19 nm and an operating voltage of 200 kV. Au_{147} DEN samples for TEM analysis were prepared by dropcasting 2.0 μL of the DEN solution onto a carbon-coated Cu TEM grid and then drying in air. STEM was used to image composite inks (described in the next section) consisting of Au_{147} DENs and Vulcan

carbon (VC). These TEM samples were prepared by diluting the DEN/VC ink 1:6 with water, sonicating for ~10 min, and then dropcasting (0.5 μL) onto a lacey-carbon-coated Cu grid. For AuPt DENs, lacey-carbon-coated Cu TEM grids were prepared by lightly swiping the electrode surface across the grid.

Electrochemical synthesis of AuPt DENs via the HT method

Electrochemical measurements were performed using a CH Instruments 627E potentiostat. For all experiments, an Hg/Hg_2SO_4 reference electrode and a glassy carbon rod counter electrode were used. Prior to use, the glassy carbon working electrodes (GCEs, 3 mm) were polished sequentially with 1.0, 0.3, and 0.05 μm alumina (2 min/pad) and then sonicated in water for ~10 min to remove excess alumina. The DENs were dispersed onto VC as follows. The VC (~1 mg) was first sonicated with 200 μL of isopropyl alcohol for ~10 min to facilitate dispersion, and then 1.0 mL of 2.0 μM DENs were added. The resulting ink was sonicated for an additional 10-15 min. The DENs were immobilized onto the GCE by dropcasting 6.0 μL of ink and drying under a gentle N_2 flow. Electrochemical cleaning of the DENs was carried out by cycling the electrode potential 20 times from 0 to 0.80 to -0.70 V at 200 mV/s in N_2-purged, 0.1 M $HClO_4$.

The HT Pt deposition was performed in a pH 4.0 solution containing 0.5 M NaCl and 3.0 mM K_2PtCl_4. To deposit Pt, the potential was first held at -0.014 V for 30 s (Step 1 in Illustration 3.1) to clean the surface. Next (Step 2), the potential was pulsed to -1.2 V for 1 s to deposit Pt and H_{ads}. Finally (Step 3, red line), the potential was pulsed back to -0.014 V for 1 s to strip off the H_{ads} layer. At this point the electrode was disconnected from the potentiostat (e.g., moved to the open circuit potential). To ensure that excess Pt^{2+} was removed from the electrode surface after HT deposition, the GCE was rinsed with DI water (~20 s), and then with 20 mL of 0.1 M $HClO_4$ (5 min, with stirring). Cyclic voltammograms (CVs) of the electrodes were subsequently recorded by scanning from 0 to 0.80 to -0.70 V at 100 mV/s in N_2-purged 0.1 M $HClO_4$. A total of six cycles were required to achieve consistent CV behavior. Electrochemical preparation of the EXAFS sample varied slightly and is discussed in detail in the Results and Discussion Section.

Energy dispersive spectroscopy (EDS)

EDS was performed using a Themis Z equipped with a monochromator, probe aberration corrector, and Super-X EDS technology. High-resolution, high angle annular dark-field (HAADF) STEM was also performed using a *DCOR+* probe aberration corrector

and *OptiSTEM+* aberration correction. A 70 μm aperture was used with a camera length of 115 nm and an accelerating voltage of 300 kV. The electron beam current for EDS was 350 pA and probe size was less than 0.1 nm. The total collection time was 6 min, and the dwell time was 23 μs. The EDS maps were acquired using a Thermo Scientific Themis Z microscope equipped with a Thermo Scientific Super-X detector system, which combines four symmetrically placed Si drift detectors around the objective lens with a high-brightness gun. This combination provides enhanced generation of X-rays and together with high detector efficiency results in a faster mapping of larger areas in EDS maps. Due to scheduling constraints, six months passed between preparation of the samples and analysis by the Themis. EDS for the EXAFS sample was performed using a JEOL 2010F TEM operated in STEM mode. One week passed between sample preparation and analysis of these materials.

Extended X-ray absorption fine structure (EXAFS)

The Au-L_3 and Pt-L_3 edge X-ray absorption fine structure (XAFS) measurements were performed in transmission and fluorescence modes at the BL2-2 beamline of the Stanford Synchrotron Radiation Lightsource (SSRL) at the SLAC National Accelerator Laboratory. Two 15 cm-long ionization detectors were used for measuring incident (with a 75:25 mixture of N2 and Ar)

and transmitted (with a 50:50 mixture of Ar and Kr) beam intensities. A third 15 cm ionization chamber (filled with a 50:50 mixture of Ar and Kr), located downstream of the transmission detector, was used to detect the beam through an Au foil reference for X-ray energy calibration and spectral alignment. The 13 channel Ge detector was used to measure fluorescence data that were used for Pt edge analysis. Both the Pt and Au regions were measured in the same scan.

Computational methods

Theoretical calculations were performed using density functional theory (DFT) implemented in the Vienna ab initio simulation package (VASP).[106,107] Core electrons were described with the projector augmented-wave (PAW) method.[108,109] The Kohn-Sham wave functions for the valence electrons were expanded in a plane-wave basis set with an energy cutoff of 300 eV. The exchange-correlation energy was treated within the framework of the generalized gradient approximation. Specifically, PBEsol[110] was used, which is a modified form of the Perdew-Burke-Ernzerhof (PBE) functional designed to improve lattice parameters and surface energies in solids. A single Γ-point was sufficient for integration of the reciprocal space due to the finite nature of the NPs.

To simulate the EXAFS spectra, an ensemble of equilibrium structures at finite temperatures is required. To avoid the expensive molecular dynamics simulations using DFT, we employed an alternative methodology to sample the equilibrium structures by using DFT-evaluated dynamical matrices. Dynamical matrices for the systems of interest were obtained using a finite difference method in which a displacement of 0.01 Å was applied to every degree of freedom of the equilibrium structure. A set of 3N−6 harmonic oscillators with their force constants and vibrational normal modes were obtained by diagonalizing the obtained dynamical matrix. Statistically independent structures at finite temperatures were then sampled by displacing the atoms in the system along each normal mode with a magnitude following a Gaussian distribution. The standard deviation of the Gaussian distribution is described by eq 3.1, which is the variance of the position of a quantum harmonic oscillator. In this equation, M is the effective mass of the harmonic oscillator, ω is the vibrational frequency, ħ is Planck's constant, k_B is Boltzmann's constant, and T is the temperature.

$$\sigma = \sqrt{\left(\frac{\hbar}{2M\omega}\right)\coth\left(\frac{\hbar\omega}{2k_BT}\right)} \qquad \text{eqn.3.1}$$

On the basis of the sampled structures, theoretical EXAFS spectra were simulated using an approach similar to that reported previously.[105,111] The Au- and Pt-L_3 edge EXAFS spectra were calculated from 300 structures by averaging the signal arising from each Au or Pt atom in the system. The multiple scattering calculations were performed using FEFF6-lite.[112] All atoms up to 6.0 Å away from each X-ray-absorbing atom were included in the scattering calculations. The experimental corrections to the photoelectron energy origin and the passive electron reduction factor were then applied to the simulated EXAFS spectra to align experimental and theoretical data in *k*-space and in amplitude, respectively.

The theoretically predicted EXAFS parameters, including coordination numbers (CNs; individual values denoted as N), average nearest neighbor bond lengths (R), and the Debye-Waller factors (σ^2), were calculated by averaging the structural data of the 300 sampled equilibrium structures for each examined system. To calculate these values, a window of 2.5 Å to 3.3 Å was used to define the first nearest neighbors in *r*-space.

Au surface segregation energies were calculated as the total energy difference between the segregated and the non-segregated models: $dE_{seg}=E_{seg}-E_{no\_seg}$. Ab-initio molecular dynamics simulations were employed to equilibrate the structures of Pt-decorated Au

nanoparticles. A time step of 1.5 fs was used and 5000 total steps (7.5 ps) were carried out for each MD simulation. The temperature was held at 300 K by rescaling the velocities of all atoms every 10 steps.

3.4. Results and Discussion

Synthesis and characterization of Au_{147} DEN cores

Details of the synthesis of the Au_{147} DENs are described in the Experimental Section. Briefly, 147 equiv of $HAuCl_4$ were mixed with G6-NH_2 dendrimers, and then the mixture was reduced using excess $NaBH_4$. As we have discussed previously, this process results in nearly size monodisperse Au DENs.[1]

A UV-vis spectrum of the Au_{147} DENs solution is shown in Figure 3.1a. It reveals a monotonic increase in absorbance in the direction of higher energy that is characteristic of NP formation.[113] A small AuNP plasmon band at ~520 nm indicates that the NP size is <2 nm.[15] STEM analysis (Figure 3.1) confirms this: the Au_{147} DENs are 1.6±0.3 nm in diameter, which is in good agreement with previous reports[14-16,105,111] and the predicted size for a 147-atom cuboctahedral Au particle (~1.6 nm).[15]

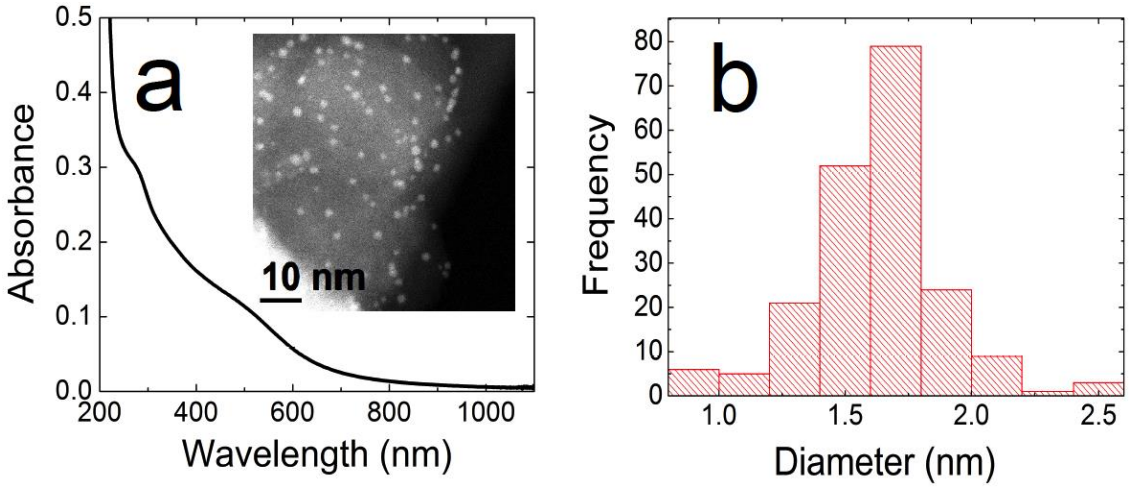

Figure 3.1

Characterization of Au_{147} DEN cores. (a) UV-vis spectrum for Au_{147} DENs. Milli-Q water was used for background subtraction, and the cuvette pathlength was 0.200 cm. The inset shows a STEM micrograph of the Au147 DENs supported on Vulcan carbon (Au_{147}/VC ink). (b) The associated size distribution (1.6±0.3 nm) histogram for the inset in (a).

Synthesis and characterization of AuPt DENs

The HT method used to deposit Pt on the Au_{147} DENs is described in detail in the Experimental Section. Briefly, a conductive ink containing ~1 mg VC/mL and 2.0 μM Au_{147} DENs was dropcast (6.0 μL) onto a polished GCE, dried under a gentle flow of N_2, and then cleaned electrochemically. Figure 3.2a (black trace) is a CV of the resulting Au_{147} DEN-modified GCE). The positive scan limit (0.80 V) was chosen such that qualitative changes in the Au electrochemically active surface area could be determined, but without changing the structure of the Au_{147} DENs. Au oxide formation is apparent positive of ~0.50 V, and the corresponding oxide reduction peak is centered at ~0.41 V. These values are in agreement with our previous reports for Au_{147} DENs.[14–16]

Following electrochemical characterization of Au_{147}, Pt was deposited following the procedure summarized by Illustration 3.1 and described in the Experimental Section. This method is very similar to that used by Moffat and coworkers,[75] with the exception that in our case the duration of Step 3 was just 1.0 s rather than 30.0 s (Illustration 3.1, red line). Following Pt deposition, the GCE was rinsed briefly in DI water and then in 0.1 M $HClO_4$ for 5 min to remove any excess Pt^{2+} that might be present. The red trace in Figure 3.2a is a CV of the resulting material, recorded

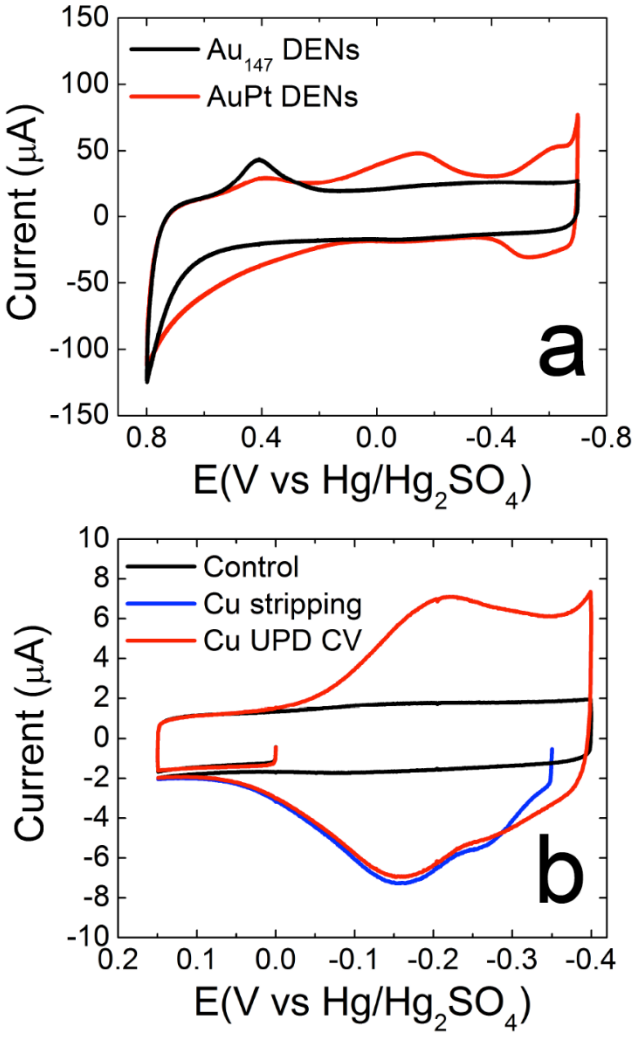

Figure 3.2

(a) Cyclic voltammograms (CVs) before (black) and after (red) HT Pt deposition on Au_{147} DENs. The electrolyte solution was N_2-purged, 0.1 M $HClO_4$ and the scan rate was 100 mV/s. (b) CVs corresponding to Cu UPD on AuPt DENs. A Cu UPD CV is shown in red, and a background CV (no Cu^{2+}) is provided for comparison (black). The blue LSV was recorded after Cu^{2+} electrodeposition for 300 s at -0.35 V. The scan rate was 10 mV/s, the electrolyte solution was N_2-purged, 0.1 M $HClO_4$ containing 5.0 mM $CuSO_4$. For both (a) and (b) the DENs were immobilized onto the GCE working electrode using a VC ink.

immediately after the acid rinse. It reveals Pt hydride waves between -0.40 and -0.67 V, a broad feature associated with Pt oxidation positive of ~0.15 V, and a Pt oxide reduction peak centered at ~-0.14 V. An Au oxide reduction peak centered at ~0.40 V is also present.

Comparing the black and red CVs in Figure 3.2a, the most notable changes after Pt deposition are the appearance of Pt-specific peaks (hydride and oxide) and attenuation of the Au oxide reduction peak. These features indicate, at least qualitatively, that some Pt is present on the surface of the Au_{147} DENs. Specifically, the potentials for the Pt hydride adsorption/desorption peaks are in good agreement with those previously reported for Au@Pt DENs[16] and Pt DENs.[45] Importantly, however, the presence of the attenuated Au oxide reduction peak suggests that both Au and Pt are present on the NP surface.

We carried out several important control experiments to provide confidence in the results described thus far. For example, Figure 3.3 shows that when the HT method is applied to Au_{147} DENs, the amount of Pt deposited is independent of pulse time within the range of 1-10 s, thus confirming that deposition is self-limited during the 1 s pulse used in our experiments. Even pulses of 100 s lead to only a slight increase in Pt deposition. Another control experiment is discussed at length in the next section. Here,

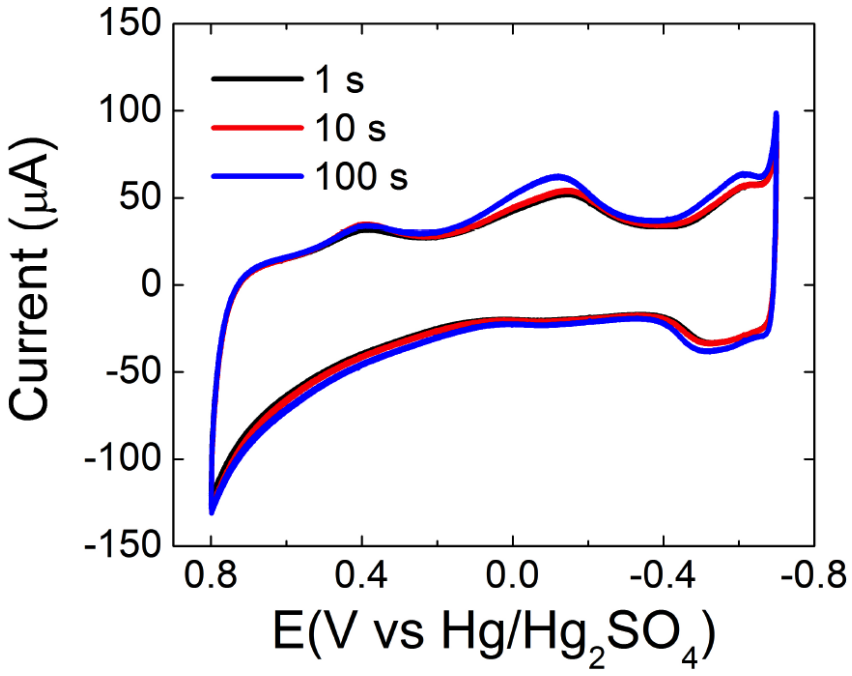

Figure 3.3

Self-termination control experiments. The figure shows CVs obtained using GCEs modified with AuPt DENs prepared by the HT method. For these CVs, the Pt deposition time (Step 2 in Illustration 3.1) was varied to determine the time range over which the HT process is self-limiting. The CVs obtained for deposition times of 1 and 10 s are coincident, and there is a small but significant increase in current for the CV corresponding to the 100 s interval. We conclude that Pt deposition times between 1-10 s lead to self-limiting behavior, which is in accord with literature reports for HT Pt deposition onto bulk Au.[75] The electrolyte solution contained N_2-purged 0.1 M $HClO_4$ and the scan rate was 100 mV/s.

electrochemical and microscopy data indicate that negligible amounts of Pt-only NPs form in the absence of the Au_{147} DEN cores. In other words, nearly all of the Pt on the GCE is deposited on the surface of the Au_{147} DEN cores.

Control experiments demonstrating that Au_{147} DEN cores are required for Pt electrodeposition

In this section, we describe control experiments that were carried out to eliminate the possibility that Pt-only NPs form on the GCE during electrosynthesis of AuPt DENs.

TEM (Figure 3.4a) obtained for an ink consisting of only VC, water, and IPA (no Au or dendrimers) indicates that the VC itself is free of NP contaminates. Next, this same ink was subjected to the electrochemical treatment used for HT Pt electrodeposition (electrochemical cleaning in $HClO_4$, pulsing the potential between -0.014 and -1.2 V in $NaCl/K_2PtCl_4$, and surface characterization in $HClO_4$). The CVs obtained before and after these steps are coincident (Figure 3.5a), indicating that if PtNPs are present, their concentration is below the detection limit of electrochemistry. TEM confirms the findings of the CV experiments (Figure 3.4b).

Next, we examined the role of dendrimers in the HT electrosynthesis. For this control experiment, the steps required

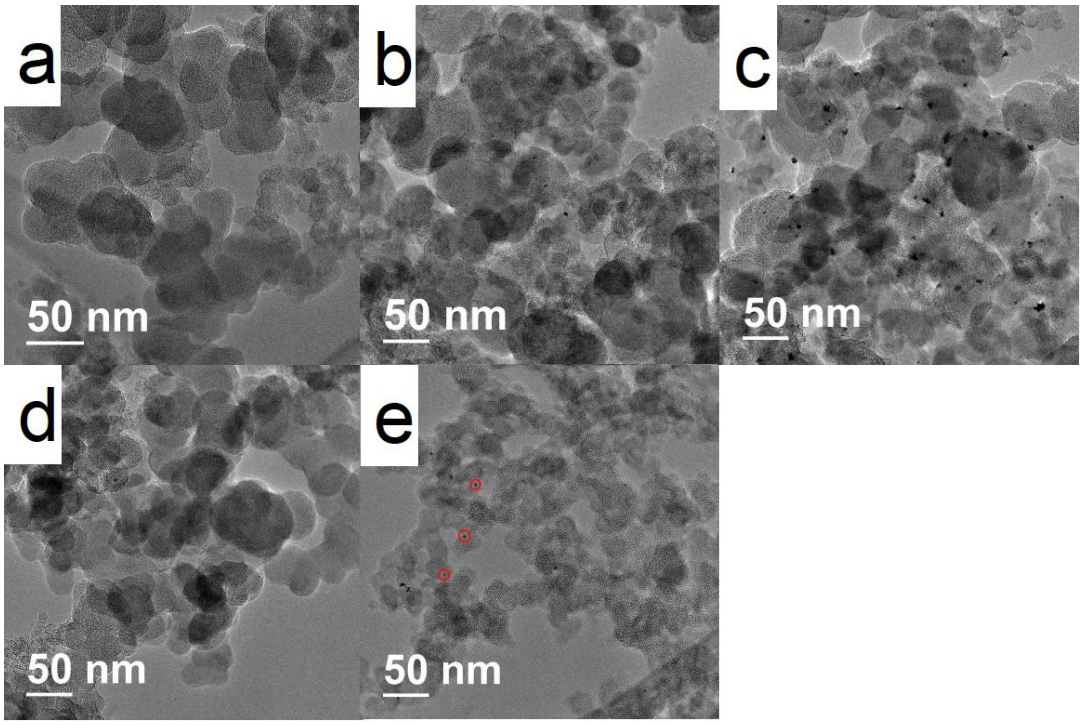

Figure 3.4

TEM for control inks. (a) TEM of an ink composed of VC only (1 mg VC/mL DI water, no Au DENs) before electrochemical treatment. (b) Same as (a), but after exposure to the HT synthesis conditions described in the Experimental Section. (c) TEM of a G6-NH_2/VC ink (1 mg VC/mL of 2.0 μM G6-NH_2 dendrimers, no AuNPs) after exposure to the HT synthesis conditions. (d-e) Same as (c), but after an acid rinse. Two regions on the same grid are shown: (d) a NP-free region and (e) a region revealing a small number of NPs (e.g., red circles). Additional micrographs revealed that most of the surface was NP free, as in (d). Note that 200 μL of IPA was added to all of the inks to aid dispersion of the VC.

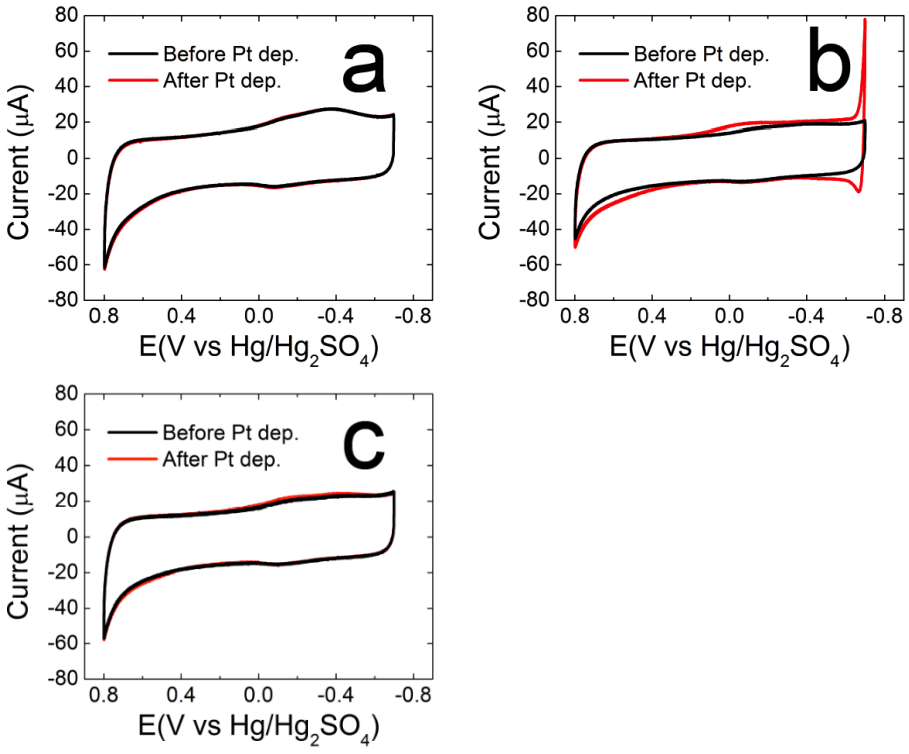

Figure 3.5

CVs corresponding to the inks defined in Figure 3.4. The black and red CVs were obtained before and after exposure of the inks to the HT synthesis conditions, but always in the absence of AuNP cores. (a) VC-only ink. (b) G6-NH_2/VC ink. (c) G6-NH_2/VC ink after treatment with an acid rinse following the HT synthesis procedure. The electrolyte solution contained N_2-purged 0.1 M $HClO_4$ and the scan rate was 100 mV/s. The fourth cycle is shown in each case.

for HT Pt electrodeposition were applied to an ink composed of VC/IPA and 2.0 μM G6-NH_2 dendrimers (no AuNPs). Hereafter, we refer to this as the G6-NH_2/VC control. Figure 3.5b compares the fourth CVs obtained before and after exposure of the G6-NH_2/VC control to the HT synthesis steps. The fourth CV is shown because after this number of cycles the CVs had obtained consistent behavior. The results suggest the presence of Pt after performing the HT electrochemical treatment, given the hydride-like features observed at potentials negative of ~-0.4 V. These CVs are further discussed in the next paragraph.

As previously indicated, the shape of the CVs stopped changing after four cycles for the G6-NH_2/VC control. Indeed, Figure 3.6a shows that only the first cycle is markedly different than the second and third. In the first cycle, a peak is present at ~0.5 V. Figure 3.6b shows that this peak does not appear when CV is performed after exposing the G6-NH_2/VC control ink to HT treatment in Pt-free 0.5 M NaCl. Therefore, although we are not completely certain what the peak corresponds to, it is associated with the presence of Pt. When Pt is involved in the HT treatment (Figure 3.6a), hydride waves are observed negative of ~-0.40 V. However, both features disappear in subsequent cycles. A sharp cathodic peak remains evident from ~-0.60 to -0.70 V. Itaya and coworkers[114] observed the same trend upon electrochemical cycling in Pt-free

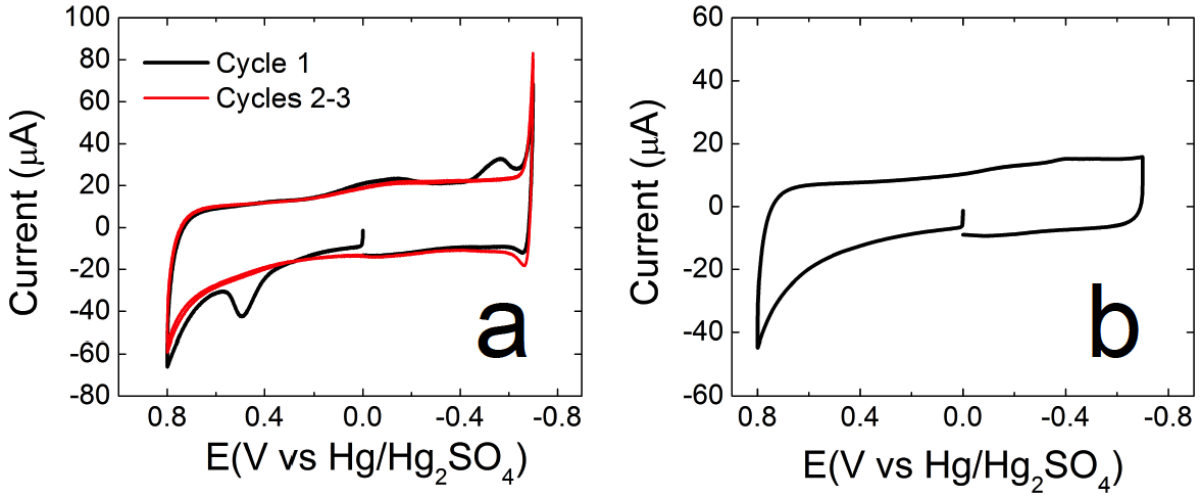

Figure 3.6

(a) Comparison of the first and second CVs for the G6-NH_2/VC control electrodes (no AuNP cores) following exposure to the HT synthesis conditions (pulsing the potential between -0.014 and -1.2 V in 0.5 M NaCl/3 mM K_2PtCl_4 at pH 4.0). These CVs are the first two CVs corresponding to the red CV shown in Figure 3.5b (no acid rinse). (b) First CV for the G6-NH_2/VC control ink after exposure to HT electrochemical steps in Pt-free 0.5 M NaCl at pH 4.0. As shown, the peak at ~0.5 V present in (a) is absent in (b). For both (a) and (b), the CVs were recorded in N_2-purged 0.1 M $HClO_4$ and the scan rate was 100 mV/s.

0.1 M $HClO_4$ following a 1 min immersion of Au(111) in a K_2PtCl_4 solution. The authors concluded that adsorbed $PtCl_4^{2-}$ was reduced during the first cycle and confirmed PtNP formation by performing *in-situ* STM during electrochemical cycling. They attributed the disappearance of the Pt specific peaks in the second cycle to a positive shift of the Pt oxide formation potential due to size effects (~3 nm NPs).

TEM results for the G6-NH_2/VC control (Figure 3.4c) confirm the presence of NPs (dark spots distributed throughout the micrograph). Importantly, the NPs are larger (clusters of NPs up to ~10 nm in diameter), have different shapes, and are much fewer in number than those observed for HT Pt electrodeposition on Au DENs (Figure 3.7). We hypothesize that the NPs shown in Figure 3.4c are composed of Pt and arise from $PtCl_4^{2-}$ entrapped within the dendrimers that is subsequently reduced during electrochemical cycling in $HClO_4$.

To test this hypothesis an additional experiment was carried out in which an electrode prepared exactly like that shown in Figure 3.4c was rinsed in 0.1 M $HClO_4$ for 5 min after HT electrochemical treatment. The resulting CVs (Figure 3.5c) are nearly coincident and are similar to the VC-only control (no dendrimer or AuNPs) shown in Figure 3.5a. In this case, TEM (Figure 3.4d-e) reveals negligible NP formation. As a result, we conclude

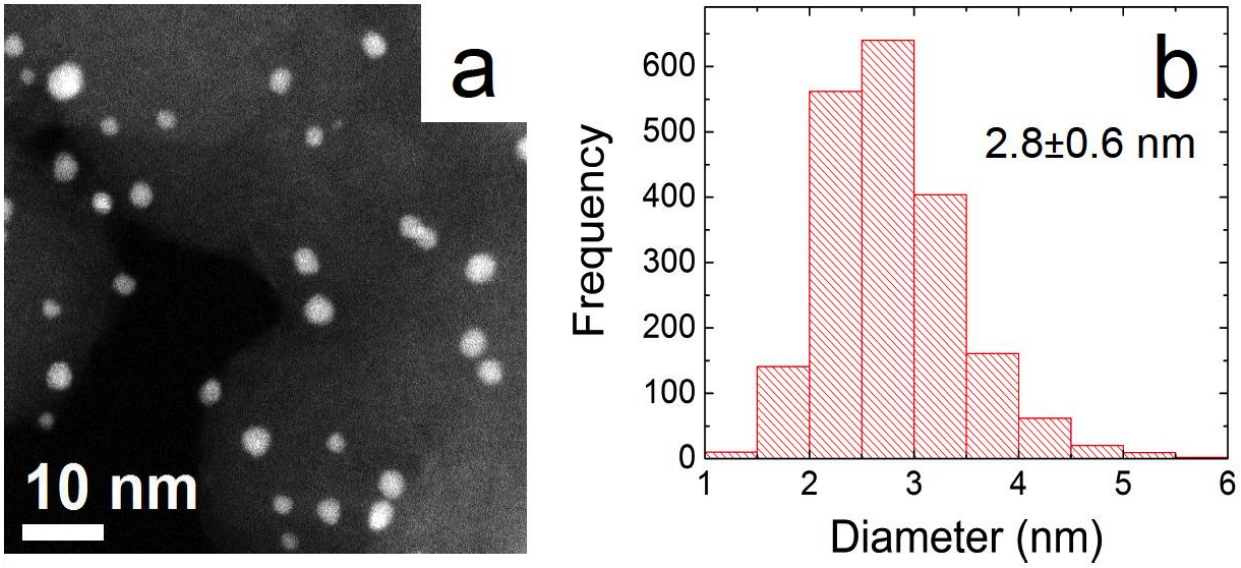

Figure 3.7

(a) STEM micrograph for the AuPt DENs. (b) A size- distribution histogram obtained using numerous micrographs like that shown in (a).

that adventitious NP formation can be effectively mitigated using a 5 min acid rinse before materials characterization. Given that a 5 min acid rinse was employed after HT Pt deposition when preparing the AuPt DENs, the only NPs present in those samples should be those associated with the Au DEN cores.

Scanning transmission electron microscopy (STEM)

Figure 3.7 displays a STEM micrograph and a size-distribution histogram for AuPt DENs synthesized using the HT method. The AuPt DENs are 2.8±0.6 nm in diameter, which can be compared to the original size of the Au_{147} DEN cores (1.6±0.3 nm) and the calculated size of a 147-atom cuboctahedral AuNP capped with a single ML of Pt (~2.1 nm).[15] Note that we have previously reported sizes of 2.3±0.4 nm for Au_{147}@Pt DENs prepared by UPD of Pb followed by Pt GE,[15] and 2.5±0.4 nm for Au_{140}@Pt DENs prepared by Cu UPD followed by Pt GE.[12] Therefore, the average NP size achieved using the HT method is, within error, consistent with results obtained for these closely related materials.

Energy dispersive spectroscopy (EDS)

EDS mapping (Figure 3.8) was used to confirm selective deposition of Pt on the AuNPs. The key result is that Au and Pt are co-localized on the same NPs. Apart from this qualitative

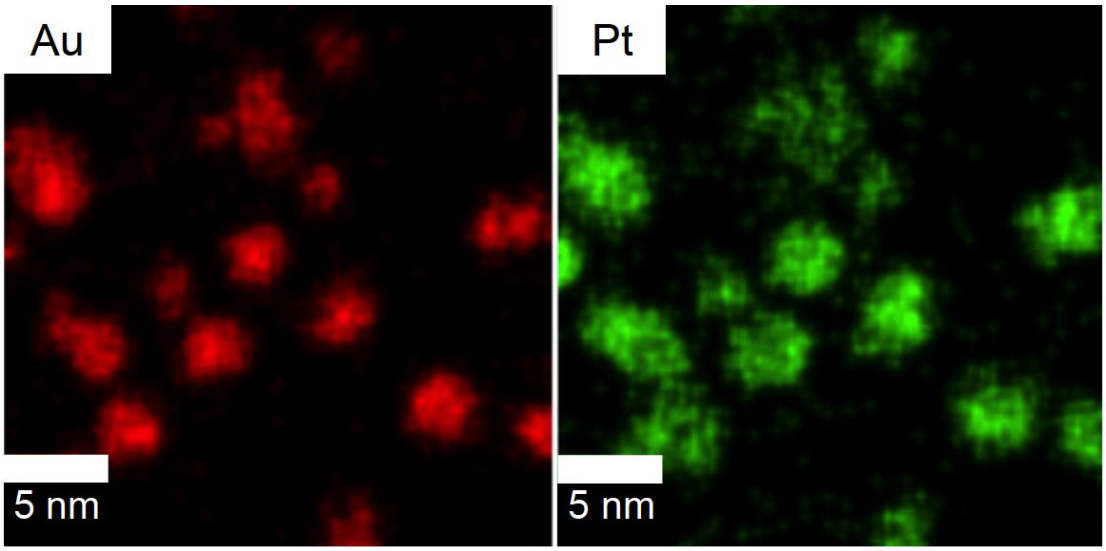

Figure 3.8

Au and Pt EDS maps for AuPt DENs prepared using a single pulse of HT Pt electrodeposition.

statement, there is insufficient resolution in the EDS data to draw quantitative conclusions about structure (i.e., the relative locations of Au and Pt). For structural information, therefore, we relied upon electrochemical methods, X-ray absorption spectroscopy (XAS), and theoretical calculations (vide infra).

Although the Pt EDS signals are primarily concentrated in regions where the NPs are located, we also note that there is a low level of stray Pt signals elsewhere. This is likely noise. Indeed, as discussed earlier, a series of control experiments showed that HT Pt deposition is selective for the NPs.

Surface composition

As discussed in the context of Figure 3.2a, hydride adsorption occurs on Pt but not Au, and therefore it can be used to estimate the surface area of Pt. Cu UPD, on the other hand, occurs on both Au and Pt,[47] and therefore it provides information about the total NP surface area. By comparing the Pt and total surface areas, the percentage of Pt on the surface of the NPs can be deduced.

Cu UPD was performed on freshly prepared AuPt DENs immediately following determination of the Pt surface area. The first step was to obtain a background CV of the AuPt DEN-modified electrode in the absence of Cu^{2+} (black trace, Figure 3.2b). This CV was obtained by holding the potential of the electrode at 0 V for 300 s, and

then scanning it between 0.15 and -0.40 V. Only capacitive current is observed.

The Cu UPD CV (red trace) was obtained by adding 100 μL of 0.50 M $CuSO_4$ to the solution used for the black trace and scanning the electrode over the same potential range. Cu UPD occurs at nearly the same potential on Au[34] and Pt[25,34,45,46] DENs, so only a single peak is observed, and it is centered at -0.22 V. Upon scan reversal, two Cu oxidation peaks are centered at -0.27 V and -0.16 V. These values are consistent with a previous report for Au_{140}@Pt DENs.[34] This experiment provides the information necessary about potential scan limits to calculate surface areas.

To obtain the total NP surface area, the following experiment was carried out. First, a ML of Cu was deposited by holding the electrode potential at -0.35 V for 300 s. Second, the ML was stripped off by scanning from -0.35 V to 0.15 V. Finally, the Cu stripping voltammogram (blue trace) was baseline subtracted (black trace) and the resulting area under the curve was integrated to obtain the total charge corresponding to Cu UPD.

The charge densities for Cu UPD on bulk Au[14] and Pt[115] are roughly equivalent (405 $\mu C/cm^2$ and 410 $\mu C/cm^2$), and therefore we used the averaged value of 407.5 $\mu C/cm^2$ to determine the total NP surface area. The amount of Pt on the surface was determined by

integrating the hydride waves (Figure 3.2a, red CV) and using the value of 210 μC/cm^2 to convert charge to surface area.[14] Using these values, and the experimentally determined charges associated with Cu UPD (103 μC) and Pt hydride (27.5 μC), we calculated total and Pt-only surface areas of 0.25 cm^2 and 0.13 cm^2, respectively. The key finding, then, is that on average ~52% of the NP surface is Pt and ~48% is Au. If the HT method resulted in Pt depositing exclusively on the NP surface, we would not expect to observe any surface Au. The fact that Au and Pt are both present in approximately equal measure on the NP surface suggests these materials have a more complex structure than a simple Au@Pt core@shell configuration.

EXAFS sample preparation and characterization

Substantially more DENs are necessary for EXAFS measurements than for the electrochemical experiments described thus far, and therefore slight adjustments to the synthetic method were required. To this end, five modified DEN inks were prepared. Each ink was made by combining 2.0 mg VC with 400 μL IPA, sonicating for 10 min, then adding 2.0 mL of 10 μM dialyzed Au_{147} and sonicating for another 10 min. Each ink was vacuum filtered using a 0.5 μm Advantec PTFE filter. Before the resulting paste was fully dry, it

was quickly spread (with a plastic spatula) onto a strip of Toray Teflon-treated carbon paper. The area of the paper covered by the paste was ~0.36 cm^2, and only this region was exposed to the electrolyte during electrochemical treatment. The five paper strips contained ~2.0 mg of paste each. The Pt electrodeposition time was set to 100 s because of the large amount of material used to prepare the EXAFS samples. The initial currents (<1 s) during Pt electrodeposition were high (>0.1 A), and therefore a low-sensitivity potentiostat (Autolab PGSTAT 128 potentiostat/galvanostat) was used for this step. The currents decayed to <10 mA within ~1 s, and the IR drop became negligible within ~3 s. IR compensation was applied manually for the Pt HT electrodeposition step due to instrumental limitations. To avoid overcompensating, the R was set to a value ~3.5 Ω lower than was measured (~12-15 Ω) in 0.1 M $HClO_4$. Except for these caveats, all other synthetic steps were identical to those described for the non-EXAFS (GCE-prepared) AuPt DENs.

The EXAFS strips were characterized by CV and TEM immediately after synthesis and within 1-2 days after synthesis, respectively. Due to high ink loading, it was necessary to use IR compensation to obtain CVs. A CHI 627E potentiostat with automatic IR compensation was used, but otherwise the CVs were performed as described for the GCE-prepared AuPt DENs. Electrochemical features

of the NPs prepared for EXAFS are in good agreement with the non-EXAFS samples (Figure 3.2), though the CVs (Figure 3.9) indicate slightly more Au on the surface of the EXAFS NPs. TEM micrographs obtained before and after Pt electrodeposition are shown in Figure 3.10. The five paper strips were stacked for EXAFS measurements. EXAFS data were collected 5-8 days after the synthesis of each strip.

Surface composition (via Cu UPD) was performed for each EXAFS strip 8-9 days after EXAFS measurements. To avoid uncertainty imposed by high background currents and poorly defined electrochemical features, we only used a small portion of each strip. To this end, we cut a small (~0.2 cm wide) portion of each EXAFS strip, scraped off the VC/DENs paste from each side, then used the resulting paste to form an electrochemical ink by sonicating with 100 μL IPA/500 μL DI water. From this ink, 6.0 μL were dropcast onto a GCE and allowed to dry in air. The magnitude of the current produced from this preparation (Figure 3.11a) was comparable to that of the non-EXAFS sample (Figure 3.2a). Cu UPD was then performed as described earlier for the non-EXAFS sample. Comparison of the Pt hydride surface area (Figure 3.11a) and total NP surface area (from Cu UPD stripping; Figure 3.11b) indicated a surface composition of 42±2% Pt, which, considering that the experiment is somewhat primitive, is reasonably similar

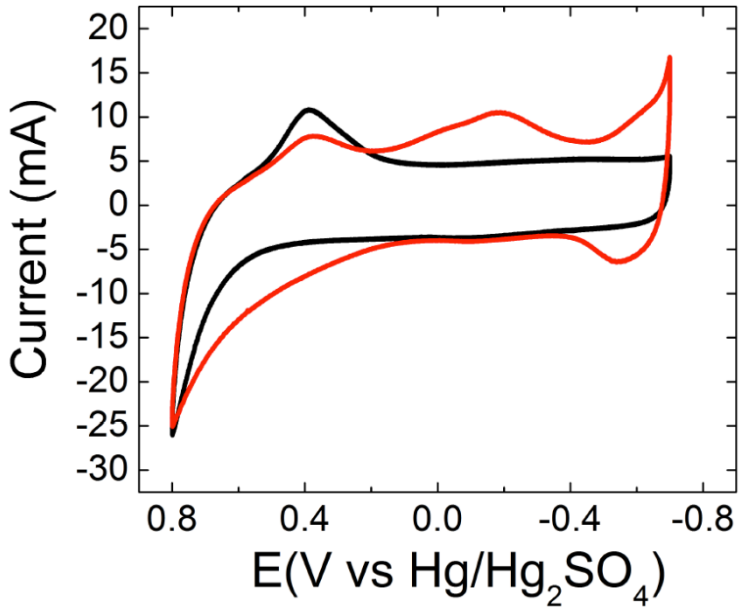

Figure 3.9

CVs for the EXAFS sample before (black trace) and after (red trace) HT Pt electrodeposition. The CVs were recorded in N_2-purged 0.10 M $HClO_4$. The scan rate was 100 mV/s.

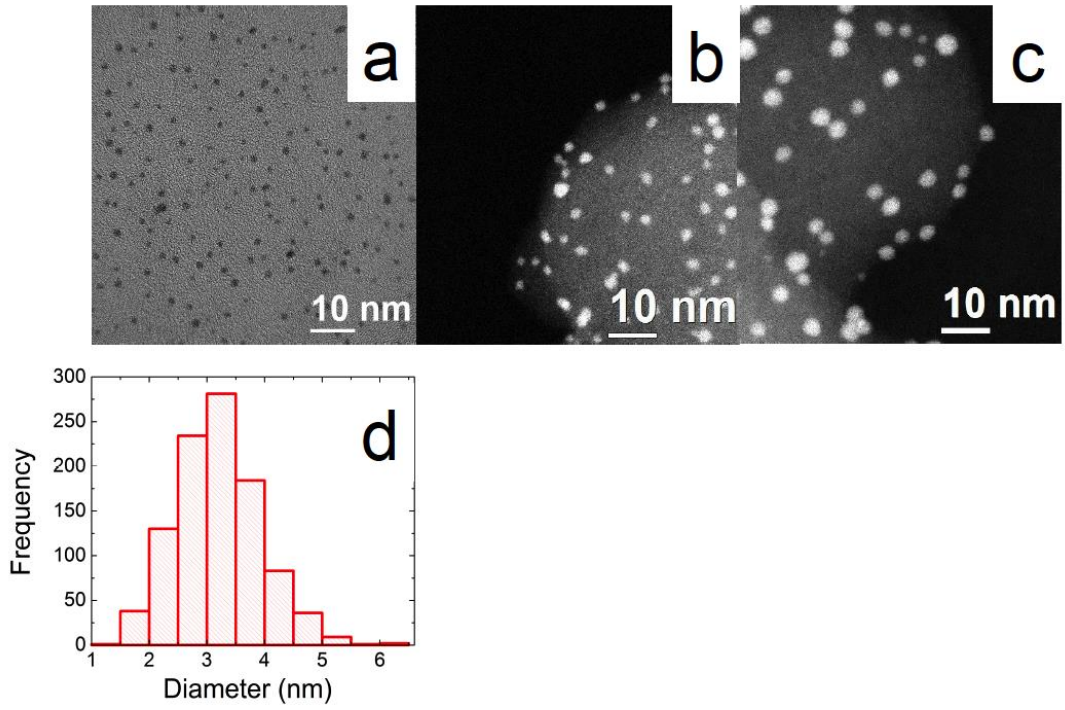

Figure 3.10

TEM for the EXAFS sample before and after HT Pt electrodeposition. (a,b) TEM micrographs for (a) dialyzed 10 μM Au147 DENs, and (b) the corresponding Au147/VC ink used for EXAFS sample preparation. The size-distributions are 1.6±0.2 nm and 2.0±0.3 nm for (a) and (b), respectively. (c) STEM micrograph and (d) the associated size-distribution histogram (3.2±0.7 nm) for the AuPt DENs EXAFS sample. The AuPt DENs size-distribution was determined using 200 NP counts for each of 5 EXAFS electrodes (a total of 1000 NPs were measured). The scale-up required for sufficient EXAFS signal necessitated high loading of DENs on the VC support. This resulted in a slight increase in the initial AuNP size from 1.6±0.2 nm (Figure 3.1) to 2.0±0.3 nm after immobilization. This in turn led to a slightly larger (though statistically identical) average AuPt DENs size (3.2±0.7 nm) relative to the non-EXAFS sample (2.8±0.6 nm; Figure 3.7).

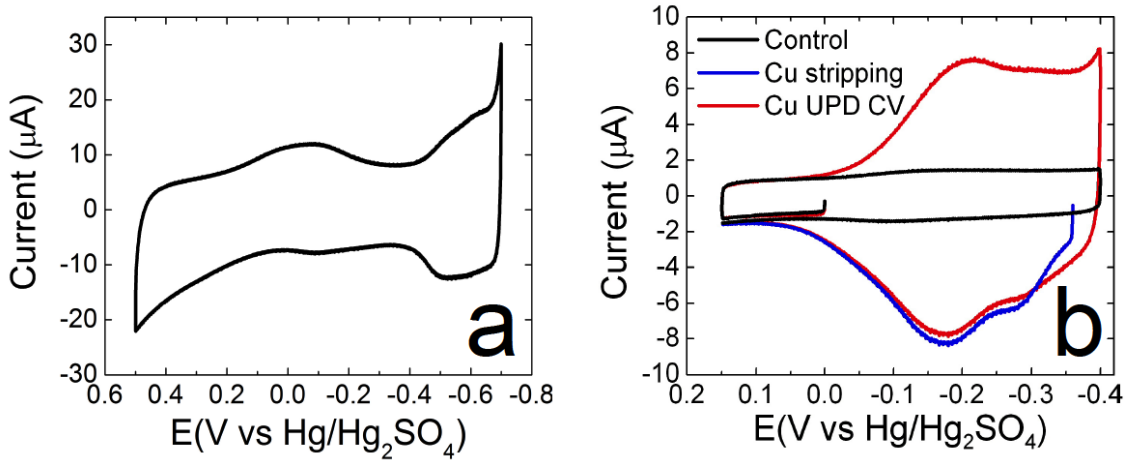

Figure 3.11

CVs obtained from the electrodes used for the EXAFS samples. (a) CV for a representative EXAFS strip before Cu UPD. The data were obtained in N_2-purged 0.1 M $HClO_4$, and the scan rate was 50 mV/s. The charge associated with the hydride waves is 28.9 μC. (b) Cu UPD control CV (black), Cu UPD CV (red), and Cu stripping (blue) on the AuPt DENs ink after 300 s Cu deposition at -0.36 V in N_2-purged 0.1 M $HClO_4$/5.0 mM $CuSO_4$. The scan rate was 10 mV/s. The charge from Cu UPD stripping is 134 μC. Using the calculation method described earlier, the Pt surface area is determined to be 0.138 cm^2 and the total surface area is 0.329 cm^2. The Pt surface coverage for this strip is therefore 42%. The average percentage of surface Pt, determined by independently evaluating 5 EXAFS strips, is 42±2%.

to the non-EXAFS sample (52±5%).

EDS for the EXAFS sample (Figure 3.12) shows that Au and Pt are co-localized within the NPs, just as they were for the non-EXAFS sample.

EXAFS

Analysis of the experimental EXAFS (Figure 3.13) was performed to further refine the AuPt NP structure. This analysis is complicated by the fact that Au and Pt have overlapping L_3-edge spectra.[116,117] As a result, it was only possible to extract the total Au and total Pt CNs: N(Au-M) and N(Pt-M). For the general case, we define N(A-M) as equal to the sum of N(A-A) and N(A-B) for elements A and B.[59] Due to the low weight loading (32%) and amount of sample (~9-10 mg VC/DENs in an ~0.36 cm^2 area), and thus the expected poor signal-to-noise ratio in the Pt-L_3 EXAFS spectrum past the Au-L_3 edge, we analyzed the Pt- and Au-L_3 edge data separately and did not employ the general analysis scheme for bimetallic compositions with overlapping edges.[116,117] Table 3.1 shows the Au-M and Pt-M CNs, bond lengths, and the associated Debye-Waller factors. We interpret these parameters in a later section.

An additional consideration for fitting the EXAFS spectra is the possibility that the overlap between the Au-L_3 and Pt-L_3

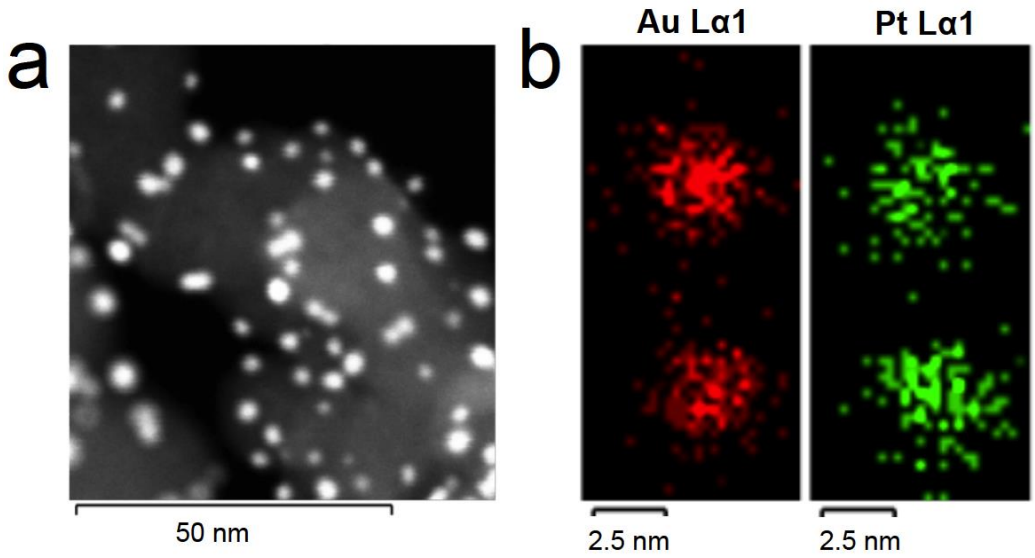

Figure 3.12

(a) STEM image of the AuPt DENs EXAFS sample. (b) EDS mapping for two of the particles shown in (a). Au is shown in red and Pt is shown in green. Note that Au and Pt are co-localized.

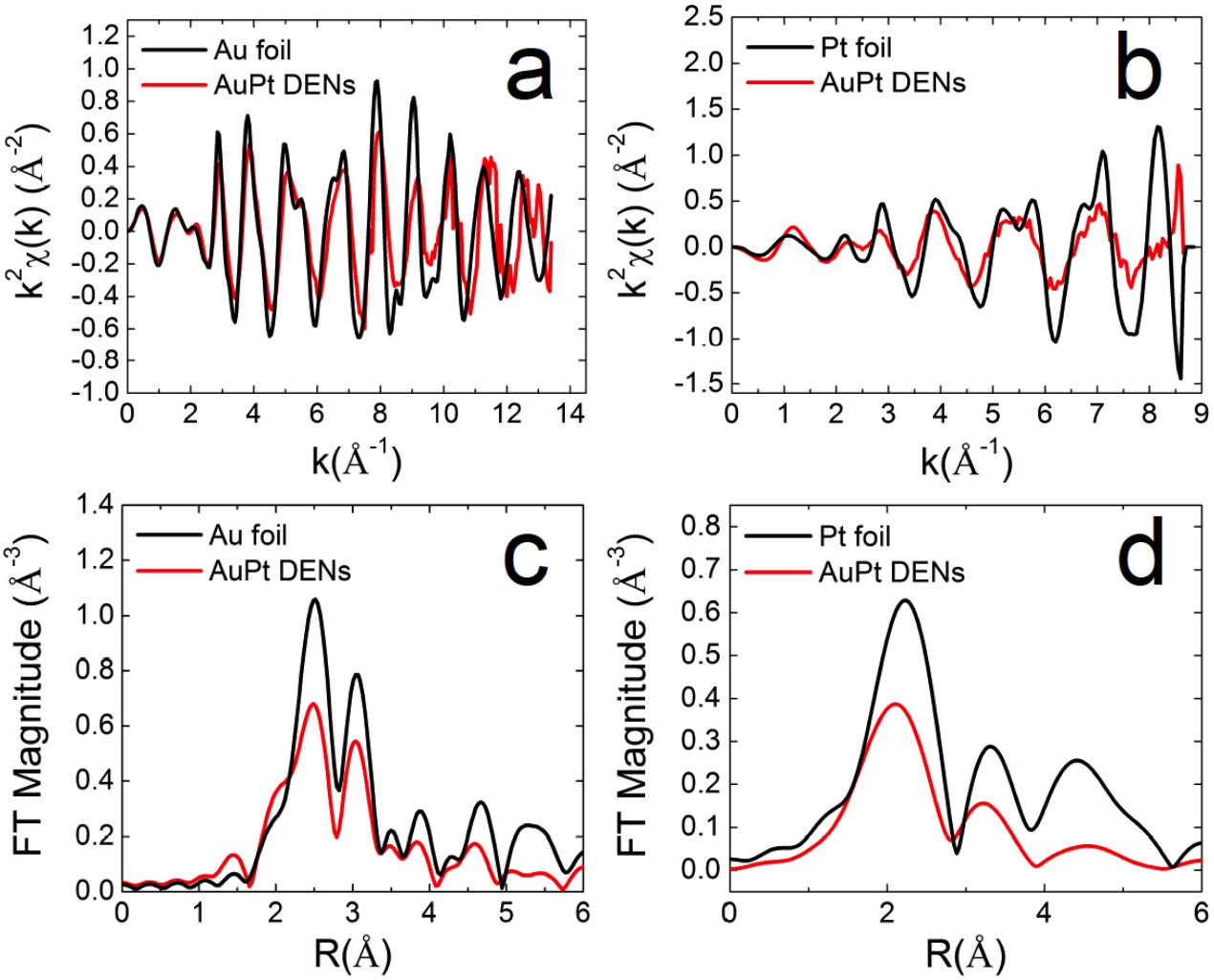

Figure 3.13

(a,b) Comparison of the *k*-space Au-L_3 and Pt-L_3 edge EXAFS spectra for AuPt DENs and Au and Pt reference foils. (c,d) Fourier-Transform (*r*-space) Au-L_3 and Pt-L_3 edge EXAFS spectra for AuPt DENs as compared to Au and Pt reference foils. The *k*-space and *r*-space ranges used for the fitting were 2.66–7.00 Å-1 and 1.50–3.77 Å, respectively, for Pt and 2.00–11.00 Å-1 and 2.19–3.28 Å, respectively, for Au. These spectra were used to determine the average coordination numbers (CNs), Au-M and Pt-M bond lengths, and the Debye-Waller factors (Table 3.1).

	N_{Au-M}	N_{Pt-M}	R_{Au-M} (Å)	R_{Pt-M} (Å)	ΔR(Å)	σ^2_{Au-M} (Å^2)	σ^2_{Pt-M} (Å^2)
Expt.	9.1(9)	10(2)	2.838(6)	2.77(2)	0.07(2)	0.0094(9)	0.008(5)
NP561 alloy	10.4	9.2	2.844	2.791	0.053	0.0128	0.0133
NP561 shell-1	10.2	9.6	2.834	2.805	0.029	0.0108	0.0117
NP453 shell-2	11.1	6.7	2.862	2.729	0.133	0.0206	0.0156
NP453 Pt cluster	10.6	7.7	2.869	2.742	0.127	0.0181	0.0213
Pt_{38}	-	7.6	-	2.697	-	-	0.0236

Table 3.1

Structural parameters extracted from fitting the Au and Pt-L_3 edge experimental (AuPt DENs) EXAFS data and DFT simulated EXAFS data. *N* is coordination number (CN), *R* is bond length, *ΔR* is the difference between *R(Au-M)* and *R(Pt-M)*, and σ^2 is the Debye-Waller factor.

edges introduces artifacts into the EXAFS analysis. There are two possible effects.

First, truncation of the data range has the potential to decrease the extracted value of the Pt-M coordination number (CN) due to backscattering from heavy neighbors (e.g., Au and Pt). As a result, special care was taken when truncating the data range. To minimize correlation between the *k*-range and the CNs, the amplitude reduction factors (S_0^2) were obtained using the same fitting range for the bulk foils and the AuPt DENs. As both the S_0^2 values from the foil and CNs from the AuPt DENs are obtained in the same *k*-range, the systematic errors are reduced. The k_{max} was selected to avoid the Au fluorescence contribution that is present at higher energies in the Pt spectra, while also ensuring enough range for reasonable background subtraction.

Second, the overlap of the Au-L_3 and Pt-L_3 edges in AuPt EXAFS introduces low frequency oscillations from the Pt-L_3 edge into the low *R*-range of the Au-L_3 edge. A standard Fourier filtering technique employed by the AUTOBK algorithm, implemented in the Athena program, was used to weaken the leak-contributions at low *k*. Setting the rbkg, the value below which AUTOBK minimizes Fourier components, to 1.7 Å dramatically reduces the anomaly observed at low *R* after Fourier transform.

To ensure that removal of the components below 1.7 Å introduced minimal impact on the CNs, we first estimated the extent of Pt-L_3 leakage by simulating that effect via a comparison of the Pt and Au foil spectra. The Pt foil L_3 EXAFS spectrum was obtained in the range of the Au foil L_3 EXAFS, and then Fourier transformed to reveal contributions present in that range. We confirmed that the leakage contributions were negligible after 1.7 Å, leading us to conclude that the CNs in this analysis have limited influence from the Pt-L_3 components due to the reduction of data below 1.7 Å.

We then compared the fitted S_0^2 of the Au foil spectra that were processed with different rbkg values (Table 3.2). We found that the Fourier components between 1.0 and 1.9 Å had no significant effect on S_0^2, and by extension the CNs and distances. Therefore, our method should not add any significant errors to the parameters calculated from these spectra. To confirm that the tail of the Pt spectrum does not change our interpretation, an advanced combined fitting approach[117] was explored. In this method, we fitted the Pt leakage in the Au spectrum rather than removing it. As shown in Table 3.3, both fitting methods are consistent with one another and support the same quasi-random alloy structure. The advanced fitting approach does not improve the results in this case, because the contribution of Pt leakage is small (due to a low Pt:Au ratio).

rbkg(Å)	**S_0^2**
1.0	0.85(5)
1.1	0.83(5)
1.2	0.84(5)
1.3	0.82(4)
1.4	0.82(4)
1.5	0.84(5)
1.6	0.83(5)
1.7	0.81(4)
1.8	0.81(4)
1.9	0.82(4)

Table 3.2

Background removal parameter (*rbkg*) vs. fitted amplitude reduction factor (S_0^2) for the Au foil.

	Au-M (Ind.)*	**Pt-M† (Ind.)**	**Au-M (Comb.)***	**Pt-M† (Comb.)**
N	9.1(9)	10(2)	11(1)	10(1)
R(Å)	2.838(6)	2.77(2)	2.833(6)	2.77(1)
σ^2_{Pt-M}(Å^2)	0.0094(9)	0.008(4)	0.0094(9)	0.008(4)
ΔE_0 (eV)	10.3(6)	6(1)	9.6(6)	5.4(9)

Table 3.3

Structural parameters extracted from fitting the Au- and Pt-L_3 edges. *N* is coordination number (CN), *R* is bond length, σ^2 is the Debye-Waller factor, and ΔE_0 is the correction to the photoelectron energy origin. Fitted parameters from the independent (Ind.) and combined (Comb.) fitting methods are shown for comparison. Results with an asterisk (*) incorporate a new Au S_0^2 that was optimized to reduce systematic errors in combined fitting. Results with a dagger (†) incorporate a new Pt S_0^2 that was optimized between k = 2.66 and 7.00 Å^{-1}.

Figure 3.13 shows the edge-step normalized, background-subtracted data in *k*- and *r*-space for the Pt-L_3 and Au-L_3 edges. Fourier transform magnitudes of the data and best fits are shown in Figure 3.14a-d for the Au and Pt edges. The Au-L_3 edge XANES spectrum for the AuPt DENs is almost identical to that of the Au foil (Figure 3.15a), indicating that the Au atoms in the NPs are in the metallic state (zerovalent). The particle size effect is evidenced by reduction of the oscillation intensity in *k*-space and Fourier transform intensities in *r*-space in the NP spectra compared to their bulk foil counterparts (Figures 3.13a and c). We note that from the similarity of the spectra to that of the Au foil alone, one cannot make a conclusion that the Au phase in the NPs is mixed with Pt or segregated. Au and Pt atoms do not have sufficient Z-contrast to make such a determination from just the visual observation of Au-L_3 edge spectra. Such analysis will be done using a theoretical fitting approach described in the next section.

As is evident in Figure 3.15b, the AuPt DENs Pt-L_3 edge is shifted towards higher energy, and has higher intensity in the whiteline region, compared to the reference Pt foil. These observations indicate that the electronic density is distributed differently around Pt atoms in the NPs compared to bulk Pt. This

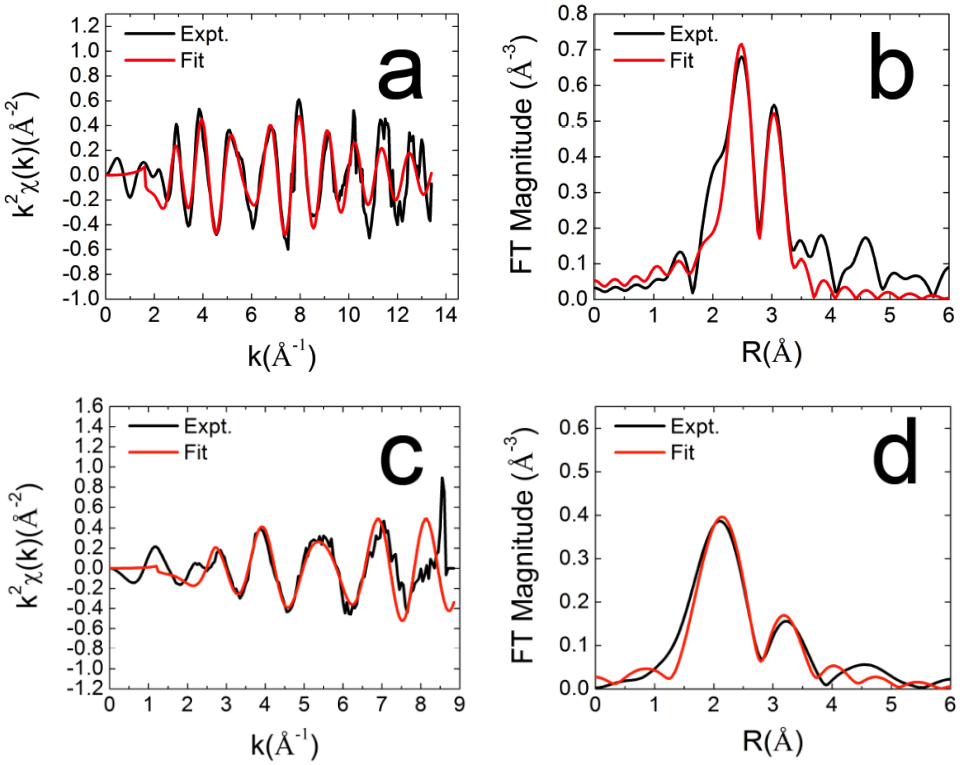

Figure 3.14

Comparison of the raw and fitted AuPt DENs EXAFS spectra in (a,c) *k*-space and (b,d) *r*-space for the (a,b) Au-L_3 and (c,d) Pt-L_3 edges. The R-factors associated with the fits to each of the Au-L_3 and Pt-L_3 edges are 0.004 and 0.017, respectively.

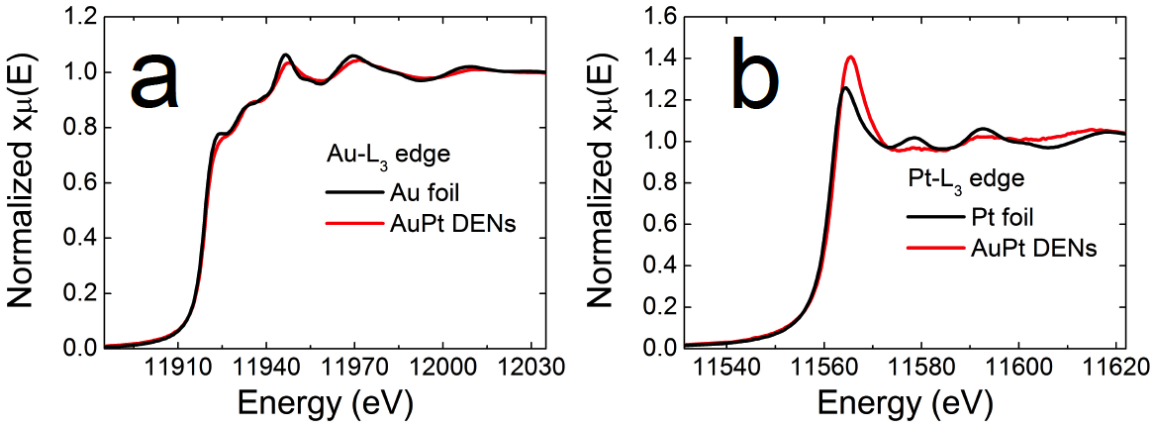

Figure 3.15

XANES spectra of the AuPt DENs and the corresponding metal foils at the (a) Au-L_3 and (b) Pt-L_3 edges.

observation would have been consistent with oxidation, but Figure 3.14c-d shows that the Pt-M contribution provides an adequate fit (R-factor=0.017) to the experimental spectra without the addition of any Pt-O contribution. This behavior is thus likely due to the alloying of Pt and Au in the NP. Yacaman and coworkers showed that for Au@Pt core@shell NPs the Pt edge XANES data was not significantly shifted relative to both PtNPs and a Pt foil, indicating segregation.[118] We will revisit this possibility below, when we interpret the results of quantitative analysis of EXAFS spectra by theoretical fitting.

The best fit values of the adjustable parameters for all the samples and their reference foils are reported in the first row of Table 3.1. Table 3.1 shows that the CNs of the Au-M (9.1±0.9) and Pt-M (10±2) contributions are the same, within the uncertainties. These CN values favor a model in which the Au and Pt atoms are distributed randomly, or quasi-randomly, within the NPs. Only in that case would the Au-M and Pt-M CNs be approximately equal, due to an Au atom having the same probability as a Pt atom to be located on the surface or interior of the NP. The proposed alloy structure is also consistent with the strongly altered shape of the Pt-L_3 edge XANES (vide supra) compared to the monometallic Pt foil. Interpretation of the extracted bond lengths is not immediately straightforward for predicting component distribution

because, in addition to the bond length dependence on the degree of mixing, it also depends on the NP size.

In summary, on the basis of the CNs of Au-M and Pt-M contributions and the modified electronic structure apparent in the Pt-L_3 edge XANES data, we propose that the structure of the AuPt DENs is an alloy. As we will discuss in the theory section, next, the alloying is likely localized primarily in the NP shell and therefore the structure is more likely a quasi-random alloy rather than a true random alloy.

The Au:Pt edge-step ratio measured by XANES (Figure 3.15) was used to determine the total NP composition for the EXAFS sample. XANES, rather than XPS, was used for this purpose because of the greater penetration depth afforded by XANES. The edge-step ratio, analyzed with XAFSmass[119], indicates that the sample is 73% Au and 27% Pt.

Theoretical modeling

Figure 3.16 demonstrates the predictive power of DFT for EXAFS signals, tested by comparing experimental and DFT-simulated Au and Pt foil *k*-space spectra. As shown, reasonable fits were obtained in terms of both amplitude and phase shift, with slightly better modeling of the Au edge relative to the Pt edge. Figures 3.17 and 3.18 compare the theoretical EXAFS signals generated with various

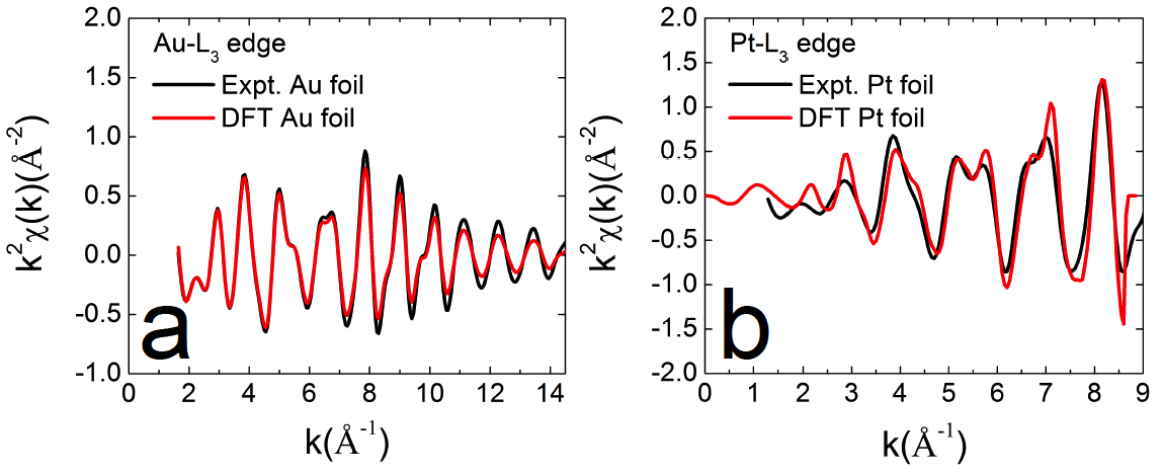

Figure 3.16

Comparison of DFT simulated (red) and experimental (black) EXAFS data for (a) Au and (b) Pt foils plotted in *k*-space. The simulated bond lengths for the Au and Pt foils are 2.893 and 2.776 Å, respectively. The simulated Debye-Waller factors (σ^2) for the Au and Pt foils are 0.00876 Å^2 and 0.00451 Å^2, respectively.

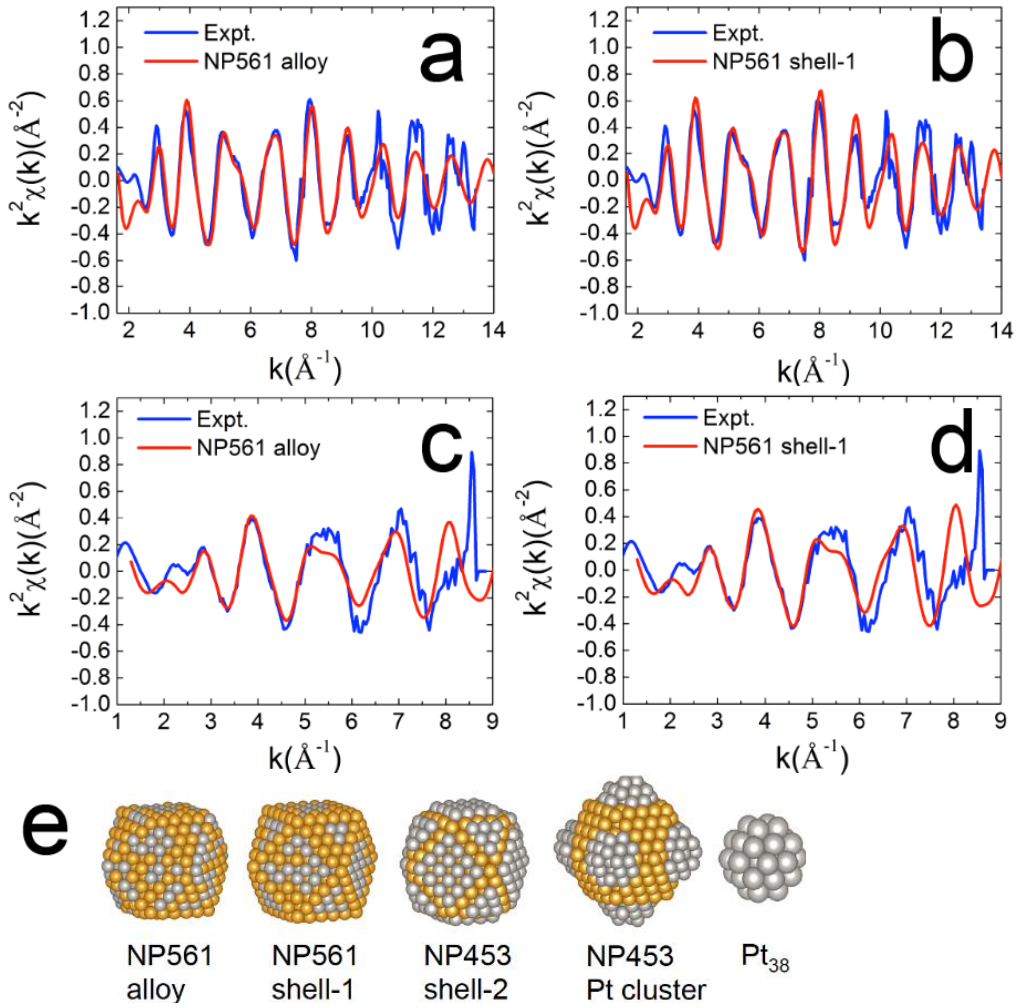
a
Expt.
NP561 alloy
b
Expt.
NP561 shell-1
c
Expt.
NP561 alloy
d
Expt.
NP561 shell-1
k²χ(k)(Å⁻²)
k(Å⁻¹)
e
NP561 alloy
NP561 shell-1
NP453 shell-2
NP453 Pt cluster
Pt38

Figure 3.17

Figure 3.17 cont.

Comparisons between DFT simulated (red) and experimentally obtained (blue) (a,b) Au-L_3 and (c,d) Pt-L_3 edge spectra, plotted in *k*-space for the (a,c) NP561 alloy and (b,d) NP561 shell-1 models. (e) Visual depictions of the models considered: random or quasi-random alloy (NP561 alloy), core@partial Pt shell with Au surface segregated to occupy the corner and edge atoms of the NP shell and 45 Pt atoms located subsurface (NP561 shell-1), two-dimensional Pt patch model (NP453 shell-2) where corner and edge atoms were removed to shrink the size of the Pt patches and shorten R(Pt-M), three-dimensional Pt cluster model (NP453 Pt cluster) with an Au core and segregated three-dimensional Pt patches, and Pt_{38} which tests the possibility of small Pt clusters in the sample. Simulated spectra for the latter three structures are located in Figure 3.18. Cuboctahedral geometry was used for all models.

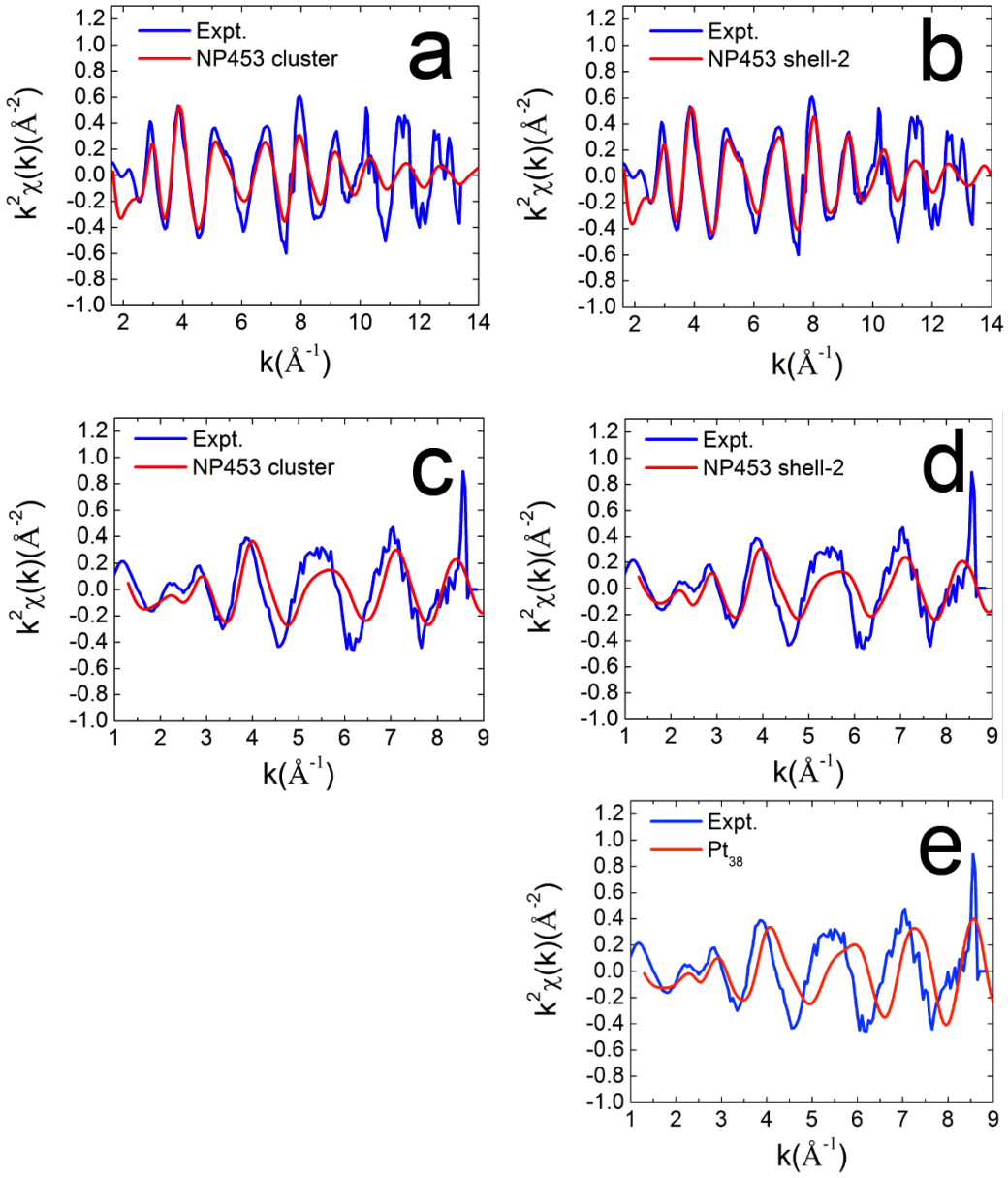

Figure 3.18

Comparison of theoretical simulations (red) and experimental (blue) EXAFS data plotted in *k*-space. (a,b) Au-L_3 edge and (c,d,e) Pt-L_3 edge plots for the (a,c) NP453 Pt cluster, (b,d) NP453 shell-2, and (e) Pt_{38} models.

atomic models with experimental measurements. First, we examined two models with cuboctahedral geometry for 561 total atoms (with 252 surface atoms) and total NP composition ($Au_{410}Pt_{151}$) determined from the XANES data. Assuming strictly two-dimensional growth, 106 Pt atoms (42% coverage according to the Cu UPD data) are randomly distributed or clustered on the surface, which are labeled as NP561 alloy and NP561 shell-1, respectively. Subtracting surface Pt composition from total Pt composition, 45 other Pt atoms are randomly distributed in the core of the NPs (overall $Au_{264}Pt_{45}@Au_{146}Pt_{106}$).

For the core@partial shell structure (NP561 shell-1), theoretical modeling shows that the most favorable arrangement is one in which the Au atoms surface segregate to occupy the corner and edge sites first. Given the short R(Pt-M) from experiment, three other models with a higher degree of Au and Pt segregation were tested: a two-dimensional Pt patch model (NP453 shell-2), which places all of the Pt atoms in the sample on the NP surface and removes the corner and edge atoms to shrink the Pt patches (effectively shortening R(Pt-M)); a three-dimensional Pt shell model (NP453 Pt cluster) having an Au core and a shell composed of three-dimensional Pt patches; and a Pt_{38} monometallic NP to test the possibility of individual Pt clusters being present in the sample. Simulated spectra for the latter three structures are

provided in the SI (Figure 3.18). The importance of including vibrational disorder in the atomic models is illustrated in Figure 3.19.

Table 3.1 compares the experimental and simulated EXAFS parameters. As shown, the NP561 alloy and NP561 shell-1 structures fit the experimental data most closely in terms of the predicted CNs (N), bond lengths (R), difference between the bond lengths (ΔR), and the Debye-Waller factors (σ^2). The shell-1 model shows slightly better prediction of N(Pt-M) than the alloy model, though both models are within error of the experimental N(Pt-M). N(Au-M) for the shell-1 model is slightly closer (10.2) to the experimental value than the alloy model (10.4). However, both models slightly overestimate the experimental N(Au-M) (8.2-10.0). This may be explained by the somewhat heterogeneous size distribution of the EXAFS sample. We discuss the bond length trends later.

Table 3.4 provides the R-factors calculated for each model for the Au-L_3 and Pt-L_3 edges. These R-factors signify the relative difference between the simulated and experimental spectra; lower values denote better fits.[120] The alloy and shell-1 models exhibit the best fits to the experimental *k*-space spectra for both the Au-L_3 and Pt-L_3 edges (Figure 3.17a-d and Figure 3.18). As shown in Figure 3.17 a-b, the shell-1 model qualitatively fits the Au- L_3 edge experimental data slightly better at high *k*-values than the

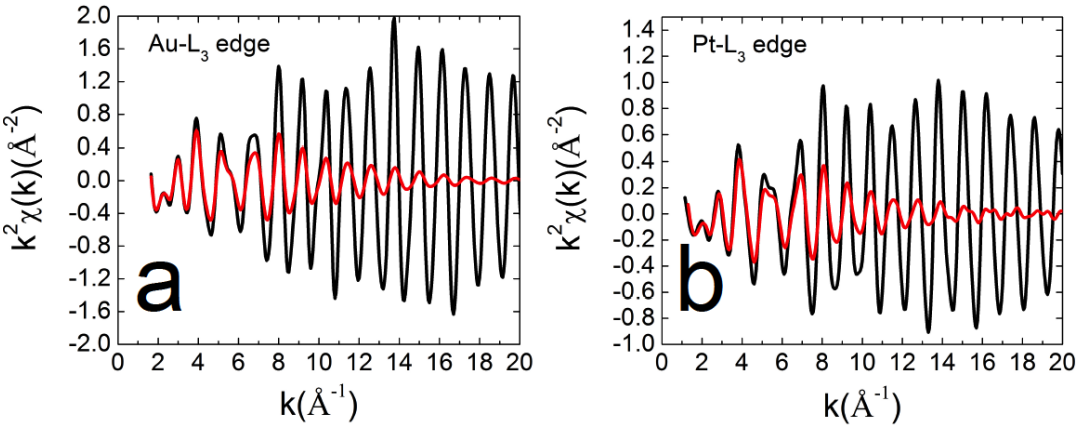

Figure 3.19

Simulated EXAFS spectra for the NP 561 alloy model with (red) and without (black) vibrational disorder (dynamical DWF) included in the atomic models for the (a) Au-L_3 and (b) Pt-L_3 edges. The simulations in the red traces use atomic models with vibrations sampled at 300 K. The black traces are simulated with a single atomic model corresponding to the relaxed equilibrium structure. The magnitudes of the oscillations for the black traces are much higher than for the red traces. Thus, excluding vibrational disorder results in insufficient damping at higher *k* values.

	NP561 alloy	**NP561 shell-1**	**NP561 shell-2**	**NP453 Pt cluster**	**Pt_{38}**
Au-L_3 edge	0.14	0.18	0.18	0.23	
Pt-L_3 edge	0.13	0.15	0.46	0.33	1.21
Total	0.27	0.33	0.64	0.56	

Table 3.4

R-factors for the simulated EXAFS spectra, calculated according to:

$$\mathrm{R} = \sum_{k_{\min}}^{k_{\max}} \left[\chi_{\exp}(k) - \chi_{\mathrm{sim}}(k)\right]^2 \Big/ \sum_{k_{\min}}^{k_{\max}} \left[\chi_{\exp}(k)\right]^2$$

where $\{k_{min}, k_{max}\}=\{2.00, 11.00\}$ for the Au-L_3 edge, and $\{k_{min}, k_{max}\}=\{2.66, 7.00\}$ for the Pt-L_3 edge. Individual values closer to 0 indicate a better fit.

alloy model. This is likely a result of slightly better modeling of disorder given that σ^2_{Au-M} is closer to the experimental value for the shell-1 model than for the alloy model. However, Table 3.4 indicates a smaller R-factor, and thus a better Au-L_3 edge fit, for the alloy model. The NP453 Pt cluster and NP453 shell-2 models (Figure 3.18a-b) qualitatively demonstrate significant inefficiency in modeling the Au-L_3 edge disorder at higher *k*-values, as shown by the poor alignment to the experimental peak amplitudes. The shell-2 model was better than the NP453 Pt cluster model in this regard and the R-factor for the shell-2 model is identical to that of the shell-1 model. The NP453 Pt cluster model demonstrates the greatest misfit (highest R-factor) of all the models to the Au-L_3 edge.

For the Pt-L_3 edge spectra (Figure 3.17c-d, Figure 3.18c-e, and Table 3.4), none of the fits are ideal, possibly as a result of the limited *k*-range due to overlapping Au-L_3 and Pt-L_3 edges. Qualitatively, the alloy (Figure 3.17c) and shell-1 (Figure 3.17d) spectra demonstrate similar fits to the experimental spectra, with a slightly better match in amplitude for the shell-1 model due to a higher CN. The R-factors for the Pt-L_3 edge reveal similar misfits for the alloy and shell-1 models, with a better match for the alloy model. The NP453 Pt cluster (Figure 3.18c) and NP453 shell-2 (Figure 3.18d) models have worse qualitative fits than the either

the alloy or shell-1 model at higher *k*-values. Indeed, the R-factors for the Pt-L_3 edge fits are significantly higher for the NP453 Pt cluster and shell-2 models than the shell-1 model. The Pt_{38} model shows both the worst qualitative (Figure 3.18e) and quantitative (R-factor=1.21) agreement with the experimental data by far and suggests that if any small Pt clusters are present, they are not the predominant form of Pt (recall that EXAFS is an ensemble technique).

Despite the slightly better agreement between predicted and experimental EXAFS parameters (Table 3.1) for the shell-1 model relative to the alloy model, the alloy model is more likely based on three features: (1) R-factors , (2) the values of ΔR (Table 3.1), and (3) the XANES data. As shown in Table 3.4, the R-factors are smallest for the alloy model, for both the Au-L_3 and Pt-L_3 edges. Thus, the best overall fit is the alloy model.

Because the bond lengths are affected by both size effects and composition, the difference, ΔR, between R(Au-M) and R(Pt-M) is more important than the exact, predicted values. The value of ΔR predicted by the alloy model (0.053 Å) fits the experimental value (0.07 Å) within the error of the experimental measurement (±0.02 Å), whereas ΔR for the shell-1 model (0.029 Å) does not. Although the three-dimensional cluster model (NP453 Pt cluster) predicts CNs close to being within error of the experimental data,

ΔR for that model is nearly double (0.127 Å) the experimental ΔR. Therefore, although the amount of segregation may be greater than predicted by the ideal alloy structure, it is much less than predicted by the NP453 cluster model. One possible explanation for why the experimental ΔR is on the high end of the predicted alloy value is heterogeneity in bond lengths as a result of heterogeneity in the NP size-distribution (3.2±0.7 nm). However, as previously mentioned, ΔR for the alloy model is still within error of the experimental value.

As discussed in the EXAFS section, the XANES data (Figure 3.15b) shows electronic modification of the Pt-L_3 edge that suggests alloying. The XANES data in combination with the experimental/theoretical agreement for the R-factors and for ΔR, indicates that the alloy structure is more likely than the shell-1 model, perhaps with a small degree of segregation. However, we believe the structure is quasi-random rather than completely random due to the higher concentration of Pt in the shell than in the core.

Mechanism of alloy formation

As we will discuss in the next section, the summation of all of our data indicates that the alloy structure is the most likely. This is not entirely surprising. While Au and Pt are immiscible,[121]

there is a tendency for Au and Pt to alloy at the nanoscale depending on the size of the NPs, the Au:Pt ratio, and the preparation method.[122] Additionally, despite classical immiscibility, there is precedent for significant bulk phase AuPt surface alloying as a result of kinetically limited Au surface segregation.[123,124] Importantly, however, our results compare structures of NP and bulk materials prepared using the same synthetic method. Scanning tunneling microscopy (STM) of the material resulting from HT Pt deposition on bulk Au(111) revealed ~85% Pt coverage and limited AuPt surface alloying.[75] Significant surface alloying was later reported,[76] but only after intensive electrochemical cycling (70-200 cycles). Therefore, the extensive NP surface alloying (42-52% Pt) observed in the present study differs substantially from the corresponding bulk material.

While the exact details of alloy formation are unclear, we wish to propose a tentative mechanism (though we acknowledge that it is imperfect). Specifically, we evaluate two possible methods for alloying: Au surface segregation and Pt absorption. We posit that the latter is dominant.

AuPt mixing is usually ascribed to Au surface segregation arising from lower Au surface energy.[122,123] Our calculations (Figure 3.20) for Au surface segregation energy ($E_{\mathrm{seg}}^{\mathrm{Au}}$) confirm favorable

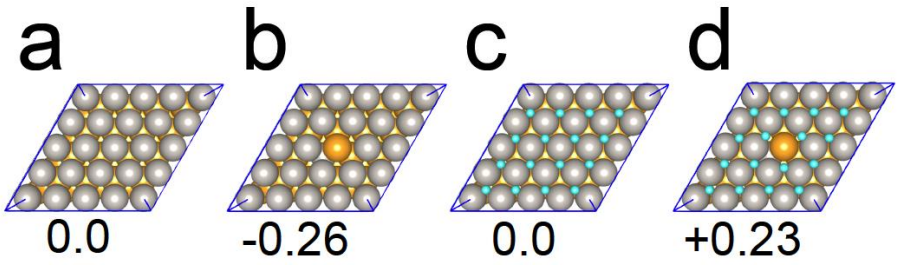

Figure 3.20

Au surface energies for (a,b) Au(111)/Pt and (c,d) Au(111)/Pt-H: (a,c) before and (b,d) after Au surface segregation. Gray, gold, and light blue spheres represent Pt, Au, and H atoms, respectively. Energies (in eV) are listed below each surface.

Au surface segregation for Au(111) covered with a Pt ML (E_{seg}^{Au}=-0.26 eV), but show that it is suppressed when H is adsorbed to Pt (E_{seg}^{Au}=+0.23 eV).

The same trend is observed for a NP model. Specifically, we calculated E_{seg}^{Au} for a slightly smaller NP model (Au_{147}@Pt) than those shown in Figure 3.17e to reduce computational cost. We expected enhanced Au surface segregation for the NP system because of the higher curvature and the surface stress exerted on Pt by the Au-Pt lattice mismatch. This prediction is confirmed in Figure 3.21a-e, where we show that Au surface segregation is more favorable at the corner, edge, and (100) facets of the Au_{147}@Pt NP as compared to the Au(111)/Pt surface. However, Au surface segregation is suppressed at the NP (111) facet. Once H is adsorbed to Pt on the NP surface (Figure 3.21 f-j), Au surface segregation becomes energetically unfavorable for all sites. These results suggest that alloying via Au surface segregation would occur after H is stripped (Step 3, Illustration 3.1) rather than during Pt deposition (Step 2, Illustration 3.1).

The second and more probable mechanism is alloying during Pt deposition. The previous arguments were based on the assumption that the HT method produces an Au@Pt core@full shell structure in the first instance. However, as we discuss in the next section,

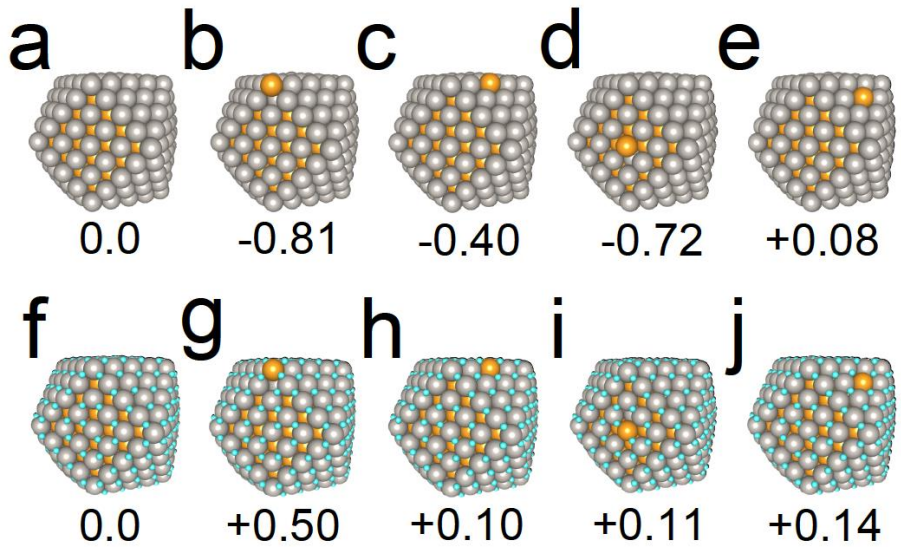

Figure 3.21

Au surface energies for (a-e) Au_{147}@Pt and (f-j) Au_{147}@Pt-H NP surfaces: (a,f) before Au surface segregation and (b-e,g-j) after Au surface segregation to the (b,g) corner, (c,h) edge, (d,i) (100) facet, or (e,j) (111) facet site. Energies (in eV) are listed below each surface.

the total Pt composition in our sample (27%) is lower than that required to form a full Pt shell (45%). As we discuss later in this section, Au surface segregation becomes unfavorable when there are a large number of Au atoms already on the NP surface.

For the following discussion, we assume that Pt atoms arrive at the AuNP surface one-by-one from all directions rather than spontaneously forming a full Pt shell. This differs from the UPD/GE technique, which uses a pre-formed (UPD) shell as a template for the Pt shell. We then carried out further calculations showing that alloying occurs rapidly during Pt deposition. Specifically, ab-initio molecular dynamics (MD) simulations were performed to equilibrate the system at 300K for 7.5 ps. The resulting structures show that the Pt adatoms and small Pt islands (Figure 3.22a) do not stay adsorbed to the outer AuNP surface; rather, they are absorbed by the AuNP and become embedded in the AuNP surface (Figure 3.22b) to increase their CNs. This effect is observed over a range of Pt compositions (6-25% or 10-50 atoms). A similar mechanism has been reported for Au absorption into Pd_6CoCu alloys.[125] The results before and after equilibration (Figure 3.22 a-b) show that absorption occurs so quickly (7.5 ps) that a Pt shell cannot form on the NP surface. Figure 3.23 shows identical results for an icosahedral NP with 25% Pt (chosen to best match

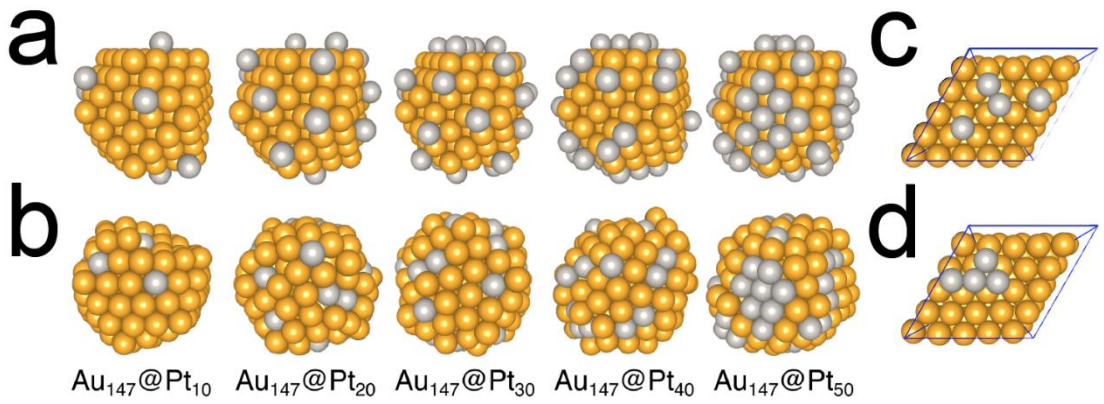

Figure 3.22

Ab-initio molecular dynamics simulations for Pt deposited on (a,b) Au_{147} NPs and (c,d) Au(111). Pt initially adsorbs to each surface (a,c). After 7.5 ps equilibration at 300 K, Pt embeds into the NP surface (b), but not into Au(111) (d). Pt incorporation into the NPs is observed over a range of Pt compositions (10-50 Pt atoms or 6-25%).

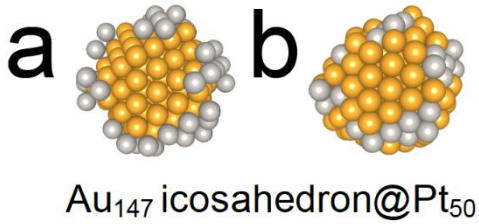

Figure 3.23

Ab-initio molecular dynamics simulations for Pt deposited on icosahedral Au_{147} (a) before and (b) after equilibration at 300 K for 7.5 ps.

the experimental composition: 27% Pt), demonstrating that Pt incorporation is not due to the particular cuboctahedral shape selected.

In contrast to AuNPs, Pt adatoms on the bulk Au(111) surface form only Pt islands after 7.5 ps of equilibration (Figure 3.22c and d). On the basis of these results, we propose that AuPt NP alloying occurs at the Pt deposition stage due to the structural flexibility of the AuNPs. Pt adatoms are expected to remain adsorbed to the more rigid bulk Au(111) surface and simply form larger Pt islands, and, eventually a Pt shell. Thus, our calculations bolster the assertion that different bulk and NP structures form upon application of HT Pt deposition on Au.

We contend that the second mechanism is more likely for three reasons. First, Pt incorporation is more rapid (7.5 ps) than the experimental Pt deposition time scale (1 s). Thus, Pt absorbs before the end of Pt deposition, during which time adsorbed H prevents competing Au surface segregation. Second, the Au surface segregation mechanism was formed based on the assumption of full Pt shell formation. However, the Pt composition (27%) is less than required for a full Pt shell (45%).

Third, the AuPt alloy formed during Pt deposition has a lower driving force for Au surface segregation after the adsorbed H is

stripped. To verify this assertion, we calculated E_{seg}^{Au} for MD equilibrated $Au_{147}@Pt_{50}$. These calculations (Figure 3.24) confirm that Au surface segregation is suppressed or even reversed when there is an incomplete Pt shell. We attribute this effect to the fact that for a Pt composition of 25%, there are already many Au atoms on the surface without the occurrence of Au surface segregation. This lowers the driving force for Au surface segregation. Hence, when the NP surface is not fully covered with Pt, Au surface segregation is not likely to be the dominant alloying mechanism.

Structure determination

On the basis of results from Moffat and coworkers for HT deposition of Pt onto bulk Au,[75] we anticipated that AuPt DENs synthesized using the HT method would yield a simple core@shell structure. However, this was not the case. In this section we provide a logical argument, based on results from TEM, EXAFS, XANES, electrochemistry, and theory, for the most consistent structure. We approach the problem using a process of elimination.

The least likely structure of the HT AuPt NPs is core@full shell. A 561-atom cuboctahedral Au@Pt NP has 252 surface atoms. In other words, this structure would contain 45% Pt if a full Pt shell

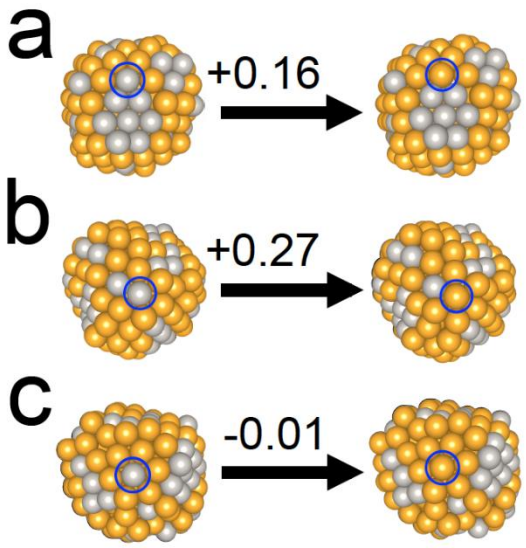

Figure 3.24

Estimated driving force for Au surface segregation after MD equilibration for $Au_{147}@Pt_{50}$. These calculations were performed in the absence of adsorbed H and thus represent the surfaces present after H is stripped (Illustration 3.1, Step 3). The NP composition (25% Pt) was chosen to best match our experimental composition (27% Pt). Three randomly chosen Pt surface atoms from the MD equilibrated structure (left side) are swapped with the underlying Au atoms, forming the structures shown on the right side. The particular atoms swapped are shown in the blue circles. The Au surface segregation energies (in eV) associated with each swap are listed above the arrows.

were deposited. The Au:Pt ratio derived from XANES is 73:27 ($Au_{410}Pt_{151}$), indicating a total of 151 Pt atoms. Even if all of these were on the NP surface, they would not constitute a full 252-atom Pt ML. Electrochemical Cu UPD results indicate ~42% (106) Pt surface atoms, which is less than the total number of Pt atoms determined by XANES. Thus, comparison of the total and surface-only Pt composition suggests that either a small amount of Pt is incorporated into the NP core or that there is three-dimensional growth of Pt nodules onto the Au core. We will discuss each of these possibilities in due course.

The EXAFS CNs similarly fail to support a full Pt shell. For an ideal cuboctahedral core@shell Au@Pt NP, we would expect N(Au-M) to be ~12, given that each core Au atom would be fully surrounded by metal atoms, and that N(Pt-M) < N(Au-M), because NP surface atoms are under-coordinated.[126] In fact, however, the EXAFS data shows that N(Au-M) ≈ N(Pt-M) within uncertainty. Therefore, XANES, Cu UPD, and EXAFS all disfavor a simple core@full shell model.

Next, we show that a core@partial-shell structure is less likely than an alloy structure. The two core@partial shell models analyzed (NP561 shell-1 and NP453 shell-2) display greater misfits to the experimental EXAFS spectra (higher R-factors) than the alloy model. This is especially true for the NP453 shell-2 fit to the Pt-L_3 edge. The NP453 shell-2 model is easier to discard due to

poor agreement with the experimental EXAFS parameters (Table 3.1) and the fact that the NP surface consists of 83 exposed core Au atoms and 144 Pt shell atoms (63% surface Pt), which is higher than experimentally observed (42% surface Pt). Elimination of the shell-1 model is based on the fact that it was built assuming the Au surface segregation mechanism discussed in the previous section, with Au atoms placed at the corner and edge sites of the NP. However, we showed that for the HT synthesis, Au surface segregation is blocked due to H adsorption (Figure 3.21f-j) during Pt deposition. Rather, alloying via rapid Pt incorporation (7.5 ps) during Pt deposition is predicted (Figure 3.22), and Au surface segregation largely loses its driving force by the time the H is stripped (Figure 3.24). The higher R-factors for the NP561 shell-1 and NP453 shell-2 models, the poor EXAFS agreement and overestimated surface Pt content for the NP453 shell-2 model, along with the mechanism we propose for structure formation, suggest that both core@partial-shell structures are unlikely.

We now consider the case of a random alloy structure. The first point in favor of a random alloy is that the values of N(Au-M), 9.1±0.9, and N(Pt-M), 10±2, extracted from EXAFS, are roughly equal within experimental error.[126] Although there is slightly better agreement between the experimental and predicted EXAFS parameters for the core@partial-shell model (NP561 shell-1), the

alloy model demonstrates the best fits (lowest R-factors) to the *k*-space spectra for both the Au-L_3 and Pt-L_3 edges and ΔR is within experimental error for the alloy model but not for the core@partial-shell model. Additionally, the XANES data suggest Pt alloying, as demonstrated by a Pt-L_3 edge shift to higher energy and the increase in whiteline intensity (coupled with a lack of evidence for Pt oxidation). Thus, EXAFS and XANES are consistent with a random alloy structure. Finally, MD simulations suggest that the random alloy structure is most likely from a kinetic point of view. However, the majority of the total Pt atoms (151) in the sample are on the surface (106). Accordingly, we believe these materials are quasi-random alloys.

Finally, we discuss the possibility of atomic arrangements incorporating three-dimensional Pt growth (NP453 Pt cluster and Pt_{38}, Figure 3.17e). The first arrangement that can be discounted is fully segregated Au and Pt NPs. The strongest evidence against this configuration is that EDS showed co-localization of Au and Pt for both the non-EXAFS (Figure 3.8) and EXAFS (Figure 3.12) NPs. The CV data also argue against segregation. Specifically, upon HT electrodeposition, the Au electrochemically active surface area decreases while the electrochemical signature of Pt simultaneously increases. This indicates that Pt covers at least some of the Au on the NP surface. Moreover, the XANES spectrum indicates charge

transfer between Au and Pt, suggesting that the two elements are in physical contact. Finally, models incorporating three-dimensional Pt growth exhibit significantly worse agreement with the experimental EXAFS data than the alloy model (Tables 3.1 and 3.4).

3.5. Summary and Conclusions

There are two major outcomes of the work reported here. First, we have shown that HT deposition of Pt onto 1.6 nm Au_{147} DENs yields a quasi-random alloy structure. This result is in contrast to the situation with bulk Au surfaces,[75,76] which leads to a nearly complete surface ML of Pt. This result is not completely surprising, given the vastly different geometries of 1.6 nm NP surfaces compared to bulk surfaces. Indeed, as our calculations have shown, the flexibility of AuNPs can enable rapid AuPt alloying during HT Pt deposition, which is not accessible for comparatively rigid bulk Au.

The second important outcome is the necessity of combining well defined experimental models (e.g., DENs), numerous physical methods (e.g., electrochemistry, TEM, EDS, and XAS), and appropriate theory to ascertain reliable structural information about such complex materials.

Finally, we point out that the present study was undertaken using just a single combination of metals (Au and Pt) and a single size of NP (1.6 nm). It is certainly possible, likely even, that application of the HT method to other metals,[89,91] as well as other NP sizes and shapes, will lead to other structures, including, perhaps core@shell NPs. Additionally, we have not begun to address the issue of multiple HT iterations,[75,76] even for the AuPt system.

Unanswered questions remain for the AuPt NPs reported here. First, the alloy formation mechanism is still tentative and lacks experimental verification. Second, in the interest of clarity the role of chemical gradients and melting point depression in alloy formation were not explored. We hope to investigate these influences in future studies. Third, we previously reported the synthesis of Au@Pt DENs using UPD followed by Pt GE, but characterization of those materials was far more limited than in the present case.[14-16] We are presently re-examining those results, using the same battery of methods used here, to determine if differences in the synthetic methods are responsible for the structural differences or if we simply drew incorrect conclusions on the basis of insufficient characterization data. The results of these studies will be reported in due course.

Chapter 4: Combined Experimental and Theoretical Study of the Structure of AuPt Nanoparticles Prepared by Galvanic Exchange[2]

4.1 Synopsis

In this article, experiment and theory are combined to analyze Pb and Cu underpotential deposition (UPD) on ~1.7 nm Au nanoparticles (NPs) and the AuPt structures that result after galvanic exchange (GE) of the UPD layer for Pt. Experimental Pb (0.49 ML) and Pt (0.50 ML) coverages are close to values predicted by density functional theory-molecular dynamics (DFT-MD; 0.59 ML). DFT-MD reveals that the AuNPs spontaneously reconstruct from cuboctahedral to a (111)-like structure prior to UPD. In the case of Pb, this results in random electrodeposition of Pb onto the Au surface. This mechanism is a consequence of opposing trends in Pb-Pb and Pb-Au coordination numbers as a function of Pb coverage. Cu UPD is more complex, and agreement between theory and experiment takes into account ligand effects (e.g., SO_4^{2-} present as the electrolyte) and the electric double layer. Importantly, AuPt structures formed upon Pt GE are found to differ markedly depending on the UPD metal. Specifically, cyclic voltammetry indicates that

[2]The research in this chapter was previously published (see below). The dissertator was the primary contributor: Lapp, A.S.; Duan, Z.; Henkelman, G.; Crooks, R.M. Combined Experimental and Theoretical Study of AuPt Nanoparticles Prepared by Galvanic Exchange. *Langmuir* **2019**, *35*, 16496-16507.

Pt coverage is ~0.20 ML greater for Cu UPD/Pt GE (0.70 ML) than for Pb UPD/Pt GE (0.50 ML). This difference is corroborated by DFT-MD theoretical predictions. Finally, DFT-MD calculations predict formation of surface alloy and core@shell structures for Pb UPD/Pt GE and Cu UPD/Pt GE, respectively.

4.2. Introduction

Nanoparticle (NP) catalysts consisting of a single- or multi-metal alloy core capped with a single-atom-thick partial or full shell are important for many different chemical and electrochemical reactions.[6,7,127] For example, they minimize the use of expensive, catalytically active metals by maximizing the number of active surface atoms.[127] Additionally, core@shell structuring enables fine tuning of the catalytically active shell by exerting control over the size, shape, composition, and ordering of the core.[1,5,57,128] Many interesting catalytic effects of these types of materials are observed, particularly when the size of the NPs is < ~3 nm.[1,2,5,129–131]

One popular method for preparing these types of materials involves electrochemical underpotential deposition (UPD) of the shell metal onto the core, followed by galvanic exchange (GE) of the shell for a second metal.[6–8,14,15,18,57,70,76] UPD is a process by which a single metallic monolayer (ML) is deposited onto a

substrate at a potential positive of bulk metal deposition.[47] GE occurs when ions of a more noble metal spontaneously replace a UPD ML with a ML of the more noble metal. For example, Au@Pt NPs active for the oxygen reduction reaction (ORR),[14] methanol oxidation reaction,[18] and formic acid oxidation (FAO)[16] have been synthesized using the UPD/GE process.[14,19] Due to their small size and complex structures, however, characterization of core@shell NPs is often incomplete. This, in turn, makes it difficult to draw structure-function correlations. For example, we recently showed that bimetallic AuPt NPs prepared by a direct Pt ML deposition technique, known as the hydride-termination method,[75-77] yields alloys[40] rather than the core@shell structure anticipated by extrapolation from macro-scale materials.[75]

There is an extensive body of literature focused on Cu and Pb UPD on macro-scale Au substrates.[19-21,47,74,132] Despite widespread use of UPD/GE for synthesizing NPs, however, understanding of UPD processes on NPs,[45,46,60,65,68-70] particularly those in the < 3 nm size range, is less well developed. Theoretical examination of UPD on NPs, in particular, has been limited in both number and depth.[11,15,45,46,64,69] Dendrimer-encapsulated NPs (DENs), which we[1,2,28,33,100] and others[29,31,101] have previously reported, are well suited for combining experimental and theoretical studies due to their small (1-2 nm) and nearly monodisperse sizes and

compositions.[1] These factors minimize computational costs, avoid the theoretical limitations of treating heterogeneity, and eliminate uncertainties associated with calculations that only consider slabs of larger NPs.

Cu UPD[12,14,25,34,45,46] and Pb UPD[15,16] have previously been studied on DEN cores. Cu UPD onto Au DENs was first used as a precursor for preparing Au@Pt NPs.[14] These Au_{147}@Pt DENs (here, "147" represents the nominal number of Au atoms in the core) were found to possess a nearly complete Pt ML (74-85% of a complete Pt ML) and were catalytically active for the ORR. However, direct immobilization of the DENs onto glassy carbon electrodes precluded complete structural characterization.

In addition to preparing Au@Pt DENs using a Cu UPD intermediate, we also reported their synthesis via Pb UPD.[15] This approach yielded considerably lower surface Pt coverage (55-57% of a full Pt ML) relative to Cu UPD/Pt GE,[14] but it still resulted in formation of electrocatalysts active for the ORR[15] and FAO.[16] Moreover, density functional calculations indicated that Pt(100) sites initially present on the surface of the cuboctahedral Au@Pt DENs undergo a rapid conversion to Pt(111).[15] This structural change was found to positively impact the electrocatalytic activity of these materials for the FAO reaction relative to Pt-only and Au-only DENs.[16]

On the basis of our earlier study,[40] which clearly demonstrated the pitfalls of extrapolating structural motifs determined for macro-scale materials to the nano-scale, we now investigate an even more interesting question. Specifically, do AuPt NPs prepared by slightly different methods have the same or different structures, and if the latter, why? The answer to this question could have a significant impact on our understanding of electrocatalysis, particularly for reactions sensitive to ensemble effects (e.g., FAO)[45,46] or for reactions where both Pt and Au are catalytically active (e.g., CO oxidation in alkaline media).[43,47] To address this question, we deposited either Cu or Pb UPD MLs onto well-defined, ~1.7 nm Au cores, and then exchanged the UPD metal for Pt. Detailed characterization reveals that the choice of the UPD metal strongly impacts the final structures of the resulting bimetallic NPs. Companion results from a first-principles density functional theory (DFT) study provide insights into the underlying reasons for these findings.

4.3. Experimental Section

Chemicals and materials

A 9.0 wt% solution of amine-terminated, sixth-generation poly(amidoamine) (PAMAM) dendrimers (G6-NH_2) in methanol was

obtained from Dendritech, Inc. (Midland, MI). The methanol was evaporated and the dendrimers were reconstituted in sufficient water to yield a 0.10 mM G6-NH_2 stock solution. A 0.50 M NaOH solution, $NaBH_4$ (99.9%), $HAuCl_4$ (≥99.9%), $Pb(NO_3)_2$ (99.9%), and HPLC grade 2-propanol (99.9%) were purchased from Sigma-Aldrich. K_2PtCl_4 (99.9%), $CuSO_4$ (98%, anhydrous), and 70% $HClO_4$ (in H_2O) were obtained from Fisher (New Jersey, USA). All solutions were prepared using deionized (DI) Milli-Q water (18.2 MΩ-cm; Millipore, Bedford, MA).

TEM grids were purchased from EM Sciences (Gibbstown, NJ, catalog numbers CF400-Cu-UL and LC400-Cu-UL). Vulcan carbon (EC-72R) was purchased from ElectroChem, Inc. (Woburn, MA). The working (glassy carbon, 3.0 mm), reference (Hg/Hg_2SO_4), and counter electrodes (glassy carbon rod) were purchased from CH Instruments (Austin, TX).

Synthesis of Au DENs

The synthesis of Au DENs (denoted as G6-NH_2(Au_{147}), where 147 reflects the $AuCl_4^-$:G6-NH_2 ratio in the precursor solution) has been reported previously and shown to result in nearly size-monodisperse AuNPs.[40,105] Briefly, a 2.0 μM aqueous G6-NH_2 dendrimer solution was prepared by adding 0.20 mL of a 0.10 mM stock to 8.65 mL of water. $AuCl_4^-$ was encapsulated within the dendrimers by

dropwise addition of $HAuCl_4$ (0.147 mL of a 20.0 mM stock) with vigorous stirring. Within 2 min, the encapsulated $AuCl_4^-$ was chemically reduced with a solution consisting of 1.0 mL of 0.30 M NaOH and an 11- to 12-fold molar excess of $NaBH_4$. For this step, NaOH was added to the $NaBH_4$ (in a weighing boat) immediately before transfer. Upon reduction, the solution changed color from light yellow to brown. Deactivation of the residual BH_4^- by air was allowed to proceed for at least 12 h before characterizing the resulting NPs.

NP characterization

UV-vis spectra were obtained using a Hewlett-Packard 8453 spectrometer. NP imaging was performed using a JEOL 2010F transmission electron microscope (TEM) with an operating voltage of 200 kV and a point-to-point resolution of 0.19 nm. TEM analysis of G6-NH_2(Au_{147}) was carried out by dropcasting 2.0 μL of a 2.0 μM DENs solution onto a carbon-coated Cu grid and then drying in air. Grids for analyzing the AuPt DENs were prepared by swiping lacey carbon-coated Cu TEM grids across the surface of the electrodes used for electrochemical synthesis and characterization.

Cyclic voltammetry (CV)

Electrochemical synthesis and characterization were carried out using a CH Instruments 630E potentiostat in conjunction with a 3.0-mm glassy carbon working electrode (GCE), glassy carbon rod counter electrode, and an Hg/Hg_2SO_4 (MSE) reference electrode. The GCEs were polished successively with 1.0, 0.3, and 0.05 μm alumina (2 min each) before use. Excess alumina was removed by sonication in Milli-Q water for ~10-15 min. DEN inks were prepared as previously described.[40] Briefly, ~1.0 mg of VC was dispersed into 0.20 mL of isopropanol (IPA) using sonication. After a homogeneous mixture was achieved (~15 min), 1.0 mL of 2.0 μM G6-$NH_2(Au_{147})$ DENs was added, the ink was sonicated for an additional 15 min, and then it was dropcast (6.0 μL) onto the GCE and dried under a gentle flow of N_2.

Electrochemical cleaning of the DENs, as well as Au and AuPt surface-characterization CVs, was carried out using a solution of N_2-purged, 0.10 M $HClO_4$. Electrochemical cleaning was performed by scanning the electrode potential between 1.57 and 0 V for 20 cycles at a scan rate of 200 mV/s. The Au and AuPt surface characterization CVs were recorded using this same potential range, but for only three and nine cycles, respectively, and at a scan rate of 100 mV/s.

Underpotential deposition and Pt galvanic exchange (UPD/Pt GE)

Pb UPD onto the immobilized G6-NH_2(Au_{147}) DENs was performed in the following manner. First, a Pb UPD CV was recorded in N_2-purged, 0.10 M $HClO_4$ containing 1.0 mM $Pb(NO_3)_2$. Specifically, the electrode potential was held at 0.60 V for 300 s and then scanned from 0.60 to 0.70 to -0.17 V at 5.0 mV/s. Pb linear sweep voltammograms (LSVs) were recorded by holding the electrode potential at -0.15 V for 300 s, and then scanning it from -0.15 V to 0.70 V at a rate of 5.0 mV/s. Cu UPD onto G6-NH_2(Au_{147}) DENs was performed in N_2-purged 0.10 M $HClO_4$ containing 5.0 mM $CuSO_4$, using an analogous process to Pb UPD with the following differences. The electrode potential was held at 0.70 V for 300 s and was then scanned from 0.70 to 0.85 to 0.30 V at a rate of 10 mV/s. Cu LSVs were recorded by holding the electrode potential at 0.32 V for 300 s, and then scanning it from 0.32 V to 0.85 V at a rate of 10 mV/s.

Pt GE was used to deposit a Pt shell onto the G6-NH_2(Au_{147}) DENs. Just prior to Pt GE, the electrode potential was held at either -0.15 V (for Pb) or 0.32 V (for Cu) for 300 s. The GCE was then raised to a position slightly above the solution level, the circuit was opened, and pre-dissolved K_2PtCl_4 (in ~1.0 mL of 0.10 M $HClO_4$) was mixed into the cell via brief agitation with a N_2-purge stream. The GCE was then lowered back into solution, and the

open-circuit potential (OCP) was monitored as a function of time for 400 s. The $PtCl_4^{2-}$ concentration was 2.5 mM.

Following Pt GE, the GCE was sequentially rinsed for ~20 s in 250 mL of Milli-Q water, 5 min in 20 mL of 0.10 M $HClO_4$ (with vigorous stirring), and then briefly in 20 mL of Milli-Q water. Both the necessity and efficacy of this rinsing process were explored in depth in a previous publication[40] for a similar AuPt DENs synthesis. The as-prepared AuPt DENs (this notation is used to indicate that structure is uncertain at this point) were then characterized by recording CVs using the same parameters as for the Au surface area CVs, with the exception that nine cycles were obtained to ensure scan reproducibility.

Density functional theory (DFT)

Theoretical calculations were performed using DFT implemented in the Vienna ab initio simulation package (VASP).[106,133] Core electrons were described with the projector augmented-wave (PAW) method.[108,109] The Kohn-Sham wave functions for the valence electrons were expanded in a plane-wave basis set with an energy cutoff of 300 eV. The exchange-correlation energy was treated within the generalized gradient approximation. Specifically, PBEsol[110] was used, which is a modified form of the Perdew-Burke-Ernzerhof (PBE) functional designed to improve lattice parameters and surface

energies in solids. A single Γ-point was sufficient for integration of the Brillouin zone due to the finite nature of the NPs.

Density functional theory-molecular dynamics (DFT-MD)

DFT-MD simulations were employed to equilibrate the structures of Pb adsorption, Cu adsorption, and Cu/SO_4 adsorption on AuNPs. A time step of 1.5 fs was used and a total time of 30 ps was carried out for each MD simulation. The temperature was held at 300 K by drawing velocities of all atoms from a Boltzmann distribution every 10 steps.

Double reference method

The double reference method[134] was used to simulate the electric double layer (EDL) and determine the equilibrium potential of Cu UPD on the Au(111) surface under constant-potential conditions. Our approach is different from the original implementation of the double reference method,[134] where explicit water molecules are used to model the metal/aqueous interface. Here, the aqueous environment is treated by the continuum solvation model developed by Hennig and coworkers as implemented in the VASPsol code.[135] The relative permittivity of the solvent was set to ϵ_{solv} = 80 to account for the presence of the aqueous electrolyte. This value corresponds to the permittivity of bulk water.

Details of the double reference method can be found elsewhere.[136,137] Briefly, the electric potential of the simulated electrochemical interface is varied by changing the number of electrons in the system. To maintain charge neutrality of the super cell, a uniform background of compensating counter charge was added. The charged slab, together with the compensating background charge, polarizes the electrolyte near the metal/solution interface thereby creating an electrostatic potential profile that simulates the EDL.

For each electrochemical interface, DFT calculations were performed at various charges by inserting or deleting electrons from the simulated system. The total free energy at each point was then fit to a quadratic equation to provide a continuous free energy as a function of potential. The quadratic form is consistent with a capacitor created by the charged-slab/background-charge system, which takes the form of eq 1.

$$\mathrm{E(U)} = -\frac{1}{2}C\left(U - U_{\mathrm{pzc}}\right)^2 + E_0 \qquad (1)$$

Here, U_{pzc} refers to the potential of zero charge (PZC), E_0 is the energy at the PZC, and C is the capacitance of the metal/aqueous interface. From the quadratic equations fit for the

bare slab and adsorption models, the binding energies as a function of electric potential are readily calculated.

Simulation of CVs

CVs of the UPD processes were simulated according to a method from the literature.[138] The current ($i(t)$) produced by the UPD processes can be calculated as shown in eq 2.

$$\mathrm{i(t)} = \pm \mathrm{K} Q_{\mathrm{tot}} \frac{d\theta}{dU} \qquad (2)$$

Here, K is the sweep rate and Q_{tot} is the total charge the surface of AuNPs can accommodate. $\frac{d\theta}{dU}$ is the inverse of $\frac{dU}{d\theta}$, which is the differential equilibrium potential of the UPD processes with respect to the surface coverage of the deposited species (Pb or Cu atoms) in this study. To calculate the equilibrium potentials of the UPD processes, we considered the hypothetical reaction route shown in eq 3, using Pb^{2+} deposition on AuNPs as an example.

$$n{\cdot}Pb\ (bulk) + Pb_N/AuNP \leftrightarrow n{\cdot}(Pb^{2+} + 2e^-) + Pb_N/AuNP \leftrightarrow Pb_{N+n}/AuNP \quad (3)$$

Here, Pb in its bulk form is dissolved and then the dissolved Pb^{2+} deposits onto the AuNP. The latter reaction is the process we

are interested in, and the average free energy change of this step is $\Delta G^{\mathrm{dep}} = (G_{\mathrm{Pb_{N+n}/AuNP}} - n\mu_{\mathrm{Pb^{2+}}} - G_{\mathrm{Pb_N/AuNP}} + 2ne\mathrm{U})/n$ where $G_{\mathrm{Pb_N/AuNP}}$ is the free energy of an AuNP coated with N Pb atoms, n is the number of Pb atoms deposited, $\mu_{\mathrm{Pb^{2+}}}$ is the chemical potential of $\mathrm{Pb^{2+}}$, and U is the applied potential. The value of $\mu_{\mathrm{Pb^{2+}}}$ can be calculated from the standard reduction potential of Pb metal ($U^0 \equiv -0.13\,\mathrm{V}$) and the concentration of $\mathrm{Pb^{2+}}$ ($c_{\mathrm{Pb^{2+}}}$) using eq 4.

$$\Delta G^{\mathrm{dep}} = \frac{\left(G_{\mathrm{Pb}_{\boldsymbol{N+n}}/\mathrm{AuNP}} - n\mu_{\mathrm{Pb,\ bulk}} - G_{\mathrm{Pb_N/AuNP}} + 2ne(U-U^0) - nk_{\mathrm{B}}\mathrm{T}\log c_{\mathrm{Pb^{2+}}}\right)}{n} \qquad (4)$$

If the vibrational entropy contributions to the free energy of solid materials are omitted, and the free energies are replaced with total energies from DFT calculations, the ΔG^{dep} term can be expressed as shown in eq 5.

$$\Delta G^{\mathrm{dep}} = \Delta E^{\mathrm{ads}} - k_{\mathrm{B}}\mathrm{T}\log\left(\frac{1-\theta}{\theta}\right) + 2\mathrm{e}(U-U^0) - k_{\mathrm{B}}\mathrm{T}\log c_{\mathrm{Pb^{2+}}} \qquad (5)$$

Here, $\Delta E^{\mathrm{ads}} \equiv (E_{\mathrm{Pb_{N+n}/AuNP}} - nE_{\mathrm{Pb,\ bulk}} - E_{\mathrm{Pb_N/AuNP}})/n$ is the differential adsorption energy of Pb atoms and $k_{\mathrm{B}}\mathrm{T}\log\left(\frac{1-\theta}{\theta}\right)$ is the differential configurational entropy of the adsorbed Pb atoms with

a surface coverage of θ ML. The equilibrium potential for the UPD process is then calculated as:

$$\mathrm{U}^{\mathrm{dep}} = -\frac{\Delta G^{\mathrm{dep}}}{2e} \quad (6)$$

Consequently, eq 6 can be inserted into eq 2 to calculate the CV current.

For the calculation of Cu/SO_4 co-adsorption on AuNPs, the reaction shown in eq 7 is assumed.

$$xCu^{2+} + ySO_4^{2-} + (2x-2y)e^- + Au(111) \leftrightarrow Cu_x(SO_4)_y/Au(111) \quad (7)$$

In this case the free energy change per deposited Cu atom is calculated as shown in eq 8.

$$\Delta G^{\mathrm{dep}} = \Delta E^{\mathrm{ads}} - k_{\mathrm{B}}\mathrm{T}\log\left(\frac{1-\theta}{\theta}\right) + (2\mathrm{x} - 2\mathrm{y})/x(\mathrm{U} - \mathrm{U}^0) - k_{\mathrm{B}}\mathrm{T}\log c_{Cu^{2+}} - y/xk_{\mathrm{B}}\mathrm{T}\log c_{SO_4^{2-}} \quad (8)$$

The calculation of ΔE^{ads} in the SO_4 co-adsorption case requires the chemical potential of the solvated SO_4^{2-} ions. For this, we employed a previously reported expression.[139] When the double reference method is used to calculate the potential dependent

energies, $\Delta E^{ads}(\theta)$ becomes $\Delta E^{ads}(\theta,U)$. For calculating the chemical potential of NO_3^-, we used the reduction reaction, $NO_3^-(aq) + 4H^+(aq) + 3e^- \rightarrow NO(g) + 2H_2O(l)$, which has a standard reduction potential of 0.96 V.

4.4. Results and Discussion

Synthesis and characterization of G6-NH_2(Au_{147}) DENs

The G6-NH_2(Au_{147}) DEN synthesis is discussed in the Experimental Section. Briefly, the DENs were prepared by combining G6-NH_2 dendrimers and sufficient $HAuCl_4$ to yield a 147:1 $AuCl_4^-$:G6-NH_2 ratio, and then reducing the resulting composites with excess $NaBH_4$. We have previously shown that this procedure reliably yields AuNPs having narrow size distributions.[40,105]

Figure 4.1 shows the UV-vis spectrum of the G6-NH_2(Au_{147}) DEN cores. Two features are important: a small, broad plasmon band centered at ~520 nm, and a monotonic increase in absorbance toward shorter wavelengths. The combination of these features is characteristic of AuNPs having sizes of <2 nm.[15] TEM (Figure 4.1) confirms the spectroscopic data by revealing an average NP size of 1.7 ± 0.3 nm for the G6-NH_2(Au_{147}) DEN cores. This value is in good agreement with both the theoretical diameter of an Au_{147}

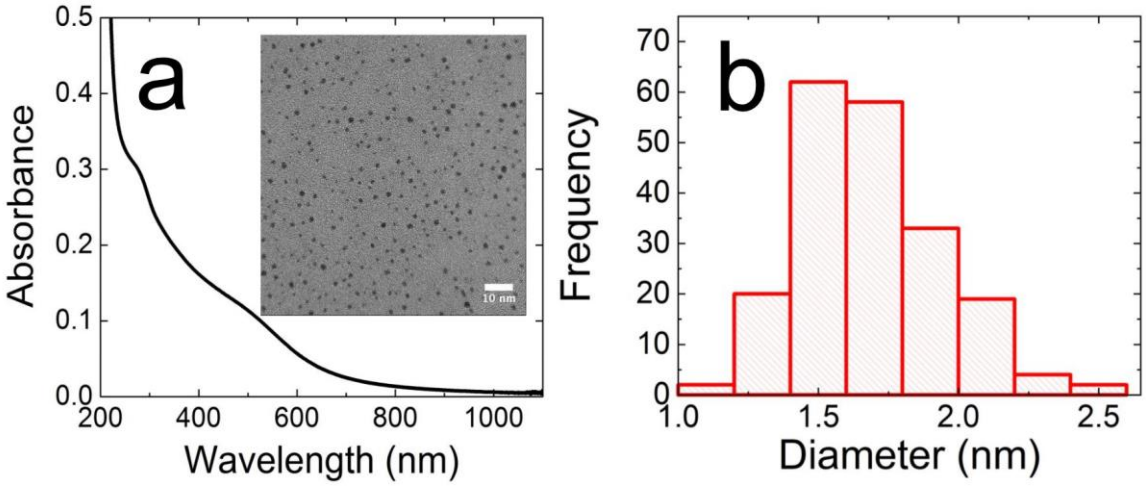

Figure 4.1

UV-Vis and TEM analysis of G6-NH_2(Au_{147}) DENs. (a) UV-vis spectrum. The pathlength of the cuvette was 0.200 cm and Milli-Q water was used as the reference. A TEM micrograph is shown in the inset. (b) Size distribution (1.7 ± 0.3 nm) histogram obtained by randomly counting 200 NPs from the inset in (a).

cuboctahedral NP (~1.6 nm)[15] and previous experimental reports.[14-16,40,105]

The first step for converting the Au cores to AuPt NPs involves immobilizing the G6-NH_2(Au_{147}) DENs onto Vulcan carbon (VC). The full details of this procedure are provided in the Experimental Section, but, briefly, G6-NH_2(Au_{147}) DENs were added to a premixed solution of VC in IPA and sonicated for ~15 min. This ink was then dropcast onto a GCE and dried under a gentle flow of N_2.

The black trace in Figure 4.2a is a CV of the G6-NH_2(Au_{147}) DENs prepared as described in the previous paragraph. The prominent peak at ~1.1 V corresponds to reduction of AuO_x, which is formed by the potential excursion to 1.57 V. This peak can be integrated and converted into the total Au surface area (SA) using the commonly accepted charge density conversion factor of 390 μC/cm^2.[140]The resulting value is Au_i = 0.28 cm^2, where the subscript *i* represents the initial Au SA prior to UPD or GE.

Synthesis of AuPt DENs via Pb UPD/Pt GE

As discussed in the Experimental Section, UPD of Pb onto the G6-NH_2(Au_{147}) DEN cores was carried out in N_2-purged, 0.10 M $HClO_4$ containing 1.0 mM $Pb(NO_3)_2$ according to the following procedure. First, a Pb UPD CV (Figure 4.2b, black trace) was recorded. This

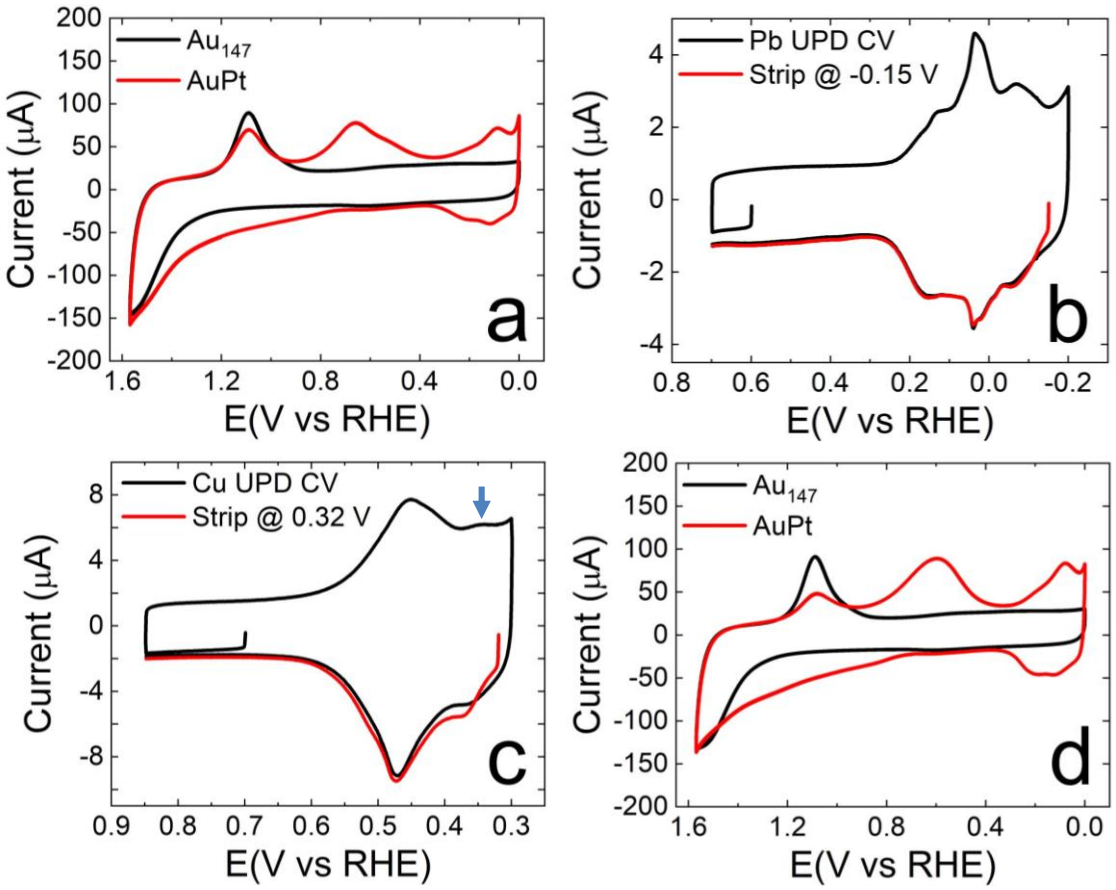

Figure 4.2

Cyclic voltammograms (CVs) before (black traces) and after (red traces) Pt deposition onto G6-NH_2(Au_{147}) DENs using (a) Pb UPD/Pt GE and (d) Cu UPD/Pt GE. CVs (black traces) corresponding to (b) Pb UPD and (c) Cu UPD on G6-NH_2(Au_{147}) DENs. The associated LSVs are shown in red. The LSVs were recorded after holding the electrode potential for 300 s at either -0.15 V (Pb) or 0.32 V (Cu). The blue arrow in (c) highlights a peak that resembles the second stage (~1.0 ML Cu) of Cu UPD onto Au(111).[47] The CVs in (a,d) were recorded in N_2-purged 0.10 M $HClO_4$ at a scan rate of 100 mV/s. The electrolyte for (b,c) was N_2-purged 0.10 M $HClO_4$ containing (b) 1.0 mM $Pb(NO_3)_2$ and (c) 5.0 mM $CuSO_4$ and the scan rates were (a) 10.0 mV/s and (c) 5.0 mV/s.

CV was used to determine the end of the Pb UPD potential range for subsequent steps, which was chosen to be just positive of the onset of bulk Pb deposition at -0.15 V. Second, to ensure that no bulk deposition of Pb occurs at this potential, the electrode was held at -0.15 V for 300 s, and then an LSV was obtained by scanning positive to 0.70 V (Figure 4.2b, red trace). The fact that the resulting LSV overlays the Pb UPD CV confirms the absence of bulk Pb deposition. This suggests that the foregoing process coats the Au_{147} cores with a single UPD ML of Pb.

Focusing now on the Pb UPD CV in Figure 4.2b, Pb deposition peaks are centered at 0.15 V, 0.04 V, and -0.07 V, and stripping peaks are present at 0.03 V and 0.16 V. These values are in accord with our prior reports of Pb UPD onto G6-NH_2(Au_{147}) DENs.[15,16] In analogy to reports of Pb deposition onto larger (~4-82 nm) AuNPs,[61-63,141] we previously discussed Pb UPD (and stripping) onto Au_{147} DENs in terms of sequential, facet-by-facet processes. For example, the two principal oxidation peaks at 0.03 V and 0.16 V were assigned to Pb stripping from the Au(100) and Au(111) facets, respectively.[15] For AuNPs as small as those used here (~1.7 nm), however, a facet-by-facet mechanism is likely an oversimplification. For instance, sharing of atoms between facets is so dominant for 147-atom cuboctahedral NPs that only a single atom is unique to a (111) facet.[46] As we will discuss later, the

Pb UPD behavior on Au DENs can be successfully interpreted without invoking a facet-by-facet mechanism.

The Pb SA (0.24 cm^2) was calculated by integrating the Pb LSV in Figure 4.2b and then converting this value to SA using a charge density of 413 $\mu C/cm^2$.[15] Recalling that the initial Au SA was Au_i = 0.28 cm^2, the Pb:Au_i SA ratio = 0.86. This value is close to that which we found in a previous report (~1.1).[15] There are multiple ways of defining UPD coverage on NPs.[15,45,141] In the present report, we define 1.0 ML of Pb as the number of atoms required to construct a closed cuboctahedral shell over the core. For example, a 147-atom cuboctahedral NP contains 92 shell atoms. The next complete shell would contain 162 atoms, which we define as representing one complete ML (1.0 ML). Multiplying the Pb:Au_i SA ratio (0.86) by the number of surface atoms on a G6-NH_2(Au_{147}) DEN (92) yields 79 Pb atoms = 0.49 ML. Using this definition, and on the basis of nine independent experiments, the Pb coverage on the G6-NH_2(Au_{147}) DENs is 0.49 ± 0.03 ML. There is one caveat regarding this value, however. As shown in Figure 4.3, the size of the G6-NH_2(Au_{147}) DENs increases from 1.7 ± 0.3 nm to 1.9 ± 0.4 nm after 20 electrochemical cleaning scans (i.e., just prior to Pb UPD). Hence, 0.49 ML represents our best estimate of the Pb coverage within the context of the error associated with the TEM size-distribution data.

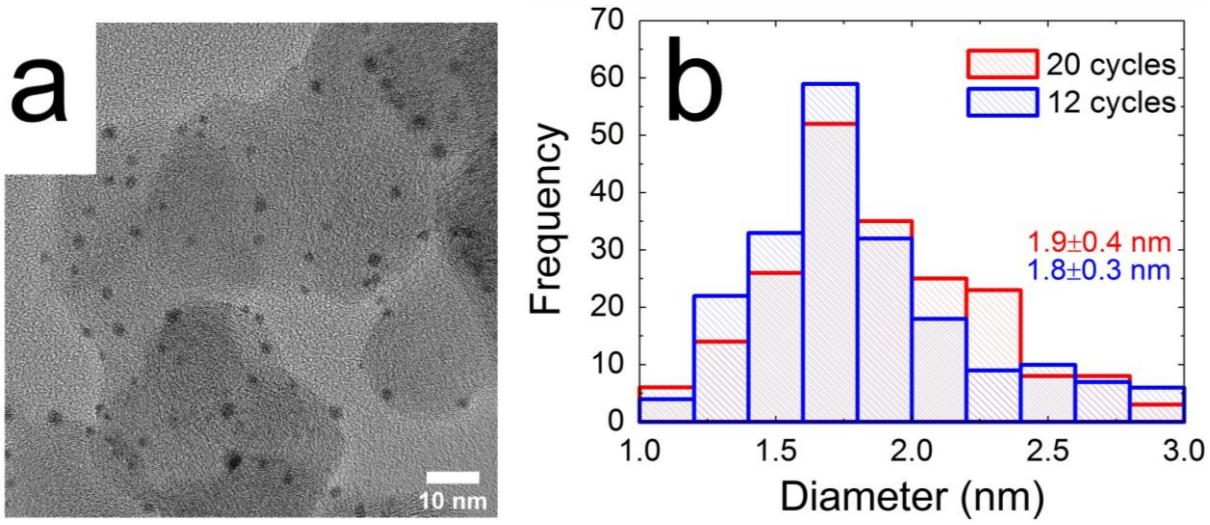

Figure 4.3

The effect of electrochemical pre-treatment on NP size. (a) TEM and (b) the associated size distribution histogram for the G6-NH_2(Au_{147}) DENs after 12 and 20 electrochemical cleaning cycles. The number of cleaning cycles (20) used prior to recording the CVs shown in Figure 4.2 was chosen for consistency with our previous publications.[14,40] NP size increases slightly from the as-synthesized size (1.7 ± 0.3 nm, Figure 4.1) to 1.9 ± 0.4 nm after 20 electrochemical cleaning cycles. Reduction of the number of cleaning cycles to 12, which was the minimum number required to obtain limiting CVs, leads to a size distribution (1.8 ± 0.3 nm) that is statistically equivalent to 20 cycles. Electrochemical cleaning was performed in N_2-purged 0.10 M $HClO_4$. The initial potential was 0.70 V, and the scans proceeded positive to 1.57 V and then negative to 0 V at a rate of 200 mV/s.

As discussed in the Experimental Section, the synthesis of AuPt DENs via Pb UPD/Pt GE proceeds in two steps. First, Pb UPD onto the G6-NH_2(Au_{147}) DENs was performed by holding the electrode potential at -0.15 V for 300 s. Second, K_2PtCl_4 was introduced into the cell to initiate Pt GE with the electrode held at the open circuit potential. This step results in replacement of the Pb UPD shell with Pt. Note that we refer to this material as AuPt, rather than Au@Pt, to indicate that at this stage in the analysis we are uncertain as to its structure (e.g., core@shell, random alloy, or a hybrid).

Figure 4.4a is a TEM micrograph of the AuPt DENs synthesized by Pb UPD/Pt GE, and Figure 4.4b is the corresponding size-distribution histogram. The average size of the AuPt NPs is 2.3 ± 0.5 nm, which is close to the size (2.1 nm) of a perfect 309-atom cuboctahedral NP consisting of a 147-atom Au core and a 162-atom Pt shell.[15] The size is also consistent with those reported previously for AuPt DENs prepared by UPD/Pt GE onto Au DENs.[12,15,16]

Figure 4.2a shows representative CVs before (black trace) and after (red trace) Pb UPD/Pt GE. As mentioned earlier, only a single peak, corresponding to AuO_x reduction, is observed (at ~1.1 V) prior to Pb UPD/Pt GE. After UPD/GE, however, the area under the AuO_x reduction wave decreases and two new features arise: a PtO_x reduction peak and hydrogen adsorption/desorption waves (Pt

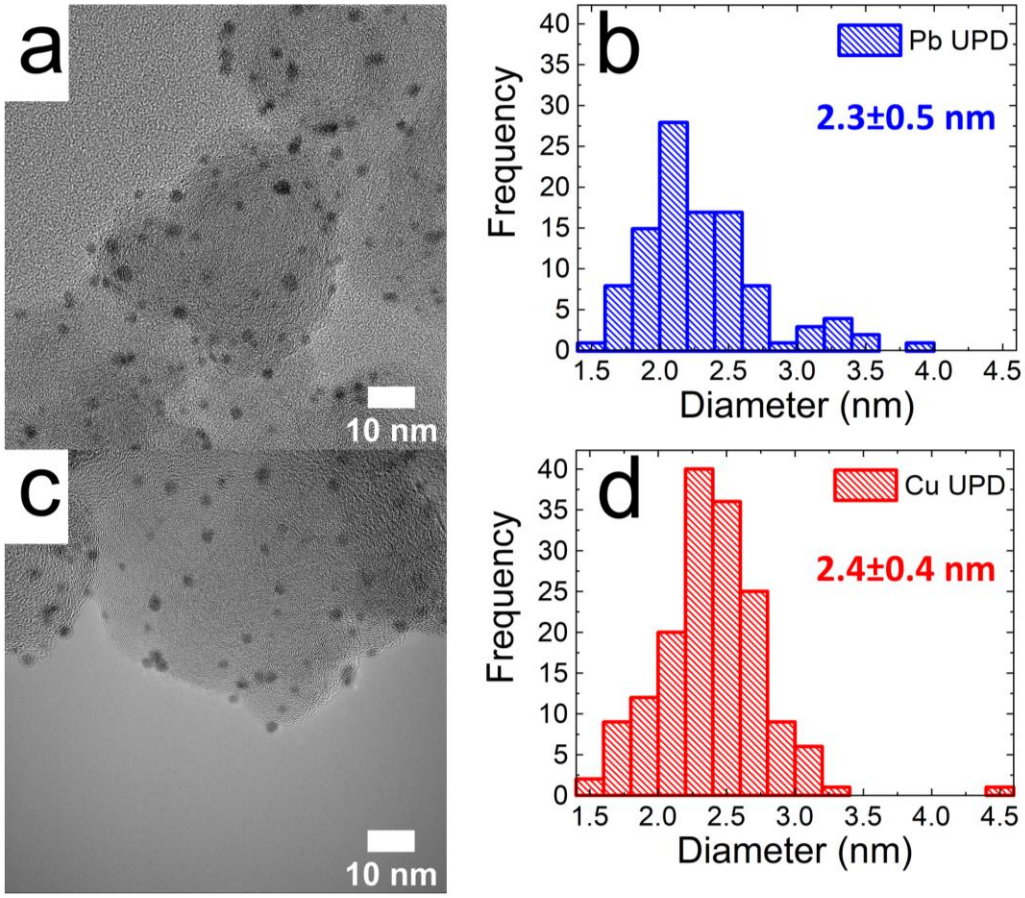

Figure 4.4

Representative TEM micrographs for AuPt DENs synthesized using (a) Pb UPD/Pt GE and (c) Cu UPD/Pt GE. (b,d) The size distributions associated with (a) and (c), respectively. Each distribution was obtained by sizing 200 randomly selected NPs.

hydride waves). The PtO_x reduction peak is centered at 0.66 V and Pt hydride waves are observed negative of ~0.30 V.

Pt coverage was calculated using two methods. The first method is $1-(Au_f/Au_i)$, where Au_i and Au_f are the Au SAs before and after UPD/Pt GE, respectively. The second method is [Pt SA/(Au_f + Pt SA)]. For the purposes of the present discussion, we refer to the former and latter estimates as $\Theta_{Pt,shell}$ and $\Theta_{Pt,total}$, respectively. $\Theta_{Pt,shell}$ depends strictly on the change in Au SA. As such, it represents two-dimensional growth directly on the AuNP surface. In contrast, $\Theta_{Pt,total}$ represents the total amount of electroactive Pt on the electrode surface, which could include adventitious Pt.

As previously mentioned, Au_i = 0.28 cm^2. Au_f was determined in the same way as Au_i, except that the red trace of Figure 4.2a was used to calculate Au_f = 0.14 cm^2. The Pt SA for the AuPt DENs synthesized using Pb UPD/Pt GE (0.19 cm^2) was calculated by integrating the Pt hydride waves in Figure 4.2a, and then using a charge density of 210 $\mu C/cm^2$,[14] to convert charge to SA. Overall, a 0.08±0.04 ML discrepancy is observed between $\Theta_{Pt,shell}$ (0.50±0.04 ML) and $\Theta_{Pt,total}$ (0.58±0.04 ML), for nine independent measurements. Therefore, an amount of Pt equivalent to ~0.08 ML is located on the electrode surface but not located in the Pt shell.

Adventitious Pt NP formation has previously been reported upon exposure of carbon surfaces to K_2PtCl_6 at open circuit

potential (OCP).[142–148] Therefore, it seems plausible that the OCP exposure of the VC-supported DENs to K_2PtCl_4 during the GE step of UPD/Pt GE could lead to formation of adventitious Pt. To isolate the effects of Pt exposure, the above possibility was investigated by executing the same steps for AuPt DENs synthesis (minus UPD), in the absence of the AuNPs. The ink used for this purpose was composed of VC, IPA, and empty 2.0 μM G6-NH_2 dendrimers. Hereafter, we refer to this ink as "VC/dend".

TEM before and after exposing the VC/dend ink to K_2PtCl_4 (Figures 4.5a and b) reveals adventitious Pt in the latter case. Figures4.5c and d show TEM of the Pb UPD/Pt GE-synthesized AuPt DENs in regions where adventitious Pt is present and absent, respectively. From 7 randomly selected TEM images, the number of AuPt NPs (6000) far outnumbers the adventitious Pt NPs (213). Thus, we believe that this adventitious Pt impurity represents a minor perturbation.

Overall, the average estimated Pt coverage ($\Theta_{Pt,shell}$ = 0.50 ± 0.04 ML) is in good agreement with the experimental Pb coverage (0.49 ± 0.03 ML), suggesting complete exchange of Pt for Pb during GE.

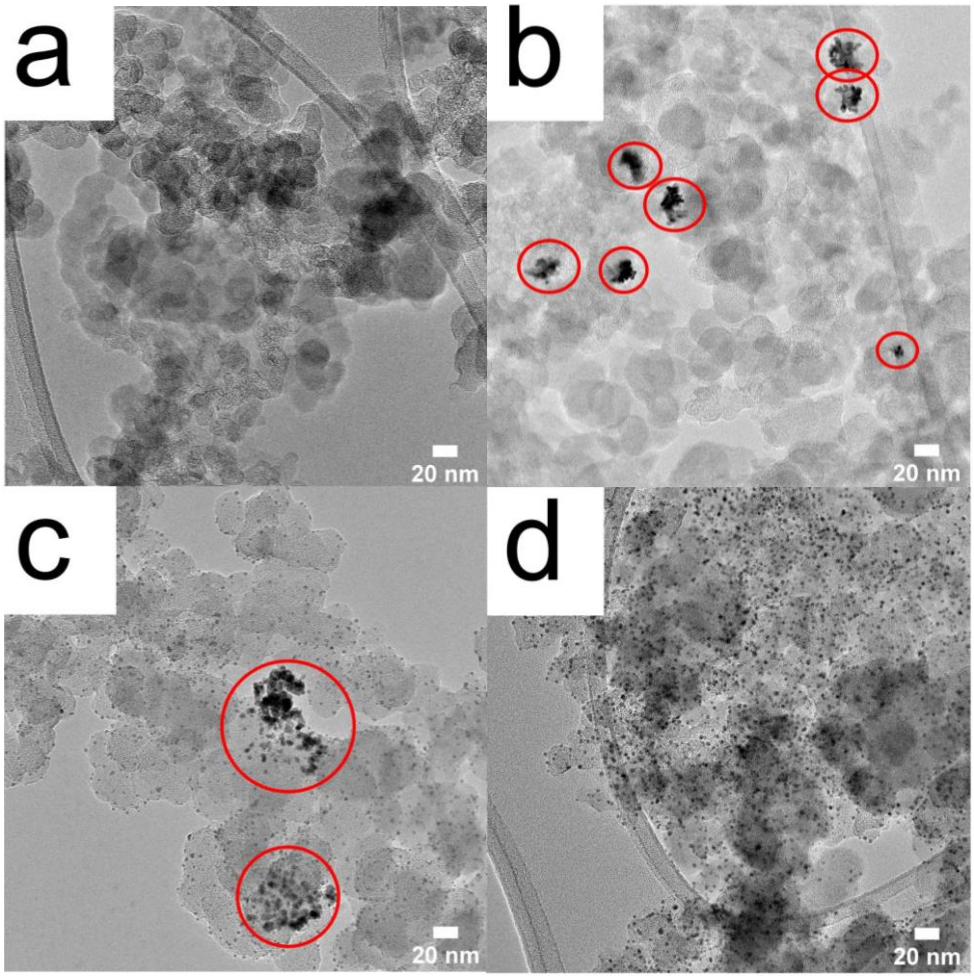

Figure 4.5

TEM images corresponding to control experiments evaluating the possibility of adventitious Pt. (a,b) VC/dend ink (a) before and (b) after exposure to 2.5 mM K2PtCl4 for 400 s. The red circles highlight instances of adventitious Pt formation. (c,d) AuPt DENs synthesized using Pb UPD/Pt GE. While adventitious Pt was observed in some of the TEM micrographs (e.g,(c)), it was absent from most (e.g.,(d)). On average, the adventitious Pt NPs had a size of 33±8 nm. From 7 randomly selected TEM micrographs, 6000 AuPt NPs and 213 adventitious Pt deposits were counted.

Synthesis of AuPt DENs via Cu UPD/Pt GE

Cu UPD was carried out as described in the Experimental Section and in a similar fashion to Pb UPD. Prior to UPD, however, a control CV (Figure 4.6) was obtained in the potential range used for Cu UPD to ensure the absence of contaminants and competing processes. An analogous CV was not obtained prior to Pb UPD, because the hydrogen evolution reaction (HER) occurs on naked Au within the relevant potential range.[47] In the presence of Pb^{2+}, however, scanning the potential in this range coats Au with Pb prior to the onset of the HER (Figure 4.7).

Cu UPD (black trace in Figure 4.2c) was carried out in a N_2-purged solution containing 5.0 mM $CuSO_4$ and 0.10 M $HClO_4$. The Au DEN-modified GCE was held at a potential of 0.70 V for 300 s and then scanned from 0.70 V to 0.85 V to 0.30 V at a rate of 10 mV/s. The corresponding LSV (red trace in Figure 4.2c) was recorded like the Pb LSV, but a deposition potential of 0.32 V was used in this case. As with Pb UPD, the Cu UPD CV and LSV overlay almost perfectly, confirming the absence of bulk Cu deposition. For the Cu UPD CV, two deposition peaks are centered at ~0.45 V and 0.34 V and two stripping peaks are centered at 0.37 V and 0.47 V. The deposition and stripping potentials are in good agreement with previous reports of Cu UPD onto Au_{147} DENs.[12,14,34,40]

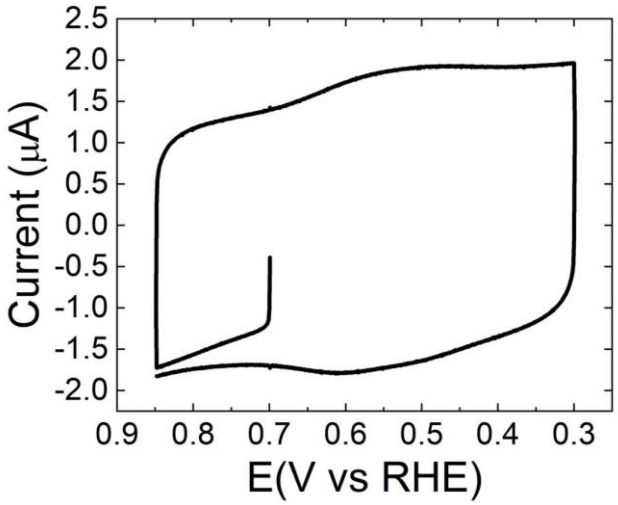

Figure 4.6

Representative background CV for G6-NH_2(Au_{147})DENs recorded in the potential range relevant to Cu UPD. The electrolyte solution was N_2-purged, 0.10 M $HClO_4$ and the scan rate was 10 mV/s. The CV is essentially featureless, indicating that no detectable, electroactive contaminants are present in solution and that no competing side reactions occur within the potential range used for Cu UPD.

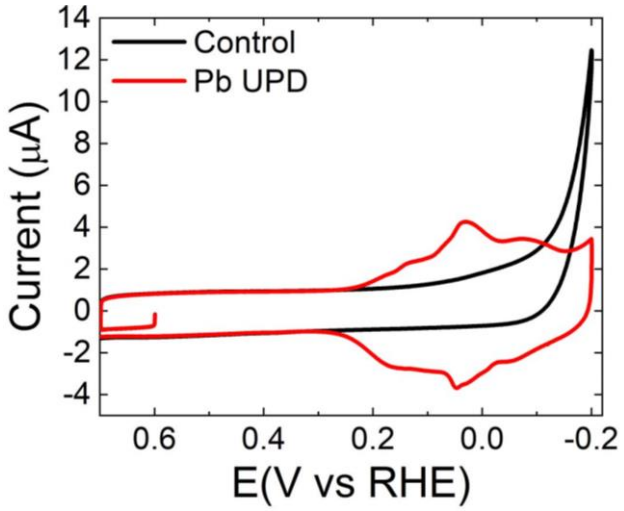

Figure 4.7

Effect of Pb UPD on CVs of Au DEN-modified electrodes. The CVs were obtained in electrolyte solutions containing N_2-purged 0.10 M $HClO_4$ in the absence (black trace) and presence (red trace) of 1.0 mM $Pb(NO_3)_2$. In the absence of Pb^{2+}, the hydrogen evolution reaction (HER) is apparent at potentials negative of ~0.10 V. The presence of Pb^{2+} results in Pb UPD prior to the onset of the HER, which is subsequently inhibited by the presence of a Pb monolayer (ML). The scan rate was 5.0 mV/s.

In previous reports of Cu UPD onto comparably sized Pt DENs,[45,46] the presence of two Cu UPD peaks was used as evidence of a facet-by-facet mechanism with Cu depositing sequentially onto (100) and (111) facets.[46] However, just like Pb UPD, this mechanism is likely an oversimplification for two primary reasons. First, as discussed in the Pb UPD section, there is extensive atomic sharing between facets for NPs in the size range of DENs. Second, SO_4^{2-} and Cu^{2+} co-adsorb onto Au in sulfate-containing media, and under these conditions Cu UPD onto bulk Au(111) has been reported to produce two UPD peaks.[47] The first peak corresponds to 0.67 ML of Cu co-adsorbed with 0.33 ML of SO_4^{2-}, and the second peak is characteristic of a full Cu ML having 0.33 ML of SO_4^{2-} adsorbed atop the Cu. Cu UPD experiments carried out using G6-NH_2(Au_{147}) DENs in electrolyte solutions with and without SO_4^{2-} (discussed below) confirm this mechanism.

As mentioned earlier, the electrolyte used for Cu UPD in Figure 4.2c is 0.10 M $HClO_4$/5.0 mM $CuSO_4$. Given the large excess of $CuSO_4$ relative to the DENs concentration, the full effect of SO_4^{2-} co-adsorption during Cu UPD should be obtained. However, for the sake of completeness, and also to more clearly visualize the second Cu UPD peak, we performed two sets of control experiments: Cu UPD in 0.10 M H_2SO_4/5.0 mM $CuSO_4$ and Cu UPD in 0.10 M HNO_3/5.0 mM $Cu(NO_3)_2$. The latter experiment was undertaken to represent the

scenario of Cu UPD in the absence of SO_4^{2-}. NO_3^- was chosen because it is a much weaker adsorbate than SO_4^{2-} and it matches the ligand used for Pb UPD.

Figures 4.8a and c show the effects of SO_4^{2-} and NO_3^- on the number, relative heights, and potentials of the Cu UPD peaks. Just like with $HClO_4/CuSO_4$ (Figure 4.2c), there are two Cu UPD peaks when $H_2SO_4/CuSO_4$ is used (Figure 4.8a). However, the peak centers shift from 0.45 V and 0.34 V to 0.44 V and 0.30 V, respectively. We note particularly two features of the second peak: (1) it is shifted more significantly (40 mV) from the first peak than the corresponding peak in Figure 4.2c ($HClO_4/CuSO_4$; 10 mV) and (2) it is more prominent. Both features are likely related to the higher concentration of SO_4^{2-}, which results in slower rearrangement of SO_4^{2-}. In 0.10 M HNO_3/5.0 mM $Cu(NO_3)_2$ (Figure 4.8c), a single UPD peak is observed (at 0.43 V). This experiment confirms that SO_4^{2-} plays a role in the definition of the second Cu UPD peak in Figure 4.2c ($HClO_4/CuSO_4$). The role of SO_4^{2-} ligands will be further discussed in the theory section.

The fractional Cu ML coverage was calculated in the same way as the Pb coverage, with some additional considerations related to co-adsorption of Cu^{2+} and SO_4^{2-}. It has previously been shown[149] that integration of the charge corresponding to Cu UPD on Au(111) in

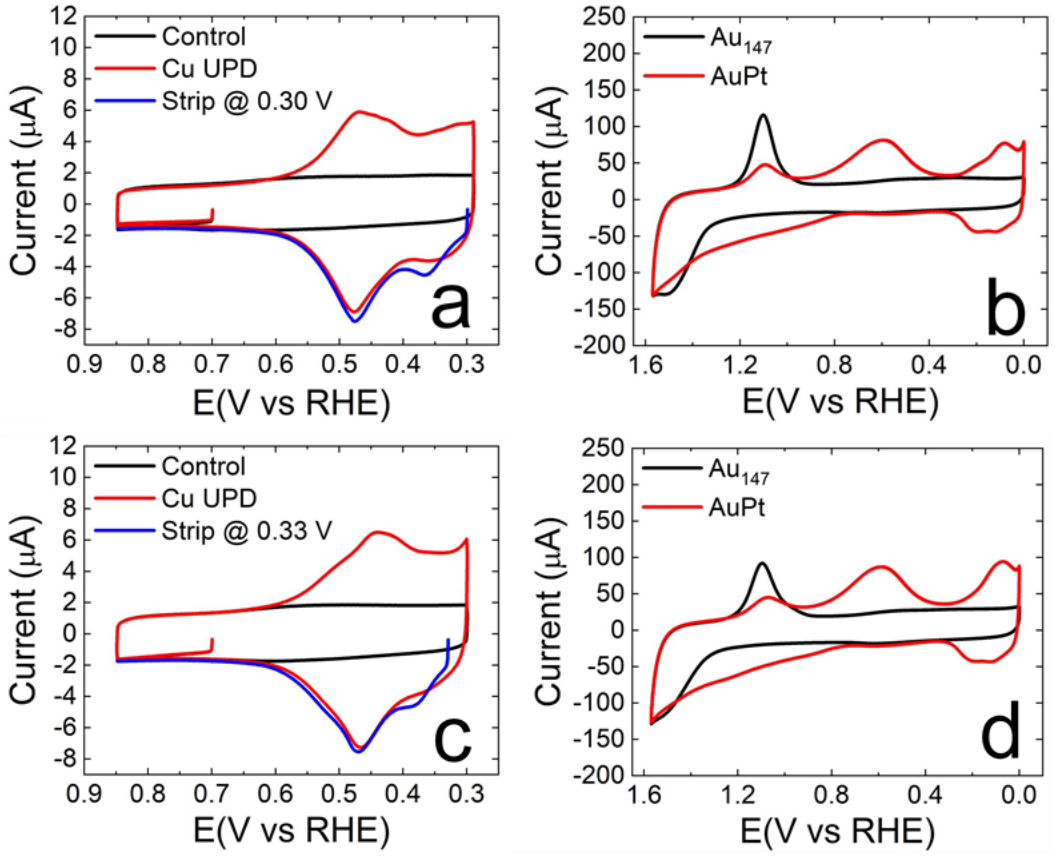

Figure 4.8

(a,c) Cu UPD onto G6-NH_2(Au_{147}) DENs in N_2-purged (a) 0.10 M H_2SO_4/5.0 mM $CuSO_4$ and (c) 0.10 M HNO_3/5.0 mM $Cu(NO_3)_2$. The black and red traces were recorded in the absence and presence of Cu^{2+}, respectively. LSVs (blue traces) were recorded after holding the electrode potential for 300 s at either 0.30 V (for $CuSO_4$) or 0.33 V (for $Cu(NO_3)_2$). This potential differed for H_2SO_4 and HNO_3 due to differences in the onset of bulk Cu deposition. (c,d) CVs obtained using Au DENs before (black traces) and after (red traces) Cu UPD/Pt GE in (c) N_2-purged 0.10 M H_2SO_4 and (d) N_2-purged 0.10 M HNO_3. The scan rate in (a,c) was 10 mV/s and the scan rate in (b,d) was 100 mV/s.

SO_4^{2-}-containing media underrepresents the amount of electrodeposited Cu. For the first Cu UPD peak, 67% of the Cu deposition is faradaic, while 33% does not involve a net charge transfer. The latter component is a result of Cu/SO_4 co-adsorption, in which the Cu^{2+} and SO_4^{2-} charges cancel. The absence of net charge transfer renders Cu electrodeposition via Cu/SO_4 co-adsorption undetectable in the Cu LSV. As a result, the Cu SA deposited for the first Cu UPD peak is expected to be 1.33 times greater than the charge under the Cu UPD peak. For the second Cu UPD peak, all of the Cu electrodeposits with charge transfer, thereby eliminating the need for corrections to the Cu SA for that peak.

Using a charge density of 405 $\mu C/cm^2$,[14] the total Cu SA determined from the Cu LSV, without any of the corrections discussed in the previous paragraph is 0.24 cm^2. Deconvolution of the Cu LSV in Figure 4.2c indicates that 80% of the total charge corresponds to the UPD peak (at 0.47 V) that involves Cu/SO_4 co-adsorption. Thus, 80% of the total Cu SA (0.19 cm^2) requires multiplication by 1.33x to correct for charge-neutral Cu deposition (yielding 0.26 cm^2). Adding this value to the Cu SA derived from the stripping peak at 0.37 V (0.048 cm^2) gives a total Cu SA of 0.31 cm^2. On the basis of six independent measurements, the $Cu:Au_i$ SA ratio is 1.01±0.05. Thus, assuming that the G6-

$NH_2(Au_{147})$ DEN core is a perfect 147-atom cuboctahedron, the Cu coverage is 0.57 ± 0.05 ML.

Synthesis of AuPt DENs via Cu UPD/Pt GE followed essentially the same procedure as Pb UPD/Pt GE with the exception that the UPD potential was 0.32 V. Figure 4.4c is a TEM micrograph of the resulting AuPt DENs, and Figure 4.4d is the corresponding size-distribution histogram. The data show that the size of the AuPt DENs is 2.4 ± 0.4 nm, which is essentially the same as the AuPt NPs prepared by Pb UPD/Pt GE (2.3 ± 0.5 nm).

Figure 4.2d compares CVs obtained before (black trace) and after (red trace) Cu UPD/Pt GE. After Cu UPD/Pt GE, the PtO_x reduction (0.60 V) and Pt hydride (negative of ~0.30 V) peaks are apparent, and the AuO_x reduction peak (at ~1.1 V) is attenuated. These changes are qualitatively similar to those observed for Pb UPD/Pt GE (Figure 4.2a).

Pt coverage was estimated in the same way as for Pb UPD/Pt GE: $1-(Au_f/Au_i)$. For Cu UPD/Pt GE, Au_i and Au_f equal 0.31 cm^2 and 0.092 cm^2, respectively. On the basis of six independent measurements, the average Pt coverage is 0.70 ± 0.01 ML. This value is higher than expected based on 1:1 exchange of the experimentally determined Cu coverage (0.57 ± 0.05 ML) for Pt. This might be a consequence of the fact that the charge density values used to calculate the Cu and Au SAs (405 μC/cm^2 and 390 μC/cm^2,

respectively) are only strictly appropriate for bulk Au,[14] and they might not be accurate for small NPs.[14] We note, however, that the (Au_f/Au_i) term used to calculate Pt coverage (1-(Au_f/Au_i)) is independent of charge density and therefore the Pt coverage here might be more accurate than the Cu coverage.

Figures 4.8b and d show CVs for the AuPt DENs prepared via Cu UPD/Pt GE in $H_2SO_4/CuSO_4$ and $HNO_3/Cu(NO_3)_2$, respectively. These CVs look qualitatively similar to one another and to the CV in Figure 4.2d ($HClO_4/CuSO_4$). Within experimental error, the Pt coverage is the same for Cu UPD/Pt GE using $H_2SO_4/CuSO_4$ (0.72 ± 0.04 ML) and $HClO_4/CuSO_4$ (0.70 ± 0.01 ML). Cu UPD in $HNO_3/Cu(NO_3)_2$ yields slightly higher Pt coverage (0.76 ± 0.03 ML) than $HClO_4/CuSO_4$. These results show that the although SO_4^{2-} ligands influence the number of Cu UPD peaks, they do not appreciably alter the AuPt NP structures obtained upon GE with Pt.

One final point. Here, we used different concentrations of $Pb(NO_3)_2$ (1.0 mM) and $CuSO_4$ (5.0 mM) for the UPD processes. This was done to be consistent with previous publications.[12,15,16] Note, however, that Figure 4.9 shows that use of 1.0 mM $Cu(NO_3)_2$, chosen to match the Pb concentration and counter ion, yields results similar to 5.0 mM $CuSO_4$ in terms of Pt coverage (0.76 ± 0.03 ML vs. 0.70 ± 0.01 ML for 5.0 mM $CuSO_4$).

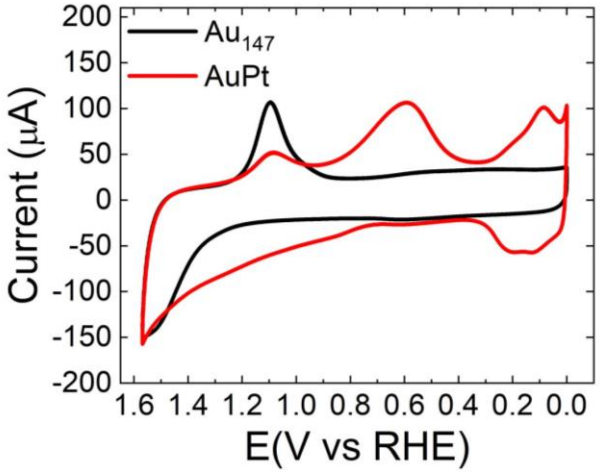

Figure 4.9

Pt coverage for UPD/Pt GE with 1.0 mM $Cu(NO_3)_2$. CVs before (black trace) and after (red trace) Cu UPD/Pt GE using 1.0 mM $Cu(NO_3)_2$. The average Pt coverage is 0.76 ± 0.03 ML, which is close to the value obtained when 5.0 mM $CuSO_4$ is used for UPD (0.70 ± 0.01 ML). The scan rate was 100 mV/s.

Comparison of AuPt DENs prepared by Pb UPD/Pt GE and Cu UPD/Pt GE

The CVs for the AuPt DENs prepared using the Pb UPD/Pt GE and Cu UPD/Pt GE methods differ in two respects: (1) the PtO_x reduction peak potential and (2) the surface coverage of Pt. With regard to (1), the PtO_x reduction peak is 60 mV more negative for the AuPt DENs synthesized using Cu UPD/Pt GE relative to those prepared using Pb UPD/Pt GE, suggesting differences in surface structure. In the case of point (2), the Pt coverage for the AuPt DENs is ~0.20 ML greater for the Cu UPD/Pt GE method than for the Pb case. This suggests that these two methods are not interchangeable and could, for example, lead to materials having very different electrocatalytic properties. Importantly, and as we will discuss in the next section, this difference in Pt coverage is predicted by theory. Specifically, theory suggests lower Pt coverage (0.59 ML) and a surface alloy-like structure for Pb UPD/Pt GE. A higher Pt coverage (1.0 ML) and a more ideal core@shell Au@Pt structure is predicted for Cu UPD/Pt GE.

Pb UPD simulations

Pb atoms were placed randomly (as opposed to facet-by-facet) and incrementally onto the surface of a cuboctahedral Au_{147} NP to simulate the Pb UPD process on G6-NH_2(Au_{147}) DENs. It should be

noted that equilibration at 300 K significantly deforms the original cuboctahedral Au_{147} NP structure. Specifically, the (100) facets reconstruct in a way that makes most of the surface close-packed. This process eliminates the distinction between (100) and (111) facets and the final surface can be best described as (111)-like. In total, 13 Pb_x/Au_{147} (x=1 to 120 with an incremental step size of 10 Pb atoms) structures were simulated. Each structure was equilibrated at 300 K, using the MD simulation method described in the Experimental Section, and was then relaxed to its equilibrium state at 0 K. The equilibrated, relaxed structures are shown in Figure 4.10. Figure 4.11a shows the differential binding energies (ΔE) of the deposited Pb atoms that were calculated for these structures as a function of Pb coverage. The ΔE values quickly increase with Pb coverage from 0 ML to 0.2 ML. At 0.2 ML, a plateau is reached, and it extends until 0.4 ML, after which ΔE rapidly increases again. Importantly, Figure 4.11a suggests that Pb UPD is energetically favorable up to ~0.60 ML coverage, after which ΔE becomes positive.

The behavior of ΔE as a function of Pb coverage can be interpreted by tracking changes in the coordination numbers (CNs) of the deposited Pb adatoms (Figure 4.12). The first data point on this plot corresponds to the adsorption of 1 Pb atom. Initially,

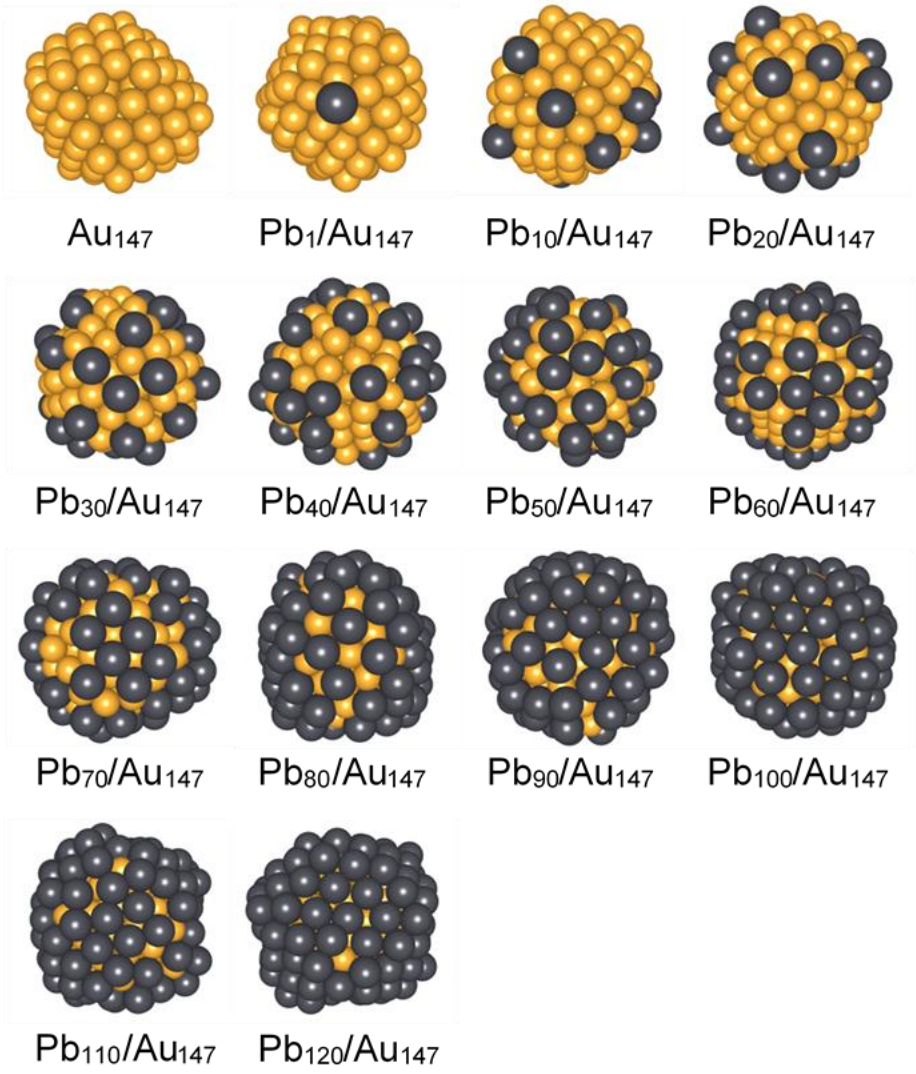

Figure 4.10

Structures for Pb adsorption onto Au_{147} NPs after MD equilibration at 300 K followed by relaxation to the equilibrium state at 0 K. Pb atoms were randomly added to the NP surface one at a time, and the NP was equilibrated after the addition of each Pb atom. Gold and gray atoms correspond to Au and Pb, respectively.

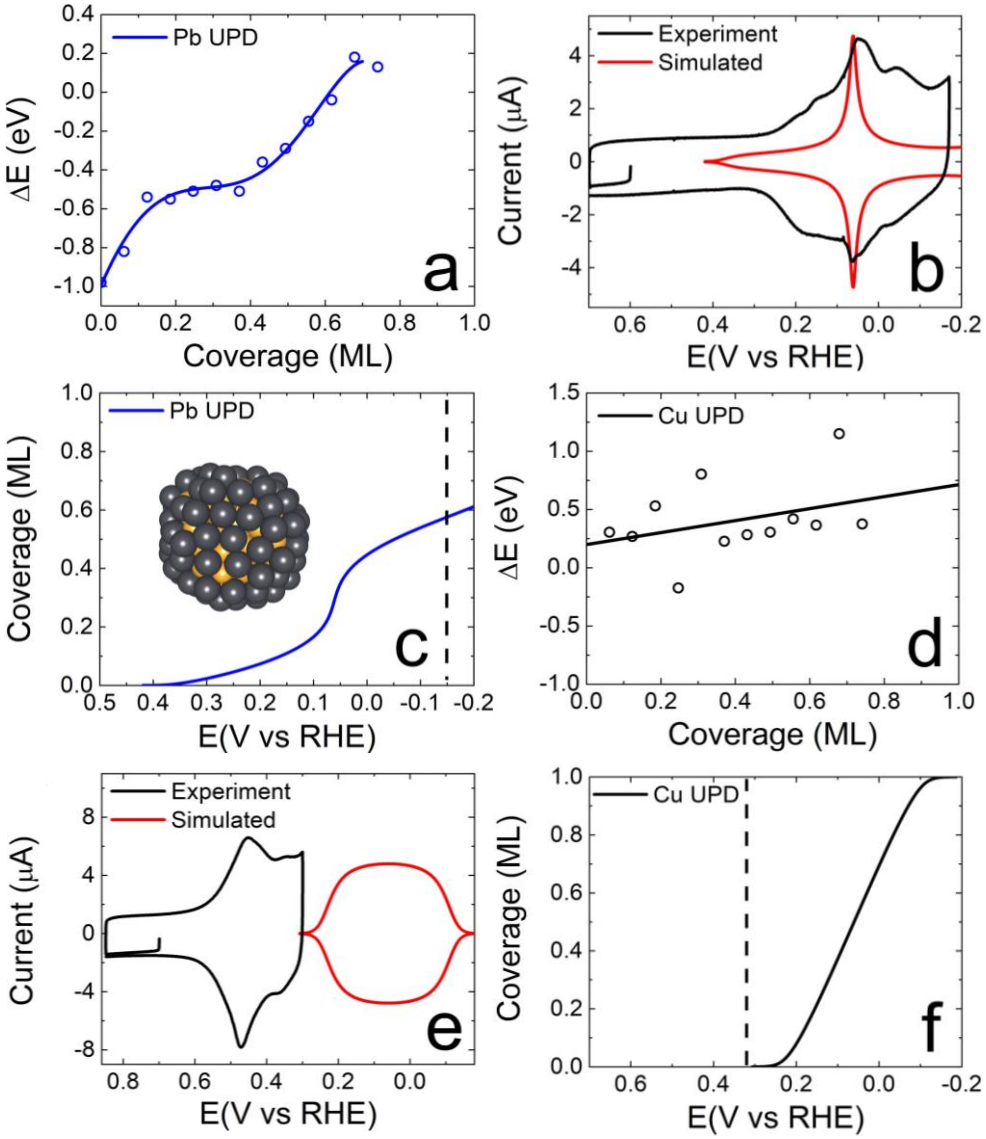

Figure 4.11

(a,d) Differential binding energy (ΔE) as a function of coverage for (a) Pb UPD and (d) Cu UPD. UPD becomes unfavorable for ΔE values greater than 0. (b,e) Comparison of experimental (black traces) and theoretically simulated (red traces) UPD CVs for (b) Pb and (e) Cu. (c,f) UPD coverage as a function of applied potential for (c) Pb and (f) Cu. The dashed lines indicate the experimental UPD potentials. The inset in (c) is an atomic model of 96 Pb atoms covering an Au_{147} core at the maximum allowed coverage of 0.59 ML.

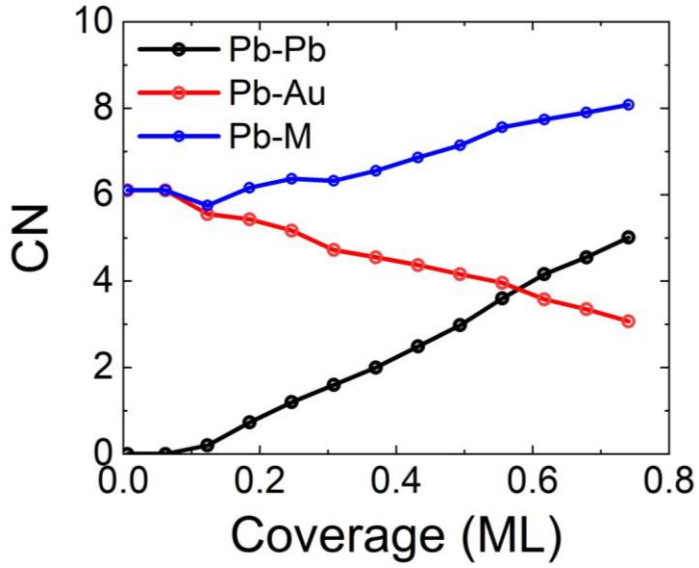

Figure 4.12

Predicted Pb coordination numbers (CNs) as a function of Pb coverage on Au_{147} NPs. The black, red, and blue traces represent the Pb-Pb, Pb-Au, and Pb-M CNs, respectively. The Pb-M CN is the sum of the Pb-Pb and Pb-Au CNs. The first data point corresponds to Au_{147} with 1 adsorbed Pb atom (not naked Au_{147}).

this single Pb atom is highly coordinatively unsaturated. As a result, the Pb adatom induces local structural reconstruction of the AuNP to stabilize its adsorption. As shown in the second frame of Figure 4.10 (Pb_1/Au_{147}), this AuNP reconstruction results in an average Pb-Au CN of 6. As Pb coverage increases, however, the average Pb-Au CN decreases from 6 to 3 and the average Pb-Pb CN increases from 0 to 5.

The foregoing behavior can be explained by considering the effects of Pb island formation on the underlying Au surface. As Pb island growth proceeds, the increase in the Pb-Pb CN alleviates reliance on Au lattice deformation to meet the Pb atom coordination requirements. Summing the Pb-Au and Pb-Pb CNs, the total Pb CN (Pb-M) increases from 6 to 8 as a function of Pb coverage. The opposing Pb-Pb and Pb-Au CN trends result in slowed growth of the Pb-M CN between 0.2 ML and 0.4 ML, thereby accounting for the plateau in ΔE (Figure 4.11a) for those coverages. The rapid increase in ΔE beyond 0.4 ML in Figure 4.11a can be attributed to the fact that as the Pb-Pb CN continues to increase and the Pb-Au CN continues to decrease, it becomes more difficult to deposit additional Pb atoms. This feature arises from the fact that Pb binds more strongly to Au than it does to itself (this is why Pb UPD is possible on Au).

The simulated Pb UPD CV (Figure 4.11b) is based on the calculated ΔE value. The main peak corresponds to the plateau in the plot of ΔE as a function of Pb coverage (Figure 4.11a). This peak is centered at 0.06 V and aligns well with the corresponding peak in the experimental CV (0.04 V; Figure 4.2b). In the experimental Pb UPD CV, there are smaller peaks before and after the main peak. The simulated CV predicts flat currents rather than peaks in these two regions due to the rapid increase of ΔE vs. Pb coverage. This discrepancy might be due to the limited resolution of the simulations, because the Pb coverage was increased using a step size of 10 Pb atoms. Accordingly, complete details about the ΔE landscape were not captured. Additionally, the timescale associated with MD simulations is limited to pico seconds. As a result, it was not possible to simulate the reorganization of Pb adatoms on the Au_{147} surface through diffusion, which might occur at longer times. Finally, there is some structural polydispersity in the DENs that could introduce nonidealities into the experimental data. Some or all of these factors could affect the correlation between experiment and simulation.

As shown in Figure 4.11c, the predicted Pb coverage as a function of applied potential can be determined by integrating the simulated CV in Figure 4.11b. The vertical dashed line indicates

the experimental potential, -0.15 V, that was used for Pb UPD onto the G6-NH_2(Au_{147}) DENs. At this potential, 96 Pb atoms are predicted to deposit on Au_{147}, corresponding to a coverage of 0.59 ML (using the definition of fractional ML coverage defined in the previous sections (1.0 ML = 162 atoms)). We note that the atomic structure in the inset of Figure 4.11c represents Pb_{100}/Au_{147} rather than Pb_{96} because, as mentioned earlier, a coverage step size of 10 Pb atoms was used in the simulations. The Pb coverage predicted for Pb UPD at -0.15 V is in good agreement with both the experimentally determined Pb coverage (0.49 ± 0.03 ML) and the Pt coverage (0.50 ± 0.04 ML) after Pt GE.

Although the Pb coverage predicted in the present report (0.59 ML) is similar to our earlier publication detailing Pb UPD on Au_{147} (0.63 ML),[15] we obtain a more realistic picture of the Pb UPD process on Au_{147} using DFT-MD in the current study. As alluded to earlier, DFT-MD reveals that the cuboctahedral Au_{147} NPs reconstruct spontaneously at 300 K leaving no distinct (100) and (111) facets on their surfaces. Consequently, the previously reported facet-by-facet growth mode is not appropriate. Instead, we envision that Pb adatoms deposit randomly on the reconstructed Au_{147} surface. Equilibration of the Pb_x/Au_{147} structures at 300 K makes it possible to consider rearrangement of the atoms at finite temperature after each Pb atom deposits. The agreement between the

simulated and experimental CVs supports the validity of this new structural model and provides a higher degree of mechanistic insight into the Pb UPD process.

Figures 4.13a and b show the structures predicted before and after the Pt GE step. For these simulations, the deposited Pb atoms in Pb_{100}/Au_{147} were replaced with Pt. The new structure was then equilibrated at 300 K for 20 ps. After Pt GE, a significant number of Au atoms are still on the NP surface. Fewer Pb atoms than Pt atoms are required for complete Au_{147} surface coverage, because Pt atoms are smaller than Pb atoms. Thus, upon Pt GE, surface coverage of the AuNP decreases. As a result, the final structure more closely resembles a surface alloy than the core@shell Au@Pt structure that was anticipated.

Cu UPD simulations

Simulation of the Cu UPD CV followed a similar approach to that of Pb UPD. The equilibrated, relaxed atomic structures for naked Au_{147} with deposited Cu are shown in Figure 4.14. In all cases, the deposited Cu atoms incorporate (alloy) into the Au_{147} core after equilibration to increase their CNs. This scenario differs from that of Pb UPD, where all UPD atoms are predicted to be adsorbed on top of the Au atoms. This difference arises from the fact that Pb atoms are larger than Cu atoms. Specifically,

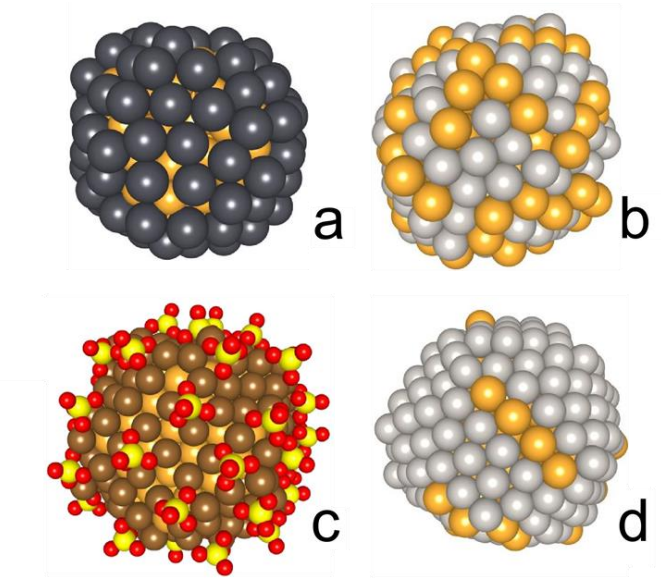

Figure 4.13

Atomic models for Au_{147} DENs. (a,c) Au_{147}@x where (a) x = Pb and (c) x = Cu with co-adsorbed $SO_4^{\delta-}$. (b,d) AuPt formed by performing Pt GE on the NPs in (a) and (c), respectively.

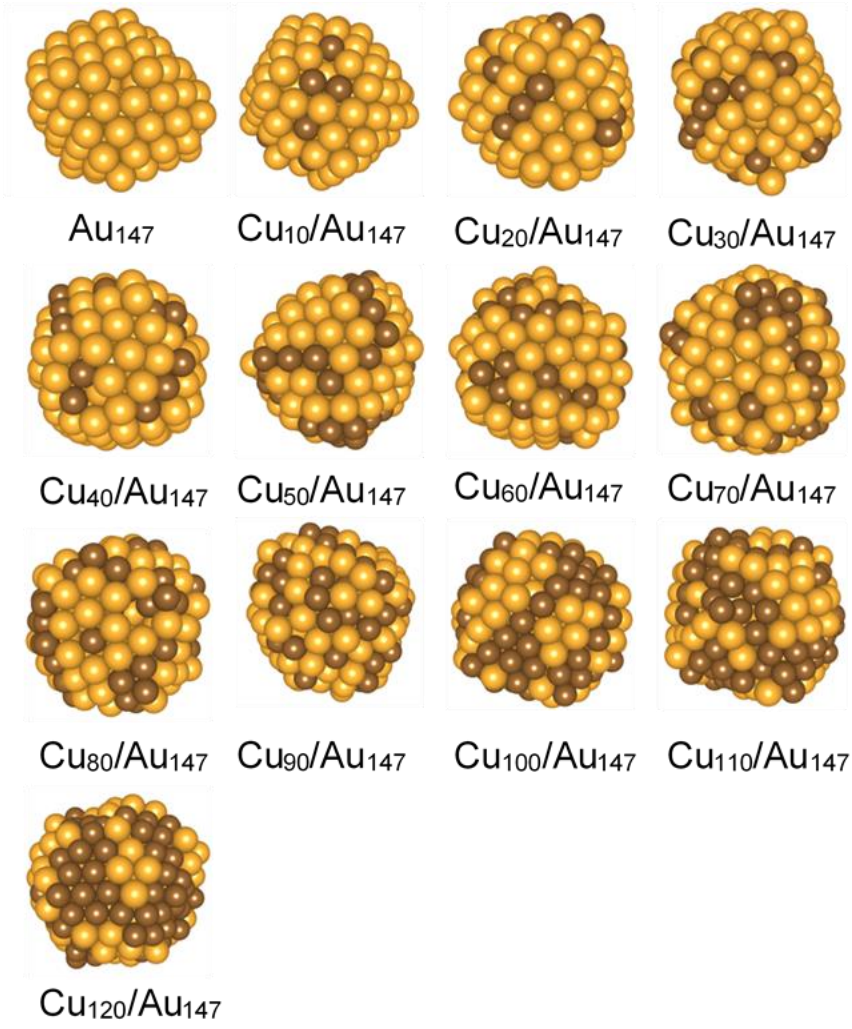

Figure 4.14

Simulated Cu deposition onto Au_{147} NPs in the absence of ligands. Gold and brown atoms correspond to Au and Cu, respectively. These structures were equilibrated using MD at 300 K, and then relaxed to their equilibrium structures at 0 K.

although PbAu alloys are stronger than CuAu alloys, PbAu alloys are kinetically more difficult to form, because there is a larger lattice mismatch between Pb and Au lattices.[47] Furthermore, the ΔE values of Cu adatoms (Figure 4.11d) are positive throughout the entire range (0 ML to 1.0 ML) of Cu coverage. Therefore, the theoretical simulations predict that Cu UPD onto naked Au_{147} NPs should not occur within the potential range used to obtain the CV shown in Figure 4.2c. This means that Cu UPD in the simulated CV (Figure 4.11e) requires a significant overpotential and thus occurs in a more negative potential range than the experimental CV. This point is further emphasized in Figure 4.11f, where the Cu UPD onset potential (~0.20 V) and the potential corresponding to a full Cu ML (~-0.10 V) are predicted to be ~250-440 mV more negative than the experimentally observed Cu UPD peak potentials (~0.45 V and 0.34 V, respectively).

The discrepancy between experiment and theory outlined above has been previously reported[46,150,151] and attributed to neglecting ligand effects in the theoretical calculations. The calculations for Cu UPD described up until this point were carried out by assuming that Cu UPD onto the surface of Au_{147} NPs results exclusively in deposition of Cu. However, experimental studies have shown that anionic ligands co-adsorb with Cu on bulk Au in the UPD potential range.[47] For example, STM studies[47] have shown

that the first of two peaks in the Cu UPD CV for Au(111) corresponds to 0.67 ML of Cu and 0.33 ML of $SO_4^{\delta-}$ ($SO_4^{\delta-}$ is used to denote uncertainty in the exact SO_4 charge upon adsorption). A full Cu ML can be obtained, but it requires scanning the potential further negative (to the second peak). As we describe next, the gap between the experimental and theoretical results for Cu UPD on Au_{147} narrows once ligand and electric double layer (EDL) effects are taken into account.

The influence of ligand/EDL effects on the Cu UPD simulations

To predict the correct equilibrium potentials for Cu UPD on Au, calculations were performed to simulate the EDL under constant potential conditions using the double reference method described in the Experimental Section. The two structures used were those determined experimentally for Cu UPD on Au(111) in the presence of $SO_4^{\delta-}$.[47] The two structures correspond to the two peaks in the Cu UPD CV for Au(111). The first is Au(111) with a partial Cu ML (Figure 4.15a) consisting of 0.67 ML of Cu co-adsorbed with 0.33 ML of $SO_4^{\delta-}$. The second structure is Au(111) having a full Cu ML and 0.33 ML of $SO_4^{\delta-}$ co-adsorbed on top of the Cu (Figure 4.15b). For simplicity, we refer to these two models as partial ML and full ML, respectively.

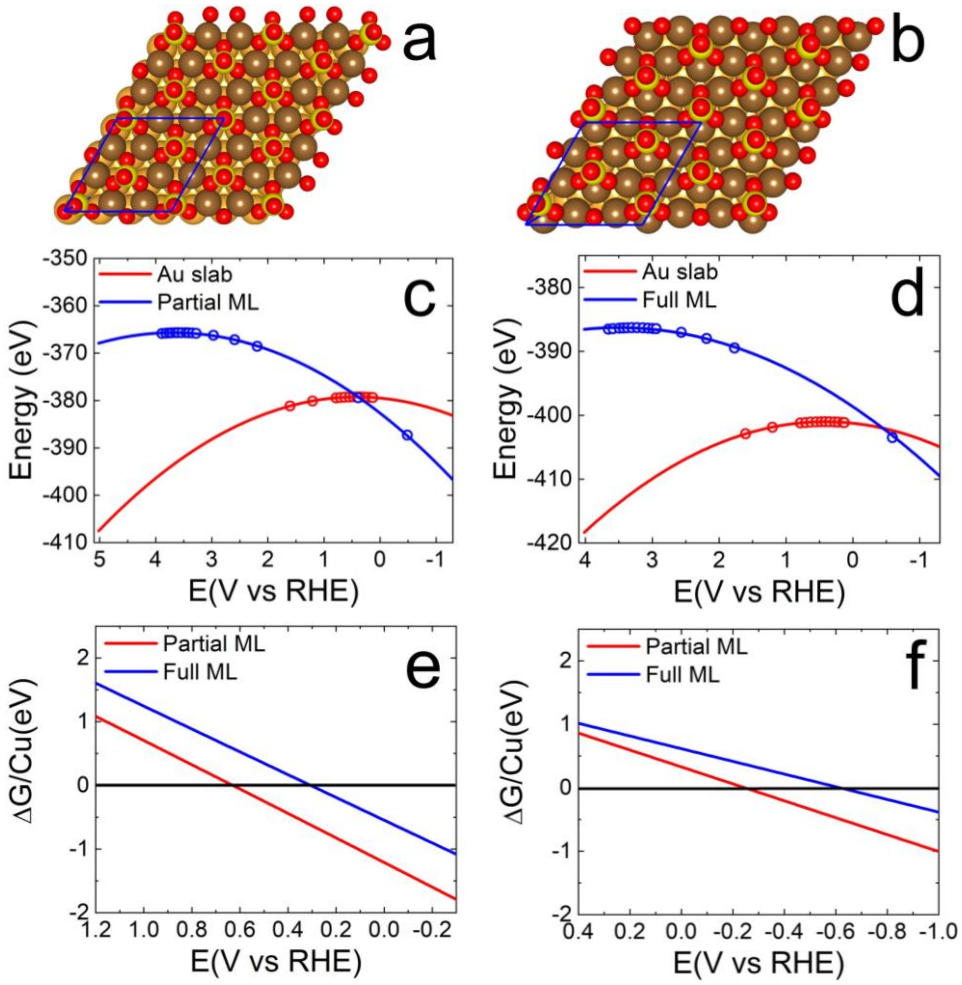

Figure 4.15

(a,b) Models of an extended Au(111) surfaces with (a) partial and (b) full Cu MLs. The partial Cu ML consists of 0.67 ML of Cu co-adsorbed with 0.33 ML of $SO_4^{\delta-}$. A layer of $SO_4^{\delta-}$ is adsorbed on top of the full Cu ML. The gold, brown, yellow, and red spheres correspond to Au, Cu, S, and O atoms, respectively. (c,d) Plots used for determining the potential of zero charge (PZC) for naked Au(111) (red traces) and Au(111) with co-adsorbed Cu and $SO_4^{\delta-}$ (blue traces) for (c) partial and (d) full Cu MLs. (e,f) Free energy (ΔG) as a function of applied electrode potential for Cu UPD onto an Au(111) slab when (e) both ligand and electric double layer (EDL) effects are taken into account and (f) when only ligand effects are considered.

Figures 4.15c and d show the total energies of naked Au(111) and Au(111) with co-adsorbed Cu and $SO_4^{\delta-}$ as a function of potential. The total energies of these interfaces display quadratic shapes because they act as capacitors. For naked Au(111) (Figure 4.15c, red trace), the predicted potential of zero charge (PZC) is 0.42 V. For the partial ML structure (Figure 4.15c, blue trace), the PZC shifts to a much higher value (3.6 V) than naked Au(111) due to electron transfer from the metal surface to adsorbed $SO_4^{\delta-}$.

As a result of the PZC shift, the adsorption energy (the difference between the blue and red traces in Figures 4.15c and d) becomes more positive at more positive potentials. In other words, as the applied potential is scanned negative during the UPD process, $CuSO_4$ co-adsorption becomes more and more stable. This variation in adsorption energy as a function of potential is mainly caused by differences in the number of electrons residing on the $CuSO_4$ co-adsorption interface vs. the naked Au(111) surface. At more negative potentials, the $CuSO_4$ co-adsorption interface accommodates more electrons than the naked Au(111) surface. This in turn leads to greater stability of the $CuSO_4$ co-adsorption interface at more negative potentials. Thus, for the potential used for Cu UPD (0.32 V), the surface of the partial ML structure harbors significantly more negative charge than naked Au(111).

Similar conclusions are obtained for the full ML structure (Figure 4.15d).

Using the calculated, potential-dependent binding energies of the $CuSO_4$ co-adsorption layers, we evaluated the reaction free energy (ΔG) of the Cu UPD process (Figure 4.15e) when both EDL and ligand effects are taken into account. The predicted equilibrium potentials for the partial (red trace) and full (blue trace) Cu MLs are 0.63 V and 0.31 V, respectively. These two potentials agree reasonably with those associated with experimentally determined Cu UPD onto Au(111) in 0.10 M H_2SO_4 (0.53 V and 0.35 V).[152] They are also in reasonable agreement with the two peaks in the experimental Cu UPD CV (Figure 4.2c) for the G6-NH_2(Au_{147}) DENs, which are centered at 0.45 V and 0.34 V. As mentioned previously, Figure 4.2c was recorded in 10.0 mL of 0.10 M $HClO_4$ containing 5.0 mM $CuSO_4$. Thus, the SO_4^{2-} concentration was in excess with respect to the AuNPs on the working electrode (6.0 µL of an ink containing 2.0 µM G6-NH_2(Au_{147}) DENs). To check if 5.0 mM SO_4^{2-} was indeed sufficient to induce co-adsorption effects, a Cu UPD CV was recorded at higher SO_4^{2-} concentration (0.10 M H_2SO_4; Figure 4.8a). The peak positions in Figure 4.8a (0.44 V and 0.30 V) are similar to those in Figure 4.2c, indicating that 5.0 mM SO_4^{2-} is adequate to observe the effect of $SO_4^{\delta-}$ on Cu UPD. Note that our prior report

of Cu UPD potentials on Pt DENs[46] considered ligand effects but not the EDL.

The importance of the EDL calculations is underscored by comparing the results in Figure 4.15e to those obtained using the $CuSO_4$ binding energies calculated at the PZC (Figure 4.15f). The latter calculations were designed to eliminate EDL effects, thereby isolating ligand effects. The calculated equilibrium potentials for the two stages of Cu UPD (-0.25 V and -0.62 V) are much more negative in the absence of EDL considerations and are significantly shifted from the experimental values (by ~560-960 mV). In fact, they are even worse than predicted for a naked Au_{147} NP (Figure 4.11f). The large errors in the predicted equilibrium potentials for Cu UPD are due to the fact that the adsorption energies calculated from the difference in the energies of the naked Au(111) surface and the $CuSO_4$ co-adsorption interface, at the PZC (zero charge calculations), are very positive. Thus, the most accurate Cu UPD results are obtained when both ligand and EDL effects are taken into account.

Given that the Pb UPD and Cu UPD experiments used different anions ($Pb(NO_3)_2$ and $CuSO_4$), we also evaluated the ligand and EDL effects of NO_3 for Cu UPD (Figure 4.16). As for the $CuSO_4$ case, the PZC for Au(111) is significantly shifted when Cu and $NO_3^{\delta-}$ are co-adsorbed (Figures 4.16a and b). Furthermore, Figure 4.16c shows

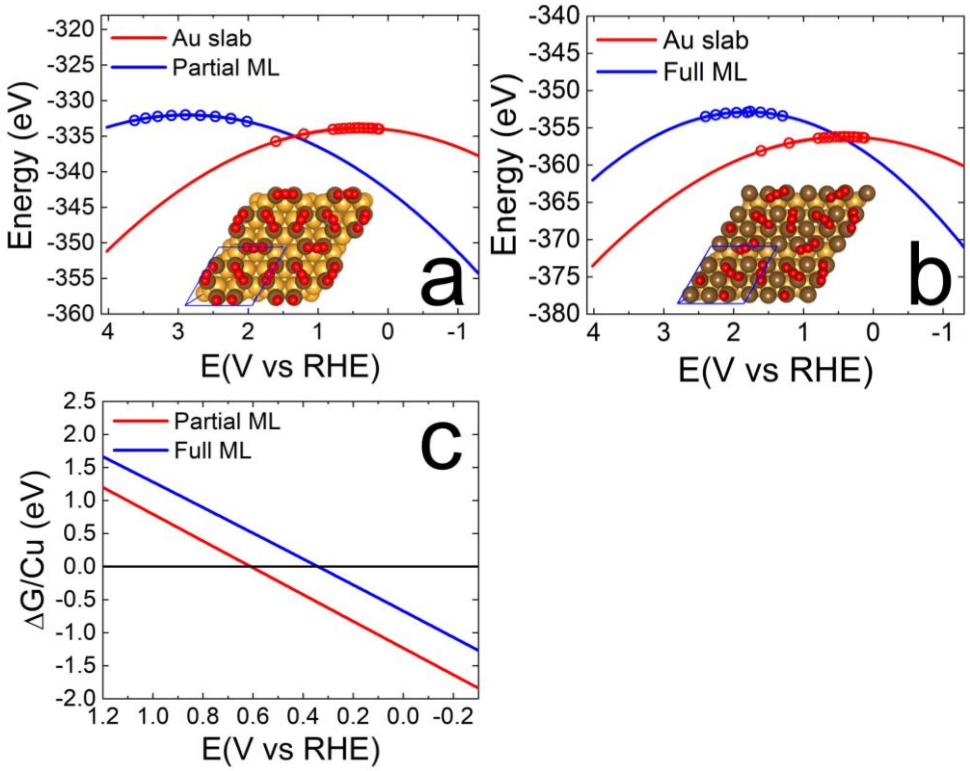

Figure 4.16

Ligand and electric double layer (EDL) effects for $Cu(NO_3)_2$ UPD onto an Au(111) slab. (a,b) Total energy as a function of applied potential for naked Au(111)(red traces) and Au(111) with (a) partial (0.67 ML) and (b) full (1.0 ML) Cu MLs (blue traces). The insets in (a) and (b) are Au(111) slab models containing partial and full Cu MLs, respectively. In each case, $NO_3^{\delta-}$ is co-adsorbed atop Cu. The gold, brown, red, and light gray spheres represent Au, Cu, O, and N, respectively.(c) Free energy (ΔG) as a function of applied electrode potential for $Cu(NO_3)_2$ UPD onto Au(111) for partial (red trace) and full (blue trace) Cu MLs. The potentials predicted to afford partial and full Cu MLs are 0.62 V and 0.33 V, respectively.

that the PZC shift for $Cu(NO_3)_2$ translates to predicted partial (0.62 V) and full (0.33 V) Cu ML potentials that are very similar to the corresponding potentials predicted for $CuSO_4$ (0.63 V and 0.31 V). Indeed, the potential predicted for a full Cu ML is very close to that experimentally observed for $Cu(NO_3)_2$ (0.32 V, Figure 4.8c). Thus, overall, $SO_4^{\delta-}$ and $NO_3^{\delta-}$ provide similar ligand/EDL effects for Cu UPD on Au(111).

Notably, the comparison of $CuSO_4$ and $Cu(NO_3)_2$ suggests that the mere presence of ligands, regardless of their identity, profoundly impacts the EDL structure and thus the Au(111) PZC associated with Cu UPD. In other words, our results suggest that the presence of any ligand will shift the Cu UPD potentials from those determined on naked Au.

These calculations further highlight the differences between Pb UPD, which does not require consideration of either ligand or EDL effects to obtain agreement between experiment and theory, and Cu UPD, which is markedly altered by these effects. This difference has been observed previously[73] and likely arises from the fact that the Pb ML is charge neutral, whereas the Cu ML possesses residual charge. Therefore, the similarity of the ligand/EDL effects for $SO_4^{\delta-}$ and $NO_3^{\delta-}$, along with the fact that Pb is relatively insensitive to ligand effects,[73] justify the comparison of AuPt NP structures synthesized using $Pb(NO_3)_2$ and $CuSO_4$.

Theoretical NP models for Cu UPD/Pt GE

The calculations detailed in the previous section confirm that $CuSO_4$ co-adsorption structures form on the Au(111) surfaces during the UPD process. We now turn to consideration of the AuNPs. In the experimental Cu UPD CV for G6-NH_2(Au_{147}) DENs (Figure 4.2c), a peak (highlighted by the arrow) resembling the second stage (~1.0 ML Cu) of Cu UPD onto Au(111) is observed at 0.34 V. This peak is more pronounced at higher SO_4^{2-} concentration (Figure 4.8a) and is absent when $Cu(NO_3)_2$ is used (Figure 4.8c), confirming its association with SO_4^{2-}. Hence, we assume that there is full coverage of Cu on the surface of the AuNP.

Accordingly, we built a full Cu shell model containing 162 Cu atoms on an Au_{147} NP and evenly placed 44 $SO_4^{\delta-}$ ligands (~0.3 ML) on top of the Cu layer. The equilibrated structure is shown in Figure 4.13c. Unlike the Pb coverage, the theoretically predicted Cu coverage (1.0 ML) differs from that determined by experiment (0.57 ± 0.05 ML). This result is not necessarily surprising for the following reasons. First, sub-ML Cu coverages have previously been reported on AuNPs.[68,70] Second, our previous reports of Cu UPD onto Au_{147} DENs[14] and comparably sized Pt DENs[45,46] have revealed ratios of Cu to surface Au or Pt atoms of 0.74-1.0; these ratios correspond to fractional ML coverages significantly lower than 1.0 ML (0.41-0.63 ML depending on core size). These discrepancies were

previously attributed to Cu UPD being energetically unfavorable on corner and edge sites.[14,45,46] Third, a completely naked Au_{147} NP model was used in our theoretical prediction of a full Cu ML (Figure 4.11f). As we have demonstrated, ligand and EDL effects have significant implications for Cu UPD. It is possible that these effects impacted the extent of Cu coverage.

Figure 4.13d shows the AuPt NP model formed by replacing the $CuSO_4$ layer (from Figure 4.13c) with Pt atoms and allowing the structure to equilibrate. As indicated, the shell consists almost entirely of Pt, which is in stark contrast with the surface alloy-like AuPt structure generated using Pb UPD/Pt GE (Figure 4.13b). Although the former structure predicts Pt coverage higher than experimentally obtained (~0.70 ML Pt coverage) for Cu UPD/Pt GE, the two UPD/Pt GE methods display a significant difference (~0.20 ML) in Pt coverage. Thus, both theory and experiment suggest that Pb UPD/Pt GE and Cu UPD/Pt GE generate different AuPt structures. Cu UPD/Pt GE is predicted to afford a more ideal core@shell AuPt structure, while Pb UPD/Pt GE yields an AuPt structure that more closely resembles a surface alloy. Importantly, the Pt ensembles on the NP surfaces differ. As we will show in a forthcoming report, differences in ensemble effects for these NPs lead to distinct catalytic signatures for FAO.

4.5. Summary and Conclusions

We have used both experiment and theory to analyze Pb and Cu UPD on ~1.7 nm AuNPs and the AuPt structures that result after galvanic exchange (GE) of the UPD layer for Pt. Experimental Pb (0.49 ML) and Pt (0.50 ML) coverages are both close to values predicted by density functional theory-molecular dynamics (DFT-MD; 0.59 ML). DFT-MD reveals that the AuNPs spontaneously reconstruct from cuboctahedral to a (111)-like structure prior to UPD. In the case of Pb, this results in random electrodeposition of Pb onto the Au surface. This mechanism is a consequence of opposing trends in Pb-Pb and Pb-Au coordination numbers as a function of Pb coverage. Cu UPD is more complex, and agreement between theory and experiment takes into account ligand effects (e.g., SO_4^{2-} present as the electrolyte) and the electric double layer.

Importantly, AuPt structures formed upon Pt GE were found to differ markedly depending on the UPD metal. Specifically, cyclic voltammetry indicates that Pt coverage is ~0.20 ML greater for Cu UPD/Pt GE (0.70 ML) than for Pb UPD/Pt GE (0.50 ML). This difference was corroborated by DFT-MD theoretical predictions and attributed to dissimilar Pb and Cu atomic sizes, as well as the higher impact of ligand and EDL effects on Cu UPD compared to Pb UPD. Finally, DFT-MD calculations predicted formation of surface

alloy and core@shell structures for Pb UPD/Pt GE and Cu UPD/Pt GE, respectively.

Moving forward, we wish to better understand the generality of these experimental and theoretical results: can they be applied to other UPD metals and different size cores? The answers to these questions are directly relevant to fundamental questions regarding the stability and phase behavior of metal NPs. The results of our studies aimed at answering these questions will be reported in due course.

Chapter 5: Multilayer electrodeposition of Pt onto 1-2 nm Au nanoparticles using a hydride-termination approach[3]

5.1. Synopsis

Here we report on hydride-terminated (HT) electrodeposition of Pt multilayers onto ~1.6 nm Au nanoparticles (NPs). The results build on our earlier findings regarding electrodeposition of a single monolayer of Pt onto Au NPs and reports relating to HT Pt electrodeposition onto bulk Au. In the latter case, it was found that electrodeposition of Pt from a solution containing $PtCl_4^{2-}$ can be limited to a single monolayer of Pt atoms if it is immediately followed by adsorption of a monolayer of H atoms. The H-atom capping layer prevents deposition of Pt multilayers. In the present report we are interested in comparing the structure of NPs after multiple HT Pt electrodeposition cycles to the bulk analog. The results indicate that a greater number of HT Pt cycles are required to electrodeposit both a single Pt monolayer and Pt multilayers onto these Au NPs compared to bulk Au. Additionally, detailed structural analysis shows that there are fundamental differences in the structures of the AuPt materials depending on whether they

[3]The work in this chapter was recently submitted for publication. The dissertator was the primary contributor: Lapp, A.S.; Crooks, R.M. Multilayer electrodeposition of Pt onto 1-2 nm Au Nanoparticles using a hydride-termination approach. *Nanoscale* **2020**, submitted for publication.

are prepared on Au NPs or bulk Au. The resulting structures have a profound impact on formic acid oxidation electrocatalysis.

5.2. Introduction

Herein, we report a hydride-termination (HT) method for electrodepositing multiple Pt layers onto ~1 to 2 nm Au nanoparticles (NPs). Compared to HT growth on bulk two-dimensional Au surfaces,[75-78] we find that a greater number of electrodeposition steps is required to achieve a single, complete Pt layer, and subsequent Pt multilayers, on Au NPs. Moreover, we find that incremental changes in Pt coverage on Au NPs significantly impact electrocatalytic activity for formic acid oxidation (FAO).

The foregoing results are important for the following reasons. First, core@Pt-shell NPs provide a means for minimizing Pt loading in electrocatalytic devices.[1,6,7] Therefore, it is important to assess the viability of methods that can be used for depositing thin Pt shells on NPs. Second, HT Pt electrodeposition[75] represents a promising alternative to other core@Pt shell NP synthesis techniques, such as underpotential deposition (UPD) followed by galvanic exchange (GE).[7,12-15,19,22,52,53,104] This is because UPD/GE necessitates multiple steps and can lead to NP contamination by residual UPD metal.[22-26] The HT approach bypasses these complications by using adsorbed H (H_{ads}) to control the extent of

Pt electrodeposition.[75] Third, our results highlight an important difference in physical properties (e.g., geometry) between bulk-phase materials and small NPs.

Pt monolayer (ML) electrodeposition is complicated by the fact that a direct approach typically leads to three-dimensional Pt growth.[9,10] A common method for circumventing this limitation is to electrodeposit a ML of a metal known to provide two-dimensional growth (e.g., UPD of Cu or Pb), and then galvanically exchange the UPD metal for Pt.[7,12–15,19,22,52,104] However, the UPD/GE route can suffer from the types of problems noted earlier.

HT Pt electrodeposition, pioneered by Moffat and coworkers,[75] is a rapid method for directly electrodepositing a Pt ML onto a second metal substrate. This method consists of three steps (Illustration 5.1). After cleaning the surface (Step 1), the electrode potential is pulsed (Step 2) to a value wherein hydrogen evolution on Pt is diffusion limited. This latter condition ensures that newly electrodeposited Pt atoms are quickly capped by adsorbed H_{ads}, which limits Pt growth to a single ML. In Step 3, the electrode potential is pulsed positive to remove the H_{ads} layer. Steps 1 to 3 can be repeated to electrodeposit Pt MLs onto bulk materials in an approximately layer-by-layer fashion.[75,76,78–80]

HT Pt electrodeposition has previously been demonstrated on bulk Au,[75,76,78,81] nanoporous Au,[83,84] star-shaped dendritic Au rods

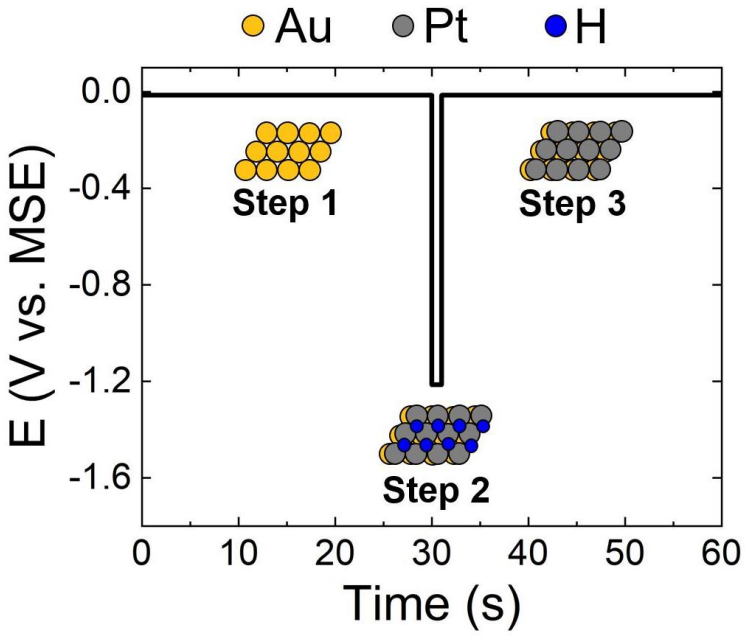

Illustration 5.1

(DARs),[79,80] Ni,[77,82] and C-based substrates.[85-88] HT electrodeposition has also proven useful for Ir electrodeposition onto bulk Pt, Au, and Ni,[89] and for synthesizing PtCoNi alloys.[90] Despite the success of the HT method on these substrates, its application on NPs is much less developed. Recently, however, our group examined HT Pt electrodeposition on ~1.6 nm Au NPs.[40] On the basis on Moffat's findings of near-ML Pt coverage (75 to 85%) on bulk Au,[75,76] we expected to find similar structures for Au NPs. A combination of experimental and theoretical investigations revealed, however, that the resulting AuPt NPs were quasi-random alloys rather than well-defined core@shell structures.[40] Moreover, density functional theory-molecular dynamics (DFT-MD) based simulations suggested that the structural divergence between the Pt MLs electrodeposited on bulk Au vs. Au NPs stemmed from inherently dissimilar structural flexibilities.[40] Specifically, the enhanced structural flexibility of small Au NPs was predicted to lead to alloying via rapid (7.5 ps) Pt absorption into the Au lattice. In contrast, the rigidity of bulk Au was predicted to support a segregated Pt ML.

Despite these interesting findings, several questions about the HT Pt electrodeposition process on Au NPs remained unanswered. For example, how many Pt atoms are able to absorb into the Au NP lattice before a structure having a complete Pt shell is produced? Indeed, is it even possible to use the HT method to prepare

core@complete-shell NP structures using multiple HT pulses? The present study addresses these questions.

The growth of consecutive Pt MLs on bulk Au[76,78] and star-shaped DARs[79,80] via the HT method has been used to study the effect of Pt layer thickness on the electrocatalytic FAO reaction,[76,79] the methanol oxidation reaction (MOR),[76,80] and the oxygen reduction reaction (ORR).[78] A few trends are evident from these reports. First, for bulk Au, a complete Pt ML is obtained after one or two iterations of the potential-pulse sequence shown in Illustration 5.1.[75–78] Second, the number of Pt layers electrodeposited corresponds closely with the number of HT Pt electrodeposition pulses.[75–77] In contrast, when the geometry is changed to star-shaped DARs, 15 iterations of Illustration 5.1 are required to obtain a complete Pt ML and 30 iterations are needed for the second ML.[79,80] These results indicate that substrate geometry plays an important role in the HT process. Given the promise of the HT method as a less complicated, more versatile, and more direct alternative to UPD/GE for Pt ML electrodeposition, the nuances of its mechanism at different scales and on different geometries are crucial to its widespread application.

In this report, we extend our earlier study, which involved the structure of AuPt NPs produced using a single electrodeposition pulse on ~1.6 nm Au NPs,[40] to structural evaluation of AuPt NPs

prepared using multiple HT pulses. The results of this study provide the following insights. First, electrochemistry, TEM, and XPS indicate that a nearly complete Pt ML is obtained after 3 to 5 pulses. This level of Pt coverage onto small Au NPs, even after this number of electrodeposition steps, is not a foregone conclusion given the high energy associated with corner and edge sites on the Au NPs and the demonstrated propensity for AuPt NP alloying.[40] Second, the fact that a AuPt-core@Pt-shell structure can be obtained, as opposed to the alloy-like structure produced upon a single HT pulse,[40] unlocks the advantages of the HT Pt electrodeposition method for NPs. Third, the number of HT pulses (3 to 5) needed to electrodeposit each Pt ML differs from bulk Au (1 to 2 pulses) and DARs (15 pulses). These results suggest that size and geometry play an important role in the HT method. Fourth, FAO activity is enhanced (5 to 110x) relative to bulk Pt and is tunable based on the number of Pt pulses applied: 1 and 10 HT pulses yield the highest and lowest activity, respectively.

5.3. Experimental Section

Chemicals and materials

A 9.0 wt% solution of generation 6.0, polyamidoamine dendrimers (G6-NH_2) in methanol was acquired from Dendritech, Inc.

(Midland, MI). The methanol was removed by evaporation, and the dendrimers were re-dissolved in water to yield a 100 µM aqueous stock solution. $HAuCl_4$ (≥99.9%), $NaBH_4$ (99.9%), formic acid (88-91%), H_2SO_4 (95-98%), HPLC grade isopropanol (99.9%), and a standardized NaOH solution (0.50 M) were purchased from Sigma-Aldrich. NaCl, K_2PtCl_4 (99.9%), and aqueous 70% $HClO_4$ were obtained from Fisher (New Jersey, USA). All solutions were made using deionized (DI) Milli-Q water (18.2 MΩ-cm; Millipore, Bedford, MA). Vulcan carbon (EC-72R) was from ElectroChem, Inc. (Woburn, MA).

Grids for TEM (catalog numbers CF400-Cu-UL and LC400-Cu-UL) were purchased from Electron Microscopy Sciences (Gibbstown, NJ). All electrodes and a 700E potentiostat were acquired from CH Instruments (Austin, TX). The counter, working, and reference electrodes were a glassy carbon rod, a 3.0 mm glassy carbon electrode (GCE), and Hg/Hg_2SO_4 (MSE), respectively. However, all potentials were converted to the reversible hydrogen electrode (RHE) scale.

Synthesis and characterization of Au147 dendrimer-encapsulated nanoparticles (DENs)

Au_{147} DENs (2.0 µM) were synthesized using a two-step procedure. First, 0.147 mL of $HAuCl_4$ (20.0 mM) was added dropwise, with vigorous stirring, to a solution containing 0.200 mL of G6-

NH_2 dendrimers (100 µM) and 8.65 mL of Milli-Q water. Second, <2 min after the first drop of $HAuCl_4$ was added to the dendrimer solution, 0.30 M NaOH (1.0 mL) was added to an 11-fold excess of $NaBH_4$ (~1.2 mg). The resulting mixture was immediately transferred to the DENs reaction vial. Reduction of the dendrimer-$AuCl_4^-$ composite led to a rapid color change from light yellow to brown. After ~7 min, the stir speed was reduced, and the DENs vial was loosely capped. Excess BH_4^- in the DENs solution was deactivated in air for ≥12 h and then the DENs were characterized.

Au_{147} DENs were characterized using UV-Vis spectroscopy and transmission electron microscopy (TEM). UV-Vis spectroscopy was performed using a Hewlett-Packard 8453 spectrometer, a 2.0 mm quartz cuvette, and Milli-Q water as a reference. For TEM, 2.0 µL of the 2.0 µM Au_{147} DENs solution was dropcast onto a carbon-film-coated Cu grid (CF400-Cu-UL) and dried in air.

Electrochemical synthesis and characterization of AuPt DENs

GCEs were polished successively using 1.0, 0.3, and 0.05 µm alumina (2 min/thickness). Subsequent sonication in Milli-Q water (10 min) was used to remove excess alumina from the electrode surface. VC-based inks for electrochemistry were prepared using the following components: ~1.0 mg VC, 0.20 mL of isopropanol, and 1.0 mL of 2.0 µM Au_{147} DENs. Prior to addition of the DENs, the VC

and isopropanol were sonicated together until a homogeneous slurry was obtained (~10 to 15 min). This step aids in dispersion of the hydrophobic VC before it contacts the aqueous DENs solution. After the DENs were added to the VC slurry, the resulting mixture was sonicated for an additional 10 to 15 min. Once the electrochemical ink was prepared, 6.0 µL was dropcast onto a polished 3.0 mm GCE and dried under gently flowing N_2.

Electrochemical cleaning of the Au_{147} DENs was carried out using cyclic voltammetry (CV; 20 cycles) in N_2-purged 0.10 M $HClO_4$. The electrode potential was scanned from 0.70 V to 1.57 V and then back to 0 V, at a scan rate of 200 mV/s. Subsequently, the Au surface area was characterized using the same parameters, but for just three CV cycles and at a scan rate of 100 mV/s.

After Au surface cleaning and characterization, Pt was deposited using the HT method[40,75] in a N_2-purged, pH 4.0 solution containing 0.50 M NaCl and 3.0 mM K_2PtCl_4. The deposition procedure followed that shown in Illustration 5.1, except that a shorter time (1.0 s) was used for Step 3. For 1 HT pulse, the electrode potential was held at 0.86 V for 30.0 s (Step 1), -0.34 V for 1.0 s (Step 2), and then 0.86 V for 1.0 s (Step 3). For multiple HT pulses, Steps 1 to 3 were repeated multiple times.

Following HT Pt electrodeposition, a three-step rinsing procedure was used: ~20 s in 250 mL of Milli-Q water, 5 min in

0.10 M $HClO_4$ with vigorous stirring, and ~5 s in 20 mL of Milli-Q water. As we showed in a previous publication,[33] this rinsing procedure prevents adventitious Pt NP formation on the GCE upon subsequent electrochemical cycling. The AuPt NP surfaces were characterized by CV in N_2-purged 0.10 M $HClO_4$ at a scan rate of 100 mV/s. The scan parameters were identical to those used for Au_{147} surface characterization, except that a total of nine cycles were used. After surface characterization, the GCE was rinsed in Milli-Q water and then swiped over the surface of a lacey carbon-coated Cu TEM grid (LC400-Cu-UL) for imaging by TEM.

Transmission electron microscopy (TEM)

Standard TEM was carried out using a JEOL 2010F TEM with 0.19 nm point-to-point resolution and an operating voltage of 200 kV. Aberration corrected scanning TEM (acSTEM) and energy dispersive spectroscopy (EDS) was performed using a JEOL NEOARM TEM using an operating voltage of 80 kV and a point-to-point STEM resolution at 80 kV of 0.11 nm.

X-ray photoelectron spectroscopy (XPS)

A Kratos Axis Ultra DLD spectrometer (Chestnut Ridge, NY) equipped with an Al K_α source was used for XPS measurements. XPS samples were prepared on TEM grids; after electrochemical

characterization and rinsing, the surfaces of the GCEs containing the AuPt DENs were swiped onto lacey carbon-coated Cu TEM grids. Care was taken to fully coat the TEM grid to ensure an adequate XPS signal-to-noise ratio. XPS spectra utilized a band pass energy of 20 eV and a step size of 0.10 eV. Peak positions were calibrated relative to C 1s (284.5 eV).[14,93,94] A Gaussian/Lorentzian model (GL90) was used to fit the Au 4f peaks, whereas the Pt 4f peaks were fit using an asymmetric Lorentzian model: LA (1.2,85,70).

Formic acid oxidation (FAO)

Prior to FAO, a control CV was recorded in N_2-purged, 0.50 M H_2SO_4. Specifically, the electrode was immersed under potential control at 0.01 V. The potential was then cycled two times from 0.01 to 1.26 V and then back to 0.01 V at a scan rate of 10.0 mV/s. After the control CV was recorded, the GCE was removed from the cell and rinsed. Formic acid (0.50 M) was then added to the cell and mixed using N_2 agitation. The same steps as for the control CV were then repeated except, to be consistent with the original report of HT deposition on macro surfaces, 20 cycles were recorded.[76]

5.4. Results and Discussion

Electrochemical synthesis and characterization of AuPt DENs

Au_{147} DENs were synthesized as described in the Experimental Section. Briefly, 147 equiv. of $HAuCl_4$ were added dropwise to an aqueous G6-NH_2 solution with rapid stirring, and then the resulting mixture was reduced with an 11-fold excess of $NaBH_4$. Our previous studies have shown that this synthesis yields ~1 to 2 nm AuNPs.[1,2,13,28,40,153] The Au_{147} DENs synthesized in the present report have a size distribution of 1.6±0.3 nm (Figure 5.1a), which is consistent with the theoretically predicted size for a perfect Au_{147} cuboctahedron (1.6 nm).[13,15]

Figure 5.2a presents a series of CVs obtained as a function of the number of HT pulse sequences (Illustration 5.1) applied to the GCE-immobilized Au_{147} DENs. The purple trace was obtained prior to Pt electrodeposition. The only notable features are an anodic current positive of ~1.3 V, arising from surface oxidation of the Au_{147} DENs, and the corresponding AuO_x reduction peak (Peak P1) at ~1.1 V. Integration of the area under this latter peak (expanded view in Figure 5.2b) and conversion of charge to the Au electrochemically active surface area (ECSA), using the generally accepted factor of 390 μC/cm^2,[15,140] yields an average of 0.26±0.03 cm^2 (based on 12 independent experiments). HT Pt electrodeposition

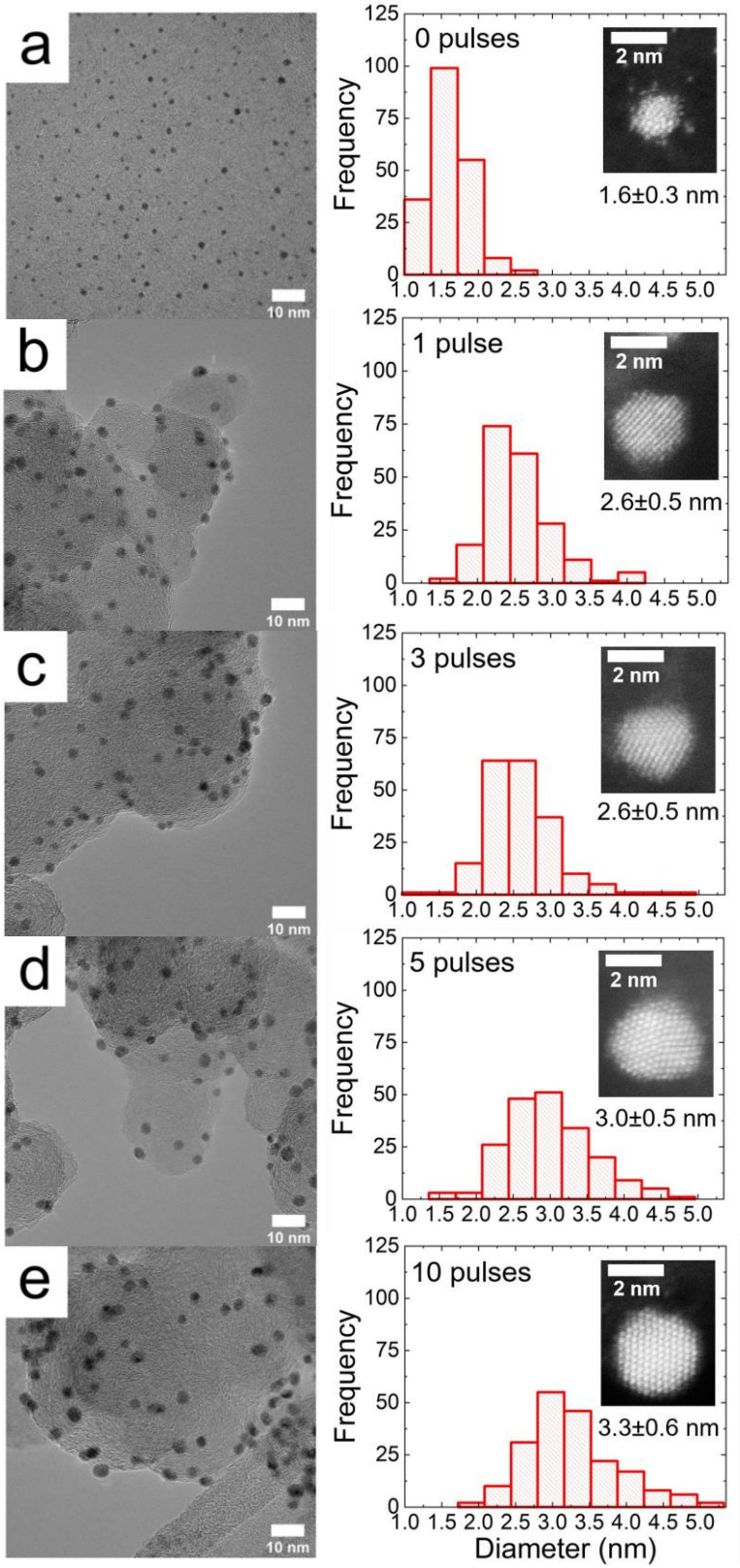
a
10 nm
0 pulses
2 nm
1.6±0.3 nm
b
10 nm
1 pulse
2 nm
2.6±0.5 nm
c
10 nm
3 pulses
2 nm
2.6±0.5 nm
d
10 nm
5 pulses
2 nm
3.0±0.5 nm
e
10 nm
10 pulses
2 nm
3.3±0.6 nm
Frequency
Diameter (nm)
0 25 50 75 100 125
1.0 1.5 2.0 2.5 3.0 3.5 4.0 4.5 5.0

Figure 5.1

Figure 5.1 cont.

TEM micrographs and the associated size-distribution histograms for HT Pt electrodeposition onto Au_{147} DENs using the indicated number of pulses. Each histogram was obtained by sizing 200 randomly selected NPs. Aberration-corrected STEM (acSTEM) micrographs of representative particles are shown in the insets of the histograms.

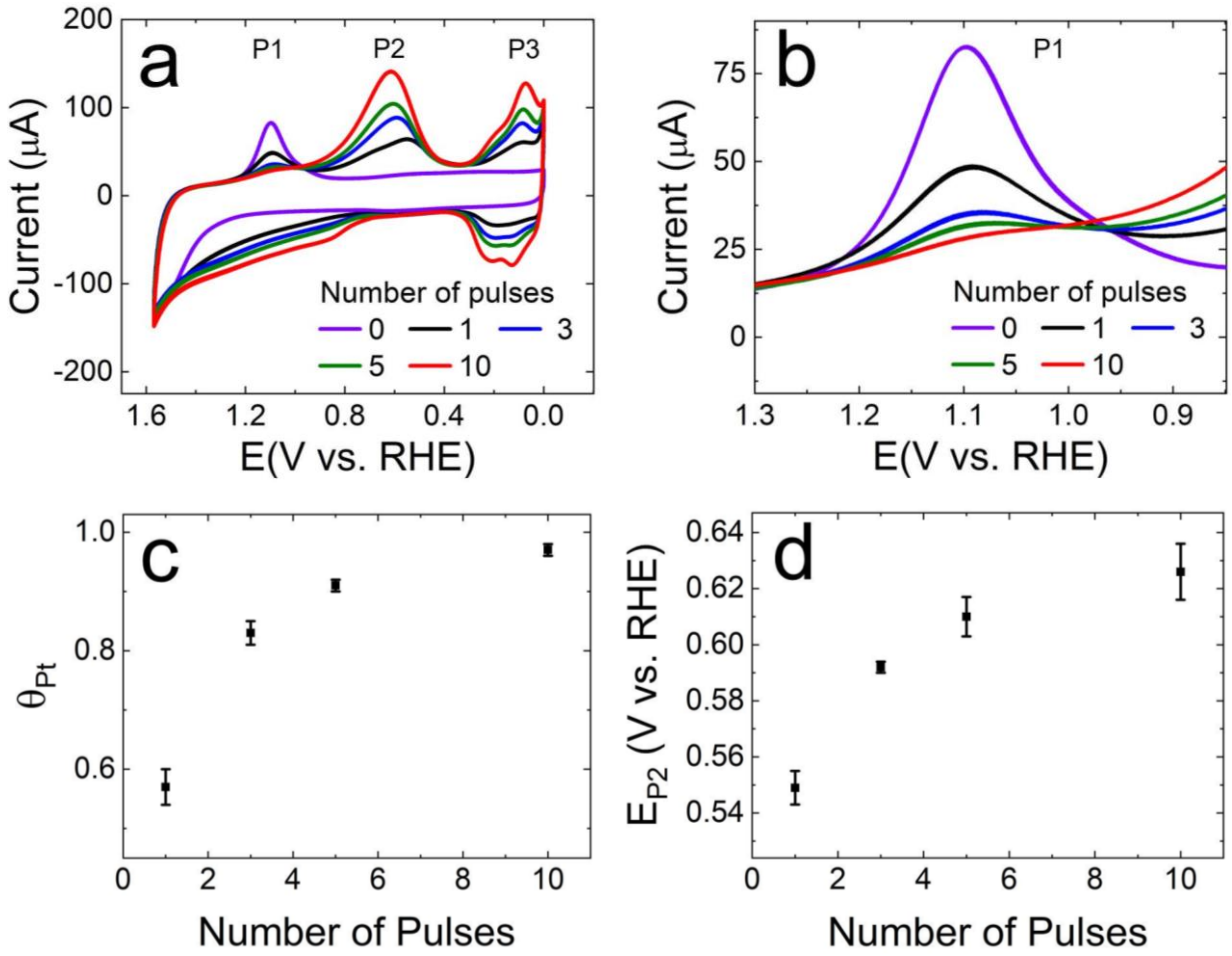

Figure 5.2

(a) CVs recorded before and after HT Pt electrodeposition onto Au_{147} DENs using the indicated number of pulses. Peaks P1, P2, and P3 correspond to the AuO_x reduction, PtO_x reduction, and Pt-H adsorption/desorption (Pt-hydride) peaks, respectively. (b) Expanded view of Peaks P1, showing that the Au_{147} NP surface is nearly completely covered after 3 to 5 HT pulses. (c) Pt coverage (Θ_{Pt}) as a function of pulse number. (d) The position of peak P2 as a function of pulse number. The electrolyte was N_2-purged 0.10 M $HClO_4$ and the scan rate was 100 mV/s.

onto the Au_{147} DEN cores was carried out as described in the Experimental Section using the method outlined in Illustration 5.1. The black trace in Figure 5.2a was obtained following 1 HT Pt electrodeposition pulse. Compared to the purple CV, Peak P1 decreases and two new peaks emerge: PtO_x reduction (Peak P2) and Pt-H adsorption/desorption (Pt-hydride; Peaks labeled P3). This general trend continues after 3, 5, and 10 HT pulse sequences. For example, Peak P2 increases in magnitude and its potential shifts slightly positive. This positive shift as a function of pulse number is consistent with previous results obtained for increasing coverages of Pt on AuNPs.[154,155] Additionally, the P3 peaks also grow as a function of the number of HT pulses.

With regard to the Au-related peaks, it is apparent that the area under Peak P1 is still significant after 1 HT pulse. This finding is consistent with our earlier report that focused on just a single HT pulse, and it clearly indicates that the NP surface contains both Au and Pt atoms.[40] After 3 and 5 HT pulse sequences, however, the area under Peak P1 becomes very small (Figure 5.2b), suggesting nearly complete Pt coverage of the original Au core. To summarize the qualitative trends in Figures 5.2a and 5.2b, the AuNP surface is nearly completely covered by Pt after 3 to 5 HT pulses, and more pulses simply expand the Pt shell. We can learn more about the HT process, however, by quantitatively examining

Figures 5.2a and 5.2b. For this purpose, we introduce several parameters related to Pt coverage: Θ_{Pt}, the Pt:Au_i ECSA ratios, $N_{Au,surf}$, and $\%Pt_{surf}$, all of which are defined in Table 5.1.

Three quantitative trends confirm the conclusions reported in the previous paragraph. First, the Pt coverage (Θ_{Pt}, Table 5.1) approaches unity after 3 (Θ_{Pt}=0.83±0.02) to 5 (Θ_{Pt}=0.91±0.01) HT pulse sequences (Figure 5.2c), confirming that the original AuNP surface is nearly completely covered by Pt. Second, the rate of change in Θ_{Pt} (Figure 5.3) slows as a function of the number of pulse sequences. Specifically, $\frac{d\theta_{Pt}}{dp}$ approaches zero after 5 HT pulses. Despite slowing growth in Θ_{Pt}, the Pt ECSA (Table 5.2) continues to increase with the number of pulses. Another way of looking at this is to consider the Pt:Au_i ECSA ratio (Table 5.1), which increases from 1.8±0.2 to 2.6±0.1 after 5 and 10 HT pulses, respectively. The experimental Pt:Au_i ECSA ratios for 5 and 10 pulses match those theoretically predicted (Table 5.3) for one (1.8) and two (2.7) complete Pt MLs, respectively, on a cuboctahedral Au_{147} NP core. Taken together, these trends support the assertion that the NP shell consists of Pt multilayers after ≥5 HT pulses.

The third point is that the center of Peak P2 in Figure 5.2a shifts positive by 79 mV as the number of HT Pt electrodeposition

Pulses	θ_{Pt}	Pt:Au_i	$N_{Au,surf}$	%Pt_{surf}
1	0.57(3)	0.62(3)	40	59(3)
3	0.83(2)	1.25(1)	16	88(1)
5	0.91(1)	1.8(2)	8	96(1)
10	0.97(1)	2.6(1)	3	99.0(4)

Table 5.1

Electrochemical surface characterization parameters for HT Pt electrodeposition onto Au_{147} DENs using the indicated number of pulses. Pt coverage, θ_{Pt}, was calculated as 1-(Au_f ECSA/Au_i ECSA) and represents the fraction of the original Au surface atoms covered by Pt. ECSAs for Au before (Au_i) and after (Au_f) HT Pt electrodeposition, as well as the associated Pt ECSAs and total AuPt NP ECSAs ($ECSA_{tot}$ = Au_f ECSA + Pt ECSA) for each pulse number, are provided in Table 5.2. Pt:Au_i is the ratio of the Pt ECSA to the original Au ECSA. $N_{Au,surf}$ is the number of naked Au surface atoms present after HT Pt electrodeposition and was calculated as (1- θ_{Pt}) multiplied by the number of surface atoms on the Au_{147} core (92). The %Pt_{surf} is the percentage of the NP surface atoms that are Pt and was calculated as the Pt ECSA, divided by $ECSA_{tot}$, and then multiplied by 100%.

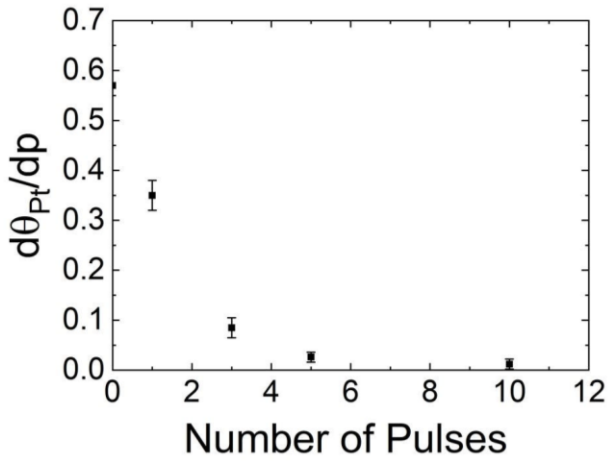

Figure 5.3

The rate of change ($d\Theta_{Pt}/dp$) in Pt coverage (Θ_{Pt}) as a function of the number of HT pulses. The rate of change approaches zero after 5 HT pulses.

Pulses	Au_i (cm^2)	Au_f (cm^2)	Pt (cm^2)	$ECSA_{tot}$ (cm^2)
1	0.260(9)	0.11(1)	0.160(7)	0.27(1)
3	0.25(3)	0.041(2)	0.31(4)	0.36(4)
5	0.26(4)	0.022(4)	0.48(8)	0.50(8)
10	0.28(3)	0.007(3)	0.74(8)	0.75(8)

Table 5.2

Pt and Au electrochemically active surface areas (ECSAs), as a function of the number of HT pulses. The Au_i ECSA corresponds to the ECSA of the naked Au_{147} NP surface (prior to HT Pt deposition). The Au_f ECSA is the remaining Au ECSA after HT Pt deposition. In each case, the area under the AuO_x reduction peak was integrated and the resulting charge was converted to ECSA using the charge density for polycrystalline Au (390 $\mu C/cm^2$).[140] Pt ECSA determination used the same procedure, except the Pt-H adsorption waves were integrated and the charge density for polycrystalline Pt (210 $\mu C/cm^2$)[140] was used to convert charge to ECSA. $ECSA_{tot}$ is the total NP ECSA (= Au_f ECSA + Pt ECSA).

Layers	N_{surf}	Pt:Au_i	d(nm)	N_{tot}	$N_{Pt,tot}$	Atomic% Pt
0 ML	92	-	1.7	147	-	-
1 ML	162	1.8	2.3	309	162	52
2 ML	252	2.7	2.8	561	414	74
3 ML	362	3.9	3.4	923	776	84
4 ML	492	5.3	4.0	1415	1268	90

Table 5.3

Theoretically predicted electrochemical, TEM, and XPS parameters for the deposition of 1 to 4 monolayers (MLs) of Pt onto a cuboctahedral Au_{147} NP. N_{surf} is the number of surface atoms (Au + Pt), Pt:Au_i is the ideal electrochemical Pt:Au_i ECSA ratio, d is the theoretically predicted NP diameter, N_{tot} is the total number of atoms (core + shell(s)) in each NP, $N_{Pt,tot}$ is the total number of Pt atoms in each NP, and atomic% Pt is the atomic Pt composition predicted for XPS. Pt:Au_i was calculated as N_{surf} in each layer divided by N_{surf} for 0 ML (corresponding to the number of surface atoms in the Au_{147} core). The values of d were calculated using cuboctahedral cluster models from the Atomic Simulation Environment (ASE) Python library.[156] The diameter of each cluster model was measured using the ASE graphical user interface. $N_{Pt,tot}$ was calculated as the sum of N_{surf} in a given layer plus N_{surf} in the preceding layer(s) (e.g., 162+252=414 for 2 ML). The atomic% Pt values were calculated as $100\% * N_{Pt,tot}/N_{tot}$. An ideal core@shell Au_{147}@Pt model was assumed in all cases.

pulses increases from 1 to 10. As shown in Figure 5.2d, about half of this total shift occurs between pulses 1 and 3. The fact that smaller shifts in the position of Peak P2 occur between 3 and 5 pulses and 5 and 10 pulses suggests that the largest change in Pt electronic properties occurs between 1 and 3 HT pulses. This result is consistent with a transition from sub-ML Pt coverage, where the interplay of ligand, ensemble, and strain effects control the potential at which Pt oxidation occurs,[76,78] to nearly complete ML coverage (after 3 to 5 pulses) where strain effects dominate (and diminish as the number of MLs increase).[78,157]

Although multiple HT pulse sequences are required to fully cover Au_{147} NPs with Pt, the fact that nearly complete Pt coverage is ultimately obtained (after ~5 pulses) is significant for two reasons. First, Au_{147} NPs have a much greater proportion of high energy sites than bulk Au (i.e., 65% corner plus edge atoms).[15,37,45] The results in Table 5.1 show that after 3 HT pulses there are 16 naked surface Au atoms ($N_{Au,surf}$ = 16). This value is much smaller than the total number of edge and corner sites (60) on Au_{147} NPs, and therefore we conclude that the majority of the high-energy sites are covered with Pt for ≥3 HT pulses. Furthermore, $N_{Au,surf}$ after 3 HT pulses is close to the number of corner sites (12) present on the original Au_{147} NPs. It is possible that these corner

sites are not receptive to Pt deposition, and this could account for the slow increase in θ_{Pt} between 3 to 10 HT pulses.

Second, the Pt coverage obtained after 3 to 5 HT pulse sequences (θ_{Pt} = 0.83±0.02 and 0.91±0.01, respectively) is greater than that previously observed using either Pb UPD/Pt GE (~0.50-0.57)[13,15,16] or Cu UPD/Pt GE (~0.70-0.80)[13,14] to prepare AuPt DENs from Au_{147} DEN cores. This result suggests that the HT method is a viable alternative to UPD/Pt GE for Pt ML electrodeposition on small AuNPs as long as a sufficient number of pulses are used. Additionally, and as alluded to in the introduction, the HT method avoids key complications associated with UPD/Pt GE, such as residual UPD metal left on the Au surface following GE,[22–26] low Pt coverages,[13,68,70] and the need for multiple deposition solutions.[21] Given that just a few residual heteroatoms can alter the catalytic properties of NPs,[25] the HT method provides a cleaner route for synthesizing core@Pt shell electrocatalytic NPs.

In order to aid our investigation of Pt growth beyond the first ML, we sought to determine whether Pt growth was two-dimensional, three-dimensional, or a combination of the two. For a macroscopic disk electrode, the surface roughness is simply defined as the ECSA divided by the geometrical SA. This estimate is not useful in our case, however, because the NPs are supported on Vulcan carbon (VC). Similarly, although the Pt:Au_i ECSA ratio

yields information about the completeness and roughness of Pt layers for Pt deposition onto bulk Au (with a ratio of 1.0 indicating a complete, two-dimensional ML), this approach is not informative for small NPs. For example, due to an enhanced surface-area-to-volume ratio for Au_{147} NPs relative to bulk Au, a complete Pt ML is expected to have a Pt:Au_i ratio of 1.8 (=162/92, e.g., Table 5.3). Therefore, the fact that Pt:Au_i ratios range from 1.25 to 2.6 after 3 to 10 HT pulses is more likely an indication of an increase in the number of Pt layers than surface roughness.

Nevertheless, we attempted to estimate the amount of surface roughness, in the form of three-dimensional Pt growth on the Au_{147} NPs. As defined in Table 5.1, Θ_{Pt} (=1-Au_f/Au_i) represents the change in Au ECSA caused by Pt atoms depositing directly on top of the original Au surface atoms. As a result, it reflects the amount of two-dimensional Pt growth. On the other hand, $\%Pt_{surf}$, measures the percentage of the total ECSA (Au_f ECSA + Pt ECSA) that corresponds to Pt. Thus, $\%Pt_{surf}$ could, in principle, include both two-dimensional and three-dimensional Pt growth. Therefore, subtracting Θ_{Pt} from $\%Pt_{surf}$ yields a crude estimate of the amount of three-dimensional Pt growth.

For 1 HT pulse, $\%Pt_{surf}$ is within experimental error of Θ_{Pt}, suggesting strictly two-dimensional Pt growth. For ≥3 HT pulse sequences, the differences between $\%Pt_{surf}$ and Θ_{Pt} (2 to 5%) are

slightly greater than the experimental error between trials (0.4 to 3%). Therefore, three-dimensional Pt growth is possible for ≥3 HT pulse sequences, but its extent is small (2 to 5%).

Transmission electron microscopy (TEM)

TEM micrographs of AuPt DENs synthesized using 1 to 10 HT pulses, and the corresponding size-distribution histograms, are shown in Figure 5.1. For comparison, theoretical predictions of NP size as a function of the number of Pt MLs electrodeposited are provided in Table 5.3.

As discussed in the previous section, Figure 5.1a indicates that the average size distribution of the Au_{147} DENs prior to HT Pt deposition (0 pulses) is 1.6±0.3 nm. Figures 5.1b and 5.1c demonstrate that both 1 and 3 HT pulses yield size distributions of 2.6±0.5 nm. Although this size distribution is larger than predicted for a perfect cuboctahedral 309 atom Au@Pt NP (2.3 nm), it is, within error, the same as we have reported for deposition of a single Pt layer on Au_{140} (2.5±0.4 nm)[12] and Au_{147}(2.4±0.4 nm)[13] DENs using UPD/Pt GE. This value is also similar to the one we have previously reported for a single HT pulse on Au_{147} DENs (2.8±0.6 nm).[40] The fact that 1 and 3 HT pulses yield equivalent AuPt NP size distributions is consistent with the electrochemical

results, which showed that at least 3 HT pulses are required to deposit a complete Pt ML.

The size distribution for the AuPt DENs synthesized using 5 HT pulse sequences (Figure 5.1d) is 3.0±0.5 nm. This size agrees well with the theoretically predicted size for the deposition of 2 ML of Pt on Au_{147} (2.8 nm). The size distribution for 10 HT pulses (Figure 5.1e) is 3.3±0.6 nm, which is in close agreement with the size theoretically predicted for the deposition of 3 ML of Pt on Au_{147} (3.4 nm). These TEM results are, within 1 ML, the same as that determined electrochemically. As shown in the next section, the TEM results also closely match XPS data.

X-ray photoelectron spectroscopy (XPS)

The NPs used in this study are sufficiently small that XPS provides elemental composition of the entire NP rather than just the surface.[95,158] In contrast, the foregoing electrochemical analysis provides information about just the surface composition. By correlating the XPS and electrochemical results, therefore, it is possible to draw conclusions about NP structure.

XPS spectra for the AuPt DENs synthesized using 1 to 10 HT pulses are shown in Figure 5.4a. Data for the naked Au_{147} DENs (0 pulses) are also shown. The Pt and Au atomic percentages for each

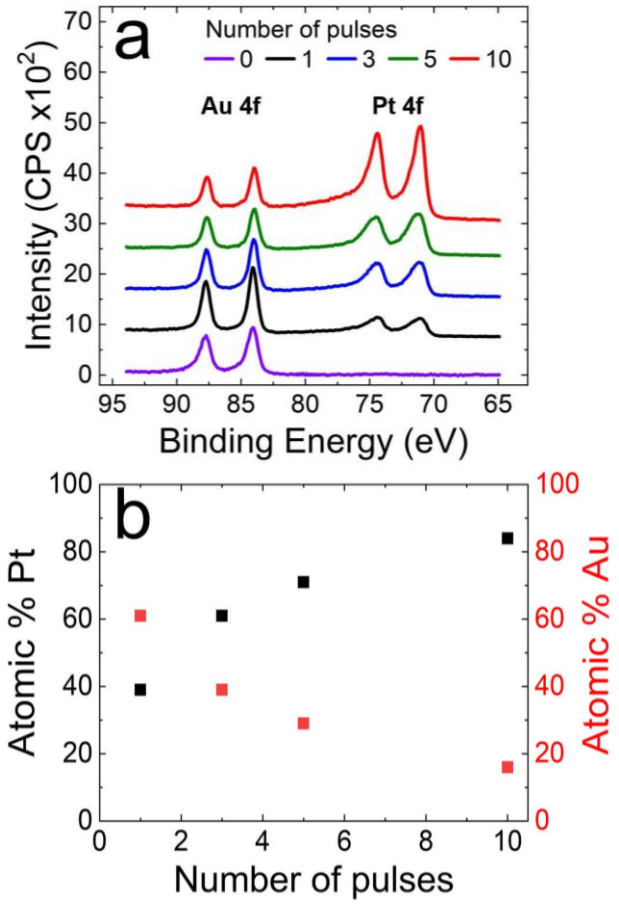

Figure 5.4

(a) XPS spectra in the Au 4f and Pt 4f regions for HT Pt electrodeposition onto the Au_{147} DENs using the indicated number of pulses. (b) Au and Pt atomic compositions as a function of pulse number. The data were obtained by integrating the peaks in (a).

NP composition (Figure 5.4b) were obtained by integrating the Pt 4f and Au 4f peaks. The number of Pt MLs deposited on Au_{147} after each HT pulse (Figure 5.5) was estimated by comparing the experimental compositions to theoretically computed values that assume all Pt is present in the outermost layers of the NPs (i.e., does not alloy into the core; Table 5.3 and Figure 5.6).

For 1 HT pulse, comparison of Figures 5.4b and 5.6 shows that the percentage of Pt determined by XPS, 39 atomic%, is insufficient to account for deposition of one complete ML of Pt (52 atomic%, Table 5.3) onto an Au_{147} core. The mismatch in the number of MLs (Figure 5.5) calculated using the XPS (0.78 ML) and electrochemistry (Θ_{Pt}=0.57 ML) data suggests that a fraction of the Pt atoms is alloyed within the NP core. This result is consistent with our past analysis for a single HT pulse on Au_{147}.[40]

For 3 HT pulse sequences, comparison of Figures 5.4b and 5.6 shows that the amount of Pt deposited (61 atomic%) is 9% greater than predicted for a single complete Pt ML (52 atomic%; Table 5.3). However, given that the electrochemical results (Table 5.1) indicate that only ~88% of the surface atoms are Pt after 3 HT pulse sequences, a fraction of the Pt atoms (~45) either alloy into the core or are present as the beginning (~0.2 ML) of a second Pt shell.

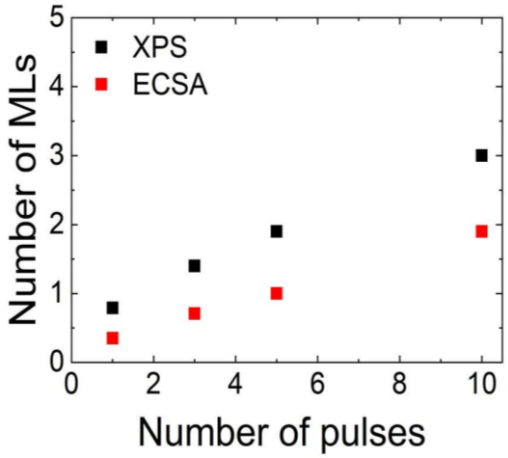

Figure 5.5

Comparison of the calculated number of Pt MLs determined from XPS and electrochemical analysis (ECSA), as a function of the number of HT pulses. For XPS, the number of Pt MLs was calculated by comparing the experimental atomic% Pt values (Figure 5.4b) to those theoretically calculated (Table 5.3 and Figure 5.6). Similarly, the number of MLs determined by electrochemistry was calculated by comparing the experimental Pt:Au_i ECSA ratios (Table 5.1) to the theoretical Pt:Au_i ECSA values (Table 5.3) for deposition of Pt on an ideal cuboctahedral Au_{147} NP.

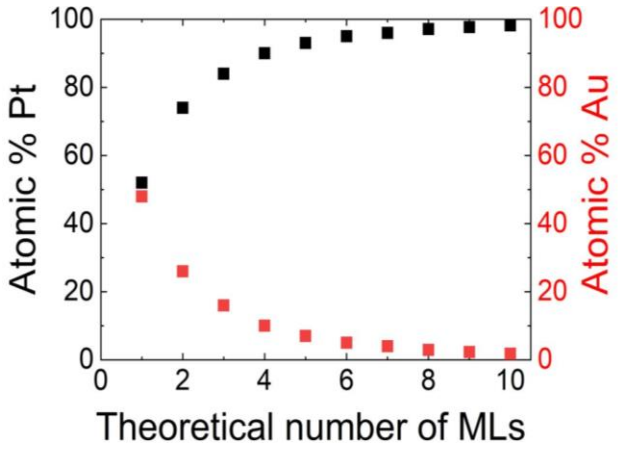

Figure 5.6

Plot of the theoretical Pt and Au compositions for an ideal cuboctahedral Au_{147} NP with 1 to 10 ML of deposited Pt.

After 5 HT pulses, the Pt composition determined by XPS (71 atomic% Pt) is close to that expected for deposition of 2 ML of Pt on Au_{147} (74 atomic% Pt, Table 5.3 and Figure 5.6). These results are also in accord with the TEM data discussed earlier, which indicated an average NP size of 3.0 nm. This value is close to that expected for the deposition of 2 ML of Pt (2.8 nm).

For 10 HT pulses, the Pt composition (84 atomic% Pt) exactly matches the expectation for Au_{147} having a Pt shell that is 3 ML thick (Table 5.3 and Figure 5.6). TEM data also support this structure: the average NP size (3.3 nm) is very close to that predicted for 3 ML of Pt on Au_{147} (3.4 nm).

The number of HT pulse sequences (3 to 5) required to deposit a single ML of Pt (Θ_{Pt} approaches 1.0, $\frac{d\theta_{Pt}}{dp}$~0, and atomic% Pt~52%) on the Au_{147} NP surface differs from both bulk Au (1 to 2 pulses)[75-78] and star-shaped DARs (15).[79,80] Similarly, the number of HT pulses required to deposit a second Pt ML (5 to 10 pulses) also differs from bulk Au (2 to 3 pulses)[75-77] and star-shaped DARs (30).[79,80] Accordingly, geometry appears to be an important consideration for HT Pt electrodeposition. This may be because small AuNPs have an increased tendency to alloy with deposited Pt relative to bulk Au.[13,40] Indeed, we have previously shown that a single HT pulse on Au_{147} NPs results in an AuPt alloy structure.[40] In that case,

theoretical calculations predicted that alloying would occur via absorption of Pt into the Au_{147} NP lattice, which is more flexible than that of bulk Au.[40]

Energy dispersive spectroscopy (EDS)

Single-particle EDS for the AuPt DENs prepared using 10 HT pulses is shown in Figure 5.7. A core@shell structure is observed (Figure 5.7a), with Pt (Figure 5.7b) concentrated towards the edges and Au (Figure 5.7c) at the center of the NP. The line profiles extracted from the combined map (Figure 5.7d) and recorded directly (to increase the line profile counts; Figure 5.8) confirm this assessment.

EDS maps for 1, 3, and 5 pulses are shown in Figures 5.9 to 5.12. These maps are less conclusive than those for 10 HT pulses due to smaller NP sizes and corresponding lower EDS counts. Additionally, the smallest AuPt DENs (prepared using 1 to 3 HT pulses) were easily damaged by the electron beam. As a result, it was challenging to find a sufficient number of NPs that were stable under the beam to collect the statistics necessary for definitive conclusions. With these caveats in mind, EDS maps for 1 HT pulse (Figure 5.9a to 5.9c) suggest an alloy structure, as indicated by overlapping Pt and Au signals. The line scan (Figure 5.9d) extracted from the map in Figure 5.9a supports this claim. However,

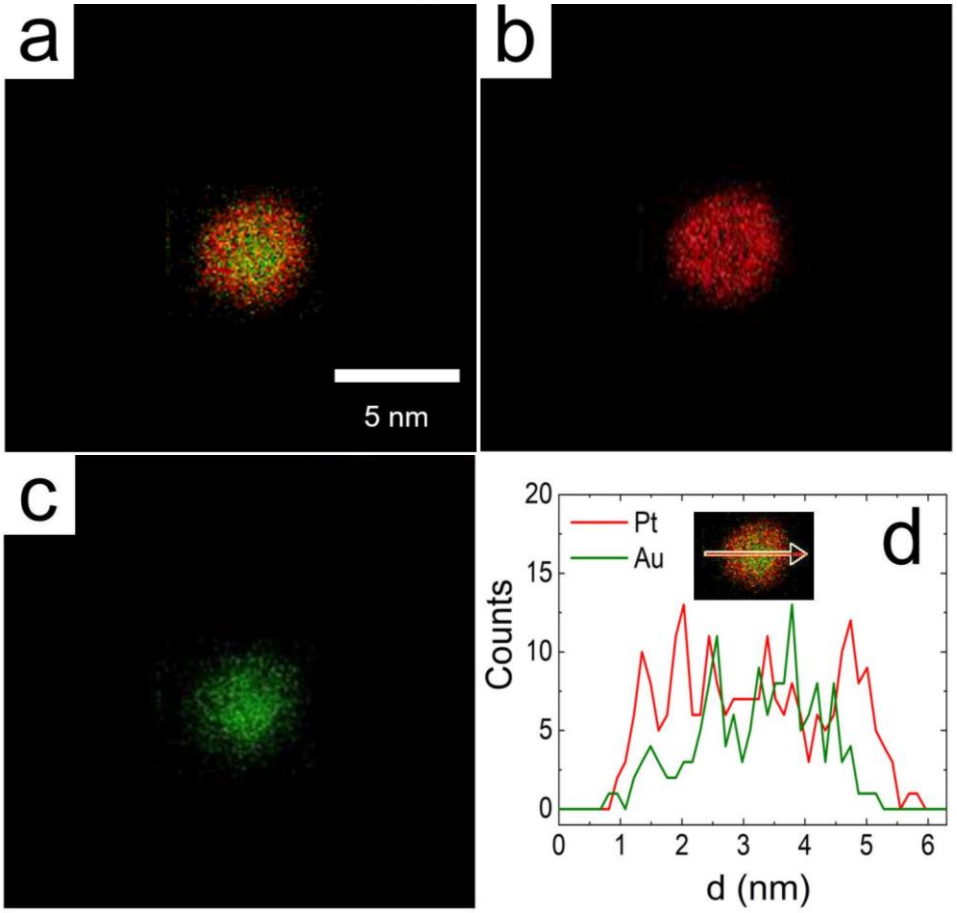

Figure 5.7

Single-particle EDS maps for HT Pt electrodeposition onto Au_{147} DENs using 10 pulses. (a) Superposition of the Pt and Au element maps. Pt and Au are shown in red and green, respectively. Individual element maps for (b) Pt and (c) Au. (d) Line profile extracted from the map in (a). The direction of the line scan along the associated map is shown in the inset and is indicated by the arrow. An additional, higher resolution line profile is provided in Figure 5.8. A core@shell structure is evident in both the maps and the line scans.

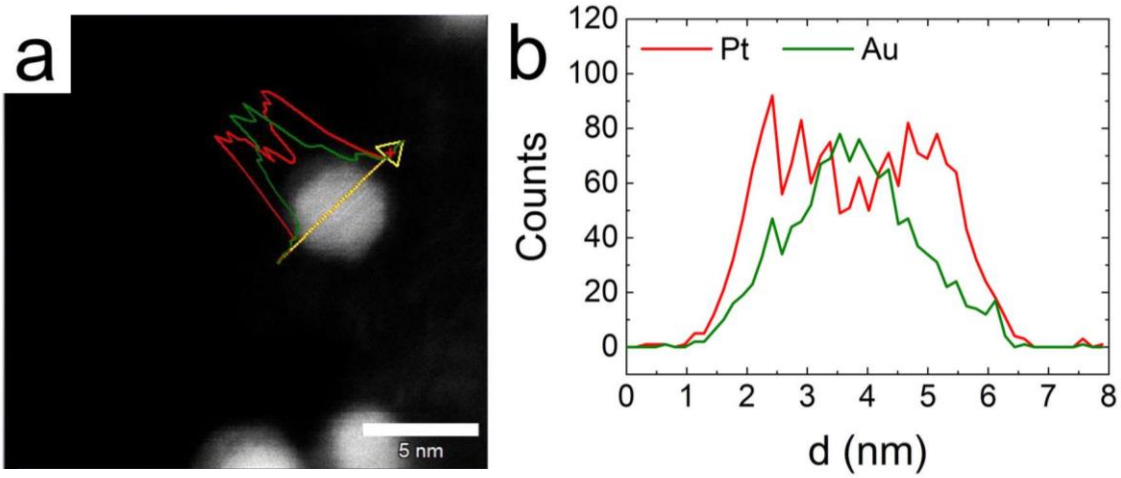

Figure 5.8

EDS line profiles for an AuPt NP prepared using 10 HT pulses (a) overlaid on the corresponding STEM micrograph and (b) a magnified view. This line scan was obtained directly (rather than being extracted from the map in Figure 5.7a). Line scan direction is indicated by the arrow in (a). As shown in (a), the line profile spans a distance that is larger than the NP. This might be due to drift during the line scan, as suggested by the larger gap between the NP and the line profile at the end of the scan (tip of the arrow) than at the beginning (arrow tail). Consequently, estimates of NP diameter and shell thickness using the x-axis in (b) are inaccurate. For example, although the diameter of the NP in the STEM micrograph corresponding to (a) is 4.2 nm, the line profile in (b) suggests NP size is between 5.2 and 5.8 nm (depending on where the baseline is drawn). Thus, the diameters in (b) are overestimated by ~1.0 to 1.6 nm. Accordingly, this line profile is only provided to highlight the core@shell structure of the NPs prepared using 10 HT pulses.

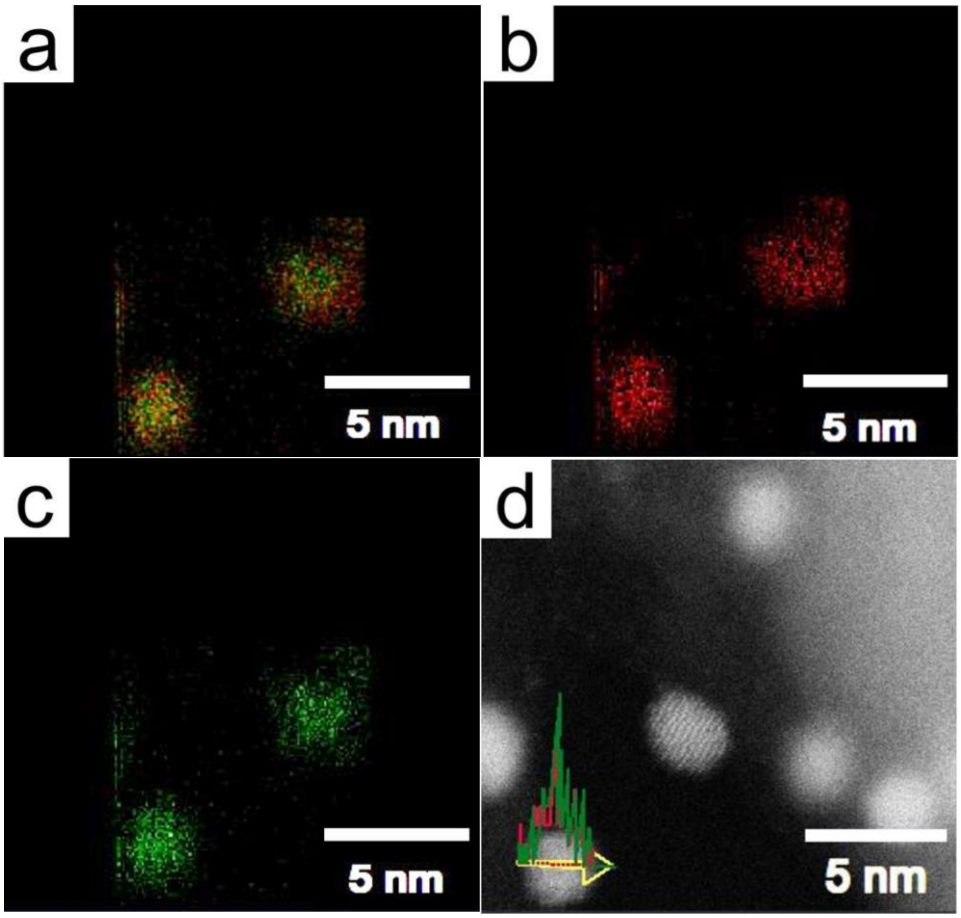

Figure 5.9

EDS for AuPt DENs prepared using 1 HT pulse. (a) Overlaid Pt (red) and Au (green) EDS maps. The NP on the lower left was stable during EDS measurements, but the NP on the right side of frame (a) may have been damaged by merging with a nearby NP during mapping. Individual (b) Pt and (c) Au maps corresponding to (a). (d) Line scan extracted from the map of the NP on the left side of frame (a) overlaid on the corresponding aberration-corrected STEM (acSTEM) micrograph.

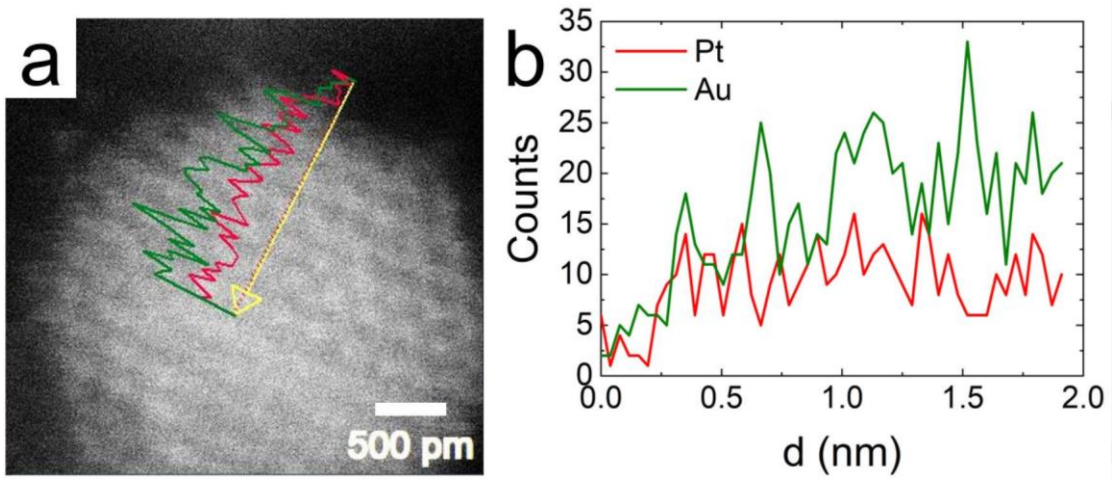

Figure 5.10

High-resolution line scan for AuPt DENs prepared using 1 HT pulse. (a) High-resolution, acSTEM micrograph, with EDS line scan overlaid. (b) Magnified view of the line scan in (a). Pt and Au may be alloyed in the outermost shell of the NP (d~0.3 to 0.6 nm; 0 to 0.3 nm in this case is just noise). Beyond ~0.6 nm, the Au counts increase, whereas the Pt counts remain approximately constant. This result suggests that the alloying observed in the surface of the NP does not extend appreciably into the core. Therefore, the AuPt DENs prepared using 1 HT pulse are likely surface alloys. This finding is consistent with our previous report.[40] We note, however, that the small number of counts, as well as the signal-to-noise ratio in (b), makes it difficult to draw firm conclusions.

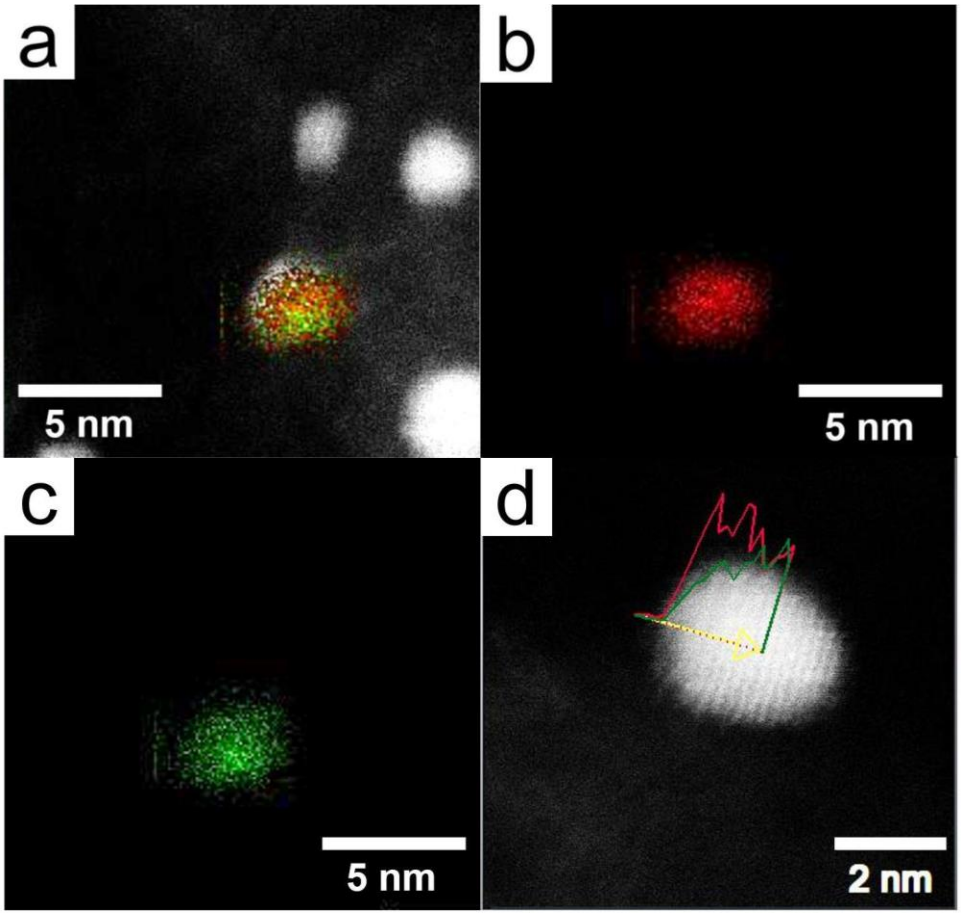

Figure 5.11

EDS for AuPt DENs prepared using 3 HT pulses. (a) Overlaid Pt (red) and Au (green) EDS maps. Individual (b) Pt and (c) Au maps for the combined map shown in (a). (d) acSTEM line scan of a representative NP. Pt is dominant in the first 0.3 nm of the NP, which corresponds to the outermost shell. Beyond 0.3 nm, Pt and Au are mixed.

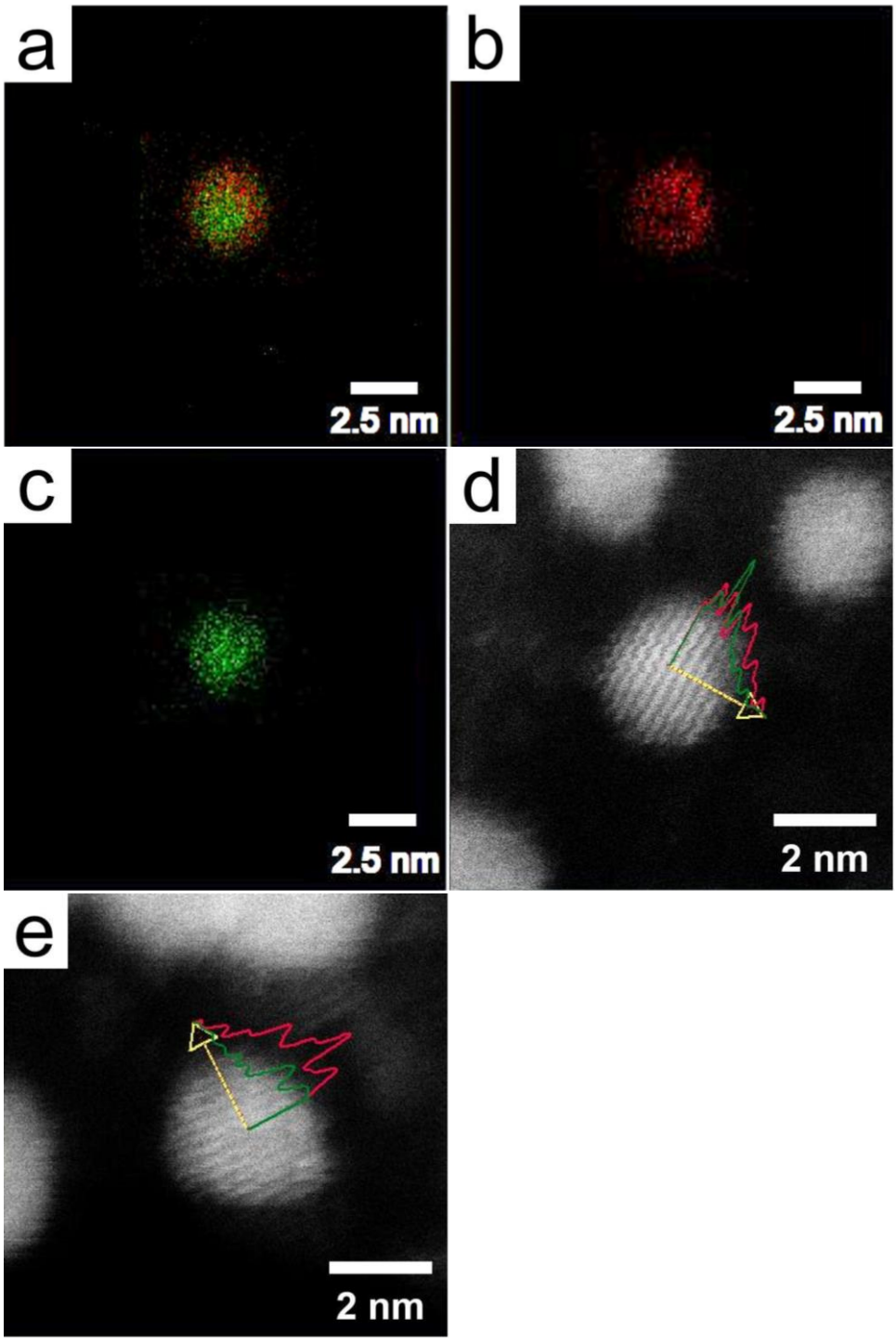

Figure 5.12

Figure 5.12 cont.

EDS for AuPt DENs prepared using 5 HT pulses. (a) Overlaid Pt (red) and Au (green) EDS maps. Individual (b) Pt and (c) Au maps of the combined map shown in frame (a). (d) acSTEM line scan of a representative NP. Pt dominates the first ~0.6 nm of the NP, which corresponds to the first two atomic columns (or MLs). This result is consistent with the XPS data (Figure 5.4). Beyond ~0.6 nm, Pt and Au appear to be mixed. (e) acSTEM line scan demonstrating variation in Pt shell thickness. Based on eight line scans, the average Pt thickness on either side of the Au NP core is 0.6±0.2 nm (adding ~1.2 nm of Pt to the original Au NP diameter).

low counts in Figure 5.9d prevent definitive conclusions. Direct line scans (as opposed to extraction from the map) over half of the NP provide higher counts and resolution, due to lower collection times and the greater number of points collected per nm. An atomic resolution line scan of the AuPt DENs synthesized via 1 HT pulse (Figure 5.10) suggests that alloying is localized in the NP shell. In other words, 1 HT pulse appears to lead to a surface alloy, which is consistent with our previous report for 1 HT pulse on Au_{147} DENs.[40]

An EDS map for the AuPt DENs synthesized using 3 HT pulses is shown in Figure 5.11. For the combined Au plus Pt map, it appears that Pt is localized in the NP shell (Figure 5.11a). Two cautionary points should be mentioned, however. First, if a Pt shell is present, it is not complete, as indicated by the presence of a few regions in the outermost layer of the NP that are dominated by Au atoms (green pixels). This result supports the electrochemical data discussed earlier, which showed that ~17% of the NP surface is Au. Second, although the combined Au plus Pt map looks core@shell-like, the individual Pt and Au maps (Figures 5.11b and 5.11c) indicate that this is an oversimplification. For example, Figure 5.11b reveals that Pt is present throughout the NP, while Figure 5.11c suggests more preference for Au in the NP core than

in the shell. Taken together, the EDS data suggest that the most appropriate structure is alloy core@Pt shell.

To gain further clarity about the 3 HT-pulse structure, atomic resolution line scans were obtained (Figure 5.11d). It should be noted that the oscillations in the Pt signals align roughly with the spacing between the atomic columns. As shown in Figure 5.11d, the first ~0.3 nm (first atomic column) of the line scan is predominantly Pt. This suggests the presence of a Pt shell in the outermost layer of the NP, given that an ~0.3 nm increase per side (~0.6 nm total) is expected (Table 5.3) upon the deposition of a single Pt ML on an ideal cuboctahedral Au_{147} NP. Beyond this point (>0.3 nm), the Pt EDS counts remain approximately constant, while the Au EDS counts increase. Approximately equal Pt and Au EDS counts in the center of the NP suggest that the NP core is alloyed. We reiterate, however, that our conclusions are limited by the small number of line scans that were collected (N=6 line scans for 3 HT pulses).

EDS maps for 5 HT pulses are shown in Figure 5.12a to 5.12c, and here a clearer core@shell-like structure is observed. An atomic resolution line scan (Figure 5.12d) confirms the presence of a Pt shell for 5 pulses. Specifically, Pt is present within the first two atomic columns, suggesting 2 ML of Pt in the shell. Beyond that point, Au and Pt are mixed. This result agrees with the number

of Pt MLs predicted by XPS for 5 HT pulses. We do note, however, that some heterogeneity in shell thickness is observed (e.g., Figure 5.12e). For the eight line scans obtained for the 5 HT-pulse NPs, the average Pt shell thickness is 0.6±0.2 nm on either side of the Au NP core (adding ~1.2 nm total diameter to the NP). Using the expected size changes predicted upon Pt deposition on Au_{147} NPs as a guide (Table 5.3), the Pt shell thickness estimated by EDS corresponds to ~1 to 3 ML of Pt.

To summarize, although a single HT pulse on Au_{147} DENs generates an alloy, as supported here and in our previous report,[40] EDS shows that the structure transforms to core@shell after 5 to 10 HT pulses. The fact that alloying is observed for 1 to 3 HT pulses, but that 10 pulses results in an Au@Pt core@shell structure is not completely surprising. It is well known that bulk Au and Pt are immiscible over a broad compositional range.[121] Although AuPt alloying can be facilitated by NP size effects,[40,122] previous theoretical simulations have shown that 2.7 to 4.3 nm AuPt NPs transition to a core@shell structure when atomic% Pt surpasses ~60%.[122] This prediction is consistent with the transition to a core@shell structure in the present report (5 to 10 HT pulses; Figure 5.4b).

Formic acid oxidation (FAO) electrocatalysis

The preceding sections showed that multilayer HT Pt electrodeposition onto Au_{147} DENs leads to different structures than on bulk Au[75–78] or star-shaped DARs.[79,80] The present section serves to compare the implications of these differences for FAO catalysis and to further validate the structural assignments made earlier.

The FAO experiments were carried out using Au_{147} DENs subjected to 1, 3, 5, and 10 HT pulses. Specifically, CVs were obtained by cycling each AuPt DEN-modified electrode 20 times between 0.01 and 1.26 V in N_2-purged 0.50 M H_2SO_4 containing 0.50 M formic acid. To be consistent with previous FAO studies obtained using HT-electrodeposited Pt MLs on bulk Au[76] and DARs,[79] we focus only on the forward-going scan of the 20th FAO CVs for each pulse sequence.

The two peaks in each forward-going scan of the FAO CVs for the AuPt DENs prepared using 1 to 10 HT pulses are shown in Figure 5.13a. These peaks correspond to the two major FAO pathways: (1) direct oxidation to CO_2 (eq 1), and (2) indirect oxidation via a CO intermediate (eq 2).[159–162]

$$HCOOH^* \rightarrow CO_2 + 2H^+ + 2e^- \quad \text{(eq 1)}$$

$$HCOOH^* \rightarrow CO^* + H_2O^* \rightarrow CO_2 + 2H^+ + 2e^- \quad \text{(eq 2)}$$

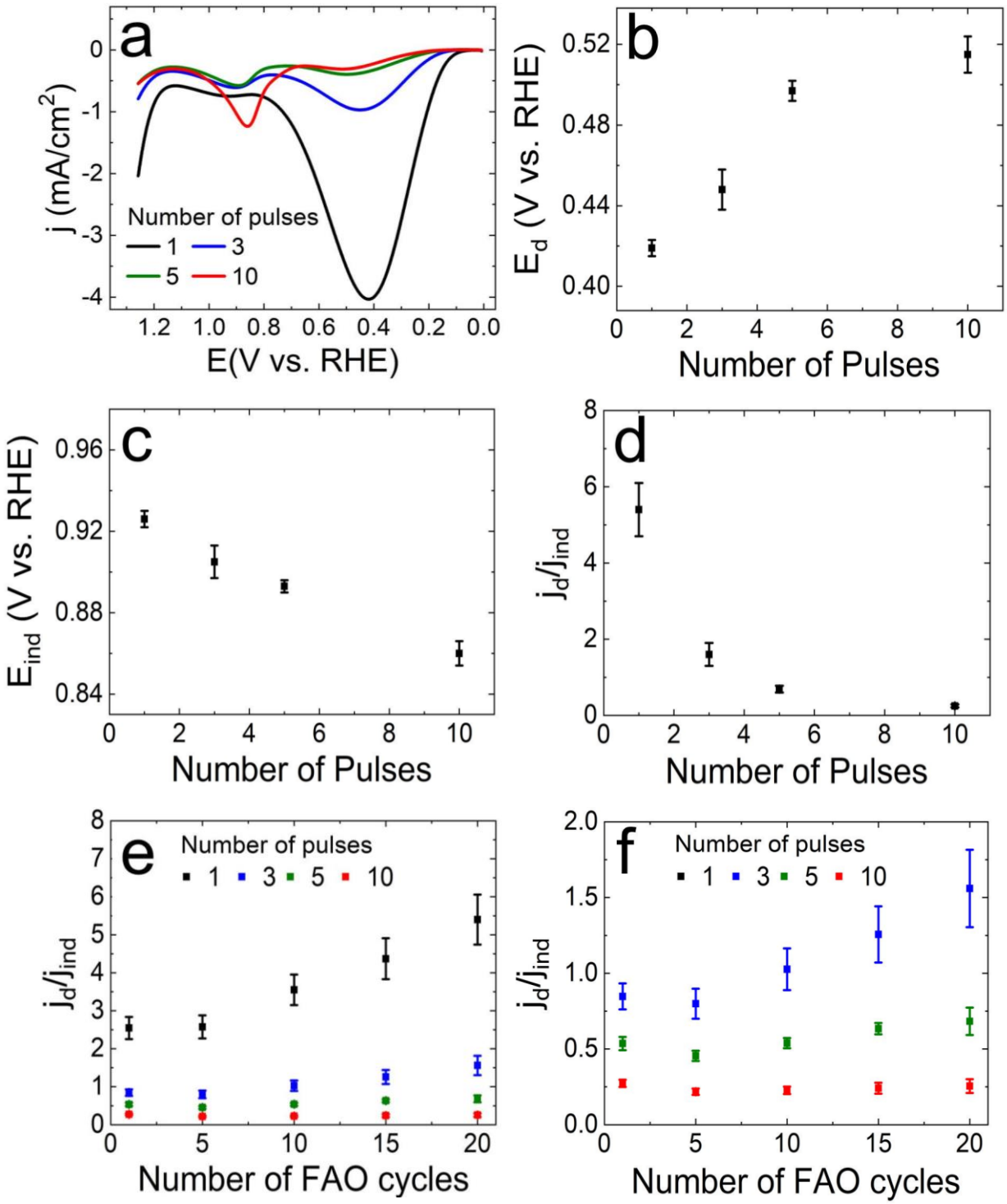
a
j (mA/cm²)
E(V vs. RHE)
Number of pulses
1
3
5
10
b
E_d (V vs. RHE)
Number of Pulses
c
E_ind (V vs. RHE)
Number of Pulses
d
j_d/j_ind
Number of Pulses
e
j_d/j_ind
Number of FAO cycles
Number of pulses
1
3
5
10
f
j_d/j_ind
Number of FAO cycles
Number of pulses
1
3
5
10

Figure 5.13

Figure 5.13 cont.

(a) FAO scans for the AuPt DENs synthesized via HT Pt electrodeposition onto Au_{147} DENs as a function of pulse number. Just the forward-going scan of the 20th FAO CV is shown. Peak positions for the (b) direct (E_d) and (c) indirect (E_{ind}) FAO pathways as a function of the number of HT Pt electrodeposition pulses. (d) The ratio of the current densities associated with the direct (j_d) and indirect (j_{ind}) FAO peaks. (e) The effects of FAO cycling on the j_d/j_{ind} ratios. (f) Expanded view of (e) for just 1 to 5 HT pulses. In all cases the electrolyte was N_2-purged 0.50 M H_2SO_4 containing 0.50 M formic acid. The scan rate was 10 mV/s.

The peak potentials for the direct pathway for the AuPt DENs (E_d, Table 5.4; larger peak in the range ~0.42 to 0.52 V in Figure 5a) are negative of E_d for bulk Pt (~0.57 to 0.59 V)[16,76] and for Pt-only DENs (~0.58 V)[16] regardless of the number of HT pulses. As shown in Figure 5.13b, however, E_d for the AuPt DENs more closely approaches that of monometallic Pt as the number of pulses increases. This suggests that the surface of the NPs becomes increasingly Pt-like with each additional HT pulse.

Figure 5.13c shows the trend in the peak potentials for the indirect pathway (E_{ind}) as a function of pulse number. For the AuPt DENs prepared using 1 to 3 HT pulses, E_{ind} (Table 5.4; 0.905 to 0.926 V) is positive of bulk Pt (~0.85 V).[16] However, after 3 HT pulses, E_{ind} (0.905±0.008 V) is close to that for Pt DENs (~0.91 V).[16] This result supports the surface characterization discussed earlier (Table 5.1), which showed nearly complete Pt coverage (θ_{Pt}=0.83±0.02) after 3 HT pulses. Comparison of Figures 5.13b and 5.13c shows that the position of E_{ind} is less sensitive to HT pulse number than E_d. Furthermore, the shifts in E_{ind} for the AuPt DENs relative to the corresponding values for bulk Pt[16,76] and Pt DENs[16] are less pronounced than for E_d. These results are consistent with a previous report showing similar trends for AuPt DENs prepared by Pb UPD/Pt GE.[16]

Pulses	E_d (V)	E_{ind} (V)	j_d/j_{ind}
1	0.419(4)	0.926(4)	5.4(7)
3	0.448(1)	0.905(8)	1.6(3)
5	0.497(5)	0.893(3)	0.69(9)
10	0.515(9)	0.860(6)	0.25(4)

Table 5.4

FAO-related parameters as a function of the number of HT Pt electrodeposition pulses (1 to 10) for the forward-going scan of the 20th FAO CV. E_d and E_{ind} are the potentials of the peaks associated with the direct and indirect FAO pathways, respectively. All potentials are reported relative to RHE. The ratio of the current densities for the direct (j_d) and indirect (j_{ind}) FAO peaks is represented by j_d/j_{ind}. Current densities are normalized to the Pt ECSA values in Table 5.5.

The trends in FAO peak potentials as a function of HT pulse number (Figures 5.13b and 5.13c) are similar to the corresponding trends for HT-electrodeposited Pt MLs on bulk Au.[76] However, in the latter case, the bulk Pt value for E_d was reached after 5 HT pulses.[76] For the AuPt DENs reported here, even after 10 HT pulses (2 to 3 ML of Pt), E_d (0.515±0.009 V) remains negative of that for bulk Pt[16,76] and Pt DENs.[16] This difference highlights the structural distinctions between HT-electrodeposited Pt MLs on small Au NPs and bulk Au.

In addition to shifts in FAO peak potentials, FAO activity changes as a function of HT pulse number. A recent mechanistic study showed that indirect FAO requires ensembles containing ≥2 adjacent Pt atoms to separately bind CO and OH dissociated from the C-OH bond of carboxylate.[160] Direct FAO, on the other hand, requires just a single Pt atom.[56,162,163] Thus, in cases with sufficiently large Pt ensembles, the ratio of the current densities for the direct (j_d) and indirect (j_{ind}) peaks (e.g., j_d/j_{ind}) reflects the relative proportions of ensembles containing multiple Pt atoms and single Pt atoms.

The AuPt DENs prepared with a single HT pulse exhibit the highest activity (highest j_d) and the greatest promotion of the direct pathway (highest j_d/j_{ind}) (Figure 5.13d). As the HT pulse number increases, both j_d and j_d/j_{ind} decrease in the direction of

the corresponding value for bulk Pt.[76] Figure 5d shows that the rate of change in j_d/j_{ind} as a function of pulse number approaches zero after ~5 HT pulses. Accordingly, the catalytic data supports the conclusion drawn from the ECSA ratios and XPS (Figure 5.5), that almost 1 Pt ML (Θ_{Pt}=0.83 to 0.91 and $\frac{d\theta_{Pt}}{dp}$~0) is achieved after 3 to 5 HT pulses. These results can be understood using the framework of the ensemble effects expected for each pulse number. Table 5.1 shows that the initial number of surface Au atoms is small for 3 HT pulses ($N_{Au,surf}$ = 16), and becomes negligible thereafter ($N_{Au,surf}$ = 3 to 8 for 5 to 10 HT pulses). Therefore, due to the scarcity of surface Au atoms, the influence of ensemble effects on FAO is expected to be minimal after 3 to 5 pulses.[160] In other words, the trends in j_d/j_{ind} as a function of HT pulse number (Figure 5.13d) are in accord with the trends in $N_{Au,surf}$ (Table 5.1).

To summarize, the individual j_d/j_{ind} ratios for AuPt DENs prepared using 1 to 10 HT pulses (Table 5.4) are ~5 to 110x higher than for FAO on bulk polycrystalline Pt under similar electrochemical conditions.[76] Likewise, j_d/j_{ind} for the AuPt DENs is ~2-, 5-, and 7-fold greater than for HT Pt electrodeposition onto bulk Au for 1, 3, and 5 HT pulses, respectively.[76] This reflects the fact that there is not as close of a correspondence between the number of HT pulses and the number of Pt MLs on Au_{147} DENs as

there is for bulk Au. For example, for the AuPt DENs prepared using 10 HT pulses, j_d/j_{ind} (0.25±0.04) is closest to the corresponding bulk Au results for just 3 HT pulses (j_d/j_{ind} ~0.3).[76]

Further corroboration of the number of Pt MLs determined in the previous sections can be gained by comparing the forward-going scans of the 20th FAO CVs (Figure 5.13a) with the forward-going scans of the first FAO CVs (Figure 5.14a). Comparison of the values of Θ_{Pt} before (Table 5.1) and after (Table 5.5) recording 20 FAO CVs, shows that Θ_{Pt} decreases upon FAO cycling. The magnitudes of the associated changes in Θ_{Pt} ($\Delta\Theta_{Pt}$) are listed in Table 5.5. A decrease in Θ_{Pt} upon extended FAO cycling has previously been attributed to Pt dissolution and/or structural rearrangement via alloying.[76,154] The $\Delta\Theta_{Pt}$ values in Table 5.5 agree well with those calculated (~0.1 to 0.3 ML for the AuPt DENs) based on previous Pt dissolution studies that employed similar electrochemical conditions.[76,164]

Whether dissolution or alloying, the surface Pt atoms directly above or adjacent to Au atoms are the most vulnerable to loss. Accordingly, a decrease in Θ_{Pt} is anticipated for AuPt DENs having ≤1 ML of Pt (3 to 5 HT pulses) but not Pt multilayers (5 to 10 HT pulses). Table 5.5 shows that the values of $\Delta\Theta_{Pt}$ observed for 1 to 20 FAO cycles are consistent with these hypotheses. Specifically, $\Delta\Theta_{Pt}$ is significant (0.23 to 0.30) for 1 to 5 HT

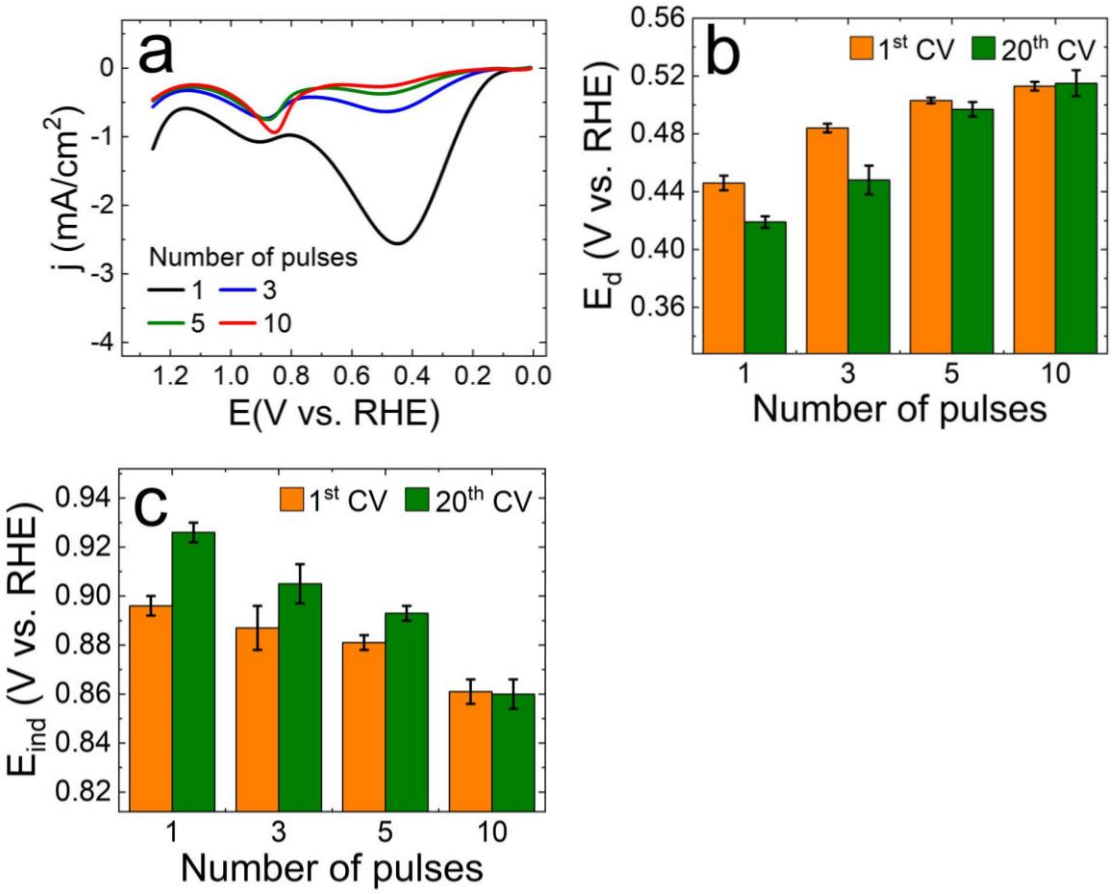

Figure 5.14

Comparison of FAO results for the forward-going scans of the first and 20th FAO CVs. (a) The forward-going scan of the first FAO CV. Comparison of (b) E_d and (c) (E_{ind}) for the forward-going scans of the first and 20th FAO CVs.

Pulses	θ_{Pt}	$\Delta\theta_{Pt}$	Au_f ECSA	Pt ECSA	$ECSA_{tot}$
1	0.31(3)	0.26(3)	0.18(1)	0.097(8)	0.28(1)
3	0.53(5)	0.30(4)	0.117(6)	0.24(3)	0.36(4)
5	0.68(1)	0.23(1)	0.084(6)	0.43(8)	0.51(8)
10	0.94(1)	0.03(1)	0.016(2)	0.7(2)	0.7(2)

Table 5.5

Electrochemical surface characterization after 20 FAO cycles. Pt coverage (θ_{Pt}) was calculated as (1-(Au_f ECSA/Au_i ECSA)), using the Au_f ECSA values after catalysis (*vide supra*) and the Au_i ECSA values from Table 5.2. The $\Delta\theta_{Pt}$ represents the magnitude of the change in θ_{Pt} after catalysis. In other words, it is the difference in the values of θ_{Pt} before catalysis (Table 5.1) and after the 20th FAO cycle (*vide supra*). The Au_f and Pt ECSAs below were determined by recording surface characterization CVs after catalysis and using the same calculation method as in Table 5.2. The units for all of the ECSAs below are cm^2. Surface characterization was performed in N_2-purged 0.10 M $HClO_4$, using the same scan parameters as the CVs in Figure 5.2a.

pulses, but it is negligible for 10 HT pulses (0.03±0.01). These results help confirm the conclusion from the previous sections that 3 to 5 HT pulses are required to completely cover the Au_{147} core with Pt.

The loss in surface Pt observed after 20 FAO cycles enhances ensemble effects for the thinnest Pt layers by enriching the number of surface ensembles that contain both Au and Pt. As mentioned earlier, multiple effects (ensemble, ligand, and strain) are present for <1 ML of Pt on Au.[78,165] For ≥1 ML of Pt, however, strain dominates due to uniform surface ensembles (all Pt) and a progressive lessening of the influence of heteroatoms in atomic sub-layers.[76,78] Thus, comparison of the forward-going scans for the first and 20th FAO CVs aids deconvolution of competing electrocatalytic factors.

Figures 5.13e and 5.13f show that j_d/j_{ind} doubles in going from 1 to 20 FAO cycles for the AuPt DENs having the highest values of $\Delta\theta_{Pt}$ (1 to 3 HT pulses, black and blue data points, respectively; Table 5.5). In contrast, the AuPt DENs with negligible values of $\Delta\theta_{Pt}$ (5 to 10 HT pulses, green and red data points, respectively) show little improvement in j_d/j_{ind}. The correspondence between altered catalytic activity and $\Delta\theta_{Pt}$ confirms the principal role of ensemble effects in catalytic improvement for the FAO using AuPt DENs. Additionally, Figures 5.14b and 5.14c reveal that E_d and E_{ind}

shift further away from the corresponding values for bulk Pt[16,76] and Pt DENs[16] for 1 to 3 HT pulses (≤1 ML of Pt) after 20 FAO cycles. For 5 (1 to 2 ML of Pt) and 10 HT pulses (2 to 3 ML of Pt), peak positions remain approximately the same between one and 20 FAO cycles.

In summary, significant changes in j_d/j_{ind}, E_d, and E_{ind} between one and 20 FAO cycles are only observed from 1 to 5 HT pulses. These results are consistent with conclusions about the surface and atomic compositions determined from electrochemistry and XPS (Figure 5.5): ~1 ML of Pt is electrodeposited by 3 to 5 HT pulses and multilayers are electrodeposited for 5 to 10 HT pulses. We reiterate that this scenario is quite different from the results obtained for HT Pt electrodeposition onto bulk Au[75–78] and DARs.[79,80]

5.5. Summary and Conclusions

In this report, we have demonstrated several important points relating to the HT Pt electrodeposition process. First, the application of multiple HT Pt pulses to electrodeposit Pt multilayers leads to significantly different results for small (~1 to 2 nm) Au NPs as compared to bulk Au[75–78] and star-shaped DARs.[79,80] Specifically, the number of HT pulses (3 to 5) required to electrodeposit nearly one complete Pt ML is higher than for bulk Au (1 to 2)[75–78] but lower than for DARs (15).[79,80] Similarly,

the threshold number of HT pulses (5 to 10) necessary for Pt multilayer electrodeposition onto small Au NPs also diverges from that of bulk Au (2 to 3)[75–78] and DARs (30).[79,80] Thus, we find that HT Pt electrodeposition is highly sensitive to the geometry of the substrate.

Second, our results suggest that the HT method could serve as a viable alternative to UPD/Pt GE for Pt ML electrodeposition on small Au NPs. Importantly, the HT method avoids complications associated with the latter method such as residual UPD metal and the necessity of using multiple deposition solutions.[22–26] Furthermore, the HT method is rapid, requiring only ~90 to 150 s (3 to 5 pulses) to electrodeposit ~1 Pt ML onto Au NPs.

Third, we showed that application of multiple HT pulses (1 to 10) on Au NPs can be used to tune their catalytic activity for the FAO. The ratio of the current densities for the direct and indirect FAO processes are ~5- to 110-fold greater than for bulk Pt and also substantially higher than for HT Pt electrodeposition onto other types of Au substrates.[76]

The findings reported here have several possible extensions. First, although our results suggested that the HT method depends on geometry, NP size effects are likely also important. Future studies, such as varying the size and geometry of the Au NP substrate, will be aimed at deconvolving these two

factors. Second, multilayer shells containing ≤3 MLs of Pt on the Au NPs were studied in this first report. Examining Pt multilayers having a greater number of MLs could help elucidate the boundary between AuPt NP and bulk Pt behavior. Furthermore, the FAO is more heavily influenced by ensemble effects than strain.[76] Studying a reaction that is more sensitive to the effects of strain (e.g., the ORR)[78] could provide further insight into determining the NP/bulk boundary in these materials. Finally, application of HT Pt multilayer electrodeposition to NPs with different core metals (monometallic and/or bimetallic) could broaden the scope of the results presented here.

Chapter 6: Conclusions and outlook

In this dissertation, we have investigated three techniques for electrodepositing Pt MLs onto small (~1-2 nm) Au NPs: the HT method, Cu UPD/Pt GE, and Pb UPD/Pt GE. We then extended this work to electrodeposit multiple Pt layers via the HT method. The results from these studies have led to the following three conclusions.

First, we have shown that electrodeposition of Pt proceeds differently on small Au NPs than it does on bulk Au. The HT method, Cu UPD/Pt GE, and Pb UPD/Pt GE all yield Pt MLs when applied to bulk Au. When we applied these techniques to ~1.6 nm Au NPs, however, an alloy structure was produced more frequently than a core@shell structure. Specifically, only one of the three techniques (Cu UPD/Pt GE) reliably provided a core@shell structure. With that being said, although the HT method initially conferred an alloy structure, a core@shell structure was still able to be obtained with extra effort (additional HT pulses). Structural differences derived from using a single HT Pt electrodeposition pulse vs. multiple HT pulses were found to considerably impact FAO electrocatalysis.

Second, our results have shed light on some of the factors that govern AuPt NP structure for each particular Pt electrodeposition technique. For example, geometry was shown to be a critical factor for the HT method. DFT-MD simulations suggested

that differentiation in the AuPt structures formed for bulk Au and small Au NPs originated from differences in surface flexibilities (e.g., rigid vs. curved). The number of HT pulses needed to deposit a Pt ML on Au_{147} DENs was also found to be geometry dependent. In particular, it was substantially higher than planar (bulk) Au, but significantly lower than star-shaped Au rods. Similar results were found for HT preparation of Pt multilayers.

For UPD/Pt GE, on the other hand, AuPt NP structure was found to depend of the choice of UPD metal. Pb UPD/Pt GE led to an alloy structure, whereas Cu UPD/Pt GE provided a core@shell structure. The combination of electrochemical methods and rigorous DFT-MD simulations (before UPD, during UPD, and after GE) led to the development of a more detailed mechanism for UPD on small NPs than we have previously described.

Third, our results have demonstrated the interdependence of experiment and theory for detailed characterization of small NPs. There are fewer reliable experimental characterization techniques for small NPs than for macroscopic systems. Theoretical calculations can help bridge this gap. The addition of theoretical calculations in the work presented here enriched mechanistic understanding of and helped validate the AuPt NP structures that formed for each electrodeposition technique.

There are several probable extensions of the research presented in this dissertation. For example, Pt electrodeposition was applied to just one geometry (cuboctahedral), one NP size (147 atoms), and one core metal (Au). Therefore, future studies could be focused on the applicability of our findings to other geometries, NP sizes, and core metals. Additionally, we have not yet explored the use of UPD metals other than Cu and Pb for UPD/Pt GE. Given the demonstrated dependence of this technique on the identity of the UPD metal, analysis with other metals could expand the reach of our work. Finally, only a single electrocatalytic reaction (FAO) was analyzed. In the future, the AuPt structures obtained for each Pt electrodeposition technique could be used to tailor electrocatalytic activity for other relevant reactions.

References

(1) Anderson, R. M.; Yancey, D. F.; Zhang, L.; Chill, S. T.; Henkelman, G.; Crooks, R. M. A Theoretical and Experimental Approach for Correlating Nanoparticle Structure and Electrocatalytic Activity. *Acc. Chem. Res.* **2015**, *48*, 1351–1357.

(2) Myers, V. S.; Weir, M. G.; Carino, E. V.; Yancey, D. F.; Pande, S.; Crooks, R. M. Dendrimer-Encapsulated Nanoparticles: New Synthetic and Characterization Methods and Catalytic Applications. *Chem. Sci.* **2011**, *2*, 1632–1646.

(3) Wilson, O. M.; Scott, R. W. J.; Garcia-Martinez, J. C.; Crooks, R. M. Synthesis, Characterization, and Structure-Selective Extraction of 1-3 Nm Diameter AuAg Dendrimer-Encapsulated Bimetallic Nanoparticles. *J. Am. Chem. Soc.* **2005**, *127*, 1015–1024.

(4) Niu, Y.; Crooks, R. M. Preparation of Dendrimer-Encapsulated Metal Nanoparticles Using Organic Solvents. *Chem. Mater.* **2003**, *15*, 3463–3467.

(5) Zhang, L.; Henkelman, G. Computational Design of Alloy-Core@Shell Metal Nanoparticle Catalysts. *ACS Catal.* **2015**, *5*, 655–660.

(6) Zhang, Y.; Hsieh, Y.-C.; Volkov, V.; Su, D.; An, W.; Si, R.; Zhu, Y.; Liu, P.; Wang, J. X.; Adzic, R. R. High Performance Pt Monolayer Catalysts Produced via Core-Catalyzed Coating in Ethanol. *ACS Catal.* **2014**, *4*, 738–742.

(7) Sasaki, K.; Naohara, H.; Cai, Y.; Choi, Y. M.; Liu, P.; Vukmirovic, M. B.; Wang, J. X.; Adzic, R. R. Core-Protected Platinum Monolayer Shell High-Stability Electrocatalysts for Fuel-Cell Cathodes. *Angew. Chem. Int. Ed.* **2010**, *49*, 8602–8607.

(8) Dai, Y.; Chen, S. Oxygen Reduction Electrocatalyst of Pt on Au Nanoparticles through Spontaneous Deposition. *ACS Appl. Mater. Interfaces* **2015**, *7*, 823–829.

(9) Xie, S.; Choi, S.-I.; Lu, N.; Roling, L. T.; Herron, J. A.; Zhang, L.; Park, J.; Wang, J.; Kim, M. J.; Xie, Z.; et al. Atomic Layer-by-Layer Deposition of Pt on Pd Nanocubes for Catalysts with Enhanced Activity and Durability toward Oxygen Reduction. *Nano Lett.* **2014**, *14*, 3570–3576.

(10) Brimaud, S.; Behm, R. J. Electrodeposition of a Pt Monolayer Film: Using Kinetic Limitations for Atomic Layer Epitaxy. *J. Am. Chem. Soc.* **2013**, *135*, 11716–11719.

(11) Zhu, S.; Yue, J.; Qin, X.; Wei, Z.; Liang, Z.; Adzic, R. R.; Brankovic, S. R.; Du, Z.; Shao, M. The Role of Citric

Acid in Perfecting Platinum Monolayer on Palladium Nanoparticles during the Surface Limited Redox Replacement Reaction. *J. Electrochem. Soc.* **2016**, *163* (12), D3040–D3046.

(12) Luo, L.; Zhang, L.; Henkelman, G.; Crooks, R. M. Unusual Activity Trend for CO Oxidation on PdxAu140-X@Pt Core@Shell Nanoparticle Electrocatalysts. *J. Phys. Chem. Lett.* **2015**, *6*, 2562–2568.

(13) Lapp, A. S.; Duan, Z.; Henkelman, G.; Crooks, R. M. Combined Experimental and Theoretical Study of the Structure of AuPt Nanoparticles Prepared by Galvanic Exchange. *Langmuir* **2019**, *35*, 16496–16507.

(14) Yancey, D. F.; Carino, E. V.; Crooks, R. M. Electrochemical Synthesis and Electrocatalytic Properties of Au@Pt Dendrimer-Encapsulated Nanoparticles. *J. Am. Chem. Soc.* **2010**, *132*, 10988–10989.

(15) Yancey, D. F.; Zhang, L.; Crooks, R. M.; Henkelman, G. Au@Pt Dendrimer Encapsulated Nanoparticles as Model Electrocatalysts for Comparison of Experiment and Theory. *Chem. Sci.* **2012**, *3*, 1033–1040.

(16) Iyyamperumal, R.; Zhang, L.; Henkelman, G.; Crooks, R. M. Efficient Electrocatalytic Oxidation of Formic Acid Using Au@Pt Dendrimer-Encapsulated Nanoparticles. *J. Am. Chem.*

Soc. **2013**, *135*, 5521–5524.

(17) Yu, Y.; Hu, Y.; Liu, X.; Deng, W.; Wang, X. The Study of Pt@Au Electrocatalyst Based on Cu Underpotential Deposition and Pt Redox Replacement. *Electrochim. Acta* **2009**, *54* (11), 3092–3097.

(18) Peng, L.; Gan, L.; Wei, Y.; Yang, H.; Li, J.; Du, H.; Kang, F. Pt Submonolayers on Au Nanoparticles: Coverage-Dependent Atomic Structures and Electrocatalytic Stability on Methanol Oxidation. *J. Phys. Chem. C* **2016**, *120* (50), 28664–28671.

(19) Brankovic, S. R.; Wang, J. X.; Adzic, R. R. Metal Monolayer Deposition by Replacement of Metal Adlayers on Electrode Surfaces. *Surf. Sci.* **2001**, *474*, L173–L179.

(20) Gokcen, D.; Bae, S.-E.; Brankovic, S. R. Reaction Kinetics of Metal Deposition via Surface Limited Red-Ox Replacement of Underpotentially Deposited Metal Monolayers. *Electrochim. Acta* **2011**, *56*, 5545–5553.

(21) Fayette, M.; Liu, Y.; Bertrand, D.; Nutariya, J.; Vasiljevic, N.; Dimitrov, N. From Au to Pt via Surface Limited Redox Replacement of Pb UPD in One-Cell Configuration. *Langmuir* **2011**, *27*, 5650–5658.

(22) Dimitrov, N. Recent Advances in the Growth of Metals,

Alloys, and Multilayers by Surface Limited Redox Replacement (SLRR) Based Approaches. *Electrochim. Acta* **2016**, *209*, 599–622.

(23) Nutariya, J.; Fayette, M.; Dimitrov, N.; Vasiljevic, N. Growth of Pt by Surface Limited Redox Replacement of Underpotentially Deposited Hydrogen. *Electrochim. Acta* **2013**, *112*, 813–823.

(24) Fayette, M.; Liu, Y.; Bertrand, D.; Nutariya, J.; Vasiljevic, N.; Dimitrov, N. From Au to Pt via Surface Limited Redox Replacement of Pb UPD in One-Cell Configuration. *Langmuir* **2011**, *27* (9), 5650–5658.

(25) Luo, L.; Zhang, L.; Duan, Z.; Lapp, A. S.; Henkelman, G.; Crooks, R. M. Efficient CO Oxidation Using Dendrimer-Encapsulated Pt Nanoparticles Activated with <2% Cu Surface Atoms. *ACS Nano* **2016**, *10*, 8760–8769.

(26) Kim, Y.-G.; Kim, J. Y.; Vairavapandian, D.; Stickney, J. L. Platinum Nanofilm Formation by EC-ALE via Redox Replacement of UPD Copper: Studies Using in-Situ Scanning Tunneling Microscopy. *J. Phys. Chem. B* **2006**, *110*, 17998–18006.

(27) Buhleier, E.; Wehner, W.; Vögtle, F. “Cascade”- and “Nonskid-Chain-like” Synthesis of Molecular Cavity Topologies. *Synthesis* **1978**, *2*, 155–158.

(28) Scott, R. W. J.; Wilson, O. M.; Crooks, R. M. Synthesis, Characterization, and Applications of Dendrimer-Encapsulated Nanoparticles. *J. Phys. Chem. B* **2005**, *109*, 692–704.

(29) Astruc, D.; Wang, D.; Deraedt, C.; Liang, L.; Ciganda, R.; Ruiz, J. Catalysis Inside Dendrimers. *Synthesis* **2015**, *47*, 2017–2031.

(30) Bronstein, L. M.; Shifrina, Z. B. Dendrimers as Encapsulating, Stabilization, or Directing Agents for Inorganic Nanoparticles. *Chem. Rev.* **2011**, *111*, 5301–5344.

(31) Ye, R.; Zhukhovitskiy, A. V.; Deraedt, C. V.; Toste, F. D.; Somorjai, G. A. Supported Dendrimer-Encapsulated Metal Clusters: Toward Heterogenizing Homogeneous Catalysts. *Acc. Chem. Res.* **2017**, *50*, 1894–1901.

(32) Trindell, J. A.; Duan, Z.; Henkelman, G.; Crooks, R. M. Well-Defined Nanoparticle Electrocatalysts for the Refinement of Theory. *Chem. Rev.* **2020**, *120*, 814–850.

(33) Zhao, M.; Sun, L.; Crooks, R. M. Preparation of Cu Nanoclusters within Dendrimer Templates. *J. Am. Chem. Soc.* **1998**, *120*, 4877–4878.

(34) Luo, L.; Duan, Z.; Li, H.; Kim, J.; Henkelman, G.; Crooks, R. M. Tunability of the Adsorbate Binding on Bimetallic

Alloy Nanoparticles for the Optimization of Catalytic Hydrogenation. *J. Am. Chem. Soc.* **2017**, *139*, 5538–5546.

(35) Ostojic, N.; Duan, Z.; Galyamova, A.; Henkelman, G.; Crooks, R. M. Electrocatalytic Study of the Oxygen Reduction Reaction at Gold Nanoparticles in the Absence and Presence of Interactions with SnOx Supports. *J. Am. Chem. Soc.* **2018**, *140*, 13775–13785.

(36) Lapp, A. S.; Crooks, R. M. Multilayer Electrodeposition of Pt onto 1-2 nm Au Nanoparticles Using a Hydride-Termination Approach. *Nanoscale* **2020**, *submitted*.

(37) Luo, L.; Zhang, L.; Duan, Z.; Lapp, A. S.; Henkelman, G.; Crooks, R. M. Efficient CO Oxidation Using Dendrimer-Encapsulated Pt Nanoparticles Activated with <2% Cu Surface Atoms. *ACS Nano* **2016**, *10*, 8760–8769.

(38) Trindell, J. A.; Clausmeyer, J.; Crooks, R. M. Size Stability and H2/CO Selectivity for Au Nanoparticles during Electrocatalytic CO2 Reduction. *J. Am. Chem. Soc.* **2017**, *139*, 16161–16167.

(39) Glasner, D.; Frenkel, A. I. Geometrical Characteristics of Regular Polyhedra: Application to EXAFS Studies of Nanoclusters. *AIP Conf. Prof.* **2007**, *882*, 746–748.

(40) Lapp, A. S.; Duan, Z.; Marcella, N.; Luo, L.; Genc, A.; Ringnalda, J.; Frenkel, A. I.; Henkelman, G.; Crooks, R. M. Experimental and Theoretical Structural Investigation of AuPt Nanoparticles Synthesized Using a Direct Electrochemical Method. *J. Am. Chem. Soc.* **2018**, *140*, 6249–6259.

(41) Luo, L.; Timoshenko, J.; Lapp, A. S.; Frenkel, A. I.; Crooks, R. M. Structural Characterization of Rh and RhAu Dendrimer-Encapsulated Nanoparticles. *Langmuir* **2017**, *33*, 12434–12442.

(42) Chaudhuri, R. G.; Paria, S. Core/Shell Nanoparticles: Classes, Properties, Synthesis Mechanisms, Characterization, and Applications. *Chem. Rev.* **2012**, *112*, 2373–2433.

(43) Cuenya, B. R. Synthesis and Catalytic Properties of Metal Nanoparticles: Size, Shape, Support, Composition, and Oxidation State Effects. *Thin Solid Films* **2010**, *518*, 3127–3150.

(44) Gates, A. T.; Nettleton, E. G.; Myers, V. S.; Crooks, R. M. Synthesis and Characterization of NiSn Dendrimer-Encapsulated Nanoparticles. *Langmuir* **2010**, *26*, 12994–12999.

(45) Carino, E. V.; Crooks, R. M. Characterization of Pt@Cu Core@Shell Dendrimer-Encapsulated Nanoparticles Synthesized

by Cu Underpotential Deposition. *Langmuir* **2011**, *27*, 4227–4235.

(46) Carino, E. V; Kim, H. Y.; Henkelman, G.; Crooks, R. M. Site-Selective Cu Deposition on Pt Dendrimer-Encapsulated Nanoparticles: Correlation of Theory and Experiment. *J. Am. Chem. Soc.* **2012**, *134*, 4153–4162.

(47) Herrero, E.; Buller, L. J.; Abruna, H. D. Underpotential Deposition at Single Crystal Surfaces of Au, Pt, Ag, and Other Materials. *Chem. Rev.* **2001**, *101*, 1897–1930.

(48) Herzog, G.; Arrigan, D. W. M. Determination of Trace Metals by Underpotential Deposition-Stripping Voltammetry at Solid Electrodes. *Tr. Anal. Chem.* **2005**, *24*, 208–217.

(49) Leiva, E. Recent Developments in the Theory of Metal UPD. *Electrochim. Acta* **1996**, *41*, 2185–2206.

(50) Waibel, H.-F.; Kleinert, M.; Kibler, L. A.; Kolb, D. M. Initial Stages of Pt Deposition on Au(111) and Au(100). *Electrochim. Acta* **2002**, 1461–1467.

(51) Hu, J.; Wu, L.; Kuttiyiel, K. A.; Goodman, K. R.; Zhang, C.; Zhu, Y.; Vukmirovic, M. B.; White, M. G.; Sasaki, K.; Adzic, R. R. Increasing Stability and Activity of Core-Shell Catalysts by Preferential Segregation of Oxide on Edges and

Vertexes: Oxygen Reduction on Ti-Au@Pt/C. *J. Am. Chem. Soc.* **2016**, *138*, 9294–9300.

(52) Sasaki, K.; Naohara, H.; Choi, Y.; Cai, Y.; Chen, W.-F.; Liu, P.; Adzic, R. R. Highly Stable Pt Monolayer on PdAu Nanoparticle Electrocatalysts for the Oxygen Reduction Reaction. *Nat. Commun.* **2012**, *3*, 2124.

(53) Adzic, R. R.; Zhang, J.; Sasaki, K.; Vukmirovic, M. B.; Shao, M.; Wang, J. X.; Nilekar, A. U.; Mavrikakis, M.; Valerio, J. A.; Uribe, F. Platinum Monolayer Fuel Cell Electrocatalysts. *Top. Catal.* **2007**, *46*, 249–262.

(54) Suntivich, J.; Xu, Z.; Carlton, C. E.; Kim, J.; Han, B.; Lee, S. W.; Bonnet, N.; Marzari, N.; Allard, L. F.; Gasteiger, H. A.; et al. Surface Composition Tuning of Au-Pt Bimetallic Nanoparticles for Enhanced Carbon Monoxide and Methanol Electro-Oxidation. *J. Am. Chem. Soc.* **2013**, *135*, 7985–7991.

(55) Tang, H.; Chen, J. H.; Wang, M. Y.; Nie, L. H.; Kuang, Y. F.; Yao, S. Z. Controlled Synthesis of Platinum Catalysts on Au Nanoparticles and Their Electrocatalytic Property for Methanol Oxidation. *Appl. Catal. A* **2004**, *275*, 43–48.

(56) Duchesne, P. N.; Li, Z. Y.; Deming, C. P.; Fung, V.; Zhao, X.; Yuan, J.; Regier, T.; Aldalbahi, A.; Almarhoon, Z.;

Chen, S.; et al. Golden Single-Atomic-Site Platinum Electrocatalysts. *Nat. Mater.* **2018**, *17*, 1033–1039.

(57) Zhang, L.; Iyyamperumal, R.; Yancey, D. F.; Crooks, R. M.; Henkelman, G. Design of Pt-Shell Nanoparticles with Alloy Cores for the Oxygen Reduction Reaction. *ACS Nano* **2013**, *7*, 9168–9172.

(58) Gokcen, D.; Bae, S. E.; Brankovic, S. R. Stoichiometry of Pt Submonolayer Deposition via Surface-Limited Redox Replacement Reaction. *J. Electrochem. Soc.* **2010**, *157*, D582–D587.

(59) Al Amri, Z.; Mercer, M. P.; Vasiljevic, N. Surface Limited Redox Replacement Deposition of Platinum Ultrathin Films on Gold: Thickness and Structure Dependent Activity towards the Carbon Monoxide and Formic Acid Oxidation Reactions. *Electrochim. Acta* **2016**, *210*, 520–529.

(60) Romero-Romo, M.; Aldana-Gonzalez, J.; Botello, L. E.; Montes de Oca, M. G.; Ramirez-Silva, M. T.; Corona-Avendano, S.; Palomar-Pardave, M. Electrochemical Nucleation and Growth of Cu onto Au Nanoparticles Supported on a Si(111) Wafer Electrode. *J. Electroanal. Chem.* **2017**, *791*, 1–7.

(61) Hernandez, J.; Solla-Gullon, J.; Herrero, E.; Aldaz, A.; Feliu, J. M. Characterization of the Surface Structure of

Gold Nanoparticles and Nanorods Using Structure Sensitive Reactions. *J. Phys. Chem. B* **2005**, *109*, 12651–12654.

(62) Hebie, S.; Kokoh, K. B.; Servat, K.; Napporn, T. W. Shape-Dependent Electrocatalytic Activity of Free Gold Nanoparticles toward Glucose Oxidation. *Gold Bull.* **2013**, *46*, 311–318.

(63) Jeyabharathi, C.; Zander, M.; Scholz, F. Underpotential Deposition of Lead on Quasi-Spherical and Faceted Gold Nanoparticles. *J. Electroanal. Chem.* **2018**, *819*, 159–162.

(64) Kumar, A.; Buttry, D. A. Size-Dependent Underpotential Deposition of Copper on Palladium Nanoparticles. *J. Phys. Chem. C* **2015**, *119*, 16927–16933.

(65) Oviedo, O. A.; Mariscal, M. M.; Leiva, E. P. M. Theoretical Studies of Preparation of Core-Shell Nanoparticles by Electrochemical Metal Deposition. *Electrochim. Acta* **2010**, *55* (27), 8244–8251.

(66) Oviedo, O. A.; Vélez, P.; MacAgno, V. A.; Leiva, E. P. M. Underpotential Deposition: From Planar Surfaces to Nanoparticles. *Surf. Sci.* **2015**, *631*, 23–34.

(67) Sanchez-Sanchez, C. M.; Vidal-Iglesias, F. J.; Solla-Gullon, J.; Montiel, V.; Aldaz, A.; Feliu, J. M.; Herrero,

E. Scanning Electrochemical Microscopy for Studying Electrocatalysis on Shape-Controlled Gold Nanoparticles and Nanorods. *Electrochim. Acta* **2010**, *55*, 8252.

(68) Price, S. W. T.; Speed, J. D.; Kannan, P.; Russell, A. E. Exploring the First Steps in Core-Shell Electrocatalyst Preparation: In Situ Characterization of the Underpotential Deposition of Cu on Supported Au Nanoparticles. *J. Am. Chem. Soc.* **2011**, *133*, 19448–19458.

(69) Oviedo, O. A.; Velez, P.; Macagno, V. A.; Leiva, E. P. M. Underpotential Deposition: From Planar Surfaces to Nanoparticles. *Surf. Sci.* **2015**, *631*, 23–24.

(70) Yu, Y.; Hu, Y.; Liu, X.; Deng, W.; Wang, X. The Study of Pt@Au Electrocatalyst Based on Cu Underpotential Deposition and Pt Redox Replacement. *Electrochim. Acta* **2009**, *54*, 3092–3097.

(71) Wang, L.-L.; Tan, T. L.; Johnson, D. D. Nanoalloy Composition-Temperature Phase Diagram for Catalyst Design: Case Study of Ag-Au. *Phys. Rev. B* **2012**, *86*, 035438.

(72) Melroy, O. R.; Samant, M. G.; Borges, G. L.; Gordon, J. G.; Blum, L.; White, J. H.; Albarelli, M. J.; McMillan, M.; Abruna, H. D. In-Plane Structure of Underpotentially Deposited Copper on Gold(111) Determined by Surface EXAFS.

Langmuir **1988**, *4*, 728–732.

(73) Futamata, M. Coadsorption of Anions and Water Molecule during Underpotential Deposition of Cu and Pb on the Au (1 1 1) Electrode Surface. *Chem. Phys. Lett.* **2001**, *333* (5), 337–343.

(74) Toney, M. F.; Gordon, J. G.; Samant, M. G.; Borges, G. L.; Melroy, O. R.; Yee, D.; Sorensen, L. B. In-Situ Atomic Structure of Underpotentially Deposited Monolayers of Pb and Tl on Au(111) and Ag(111): A Surface X-Ray Scattering Study. *J. Phys. Chem.* **1995**, *99*, 4733–4744.

(75) Liu, Y.; Gokcen, D.; Bertocci, U.; Moffat, T. P. Self-Terminating Growth of Platinum Films by Electrochemical Deposition. *Science (80-.).* **2012**, *338*, 1327–1330.

(76) Ahn, S. H.; Liu, Y.; Moffat, T. P. Ultrathin Platinum Films for Methanol and Formic Acid Oxidation: Activity as a Function of Film Thickness and Coverage. *ACS Catal.* **2015**, *5*, 2124–2136.

(77) Liu, Y.; Hangarter, C. M.; Garcia, D.; Moffat, T. P. Self-Terminating Electrodeposition of Ultrathin Pt Films on Ni: An Active, Low-Cost Electrode for H2 Production. *Surf. Sci.* **2015**, *631*, 141–154.

(78) Deng, Y.-J.; Tripkovic, V.; Rossmeisl, J.; Arenz, M. Oxygen Reduction Reaction on Pt Overlayers Deposited onto a Gold Film: Ligand, Strain, and Ensemble Effects. *ACS Catal.* **2016**, *6*, 671–676.

(79) Jeong, H.; Kim, J. Insights into the Electrooxidation Mechanism of Formic Acid on Pt Layers on Au Examined by Electrochemical SERS. *J. Phys. Chem. C* **2016**, *120*, 24271–24278.

(80) Jeong, H.; Kim, J. Methanol Dehydrogenation Reaction at Au@Pt Catalysts: Insight into the Methanol Electrooxidation. *Electrochim. Acta* **2018**, *283*, 11–17.

(81) Pfisterer, J. H. K.; Liang, Y.; Schneider, O.; Bandarenka, A. S. Direct Instrumental Identification of Catalytically Active Surface Sites. *Nature* **2017**, *549*, 74–77.

(82) Li, M.; Ma, Q.; Zi, W.; Liu, X.; Zhu, X.; Liu, S. Pt Monolayer Coating on Complex Network Substrate with High Catalytic Activity for the Hydrogen Evolution Reaction. *Sci. Adv.* **2015**, *1*, e1400268.

(83) Lee, E.; Sung, M.; Wang, Y.; Kim, J. Atomic Layer Electrodeposition of Pt on Nanoporous Au and Its Application in PH Sensing. *Electroanalysis* **2018**, *30*, 2028–2034.

(84) Wang, Y.; Kim, J. Oxygen Evolution Reaction on Nanoporous Gold Modified with Ir and Pt: Synergistic Electrocatalysis between Structure and Composition. *Electroanalysis* **2019**, *31*, 1026–1033.

(85) Pang, L.; Zhang, Y.; Liu, S. Monolayer-by-Monolayer Growth of Platinum Films on Complex Carbon Fiber Paper Structure. *Appl. Surf. Sci.* **2017**, *407*, 386–390.

(86) Ercolano, G.; Farina, F.; Cavaliere, S.; Jones, D. J.; Roziere, J. Towards Ultrathin Pt Films on Nanofibres by Surface-Limited Electrodeposition for Electrocatalytic Applications. *J. Mater. Chem. A* **2017**, *5*, 3974–3980.

(87) Kim, H.; Choe, S.; Park, H.; Jang, J. H.; Ahn, S. H.; Kim, S.-K. An Extremely Low Pt Loading Cathode for a Highly Efficient Proton Exchange Membrane Water Electrolyzer. *Nanoscale* **2017**, *9*, 19045–19049.

(88) Alpuche-Aviles, M. A.; Farina, F.; Ercolano, G.; Subedi, P.; Cavaliere, S.; Jones, D. J.; Roziere, J. Electrodeposition of Two-Dimensional Pt Nanostructures on Highly Oriented Pyrolytic Graphite (HOPG): The Effect of Evolved Hydrogen and Chloride Ions. *Nanomaterials* **2018**, *8*, 668.

(89) Ahn, S. H.; Tan, H.; Haensch, M.; Liu, Y.; Bendersky, L.

A.; Moffat, T. P. Self-Terminated Electrodeposition of Iridium Electrocatalysts. *Energy Environ. Sci.* **2015**, *8*, 3557–3562.

(90) Hangarter, C. M.; Liu, Y.; Pagonis, D.; Bertocci, U.; Moffat, T. P. Electrodeposition of Ternary Pt100-x-YCoxNiy Alloys. *J. Electrochem. Soc.* **2014**, *161*, D31–D43.

(91) Wang, R.; Bertocci, U.; Tan, H.; Bendersky, L. A.; Moffat, T. P. Self-Terminated Electrodeposition of Ni, Co, and Fe Ultrathin Films. *J. Phys. Chem. C* **2016**, *120*, 16228–16237.

(92) Zhang, J.; Mo, Y.; Vukmirovic, M. B.; Klie, R.; Sasaki, K.; Adzic, R. R. Platinum Monolayer Electrocatalysts for O2 Reduction: Pt Monolayer on Pd(111) and on Carbon-Supported Pd Nanoparticles. *J. Phys. Chem. B* **2004**, *108*, 10955–10964.

(93) Anderson, R. M.; Yancey, D. F.; Loussaert, J. A.; Crooks, R. M. Multistep Galvanic Exchange Synthesis Yielding Fully Reduced Pt Dendrimer-Encapsulated Nanoparticles. *Langmuir* **2014**, *30*, 15009–15015.

(94) Ostojic, N.; Thorpe, J. H.; Crooks, R. M. Electron Transfer Facilitated by Dendrimer-Encapsulated Pt Nanoparticles Across Ultrathin, Insulating Oxide Films. *J. Am. Chem. Soc.* **2016**, *138*, 6829–6837.

(95) Mourdikoudis, S.; Pallares, R. M.; Thanh, N. T. K. Characterization Techniques for Nanoparticles: Comparison and Complementarity upon Studying Nanoparticle Properties. *Nanoscale* **2018**, *10*, 12871–12934.

(96) Vanpaemel, J.; Sugiura, M.; Cuypers, D.; van der Veen, M. H.; De Gendt, S.; Vereecken, P. M. Electrochemical Deposition of Subnanometer Ni Films on TiN. *Langmuir* **2014**, *30*, 2047–2053.

(97) Ritzert, N. L.; Moffat, T. P. Ultramicroelectrode Studies of Self-Terminated Nickel Electrodeposition and Nickel Hydroxide Formation upon Water Reduction. *J. Phys. Chem. C* **2016**, *120*, 27478–27489.

(98) Achari, I.; Ambrozik, S.; Dimitrov, N. Electrochemical Atomic Layer Deposition of Pd Ultrathin Films by Surface Limited Redox Replacement of Underpotentially Deposited H in a Single Cell. *J. Phys. Chem. C* **2017**, *121*, 4404–4411.

(99) Wang, H.; Jiang, K.; Chen, Q.; Xie, Z.; Cai, W.-B. Carbon Monoxide Mediated Chemical Deposition of Pt or Pd Quasi-Monolayer on Au Surfaces with Superior Electrocatalysis for Ethanol Oxidation in Alkaline Media. *Chem. Commun.* **2016**, *52*, 374–377.

(100) Yeung, L. K.; Lee, C. T.; Johnston, K. P.; Crooks, R. M.

Catalysis in Supercritical CO2 Using Dendrimer-Encapsulated Palladium Nanoparticles. *Chem. Commun.* **2001**, No. 21, 2290–2291.

(101) Bronstein, L. M.; Shifrina, Z. B. Dendrimers as Encapsulating, Stabilizing, or Directing Agents for Inorganic Nanoparticles. *Chem. Rev.* **2011**, *111*, 5301–5344.

(102) Bakos, I.; Szabo, S.; Pajkossy, T. Deposition of Platinum Monolayers on Gold. *J. Solid State Electrochem.* **2011**, *15*, 2453–2459.

(103) Pande, S.; Weir, M. G.; Zaccheo, B. A.; Crooks, R. M. Synthesis, Characterization, and Electrocatalysis Using Pt and Pd Dendrimer-Encapsulated Nanoparticles Prepared by Galvanic Exchange. *New J. Chem.* **2011**, *35*, 2054–2060.

(104) Zhang, J.; Sasaki, K.; Sutter, E.; Adzic, R. R. Stabilization of Platinum Oxygen-Reduction Electrocatalysts Using Gold Clusters. *Science* **2007**, *315*, 220–222.

(105) Yancey, D. F.; Chill, S. T.; Zhang, L.; Frenkel, A. I.; Henkelman, G.; Crooks, R. M. A Theoretical and Experimental Examination of Systematic Ligand-Induced Disorder in Au Dendrimer-Encapsulated Nanoparticles. *Chem. Sci.* **2013**, *4*, 2912–2921.

(106) Kresse, G.; Furthmuller, J. Efficiency of Ab-Initio Total Energy Calculations for Metals and Semiconductors Using a Plane-Wave Basis Set. *Comput. Mater. Sci.* **1996**, *6*, 15–50.

(107) Kresse, G.; Furthmueller, J. Efficient Iterative Schemes for Ab Initio Total-Energy Calculations Using a Plane-Wave Basis Set. *Phys. Rev. B* **1996**, *54*, 11169–11186.

(108) Blochl, P. E. Projector Augmented-Wave Method. *Phys. Rev. B* **1994**, *50*, 17953.

(109) Kresse, G.; Joubert, D. From Ultrasoft Pseudopotentials to the Projector Augmented-Wave Method. *Phys. Rev. B* **1999**, *59*, 1758–1775.

(110) Perdew, J. P.; Ruzsinszky, A.; Csonka, G. I.; Vydrov, O. A.; Scuseria, G. E.; Constantin, L. A.; Zhou, X.; Burke, K. Restoring the Density-Gradient Expansion for Exchange in Solids and Surfaces. *Phys. Rev. Lett.* **2008**, *100*, 136406.

(111) Duan, Z.; Li, Y.; Timoshenko, J.; Chill, S. T.; Anderson, R. M.; Yancey, D. F.; Frenkel, A. I.; Crooks, R. M.; Henkelman, G. A Combined Theoretical and Experimental EXAFS Study of the Structure and Dynamics of Au147 Nanoparticles. *Catal. Sci. Technol.* **2016**, *6*, 6879–6885.

(112) Zabinsky, S. I.; Rehr, J. J.; Ankudinov, A.; Albers, R.

C.; Eller, M. J. Multiple-Scattering Calculations of X-Ray Absorption Spectra. *Phys. Rev. B* **1995**, *52*, 2995.

(113) Kim, Y. G.; Oh, S.-K.; Crooks, R. M. Preparation and Characterization of 1-2 Nm Dendrimer-Encapsulated Gold Nanoparticles Having Very Narrow Size Distributions. *Chem. Mater.* **2004**, *16*, 167–172.

(114) Nagahara, Y.; Hara, M.; Yoshimoto, S.; Inukai, J.; Yau, S.-L.; Itaya, K. In Situ Scanning Tunneling Microscopy Examination of Molecular Adlayers of Haloplatinate Complexes and Electrochemically Produced Platinum Nanoparticles on Au(111). *J. Phys. Chem. B* **2004**, *108*, 3224–3230.

(115) Machado, S. A. S.; Tanaka, A. A.; Gonzalez, E. R. Underpotential Deposition of Copper and Its Influence in the Oxygen Reduction on Platinum. *Electrochim. Acta* **1991**, *36*, 1325–1331.

(116) Frenkel, A. I. Applications of Extended X-Ray Absorption Fine-Structure Spectroscopy to Studies of Bimetallic Nanoparticle Catalysts. *Chem. Soc. Rev.* **2012**, *41*, 8163–8178.

(117) Menard, L. D.; Wang, Q.; Kang, J. H.; Sealey, A. J.; Girolami, G. S.; Teng, X.; Frenkel, A. I.; Nuzzo, R. G. Structural Characterization of Bimetallic Nanoparticles with Overlapping X-Ray Absorption Edges. *Phys. Rev. B* **2009**, *80*,

064111.

(118) Garcia-Gutierrez, D. I.; Gutierrez-Wing, C. E.; Giovanetti, L.; Ramallo-Lopez, J. M.; Requejo, F. G.; Jose-Yacaman, M. Temperature Effect on the Synthesis of Au-Pt Bimetallic Nanoparticles. *J. Phys. Chem. B* **2005**, *109*, 3813–3821.

(119) Klementiev, K. V. XAFSmass, freeware.

(120) Calvin, S. *XAFS for Everyone*; CRC Press: Taylor & Francis Group: Boca Raton, FL, 2013.

(121) Zhou, S.; Jackson, G. S.; Eichhorn, B. AuPt Alloy Nanoparticles for CO-Tolerant Hydrogen Activation: Architectural Effects in Au-Pt Bimetallic Nanocatalysts. *Adv. Func. Mater.* **2007**, *17*, 3099–3104.

(122) Divi, S.; Chatterjee, A. Understanding Segregation Behavior in AuPt, NiPt, and AgAu Bimetallic Nanoparticles Using Distribution Coefficients. *J. Phys, Chem. C* **2016**, *120*, 27296–27306.

(123) Pedersen, M. O.; Helveg, S.; Ruban, A.; Stensgaard, I.; Laegsgaard, E.; Norskov, J. K.; Besenbacher, F. How a Gold Substrate Can Increase the Reactivity of a Pt Overlayer. *Surf. Sci.* **1999**, *426*, 395–409.

(124) Irissou, E.; Laplante, F.; Garbarino, S.; Chaker, M.; Guay, D. Structural and Electrochemical Characterization of Metastable PtAu Bulk and Surface Alloys Prepared by Crossed-Beam Pulsed Laser Deposition. *J. Phys. Chem. C* **2010**, *114*, 2192–2199.

(125) Wang, D.; Liu, S.; Wang, J.; Lin, R.; Kawasaki, M.; Rus, E.; Silberstein, K. E.; Lowe, M. A.; Lin, F.; Nordlund, D.; et al. Spontaneous Incorporation of Gold in Palladium-Based Ternary Nanoparticles Makes Durable Electrocatalysts for Oxygen Reduction Reaction. *Nat. Commun.* **2016**, *7*, 11941.

(126) Weir, M. G.; Knecht, M. R.; Frenkel, A. I.; Crooks, R. M. Structural Analysis of PdAu Dendrimer-Encapsulated Bimetallic Nanoparticles. *Langmuir* **2010**, *26*, 1137–1146.

(127) Shao, M.; Chang, Q.; Dodelet, J.-P.; Chenitz, R. Recent Advances in Electrocatalysts for Oxygen Reduction Reaction. *Chem. Rev.* **2016**, *116*, 3594–3657.

(128) Guo, S.; Zhang, S.; Sun, S. Tuning Nanoparticle Catalysis for the Oxygen Reduction Reaction. *Angew. Chem. Int. Ed.* **2013**, *52*, 8526–8544.

(129) Turner, M.; Golovko, V. M.; Vaughan, O. P. H.; Abdulkin, P.; Berenguer-Murcia, A.; Tikhov, M. S.; Johnson, B. F. G.; Lambert, R. M. Selective Oxidation with Dioxygen by Gold

Nanoparticle Catalysts Derived from 55-Atom Clusters. *Nature* **2008**, *454*, 981–983.

(130) Kwangjin, A.; Somorjai, G. A. Size and Shape Control of Metal Nanoparticles for Reaction Selectivity in Catalysis. *Chem. Cat. Chem.* **2012**, *4*, 1512–1524.

(131) Roduner, E. Size Matters: Why Nanomaterials Are Different. *Chem. Soc. Rev.* **2006**, *35*, 583–592.

(132) Green, M. P.; Hanson, K. J.; Carr, R.; Lindau, I. STM Observations of the Underpotential Deposition and Stripping of Pb on Au(111) under Potential Sweep Conditions. *J. Electrochem. Soc.* **1990**, *137*, 3493–3498.

(133) Kresse, G.; Hafner, J. Ab Initio Molecular Dynamics for Liquid Metals. *Phys. Rev. B* **1993**, *47*, 558–561.

(134) Taylor, C. D.; Wasileski, S. A.; Filhol, J.-S.; Neurock, M. First Principles Reaction Modeling of the Electrochemical Interface: Consideration and Calculation of a Tunable Surface Potential from Atomic and Electronic Structure. *Phys. Rev. B* **2006**, *73*, 165402.

(135) Matthew, K.; Sundararaman, R.; Letchworth-Weaver, K.; Arias, T. A.; Hennig, R. G. Implicit Solvation Model for Density-Functional Study of Nanocrystal Surfaces and

Reaction Pathways. *J. Phys. Chem.* **2014**, *140*, 084106.

(136) Duan, Z.; Henkelman, G. Calculations of the PH-Dependent Onset Potential for CO Electro-Oxidation on Au(111). *Langmuir* **2018**, *34*, 15268–15275.

(137) Duan, Z.; Henkelman, G. Theoretical Resolution of the Exceptional Oxygen Reduction Activity of Au(100) in Alkaline Media. *ACS Catal.* **2019**, *9*, 5567–5573.

(138) Karlberg, G. S.; Jaramillo, T. F.; Skulason, E.; Rossmeisl, J.; Bligaard, T.; Norskov, J. K. Cyclic Voltammograms for H on Pt(111) and Pt(100) from First Principles. *Phys. Rev. Lett.* **2007**, *99*, 126101.

(139) Weitzner, S. E.; Dabo, I. Quantum-Continuum Simulation of Underpotential Deposition at Electrified Metal-Solution Interfaces. *npj Comput. Mater.* **2017**, *3*, 1.

(140) Trasatti, S.; Petrii, O. A. Real Surface Area Measurements in Electrochemistry. *Pure Appl. Chem.* **1991**, *63*, 711–734.

(141) Hernández, J.; Solla-Gullón, J.; Herrero, E. Gold Nanoparticles Synthesized in a Water-in-Oil Microemulsion: Electrochemical Characterization and Effect of the Surface Structure on the Oxygen Reduction Reaction. *J. Electroanal. Chem.* **2004**, *574* (1), 185–196.

(142) Zoval, J. V.; Lee, J.; Gorer, S.; Penner, R. M. Electrochemical Preparation of Platinum Nanocrystallites with Size Selectivity on Basal Plane Oriented Graphite Surfaces. *J. Phys. Chem. B* **1998**, *102*, 1166–1175.

(143) Shen, P.; Chi, N.; Chan, K.-Y.; Phillips, D. L. Platinum Nanoparticles Spontaneously Formed on HOPG. *Appl. Surf. Sci.* **2001**, *172*, 159–166.

(144) Juarez, M. F.; Fuentes, S.; Soldano, G. J.; Avalle, L.; Santos, E. Spontaneous Formation of Metallic Nanostructures on Highly Oriented Pyrolytic Graphite (HOPG): An Ab Initio and Experimental Study. *Faraday Discuss.* **2014**, *172*, 327–347.

(145) Arroyo Gomez, J. J.; Garcia, S. G. Spontaneous Deposition of Pt-Nanoparticles on HOPG Surfaces. *Surf. Interface Anal.* **2015**, *47*, 1127–1131.

(146) Lu, G.; Zangari, G. Electrodeposition of Platinum on Highly Oriented Pyrolytic Graphite. Part I: Electrochemical Characterization. *J. Phys. Chem. B* **2005**, *109*, 7998–8007.

(147) Lu, G.; Zangari, G. Electrodeposition of Platinum Nanoparticles on Highly Oriented Pyrolytic Graphite. Part II: Morphological Characterization by Atomic Force Microscopy. *Electrochim. Acta* **2006**, *51*, 2531–2538.

(148) Arroyo-Gomez, J. J.; Garcia, S. G. Platinum Nanoparticles Spontaneously Formed on Glassy Carbon Substrates. *J. Nanopart. Res.* **2018**, *20*, 1–8.

(149) Frittmann, S.; Schuster, R. Role of Anions During the Cu Underpotential Deposition on Au(111): A Microcalorimetric Investigation. *J. Phys. Chem. C* **2016**, *120*, 21522–21535.

(150) Velez, P.; Cuesta, A.; Leiva, E. P. M.; Macagno, V. A. The Underpotential Deposition That Should Not Be: Cu(1x1) on Au(111). *Electrochem. Commun.* **2012**, *25*, 54–57.

(151) Sanchez, C.; Leiva, E. P. M. Cu Underpotential Deposition on Au(111) and Au(100). Can This Be Explained in Terms of the Energetics of the Cu/Au System? *Electrochim. Acta* **1999**, *45*, 691–697.

(152) Borges, G. L.; Kanazawa, K. K.; Gordon, J. G. An In-Situ Electrochemical Quartz Crystal Microbalance Study of the Underpotential Deposition of Copper on Au(111) Electrodes. *J. Electroanal. Chem.* **1994**, *364*, 281–284.

(153) Garcia-Martinez, J. C.; Crooks, R. M. Extraction of Au Nanoparticles Having Narrow Size Distributions from Within Dendrimer Templates. *J. Am. Chem. Soc.* **2004**, *126*, 16170–16178.

(154) Hong, W.; Li, C. W. Microstructural Evolution of Au@Pt Core-Shell Nanoparticles under Electrochemical Polarization. *ACS Appl. Mater. Interfaces* **2019**, *11*, 30977–30986.

(155) Krstajic Pajic, M. N.; Stevanovic, S. I.; Radmilovic, V. V.; Gavrilovic-Wohlmuther, A.; Zabinski, P.; Elezovic, N. R.; Radmilovic, V. R.; Gojkovic, S. L.; Jovanovic, V. M. Dispersion Effect in Formic Acid Oxidation on PtAu/C Nanocatalyst Prepared by Water-in-Oil Microemulsion Method. *Appl. Catal. B* **2019**, *243*, 585–593.

(156) Larsen, A. H.; Mortensen, J. J.; Blomqvist, J.; Castelli, I. E.; Christensen, R.; Dulak, M.; Friis, J.; Groves, M. N.; Hammer, B.; Hargus, C. The Atomic Simulation Environment-a Python Library for Working with Atoms. *J. Phys. Condens. Matter* **2017**, *29*, 273002.

(157) Yu, Y.; Lim, K. H.; Wang, J. Y.; Wang, X. CO Adsorption Behavior on Decorated Pt@Au Nanoelectrocatalysts: A Combined Experimental and DFT Theoretical Calculation Study. *J. Phys. Chem. C* **2012**, *116*, 3851–3856.

(158) Jablonski, A.; Powell, C. J. Information Depth and the Mean Escape Depth in Auger Electron Spectroscopy, and x-Ray Photoelectron Spectroscopy. *J. Vac. Sci. Technol. A* **2003**, *21*, 274–283.

(159) Koper, M. T. M. Structure Sensitivity and Nanoscale Effects in Electrocatalysis. *Nanoscale* **2011**, *3*, 2054–2073.

(160) Ferre-Vilaplana, A.; Perales-Rondon, J. V.; Buso-Rogero, C.; Feliu, J. M.; Herrero, E. Formic Acid Oxidation on Platinum Electrodes: A Detailed Mechanism Supported by Experiments and Calculations on Well-Defined Surfaces. *J. Mater. Chem. A* **2017**, *5*, 21773–21784.

(161) Capon, A.; Parsons, R. The Oxidation of Formic Acid at Noble Metal Electrodes. Part III. Intermediates and Mechanism on Platinum Electrodes. *J. Electroanal. Chem. Interfacial Electrochem.* **1973**, *45*, 205–231.

(162) Neurock, M.; Janik, M.; Wieckowski, A. A First Principles Comparison of the Mechanism and Site Requirements for the Electrocatalytic Oxidation of Methanol and Formic Acid over Pt. *Faraday Discuss.* **2009**, *140*, 363–378.

(163) Cuesta, A.; Escudero, M.; Lanova, B.; Baltruschat, H. Cyclic Voltammetry, FTIRS, and DEMS Study of the Electrooxidation of Carbon Monoxide, Formic Acid, and Methanol on Cyanide-Modified Pt(111) Electrodes. *Langmuir* **2009**, *25*, 6500–6507.

(164) Topalov, A. A.; Cherevko, S.; Zeradjanin, A. R.; Meier, J. C.; Katsounaros, I.; Mayrhofer, K. J. J. Towards a

Comprehensive Understanding of Platinum Dissolution in Acidic Media. *Chem. Sci.* **2014**, *5*, 631–638.

(165) Li, H.; Shin, K.; Henkelman, G. Effects of Ensembles, Ligand, and Strain on Adsorbate Binding to Alloy Surfaces. *J. Chem. Phys.* **2018**, *149*, 174705.